An Impedance Frequency Response Approach for Analyzing Interactions in Ac-dc Systems

By

Yi Qi

A Thesis submitted to the Faculty of Graduate Studies of
The University of Manitoba
in partial fulfillment of the requirements for the degree of

Doctor of Philosophy

Department of Electrical and Computer Engineering
The University of Manitoba
Winnipeg, Manitoba, Canada

Acknowledgements

I want to show my deepest gratitude to Dr. Aniruddha Gole for his supervision, time and patience in the period of the program, and will always learn from him in the future.

I want to say thank you very much to Dr. Yi Zhang for being my committee helping me all the time.

I want to say thank you to Dr. R. Sri Ranjan and Dr. Wilsun Xu for being my committee.

I acknowledge the support from NSERC and MITACS with Manitoba Hydro, as well as the academic help from Dr. Ioni Fernando.

I appreciate my co-authors for their help in the research work and the big lab family for their support and friendship.

I also want to say thank you to Prof. Chen Chen my Master program's supervisor.

Last but not least, I appreciate the support and love from my family, including my parents, inlaws, wife Wei, and kids Anthony and Ivy.

Yi Qi

Abstract

This thesis presents an integrated technique for screening the interaction level between the ac side system and dc side converters. The system resonances in the sub-synchronous and super-synchronous frequency range are identified and stability determined. This approach applies the Generalized Nyquist stability Criterion (GNC) assuming that the frequency dependent impedance responses are available.

The frequency responses of the subsystems are obtained using two different techniques. One is an analytical state variable analysis requiring the mathematical model of the system elements; and the other is a simulation-based frequency scanning approach which does not rely on detailed knowledge of the internal system. These two techniques can be applied in different situations. The state variable analysis is useful when a small signal model is derivable, e.g., for the HVdc converter system, and the frequency scanning method is useful if only 'black boxed' models are available. For stability analysis, the systems are represented in the dq0 domain which gets rid of the coupling between frequencies.

The frequency scanning is conducted on two Electromagnetic Transients (EMT) simulation platforms, the off-line PSCAD/EMTDC and the real-time RTDS. PSCAD/EMTDC uses a highly-accurate bi-valued resistor model for the switches and its scanned impedance response matches the analytically derived result very well. The RTDS uses a more approximate technique that allows high speed simulation. The impedance scans from RTDS also agree with the analytical results showing that the scanning technique is also a mechanism for validating various new models.

An important contribution of this research is the development of an improved small signal analytical model of the Line Commutated Converter (LCC). Traditional studies neglected the transient dynamics of the commutation inductor and modeled it as the reactance of fundamental frequency. The model realized here assumes an infinite series-connected 6-pulse converters and regards the 12-pulse converter as one of its sampled versions. With this treatment, the waveforms of the currents and voltages are ripple-free, and the measured angles, i.e., the overlap angle and the extinction angle become continuous. This model is validated by comparing the analytical converter response with the one obtained from the frequency scanning. Moreover, this LCC model is interfaced with an arbitrary external system, where the system stability is determined using GNC.

Based on the impedance responses, the ac-dc system is represented as a closed-loop system, in which the dc side impedance is the forward gain and the ac side admittance is the feedback, or vice versa. The GNC is applied on the closed-loop system and a new index "Harmonic Stability Margin" is proposed to indicate how much a gain or other parameter can be scaled so that the system reaches the boundary of instability. As the index can parameterize the ac-dc interaction level, HSM is then used in several case systems to study the Sub-Synchronous Control Interaction (SSCI), the impact of detailed modeling of remote side converter, as well as the multi-infeed system study. All the results are validated by EMT simulations.

Index Terms: Ac-dc interaction; impedance response; Electromagnetic Transients (EMT) simulations; frequency scan; LCC improved model; Generalized Nyquist stability Criterion (GNC); Harmonic Stability Margin (HSM)

Contents

List of Symbols

Z/G	*Impedance / Admittance (matrix)*
f	*Frequency of sinusoidal wave or reference system*
ω	*Rotation speed of sinusoidal wave or reference system*
$\varphi,\ \delta$	*Phase angle*
t	*Time*
i, j	*Complex operator*
a, b	*Symmetrical operator*
ω_0	*Steady state power network speed*
V	*Voltage*
I	*Current*
LCC	*Line commutated converter*
VSC	*Voltage source converter*
MMC	*Modular multi-level converter*
X_{abc}	*Component in abc phase domain*
X_{+-0}	*Component in positive, negative and zero domain*
X_{dq0}	*Component in direct, quadrature and zero domain*
min {}	*minimum value in the bracket*
max {}	*maximum value in the bracket*
C_f	*Filter capacitance connected to the PCC bus*
α	*Firing angle in LCC converter*
μ	*Overlap angle in LCC converter*
γ	*Extinction angle in LCC converter*
X_c	*Commutation reactance in LCC converter*
L_t, R_t	*Transformer inductance and resistance in VSC converter*
A, B, C, D	*System matrices in state space representation*
θ_{pll}	*Transient term of the PLL angle*
*K**	*LCC converter matrix relating the inputs to outputs in traditional definition*
K	*LCC converter matrix developed in this thesis*
SCR	*Short Circuit Ratio*
HSM	*Harmonic stability margin*

List of Figures

List of Tables

1 Introduction

1.1 Background

Before the introduction of power electronic switches, the traditional power system mainly consisted of elements like generators, transformers and power loads [1]. Because of the slow response of these units, the steady state analysis, combined with electromechanical transient study were accurate enough to investigate the system stability and oscillation characteristics. However, modern-day power electronic converters based on the thyristor and the Insulated Gate Bipolar Transistor (IGBT) have faster reaction speeds and controllable characteristics of switching valves [2-5]. The interaction between the ac network and power electronic equipment which can result in the system resonance or even instability has been a topic of considerable interest [2-7].

Back in the 1950s, the modern Direct Current (dc) transmission technology was developed based on mercury-arc valves, which enabled two ac networks to be connected via a dc link. Later, these valves were upgraded to semiconductor valves, i.e., thyristors. Thyristors are more robust as compared to mercury-arc valves as they are not subjected to problems such as arc-back and arc-through. They can be turned on with a firing pulse but require the network voltage to establish the reverse bias for turn-off [8]. More recently, new switching semiconductor valves such as IGBTs have become available, which in addition to capable

of being turned on, can also be turned off with a gate pulse, allowing for greater flexibility in operation [9]. Based on these two kinds of controllable switching valves, two different type of ac-dc converters are in service nowadays:

(1) The Line Commutated Converter (LCC), which is also known as a current source converter [10]. This type of converter uses thyristor switches [8] which can be turned on by a gating signal but rely on the ac system voltage to provide the reverse bias for turn-off. The dc current is sustained around its steady state value with a dc smoothing reactor [2].

(2) The Voltage Source Converter (VSC) utilizes controllable IGBT [9] switches capable of both turn-on and turn-off with gating commands. The dc side voltage is maintained nearby a constant value (using a dc capacitor if needed). The (three phase) ac side voltages are generated from the dc voltage with the Pulse Width Modulation (PWM) technique, and hence contain not only fundamental frequency component, but also high frequency harmonics. This kind of converter came out in the 1990s [5]. More recently, a new topology of the VSC, i.e., the Modular Multi-Level Converter (MMC) is becoming popular [11]. It generates a voltage waveform which is largely ripple free and requires no filtering.

Operation of the HVdc converter connected to the ac system can sometimes result in undesirable interaction, one of these being unexpected harmonic resonance. Under some specific operating conditions, a disturbance to the ac-dc system could produce voltage and current oscillation at one or more frequencies or even result in instability [12-14]. This

interaction between the ac and dc subsystems is the main concern for this study.

The literature review of the ac-dc system interaction study is presented below. At first, with LCC projects, the ac system was represented in a very simple manner, i.e., by the fundamental frequency impedance to quantify system interaction level [6, 15-24]. The dc converter characteristics were also very important to decide the power and voltage stability, and linearized models [25] of the LCC were developed [26-30]. These approaches considered steady-state power-voltage instability (akin to voltage stability in purely ac networks) and did not involve the transient dynamics of the system. Later, the state space analysis of the LCC based system were put forward to study the system stability, and Electromagnetic Transients (EMT) simulation was used to validate the result [31-36]. However, as the turn-off of the valves is related to the system behavior, the modeling of the LCC is very tough, and the models proposed cannot accurately represent the frequency response of the converters.

In 1990s, the emerging VSC, which used switch-off capable devices such as the IGBT began to become widely used. It was relatively easy to obtain the linearized state equations, and then to predict the behavior using the well-established linear system theory [5, 37-43]. Also, the frequency responses of the ac side impedance had to be considered in the analysis rather than only the fundamental frequency representation [44-50]. Hence, the ac side frequency responses were studied based on techniques such as frequency scanning and analytical modeling [51-60], with which the stability of the combined ac-dc system can be analyzed with techniques such as the Nyquist Stability Criterion (NSC) [61-64].

1.1.1 Representation of the ac system in fundamental frequency

Traditionally, ac-dc system interaction studies focused on the real power transfer limits, harmonic instability and transient overvoltage (TOV) resulting from converter blocking [6]. For such studies, engineers generally modeled the ac network as a Thevenin voltage source in series with a simple passive network, a typical configuration being a series R-L circuit. The short circuit current [15], or Short Circuit Ratio (SCR) [6, 16-17] at fundamental frequency was introduced as the indicator of ac system strength. The SCR was defined as the ratio of converter bus short circuit capacity to dc rated power. The CIGRE Working Group 14.07 (1992) [6] proposed the Effective Short Circuit Ratio (ESCR) to include the effect of the ac filters and shunt capacitors connected to the ac conversion bus. Heuristically, the condition "ESCR <=2" was a threshold below which the system was vulnerable to transient disturbances, such as the load rejection overvoltage and harmonic instability.

A system where many dc converters are connected to the same ac network, is referred to as a multi-infeed system. For this kind of system, Denis Lee Hau Aik (1997) [18] employed the power flow Jacobian matrix to study the voltage stability and interaction between different dc converters. In his Ph. D thesis [19], the equivalent ESCR, as well as some other Jacobian matrix-based indices were proposed for multi-infeed systems. Almost at the same time, Paulo Fischer de Toledo (2005) [20] introduced the Multi-infeed Effective Short Circuit Ratio (MESCR) based on the node admittance matrix. CIGRE working group B4.41

(2008) [7] recommended another index - Multi-Infeed Interaction Factor (MIIF), which was a measure of voltage sensitivity, i.e., how much a small change of voltage at one converter's busbar would affect the voltage at another converter's busbar. MIIF can be calculated from the power flow Jacobian matrix, from an Electromagnetic Transients (EMT) simulation or from experimental measurements on an actual system. It was applied in systems with both inverter and rectifier infeed [21][22]. There were also some other indices such as MIESCR and IESCR [23][24].

Using the indices such as ESCR / MIESCR for representing the ac system, graphical representations such as the "Maximum Available Power" (MAP) curves was developed. The MAP curve is a plot of the delivered power as a function of the dc current. For low dc currents, the power is almost proportional to the current; however larger currents cause a drop in the ac voltage and consequently in the dc voltage. This makes the MAP curve to reverse direction. The peak point of the MAP curve is referred to as the "Maximum Available Power" point and determines the maximum power that can be transmitted. Also, if the converter is in power control with dc current controlling the power, operation in the right of the MAP point results in instability. The MAP curves were then plotted as a function of SCR value as in Fig. 1-1, in which the Critical SCR (CSCR) value (shown as 2.1 in Fig. 1-1) indicating marginally stable system can be found as the derivative dP_{dc}/dI_{dc} was zero at the rated power [6, 18-24]. The system with an SCR smaller than CSCR would be determined as unstable.

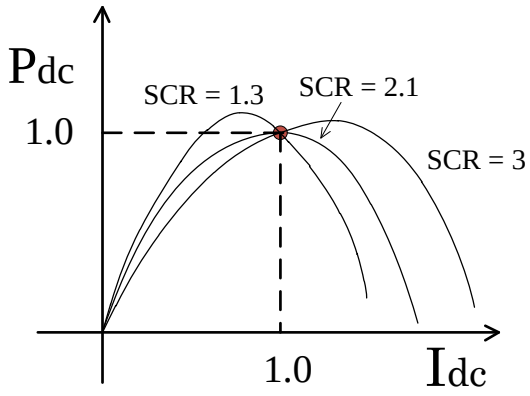

Figure 1-1. MAP curves for different SCR values

1.1.2 Representation of LCC using linearized algebraic equations

Although non-linear analysis using the MAP approach was successful in studying the steady-state behavior of the ac-dc system, the non-linear representation made it difficult to learn the converter's dynamic performance. Linearizing the behavior of the converter allowed easier investigation into the dynamic performance, as linear system theory [25] provides a powerful framework for analysis of system stability. However, to do so for a non-linear system, it requires the system to be linearized around its operating point. In some works, the linearization was only applied on the algebraic equations [17] to investigate power-voltage instability phenomena, and the differential equations of the system were not included. Later, E. V. Persson (1970) [26] represented the LCC system as transfer function blocks. In this approach, the frequency dependent characteristics caused by the commutation overlap and the control system were included. A locus of the real and imaginary components as a function of frequency was plotted to determine the system stability using Nyquist analysis [25], where stability could be determined by investigating

whether the locus encircled the -1+j0 point or not. In 1995, A. R. Wood [27][28] improved Persson's work by a more accurate modelling of the commutation overlap. The Electromagnetic Transients Program (EMTP) was used to validate the model. In his Ph. D thesis [29], he also improved the analysis accuracy by combining the coupled positive and negative sequence impedances to predict stability at harmonic frequencies. In his later study, the Phase Locked Loop (PLL) and the ac filter were included [30].

1.1.3 State space analysis of the LCC

Modern linear control theory [25] concerns itself with solution of the stability problems by a state space representation in the Laplace domain (i.e., s-domain) of the form $sX = AX + BU$ where X is the n-dimensional state variable vector, U is the m-dimensioned input vector, A is the state matrix and B is the input matrix of dimension n x m. The system stability can be determined from the eigenvalues of A. In 1990, P. Kundur introduced an integrated analysis program called "Small Signal Stability Program (SSAP)" for stability analysis and controller design, which utilized the eigenvalue analysis of the state space model of the power system [31]. Inside the program users could create self-defined elements in addition to a default library of elements. S. Arabi (1991) [32] used this feature to develop the models of HVdc and Static Var Compensator (SVC) in state equation form.

The state space form also makes itself available for investigating stability with novel control strategies. S. Venkataraman (1994) [33] designed the controller of HVdc using robustness methodology based on the L_∞ theory to enhance the system damping. In 1999,

Dragan Jovcic studied the stability of LCC whose controller included a PLL [34]. Ac and dc network dynamics were modeled by representing these networks using resistors, capacitors and inductors. The root locus with respect to the PLL gain was plotted to determine the stability. A comparison between the time domain responses obtained from the analytical model and from an EMT simulation program PSCAD/EMTDC [35] (Power System Computer Aided Design / Electromagnetic Transients including DC) was made for validation purposes. In 2009, Chandana Karawita [36] modeled the HVdc system as a control block diagram and interfaced this to an ac system which consisted of synchronous machines, exciters and governor-turbine systems. In his research, mode shapes and participation factor were used to quantify how the eigenvalues were affected by some system parameters.

1.1.4 State space representation of the VSCs

In 1997, ABB Power Systems put forward the new VSC technology [5], which used IGBT valves capable of both turn-on and turn-off by the gating signal. Thus, the reliance on ac voltage in the commutation process was no longer necessary. This kind of converter was less prone to ac side disturbances and had better transient performances when connected to low SCR systems. The recovery speed after fault was improved. A prototype 3MW system was constructed to demonstrate the configuration. A switching function based small signal model of VSC-HVDC which led to a state variable representation was presented soon thereafter [37][38]. Due to the precise control of turn-on and turn-off instants, the models were significantly simpler to that of the LCC.

There are mainly two popular control approaches for VSC converters: power-angle control [39] and vector current control [40]. Power-angle control typically uses one Proportional-Integral (PI) controller and the vector current control use two PI controllers in each of the two loops, referred to Fig. 3-5 later. Zheng Chao (2006) [41] included the power-angle control system in the ac-dc system model and enhanced the system stability by adding a damping controller. This model was verified using the Power System Analysis Software Package (PSASP/UPI).

The vector current control can decouple the active and reactive power control loops. For example, when a change in active current is ordered, the reactive current remains constant and vice versa. State variable models of VSC with vector current control were developed [42][43]. In the work of J. Zhou (2014) [43], a detailed state space model of VSC system was constructed including the electrical circuits, vector current control system and PLL. The current and voltage measuring transducers were modeled as first-order transfer functions. Moreover, the model was validated by comparing the step response of the analytical model with the response obtained from EMT simulation. Unexpectedly, it was found that the angle tracking of the PLL was still a significant restriction for power transmission when the converters were connected to low SCR systems. In these situations, a high proportional or integral (PI) gain would worsen the power transmission capability and small signal stability.

Lidong Zhang (2010) [42] proposed a power synchronized control other than the two

control algorithms above. The main feature of this controller was, the voltage angle of VSC would increase if the converter receives more active power than the reference value, and the VSC performs like a virtual synchronous generator. However, this control philosophy did not receive wide application due to the poor performance in large disturbance transients. Another important part of his work was the introduction of a dynamic frequency dependent Jacobian transfer matrix. In contrast with the scalar Jacobian matrix of Section 1.1.1 which only considered the fundamental frequency response, this Jacobian transfer matrix included the frequency response. Time domain simulations in PSCAD/EMTDC were used to validate the frequency responses of the converters.

1.1.5 Ac system representation with frequency dependence

The modeling of ac system is challenging since it can include thousands of buses, generators, and other equipment. Also, for commercial or security related reasons, sometimes part of the system is only available as a 'black box' with no internal details. Hence, simplified representations are usually employed where the precise details of the network are unavailable. However, such representations should capture the essential behavior of the larger network at all frequencies of interest which they represent.

To address this concern, N.G. Hingorani (1970) [44] utilized an equivalent linear circuit to fit the impedance response of an ac system. N. R. Watson (1987) [45] employed direct synthesis and multivariable optimization techniques to derive this equivalent circuit. The optimization ensured a close fit with the performance of the original network. He also

showed that the mutual coupling impedance between the three phases should be considered in high frequency analysis.

More recently, a frequency dependent network equivalent (FDNE) [46] technique was proposed to represent the ac system as a single-port or multi-port system. Xi Lin (2010) [47] used the vector fitting algorithm [48-50] to form an s-domain transfer function which had the same frequency response characteristic as the original network. This transfer function representation was then implemented as an FDNE block on an EMT simulator (RTDS). Using this approach, he was able to model a 470-bus (3-phase) on six RTDS racks. Implementing the full system would have required more than 20 racks. He showed that the simulation results of the simplified system matched very well with the results from the detailed system's simulation.

1.1.6 Measurement of frequency impedance responses

The FDNE mentioned above assumed that the ac network to be simplified was linear and passive systems. Although this is approximately true of most ac transmission networks, sometimes the system contains non-linear elements, such as non-linear loads, HVdc and Flexible AC Transmission Systems (FACTS). The frequency domain representations of these elements are only valid when the system is linearized for small excursions around an operating point. The resulting linearized model is referred to as the "small signal" model. Naturally, this small signal model is dependent on the operating points.

The impedance responses for three-phase systems were considered in the phase ‘abc’ domain at first. To measure the responses, A. de Oliveira (1991) [51] proposed a simulation-based approach which simulated the system at an operating point and then injected a small disturbance (the perturbation signal). The response at characteristic frequency was determined with one frequency order at a time. Similar approach was also proposed in [52].

An early example where this impedance measuring technique was used to identify resonances in a network was with the prediction of the oscillation frequency in the LCC CIGRE Benchmark model [53]. When this model was originally proposed, it was designed with a resonance frequency at second harmonic frequency on the ac system side and the complementary fundamental frequency on the dc side. Hence it was predicted that the system would resonate at 2^{nd} harmonic on the ac side, as these two complementary resonances on the ac and dc side would result in the oscillation amplification. However, this behavior was not observed in the time domain simulation. It was then realized that, the impedance of the dc side when viewed from the converter’s ac terminals in parallel with the ac side impedance was not tuned to second harmonic. Xiao Jiang (1993) [54] scanned the frequency dependent impedance to validate this inference by injecting a harmonic current to the PCC bus of the system in an EMT type program, as in Fig. 1-2.

This injected current contained component with wide band frequencies (with same interval commonly). By adding a frequency dependent phase shift, the peak value of the multi-sine current can be effectively suppressed, as shown in (1.1).

$$I_h = \sum_{n=1}^{120} A \sin(2\pi f_n t + k \frac{\pi}{180} n^2) \quad (1.1)^{[54]}$$

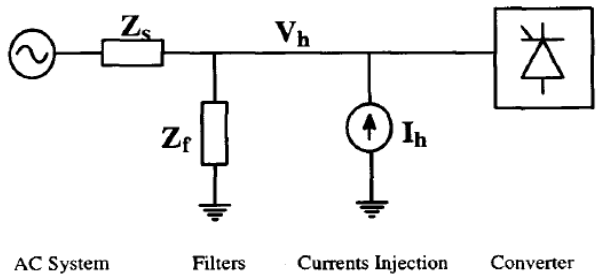

Figure 1-2. The figure in [54] illustrating the current injection

Where, A is the magnitude, f_n is the frequency range interested, e.g., 81-200 Hz, k is a constant coefficient. Using this special "energy dispersed" probing signal, the response at many frequencies can be scanned in one series of simulation. Using this technique on the CIGRE Benchmark model, the scanned system impedance looking from the PCC bus was shown to have a resonance frequency about 125 Hz, slightly higher than the 2nd harmonic. Thus, the instability at second harmonic cannot be observed.

Wilsun Xu (2001) [55] extended the frequency scanning technique to the alpha-beta-zero (Clark Transformation, $\alpha\beta0$) domain, since the impedance matrix of a three-phase balanced system in the $\alpha\beta0$ domain was shown as a diagonal matrix. He applied the $\alpha\beta0$ domain scanning on a practical case system and verified the resonance between the ac system and the shunt capacitor connected to one ac bus.

Later, it was found that for a system including a converter, there was a frequency coupling

phenomenon in the ac voltages and currents in the phase 'abc' domain. For example, an injection of three-phase voltages at frequency f on the ac side can generate ac currents of frequency f and $f \pm 2f_0$, where f_0 is the fundamental frequency [56]. This was caused by the time-varying characteristic of the converters' switching functions relating the phase domain ac current and dc current, or the phase domain ac voltage and dc voltage. If the system was represented in the direct-quadrate-zero (dq0) domain using Park's transformation [57], the coupling between different frequencies can be eliminated. This is caused by the switching functions relating the dq0 domain components and dc components becoming time-invariant. Subsequently, the impedance measurement techniques in the dq0 domain as well as the analytical modeling approaches were developed [58-60].

Once the impedance response is obtained, how can it be used for power system stability analysis? One approach is purely graphical and uses the Generalized Nyquist Stability Criterion (GNC) [61-64]. Another is to fit this impedance characteristic with an s-domain rational transfer function by a technique such as vector fitting [48]. Then the problem becomes tractable by using s-domain stability analysis methods such as the root locus.

1.2 Gaps in the existing research

Today, large ac-dc networks can be accurately simulated in EMT programs. However, such simulations are expensive in computer time, and designing optimal controller parameter values is a matter of time-consuming trial and error. Also, EMT simulation doesn't directly provide an insight into margin of stability and so on. Therefore, as stated above, two

important methodologies are used to study ac-dc system interaction problems - the state space approach and the GNC approach based on impedance frequency responses. To prevent frequency coupling, it is preferred to represent the equations in the dq0 domain.

The state space approach is restricted by the modeling accuracy. The model becomes impractical if the ac side system is very large and complicated. Also, state space models may involve approximations, such as switching functions for power electronic switches and other linearization. Moreover, in many simulation programs a part of the system may be ‘black boxed’, i.e., it can be simulated but, for proprietary reasons, the internal structure is not available to the user.

On the other hand, the GNC approach requires accurate impedance responses which can be obtained from state equation modeling, or the frequency scanning. However, the scanning has to be applied in an EMT program and cannot be used in cases where the simulation is unstable. For each set of parameters, the scanning needs to be repeated which is very time-costly, making controller design very difficult. Furthermore, the previous application of GNC generally focused on the stability determination of an overall system, and the interaction between the ac subsystem and the dc subsystem was not given special consideration.

1.3 Purpose of this research

The general purpose of this study is to propose an integrated technique to determine

stability and resonance in an ac-dc system, based on the theoretically determined as well as the scanned frequency responses.

In Fig. 1-3a, the ac and dc subsystems are represented by their impedance responses $\mathrm{Z}_{ac}(f)$ and $\mathrm{Z}_{dc}(f)$. Analytical modeling using a state space approach is one way to determine these impedance responses. With state space models, the systems can be investigated in a more flexible manner. This is because that the frequency response is made available in the form of an analytical formula which can be function of controller gains, etc. Hence, one important part of this thesis is the improvement of the analytical model for the frequency response of the HVdc converter.

An analytical model can (and should) be used for other parts of network if possible. However, when these are too large or black boxed, it is generally not possible. Under this circumstance, frequency scanning of an EMT model is another approach that can be conducted. In this thesis, the scanning technique using both off-line (PSCAD/EMTDC) and real-time (RTDS) simulators are investigated. As an example, a small magnitude harmonic current ΔI_h can be injected to the Point of Common Coupling (PCC) bus as in Fig. 1-3a, and the frequency dependent impedance responses $\mathrm{Z}_{ac}(f)$ and $\mathrm{Z}_{dc}(f)$ can be calculated from the generated voltage ΔV_h and currents ΔI_{ach} and ΔI_{dch} as in (1.2). To do this, the time domain measurements in the EMT program have to be converted to the frequency domain using a Fast Fourier Transform (FFT) or Discrete Fourier Transform (DFT).

$$\mathrm{Z}_{ac}(f) = \frac{\Delta V_h(f)}{\Delta I_{ach}(f)};\ \mathrm{Z}_{dc}(f) = \frac{\Delta V_h(f)}{\Delta I_{dch}(f)} \tag{1.2}$$

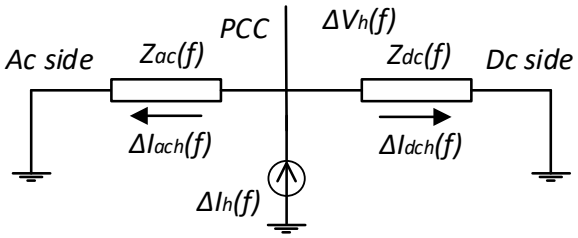

a) Impedance model of the ac and dc side system

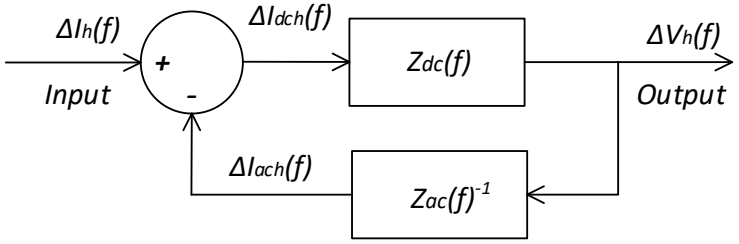

b) Feedback block

Figure 1-3. Representing the ac-dc system as: a) impedance model; b) closed-loop blocks

Then the impedance responses of the ac system and the converter system(s) can be combined and represented by the closed-loop blocks shown in Fig. 1-3b. The system stability can be determined using the Nyquist Stability Criterion (NSC) or GNC. A typical Nyquist plot is shown in Fig. 1-4.

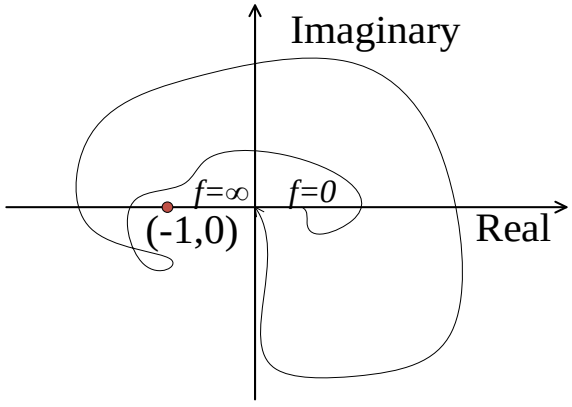

Figure 1-4. A typical Nyquist contour plot

Here we take NSC as an example to determine stability. The loop gain matrix of the system in Fig. 1-3, i.e., $G(f) = \mathrm{Z}_{dc}(f)\mathrm{Z}_{ac}(f)^{-1}$ should encirclement the point (-1, 0) on the complex plane N times such that [61]:

$$N = Z - P \tag{1.3}$$

In (1.3), Z is the number of positive plane zeros of $1 + G(f)$, and P is number of positive plane poles of $G(f)$. By observing the contour, N can be determined. If the open loop system is stable, then $P = 0$ and $N = Z$. Since the zeros of $1 + G(f)$ is the poles of the closed-loop transfer function, then the system can be determined as unstable if $Z = N > 0$.

If the state space model of the system is available with full details, the system can be studied in a very simple manner using the linear control theories. However, it can be very difficult for practical systems. Hence, this thesis mainly focuses on the situation that only part of the system can be represented as the state space model, and for the rest, only the external impedance response can be obtained using the scan. Then the Generalized Nyquist Stability Criterion (GNC) is applied to investigate the system stability and resonance. Case studies for both single-infeed and multi-infeed systems are going to be conducted.

1.4 Organization of this thesis

This thesis is organized as:

Chapter 1 is the literature review and thesis framework.

Chapter 2 concludes that the switching functions of the converters (both the LCCs and VSCs) can be represented by fundamental frequency sinusoidal waveforms. Then the converters and the nearby systems are modeled as state equations. These equations are time-varying if the ac voltages and currents are presented in phase 'abc' domain, resulting in the 'frequency coupling' characteristics. After using proper transformation, i.e., the dq0 transformation, the state equations become time-invariant, and further analysis based on linear control theory can be conducted.

Chapter 3 gives the details of a fast and reliable impedance scanning technique that can be used to measure the system impedance responses in the dq0 domain. This technique is applied in a case system including a VSC and a synchronous generator in PSCAD/EMTDC program. The impedance responses of the ac system side and converter side are both extracted and then compared to the responses got from the small signal analytical model.

Chapter 4 presents an interesting application of the frequency scanning technique for validating the converter models used in a real-time EMT simulation platform – RTDS. Due to constraints of real time, certain shortcuts are taken, i.e., interpolation is generally not used and more approximate VSC converter models have sometimes to be used. The impedance responses of the subsystems including these more approximate converter models are obtained from the frequency scanning. The results are then compared to the responses obtained from the analytical model, from which the accuracy of the RTDS

converter models is validated. However, it is also revealed that the non-interpolation characteristic in RTDS restricts the accuracy of frequency scanning technique. The resulting ripples in the responses make further system analysis very difficult.

Chapter 5 puts forward a new approach for increasing the accuracy of the traditional analytical model of an LCC. It proposes to use the artifact of an infinite number of series-connected six-pulse converters. With this approach, the measurement of firing and extinction angles becomes continuous, and the characteristic harmonics in voltages and currents are eliminated. As the real-world converter is finite-pulse, additional sample and hold units are required to interface measured quantities such as firing and extinction angles to account to and from the model. From this approach, the responses of the converter relating the inputs and the outputs are obtained. This improved model is then applied to the study the stability of various HVdc system scenarios and is proved to have better accuracy than traditional models.

Chapter 6 represents the ac subsystem as forward gain and the dc subsystem as feedback (or vice-versa), forming a closed-loop system. The Generalized Nyquist stability Criterion is then applied to the closed-loop system. With several simple assumptions, a new index, the “Harmonic Stability Margin (HSM)” is proposed to screen the interaction level between the ac and dc systems. A value of HSM larger than 1.0 indicates stable system and the higher this value, the more margin the system has away from marginal stability. This index is used to analyze power system problems, including Sub-Synchronous Control Interaction (SSCI), the influence of system simplification on the stability, and multi-infeed system

studies. Each case study is also validated by EMT simulation.

Chapter 7 summarizes the thesis, including the conclusions and recommendations for future work.

2 Representation of power electronic converter systems by state equations

This chapter discusses the frequency dependent impedance / admittance response of the converter side looking from the point of interest (i.e., the PCC bus). Assuming that the response of the connected ac system is available, once the converter side's characteristic is obtained, the Nyquist Stability Criterion (NSC) or Generalized Nyquist stability Criterion (GNC) can be applied to determine the stability by graphically observing the contour of the combined impedance. The system impedance / admittance response is investigated in either the 'abc' (i.e., phase) domain or the dq0 domain [54-60].

Following sections show that for both the LCC and VSC converter, the converter operation can be represented by fundamental frequency algebraic switching functions relating the currents and voltages. Using this algebraic relationship, the characteristics of one converter can be represented by differential equations, which can be further developed in a state space form after linearization. This provides an analytical expression for the impedance / admittance frequency responses for the converter.

2.1 Averaging of ac-dc switching functions

The switching of the converters' valves changes the electrical circuit configuration. In the

steady state, the switching function is a periodic function with a base frequency equal to the system frequency (i.e., 60Hz in North America). This allows the switching function to be expressed as a Fourier series of harmonics of the base frequency, obtained using the Discrete Fourier Transform (FFT) [65]. Additionally, using the averaging method [66-68], the fundamental frequency component can be retained, and high order harmonics neglected due to their generally small magnitudes. It was found that for an LCC, sufficient accuracy can be maintained using averaging [69].

2.1.1 Switching functions of the LCC converter

The configuration of a six-pulse LCC converter is presented in Figure. 2-1 showing the commutation from valve 5 to valve 1, here it is operating as a rectifier. Commutation happens in each valve once in every fundamental cycle, with the commutation voltage and current plotted in Figure. 2-2.

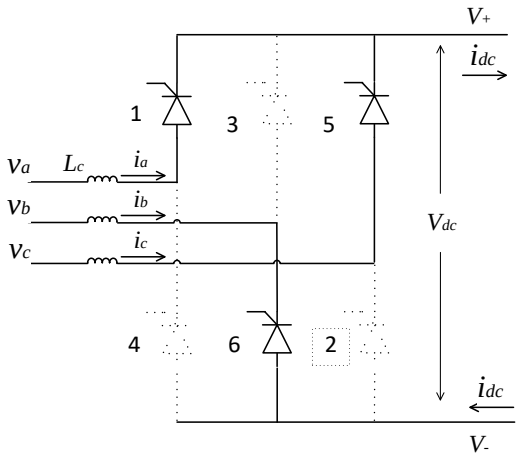

Figure 2-1. The configuration of one six-pulse LCC

As seen in Fig. 2-2, both the phase ‘a’ current (Fig. 2-2a) and dc side voltage (Fig. 2-2b) are not ideal waveforms and include harmonics [2]. The dc side voltage contains a dc (i.e. non-zero average) component as well as harmonic components of order $6k$ ($k \in N$), and ac side current includes the base frequency component and harmonic components of order $6k \pm 1$. However, the high order current harmonics entering the system can be greatly reduced by the ac filters.

For each valve in the converter, there are two different intervals: commutation (or overlap) and normal conduction. The valves are turned on by the firing angle pulse from the control system, which indicate the beginning of the commutation interval. During the commutation, both the incoming and outgoing valves conduct and there is a period (μ) where the conducting of these two overlaps. The end of commutation occurs when the current transfers to the incoming valve completely. This happens when the following condition is satisfied:

$$\cos\alpha - \cos(\alpha + \mu) = \frac{2I_{dc}X_c}{\sqrt{3}V_{ac}} \tag{2.1}$$

In (2.1), α is the firing angle, μ, the overlap angle, X_c, the commutation reactance, I_{dc}, the dc current, and V_{ac}, the magnitude of the ac voltage (phase to ground). The switching function relating phase ‘a’ voltage to the dc voltage is also shown in Fig. 2-2c. Here we have the assumption of balanced three-phase commutation voltages to simplify the analysis:

$$\begin{cases} v_a = V\cos(\omega_0 t + \varphi_v) \\ v_b = V\cos(\omega_0 t + \varphi_v - \frac{2\pi}{3}) \\ v_c = V\cos(\omega_0 t + \varphi_v + \frac{2\pi}{3}) \end{cases} \tag{2.2}$$

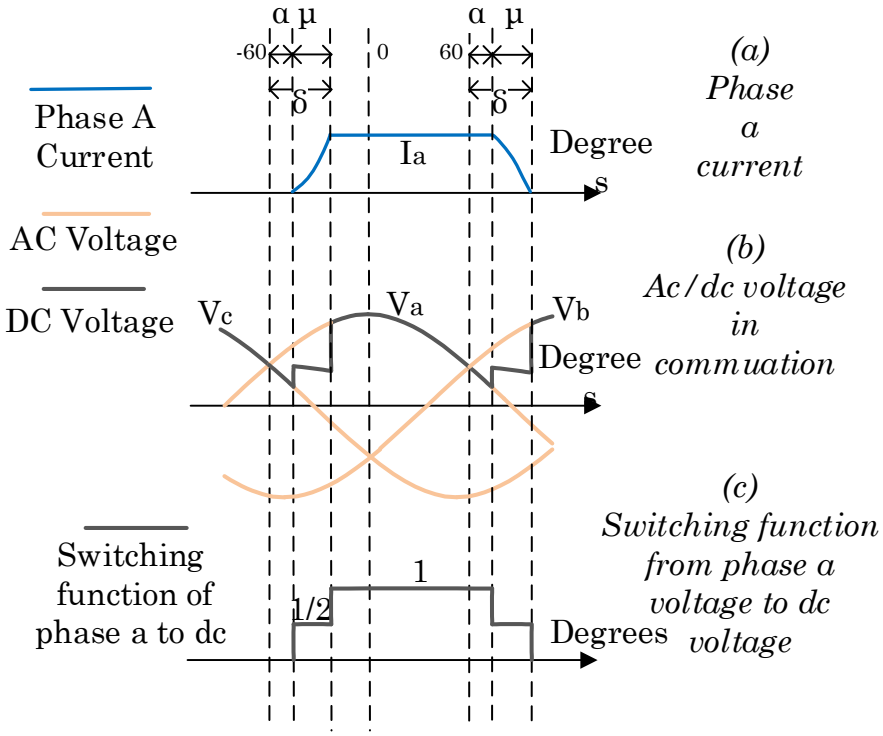

Figure 2-2. Commutation process of the converter in 1/2 electric cycle

Applying the Fourier Transform (FT) to the voltage switching function $Sw(\varphi)$ (from phase 'a' voltage to dc voltage), the fundamental component can be extracted in phasor form with the phase reference being the phase of the 'a' phase voltage φ_v:

$$\overrightarrow{S_{phv}} = \frac{1}{\pi}\int_{\alpha-\frac{1}{3}\pi}^{\delta+\frac{1}{3}\pi} Sw(\varphi)e^{-j\varphi}d\varphi = \frac{\sqrt{3}}{2\pi}\left(e^{-j\alpha} + e^{-j\delta}\right) \tag{2.3}$$

Here, $\delta = \alpha + \mu$ denotes the commutation end angle. Then the dc component of the dc side voltage can be calculated as:

$$V_{dc} = S_{av\_lcc} v_a + S_{bv\_lcc} v_b + S_{cv\_lcc} v_c \tag{2.4}$$

Where v_a, v_b and v_c are given as in (2.2). In general, the steady-state switching function will be periodic at fundamental frequency but have a non-sinusoidal shape [27-29]. Retaining only the dominant fundamental frequency component (i.e. ignoring higher order harmonic terms), the three switching functions are:

$$\begin{cases} S_{av\_lcc} = |\overrightarrow{S_{phv}}|\cos[\omega_0 t + \varphi_v + \arg(\overrightarrow{S_{phv}})] \\ S_{bv\_lcc} = |\overrightarrow{S_{phv}}|\cos\left[\omega_0 t + \varphi_v + \arg(\overrightarrow{S_{phv}}) - \frac{2\pi}{3}\right] \\ S_{cv\_lcc} = |\overrightarrow{S_{phv}}|\cos\left[\omega_0 t + \varphi_v + \arg(\overrightarrow{S_{phv}}) + \frac{2\pi}{3}\right] \end{cases} \tag{2.5}$$

For phase 'a' current, the analytical equation in half the conducting cycle (the other half is symmetrical) can be given by:

$$i_a(\varphi) = \begin{cases} \frac{\sqrt{3}V}{2X_c}\left[cos\alpha - cos\left(\varphi + \frac{\pi}{3}\right)\right] & if\ \varphi \in [\alpha - \frac{1}{3}\pi, \delta - \frac{1}{3}\pi] \\ I_{dc} = \frac{\sqrt{3}V}{2X_c}[cos\alpha - cos\delta] & if\ \varphi \in \left[\delta - \frac{1}{3}\pi, \alpha + \frac{1}{3}\pi\right] \\ \frac{\sqrt{3}V}{2X_c}\left[cos\left(\varphi - \frac{\pi}{3}\right) - cos\delta\right] & if\ \varphi \in [\alpha + \frac{1}{3}\pi, \delta + \frac{1}{3}\pi] \end{cases} \tag{2.6}$$

Using the FT, the phasor form of the switching function to determine phase currents in terms of the dc current (with respect to the phase 'a' voltage) can be given as:

$$\overrightarrow{S_{phı}} = \frac{1}{\pi}\int_{\alpha^* - \frac{1}{3}\pi}^{\delta^* + \frac{1}{3}\pi} \frac{i_a(\varphi)}{I_{dc}} e^{-j\varphi} d\varphi = \frac{\sqrt{3}}{2\pi(cos\alpha - cos\delta)}\left(-j2\mu + e^{-j2\alpha} - e^{-j2\delta}\right) \tag{2.7}$$

The three-phase currents are the product of the switching functions and the dc current:

$$\begin{cases} i_a = S_{ai\_lcc} I_{dc} \\ i_b = S_{bi\_lcc} I_{dc} \\ i_c = S_{bi\_lcc} I_{dc} \end{cases} \tag{2.8}$$

Where the switching functions for the currents are:

$$\begin{cases} S_{ai\_lcc} = |\overrightarrow{S_{phl}}|\cos[\omega_0 t + \varphi_v + \arg(\overrightarrow{S_{phl}})] \\ S_{bi\_lcc} = |\overrightarrow{S_{phl}}|\cos\left[\omega_0 t + \varphi_v + \arg(\overrightarrow{S_{phl}}) - \frac{2\pi}{3}\right] \\ S_{ci\_lcc} = |\overrightarrow{S_{phl}}|\cos\left[\omega_0 t + \varphi_v + \arg(\overrightarrow{S_{phl}}) + \frac{2\pi}{3}\right] \end{cases} \quad (2.9)$$

2.1.2 Switching functions of the VSC converter

Fig. 2-3 shows a schematic of the VSC where a two-level configuration is assumed. 'L_t' represents the leakage inductance of the ac transformer connecting the VSC and the PCC bus (resistance of the transformer neglected). The transformer turns ratio is not shown, as the diagram has been referred to the valve side winding of the transformer. Pulse-width modulation (PWM) is used to issue the valve gating pulses whose typical waveform is given as in Fig. 2-4. Compared to the LCC, this kind of converter is able to control the voltage magnitude and phase angle in converter terminal as the reference waveform provided by the control system. Hence it is equivalent to a controlled ac voltage source if higher order harmonics are sufficiently small.

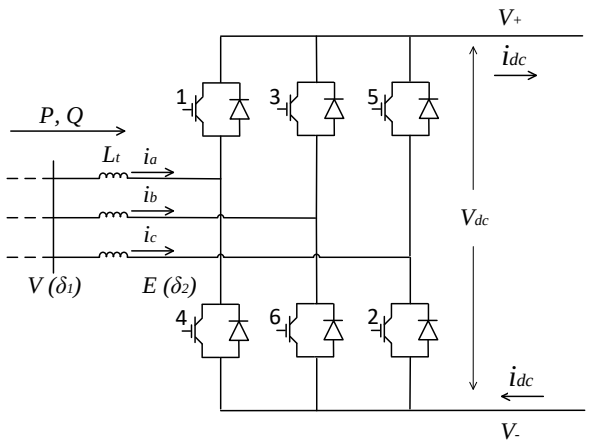

Figure 2-3. Configuration of VSC converter and ac transformer

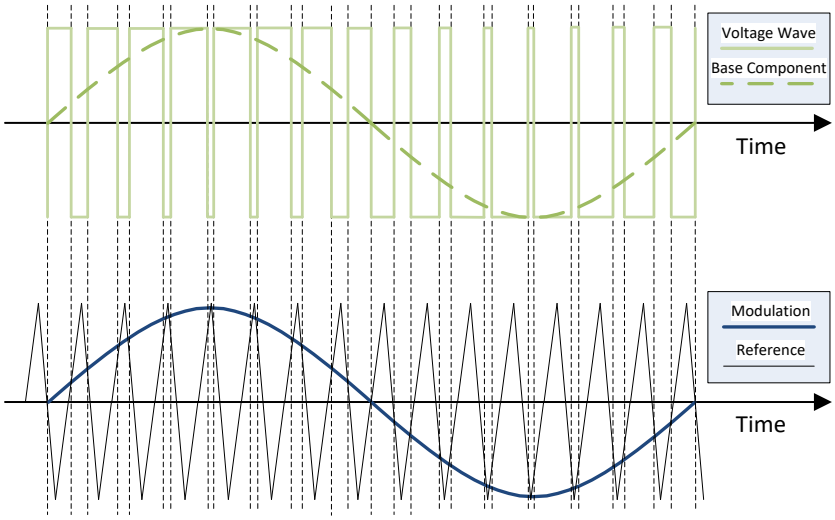

Figure 2-4. A typical PWM waveform in one cycle

Let the voltage and phase angle at the PCC bus be V and δ_1, and the converter terminal voltage and phase angle be E and δ_2 as in Fig. 2-3. Then the power flowing from the PCC bus to the converter can be represented as shown in reference [1] (Here $X_t = \omega_0 L_t$):

$$\begin{cases} \mathrm{P} = \dfrac{VE}{X_t}\sin(\delta_1 - \delta_2) \\ \mathrm{Q} = \dfrac{V^2 - VE\cos(\delta_1 - \delta_2)}{X_t} \end{cases} \tag{2.10}$$

Typically, PWM uses the comparison between a high frequency triangle waveform carrier, and a reference sinusoidal waveform from the control system, as in Fig. 2-4. The firing pulses to turn on the upper VSC valves are issued when the sine wave signal exceeds the triangle wave carrier, and conduction is maintained till the triangle wave carrier exceeding the sine wave. The lower valve firing pulses are the binary complements of the corresponding upper arm ones. Assuming a constant dc voltage, the phase voltage will be identical in shape to the PWM reference waveform. The generated PWM waveform essentially has a low frequency component proportional to the reference sine wave and

high frequency components clustered around the carrier frequency. As long as the carrier frequency f_c is much larger than the fundamental frequency f_0, the switching components are easily suppressed by the filter circuits and can be neglected in the analysis [70].

For the conversion of currents and voltages, the switching functions are the same. If the modulation index of the reference waveform is m_{vsc} and the phase angle shift is δ_{vsc} from the control system, then the transformation equations of the VSC converters can be given by:

$$i_{dc} = S_{a\_vsc} i_a + S_{b\_vsc} i_b + S_{c\_vsc} i_c \tag{2.11}$$

$$\begin{cases} v_a = S_{a\_vsc} V_{dc} \\ v_b = S_{b\_vsc} V_{dc} \\ v_c = S_{c\_vsc} V_{dc} \end{cases} \tag{2.12}$$

Where the three phase switching functions are:

$$\begin{cases} S_{a\_vsc} = m_{vsc} \cos[\omega_0 t + \varphi_v + \delta_{vsc}] \\ S_{b\_vsc} = m_{vsc} \cos\left[\omega_0 t + \varphi_v + \delta_{vsc} - \frac{2\pi}{3}\right] \\ S_{c\_vsc} = m_{vsc} \cos\left[\omega_0 t + \varphi_v + \delta_{vsc} + \frac{2\pi}{3}\right] \end{cases} \tag{2.13}$$

2.2 State space representation for the converter

With the switching functions as (2.5), (2.9) and (2.13), the converters can be modeled as a set of algebraic equations. Here a VSC is taken as example to simplify the analysis, as the voltages and currents have the same switching function.

If only the converter itself is considered (i.e. ac or dc networks re excluded), then the input-output relationship can be given by equations (2.14) and (2.15) where $\boldsymbol{x_{abc}}$ represents $[x_a \quad x_b \quad x_c]^T$.

$$\boldsymbol{e_{abc}} = \boldsymbol{S_{abc}} U_{dc} \tag{2.14}$$

$$I_{dc} = \boldsymbol{S_{abc}}^{\boldsymbol{T}} \boldsymbol{i_{abc}} \tag{2.15}$$

Where, $\boldsymbol{S_{abc}} = m[\cos(\omega_0 t + \delta) \quad \cos(\omega_0 t + \delta - \frac{2\pi}{3}) \quad \cos(\omega_0 t + \delta + \frac{2\pi}{3})]^T$ is the switching function vector, with m and δ being the modulation index and phase angle from the control system.

At first, the dc side only has a resistor to simplify the analysis and dc voltage is given by:

$$U_{dc} = R_{dc} I_{dc} \tag{2.16}$$

Combing (2.14), (2.15) and (2.16), the voltage-current relationship is given as in (2.17a), and the impedance matrix $\boldsymbol{Z_{abc}}$ relating three phase currents to the voltages in (2.17b).

$$\boldsymbol{e_{abc}} = \boldsymbol{S_{abc}} R_{dc} \boldsymbol{S_{abc}}^{\boldsymbol{T}} \boldsymbol{i_{abc}} = R_{dc} \boldsymbol{S_{abc}} \boldsymbol{S_{abc}}^{\boldsymbol{T}} \boldsymbol{i_{abc}} \tag{2.17a}$$

$$\boldsymbol{Z_{abc}} = R_{dc} \boldsymbol{S_{abc}} \boldsymbol{S_{abc}}^{\boldsymbol{T}} \tag{2.17b}$$

In (2.17b), all the elements of $\boldsymbol{Z_{abc}}$ contain a dc component and a second order harmonic component of frequency $2f_0$, due to each term of $\boldsymbol{S_{abc}} \boldsymbol{S_{abc}}^{\boldsymbol{T}}$ being a multiplication of two sinusoids of the same frequency. The magnitudes of these two components are the same. Thus, a signal containing a frequency f in the input ac currents can generate three frequencies' component in the ac voltages (at frequencies: f, $f - 2f_0$ and $f + 2f_0$). This is referred to as 'frequency coupling'.

Now consider a case system as in Fig. 2-5, where the ac side consists of a series resistor-inductor (R_t-L_t) in series with the ac source, and the dc side consists of a parallel resistor-capacitor (R_{dc}//C_{dc}), which is a more typical configuration.

The state equations of this system are given below:

$$L_t \frac{d\boldsymbol{i_{abc}}}{dt} + R_t \boldsymbol{i_{abc}} = \boldsymbol{v_{abc}} - \boldsymbol{e_{abc}} = \boldsymbol{v_{abc}} - \boldsymbol{S_{abc}} U_{dc} \tag{2.18}$$

$$C_{dc} \frac{dU_{dc}}{dt} = I_{dc} - \frac{U_{dc}}{R_{dc}} = \boldsymbol{S_{abc}}^{\boldsymbol{T}} \boldsymbol{i_{abc}} - \frac{U_{dc}}{R_{dc}} \tag{2.19}$$

The input variables are defined as: $\boldsymbol{U_c} = [v_a \quad v_b \quad v_c]$; the state variables: $\boldsymbol{X_c} = [i_a \quad i_b \quad i_c \quad \mathrm{U}_{dc}]^T$; and the state space form of the system can be given by:

$$\dot{\boldsymbol{X}}_{\boldsymbol{c}} = \boldsymbol{A_c X_c} + \boldsymbol{B_c U_c} \tag{2.20}$$

$$\boldsymbol{A_c} = \begin{bmatrix} \frac{-\mathrm{R}_t}{\mathrm{L}_t} * \boldsymbol{I_{3*3}} & \boldsymbol{S_{abc}} \\ \boldsymbol{S_{abc}}^{\boldsymbol{T}} & -\frac{1}{R_{dc}} \end{bmatrix}; \boldsymbol{B_c} = \begin{bmatrix} \frac{1}{\mathrm{L}_t} \boldsymbol{I_{3*3}} \\ 0 \end{bmatrix}$$

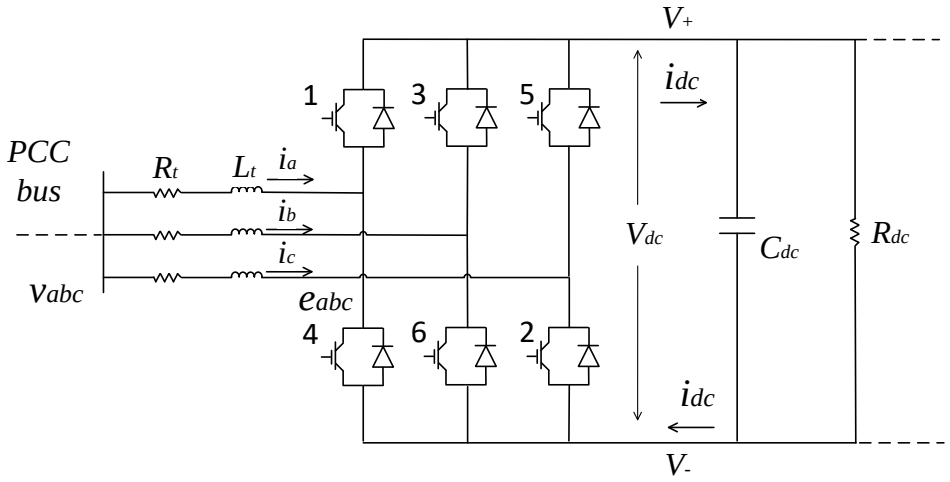

Figure 2-5. A typical VSC system (part)

In (2.20) $\boldsymbol{I_{3*3}}$ is a 3 x 3 identity matrix. The system state space matrix $\boldsymbol{A_c}$ in (2.20) is time-varying due to the time-varying characteristics of the switching function vector $\boldsymbol{S_{abc}}$, and the ensuing coupling phenomenon between frequencies makes the analysis based on linear control theory not directly possible.

2.3 Transformations to the converter state space system

Although $\boldsymbol{A_c}$ shown as a time-varying matrix, the eigenvalues of $\boldsymbol{A_c}$ are constant and only dependent on the modulation index m:

$$\lambda = \begin{cases} -R_t/L_t \\ -R_t/L_t \\ \dfrac{-R_t - \sqrt{{R_t}^2 + 6m^2{L_t}^2}}{2L_t} \\ \dfrac{-R_t + \sqrt{{R_t}^2 + 6m^2{L_t}^2}}{2L_t} \end{cases} \tag{2.21}$$

This implies that with a proper time-varying transformation to the state variable vector $\boldsymbol{X_c}$, $\boldsymbol{A_c}$ could be transformed to be time-invariant.

This section discusses the two popular transformations applying on the ac side currents and voltages, one is the Park transformation originally developed for the analysis of the synchronous generator, and the other is the symmetrical component transformation initially proposed for the study of unbalanced three-phase system. In each of these transformations, the state vector $\boldsymbol{X_c}$ is transformed to a new, more convenient state vector, as will be discussed below.

2.3.1 Park transformation

R. H. Park invented the direct-quadratic-zero (dq0) transformation to resolve the time-varying inductance problem in the synchronous generator [57]. This transformation has also been used widely in converter modeling. The time invariant (in the steady-state) variables are obtained by multiplying the three-phase variables by a time-varying matrix as shown in (2.22).

$$\boldsymbol{T_{dq0}} = \frac{2}{3}\begin{bmatrix} cos(\omega_0 t + \theta_0) & cos(\omega_0 t + \theta_0 - \frac{2\pi}{3}) & cos(\omega_0 t + \theta_0 + \frac{2\pi}{3}) \\ -sin(\omega_0 t + \theta_0) & -sin(\omega_0 t + \theta_0 - \frac{2\pi}{3}) & -sin(\omega_0 t + \theta_0 + \frac{2\pi}{3}) \\ \frac{1}{2} & \frac{1}{2} & \frac{1}{2} \end{bmatrix} \quad (2.22)$$

Here, θ_0 is a constant offset angle. With this transformation applied on the ac side variables in (2.20), the new state vector $\mathbf{X_{c\_dq0}}$ and input $\mathbf{U_{c\_dq0}}$ are given as:

$$\mathbf{X_{c\_dq0}} = \begin{bmatrix} \boldsymbol{T_{dq0}} & \mathbf{0} \\ 0 & 1 \end{bmatrix} \boldsymbol{I_{3*3}};\ \mathbf{U_{c\_dq0}} = \boldsymbol{T_{dq0}}\mathbf{U_c} \quad (2.23)$$

With (2.23), we can replace $\boldsymbol{X_c}$ and $\boldsymbol{U_c}$ with $\boldsymbol{X_{c\_dq0}}$ and $\boldsymbol{U_{c\_dq0}}$ to give a time-invariant state equation:

$$\frac{d\mathbf{X_{c\_dq0}}}{dt} = \begin{bmatrix} \boldsymbol{T_{dq0}} & \mathbf{0} \\ 0 & 1 \end{bmatrix} [\boldsymbol{A_c X_c} + \boldsymbol{B_c U_c}] + \begin{bmatrix} \frac{d\boldsymbol{T_{dq0}}}{dt} & \mathbf{0} \\ 0 & 1 \end{bmatrix} \mathbf{X_c}$$

$$= \left\{ \overbrace{\begin{bmatrix} \boldsymbol{T_{dq0}} & \mathbf{0} \\ \mathbf{0} & 1 \end{bmatrix} \boldsymbol{A_c} \begin{bmatrix} \boldsymbol{T_{dq0}} & \mathbf{0} \\ \mathbf{0} & 1 \end{bmatrix}^{-1}}^{time-invariant} + \overbrace{\begin{bmatrix} \frac{d\boldsymbol{T_{dq0}}}{dt} & \mathbf{0} \\ \mathbf{0} & 1 \end{bmatrix} \begin{bmatrix} \boldsymbol{T_{dq0}} & \mathbf{0} \\ 0 & 1 \end{bmatrix}^{-1}}^{time-invariant} \right\} \mathbf{X_{c\_dq0}}$$

$$+\begin{bmatrix} \boldsymbol{T_{dq0}} & \mathbf{0} \\ 0 & 1 \end{bmatrix} \boldsymbol{B_c} \boldsymbol{T_{dq0}}^{-1} \mathbf{U}_{\boldsymbol{c\_dq0}} \tag{2.24}$$

The transformed state space representation of the system is now given by:

$$\dot{\boldsymbol{X}}_{\boldsymbol{c\_dq0}} = \boldsymbol{A}_{\boldsymbol{c\_dq0}} \boldsymbol{X}_{\boldsymbol{c\_dq0}} + \boldsymbol{B}_{\boldsymbol{c\_dq0}} \boldsymbol{U}_{\boldsymbol{c\_dq0}} \tag{2.25}$$

$$\boldsymbol{A_{c\_dq0}} = \begin{bmatrix} -R_t/L_t & \omega_0 & 0 & mcos(\delta-\theta_0) \\ -\omega_0 & -R_t/L_t & 0 & msin(\delta-\theta_0) \\ 0 & 0 & -R_t/L_t & 0 \\ \frac{3}{2}mcos(\delta-\theta_0) & \frac{3}{2}msin(\delta-\theta_0) & 0 & -\frac{1}{R_{dc}} \end{bmatrix}; \ \boldsymbol{B_{c\_dq0}} = \boldsymbol{B_c}$$

The time-varying system indicated in equation (2.20) becomes time-invariant as in (2.25), with the ac side currents and voltages transformed to the dq0 domain. The transfer (admittance) matrix relating the three-phase ac voltages to the ac currents in dq0 domain is frequency dependent and time-invariant.

2.3.2 Symmetrical component transformation

Another frequently used transformation is the symmetrical component transformation [1, 64] for the study of the unbalance three-phase system. The transformation matrix is based on the phase operator including the phase lag between two phases:

$$\begin{cases} a = e^{j\frac{2\pi}{3}} \\ \boldsymbol{T_{+-0}}^{*} = \frac{1}{3}\begin{bmatrix} 1 & a & a^{-1} \\ 1 & a^{-1} & a \\ 1 & 1 & 1 \end{bmatrix} \end{cases} \tag{2.26}$$

The three-phase voltages (or currents) are transformed to the positive, negative and zero sequence components, whose phasor diagrams are shown in Fig. 2-6.

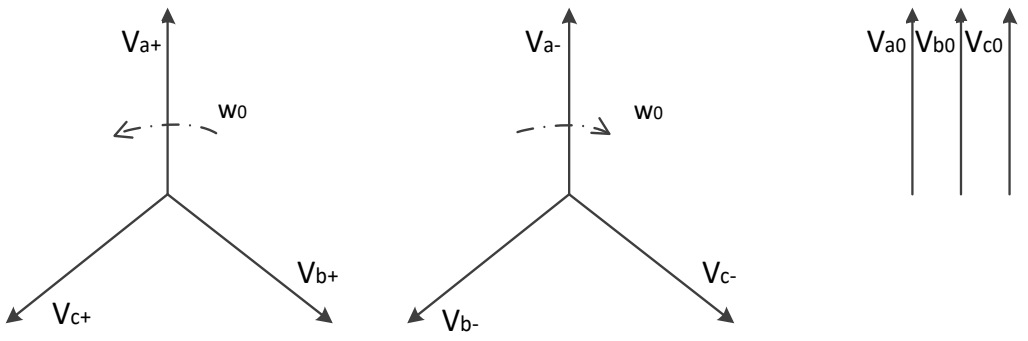

Figure 2-6. Symmetrical components

In some studies, the synchronous speed operator 'b' is added to the transformation matrix that:

$$\begin{cases} b = e^{j(\omega_0 t+\theta_0)} \\ \boldsymbol{T_{+-0}} = \frac{1}{3}\begin{bmatrix} b^{-1} & b^{-1}a & b^{-1}a^{-1} \\ b & ba^{-1} & ba \\ 1 & 1 & 1 \end{bmatrix} \end{cases} \tag{2.27}$$

Multiplying the ac currents and voltages by the matrix $\boldsymbol{T_{+-0}}$ in (2.27), the system described in (2.20) is represented in sequence domain as:

$$\dot{\boldsymbol{X}}_{\boldsymbol{c\_+-0}} = \boldsymbol{A_{c\_+-0}X_{c\_+-0}} + \boldsymbol{B_{c\_+-0}U_{c\_+-0}} \tag{2.28}$$

Where,

$$\boldsymbol{X_{c\_+-0}} = \begin{bmatrix} \boldsymbol{T_{+-0}} & \mathbf{0} \\ 0 & 1 \end{bmatrix}\mathbf{X_c};\ \mathbf{U_{c\_+-0}} = \boldsymbol{T_{+-0}}\mathbf{U_c}$$

$$\mathbf{A_{c\_+-0}} = \begin{bmatrix} -R_t/L_t - j\omega_0 & 0 & 0 & \frac{1}{2}me^{j(\delta-\theta_0)} \\ 0 & -R_t/L_t + j\omega_0 & 0 & \frac{1}{2}me^{j(\delta-\theta_0)} \\ 0 & 0 & -R_t/L_t & 0 \\ \frac{3}{2}me^{j(\delta-\theta_0)} & \frac{3}{2}me^{j(\delta-\theta_0)} & 0 & -\frac{1}{R_{dc}} \end{bmatrix};\ \boldsymbol{B_{c\_+-0}} = \boldsymbol{B_c}$$

The synchronous speed produced by the switching function is eliminated by the synchronous speed in the operator $'b'$, and the system represented by (2.28) is time-

invariant. Actually, the transformation matrix $\boldsymbol{T_{+-0}}$ is a linear transformation of $\boldsymbol{T_{dq0}}$:

$$\boldsymbol{T_{+-0}} = \begin{bmatrix} \frac{1}{2} & \frac{j}{2} & 0 \\ \frac{1}{2} & -\frac{j}{2} & 0 \\ 0 & 0 & 1 \end{bmatrix} \boldsymbol{T_{dq0}} \tag{2.29}$$

Additionally, if the transformation is applied using the matrix $\boldsymbol{T_{+-0}}^{*}$ in (2.26), the frequency coupling still happens.

2.4 Summary

This chapter analyzes the switching functions of the LCC and VSC, which can both be represented by fundamental frequency sinusoidal functions. If the converter systems are represented as time-varying system in the phase 'abc' domain, the well-known "frequency coupling" phenomenon occurs. The impedance (admittance) expression includes cross-coupling terms where the input of one frequency can generate the output with other frequencies. Hence linear control theory is not directly applicable.

After suitable transformation (e.g., the dq0 transformation) to the ac voltages and currents, the system is represented by time-invariant equations. This system can be linearized and easily analyzed based on the linear control theory. If the system is represented in the dq0 domain, the state matrix $\mathbf{A}_{\boldsymbol{c\_dq0}}$ includes only real numbers as in (2.25); and if the system is studied in the sequence domain as in (2.28), there would be complex numbers in the system matrix $\boldsymbol{A_{c\_+-0}}$ which may bring difficulties for further analysis. Thus, the treatment in the following chapters considers the ac voltages and currents in the dq0

domain.

In addition, the switching function of VSC can be easily applied in the further modeling of the system, as the control system alone determines the turn-on and turn-off instance of the valves. However, determining the switching function for an LCC converter is more challenging than for a VSC converter. It includes the term of dynamic overlap angle as in (2.5) and (2.9), and the overlap angle is a complicated function of phase currents and voltages and not be merely determined by the firing pulses applied.

3 The impedance scanning technique

To study system stability, state space analysis is a widely used approach. It can provide information such as the root loci of eigenvalues, which determines the stability status as well as other information such as how far the system is from the stability boundary. In general, state space analysis requires a linearized analytical model of the system. But, sometimes parts of the system may not be readily available for determining a linearized analytical model, either because that size and complexity makes it difficult to do so, or sometimes such parts are only available, for security reasons, as a “black box” model precluding the possibility of knowing its exact internal structure. Under this circumstance, frequency scanning [54] can be applied to obtain the frequency response characteristics of this part of system as viewed from its driving point nodes.

This chapter discusses the details of the frequency scanning technique to obtain the impedance (or admittance) responses for a portion of system. An example system including the ac subsystem and dc converter is built in the EMT simulation program PSCAD/EMTDC as shown later in Fig. 3-4. The dc side includes a VSC converter, a dc capacitor and a dc source. The ac subsystem is made up of a synchronous machine in series with a linear (RLC) Thevenin equivalent representing a transmission line and associated circuits. For both sides, the impedance responses are scanned, and the accuracy of the frequency scanning is validated.

With the impedance response of the subsystem of interest scanned, the stability of the subsystem connected to an arbitrary external network can be determined by approaches such as (Generalized) Nyquist Stability Criterion (NSC) [61-64] by plotting their combined frequency response in the complex plane and graphically observing the encirclement of the contour on either (-1, 0) or the origin point.

In this work, mostly PSCAD/EMTDC is employed as the program to model the case system and to scan the impedance response, which is the most widely used tool of its kind worldwide with over 30,000 licensed users. It was developed by Manitoba Hydro and the University of Manitoba. RSCAD is another EMT program used in this thesis for real time simulation studies.

3.1 Frequency scanning technique

3.1.1 Traditional scanning in the EMT platform

In this work, all the scans are conducted using an EMT model. EMT simulation represents the non-linearity and the transient dynamics in detail [71], and so the scan yields the small signal frequency response at the operating point. In traditional studies [51][52], one very slow and contra-recommended approach is to inject a current (or voltage) perturbation signal with small magnitude at one specific frequency and measure the resulting voltage (or current). The ratio of the resultant and injected quantities gives the impedance (or

admittance) magnitude and phase angle at the perturbation frequency. It was [55] proposed that this perturbation signal should be superposed on the steady state value, and the impedance at frequency f is calculated by:

$$Z(f) = \frac{V_{post\_dist}(f) - V_{pre\_dist}(f)}{I_{post\_dist}(f) - I_{pre\_dist}(f)} \tag{3.1}$$

Subscript 'pre_dist' denotes for the pre-disturbance steady state value (in most cases it would be zero for harmonics), and 'post_dist' means post-disturbance steady state value after the transients settle down. Figure 3-1 shows an example waveform of pre-disturbance and post-disturbance interval of one arbitrary signal.

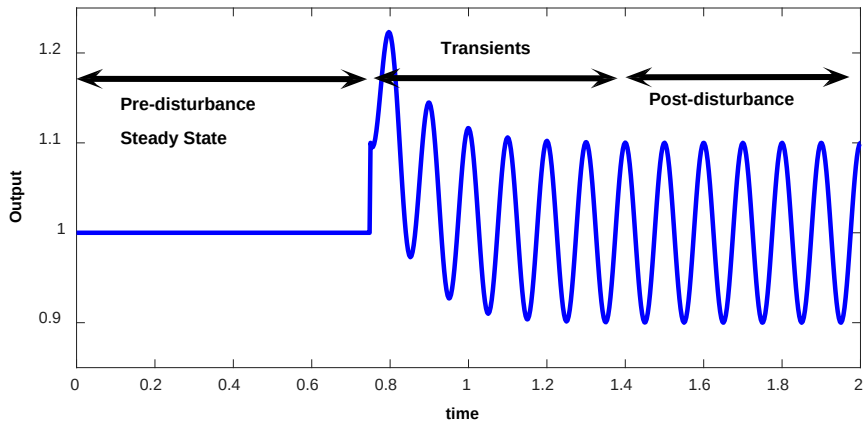

Figure 3-1. Example of pre- and post- disturbance of one signal

An alternative and faster approach to identify the impedance responses in this work, based on the technique in [54], will be discussed in the next section.

3.1.2 Multi-sine harmonic injection

Instead of injecting one frequency at a time, the admittance or impedance scan can be

generated much faster if a multi-frequency signal is injected. Then the impedance (or admittance) frequency response can be obtained by dividing the discrete Fourier series of the resulting voltage (current) by the discrete Fourier series of the input current (voltage). The configuration of the injection is shown in Fig. 3-2.

In superposition theory, the current source is treated as an open circuit and the voltage source as a short circuit. So, the harmonic current can be injected to a bus connected to multiple subsystems, and the harmonic voltage should be inserted to a branch.

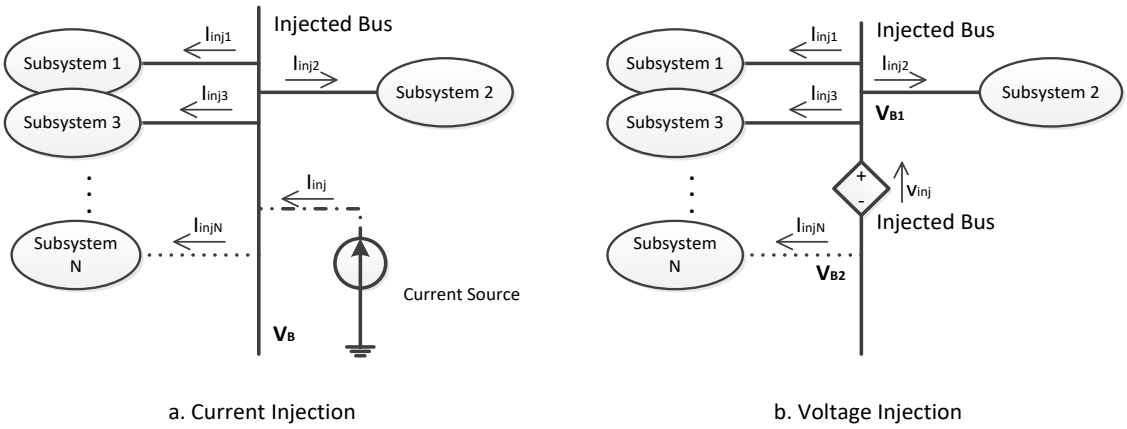

a. Current Injection b. Voltage Injection

Figure 3-2. Configuration of current injection and voltage injection

In this work, the current source injection is chosen for convenience. As in Fig. 3-1, there is a settling down time before the steady state is reached. This settling time can be quite long (several seconds or even more), depending on the system characteristics. The total simulation time would be very long if multiple frequencies' responses have to be scanned one by one. Hence, to hasten the scan, a "multi-sine" signal $X_{inj}(t)$ as in (3.2) [54] is generated and injected to the studied system, which consists of several equal magnitude

components at equally spaced frequencies. The phase shift $k_{inj}(f_{min} + n\Delta f)^2$ distributes the energy over a longer period and thereby prevent large localized magnitudes. The number of N (e.g., 60) and the magnitude k_{mag} is properly selected so that the overall signal's magnitude is small enough to be considered a small signal, yet large enough to be reliably measured.

$$X_{inj}(t) = \sum_{n=0}^{N} k_{mag} cos[2\pi(f_{min} + n\Delta f)t + k_{inj}(f_{min} + n\Delta f)^2] \quad (3.2)$$

This signal is injected with the system operating in the steady state condition, so assuming a small magnitude of the probing signal, the operating point is not affected. Then the impedance of many frequencies can be extracted in one simulation. Multiple scans can be carried out on the EMT simulation model to get a spectrum with the desired frequency range.

3.1.3 DQ0 domain scanning

As discussed in Chapter 2, injecting a phase domain quantity at frequency f results components at other frequencies [56]. However, if the scanning is made in the dq0 domain, there is no cross coupling between frequencies, although there is a cross-coupling of d- and q- axis quantities at the same frequency. So, the harmonic current (voltage) is injected in the dq0 domain which is a three-dimension vector, as in Fig. 3-3. The zero-sequence signal X_0 is usually given as zero, as it is generally not of interest. The d- and q- axis injected signals, X_d and X_q, are given based on the value from equation (3.2) (the frequencies contained in the d- and q- axis currents are the same, but the magnitude and phase shift

should be different). Then the inverse dq0 transformation is applied to the dq0 domain signals X_d, X_q and X_0 to get the values of the phase domain signals X_a, X_b and X_c, as in Fig. 3-3.

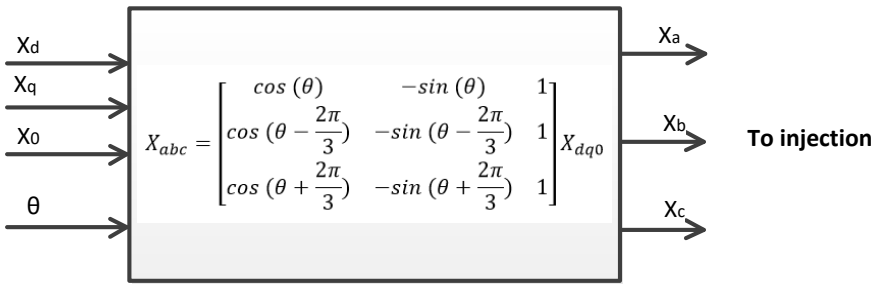

Figure 3-3. Transformation from dq0 to abc domain

The reference angle of the dq0 transformation is:

$$\theta = \omega_0 t + \theta_0 \tag{3.3}$$

Where ω_0 is the synchronous speed and θ_0 is a properly selected offset value.

3.1.4 Signal processing

In (3.1), the frequency domain values of the currents and voltages are required to calculate the impedance. These values are obtained by applying the Discrete Fourier Transform (DFT) [65] to the recorded time domain signals:

$$\mathrm{X}_f = \frac{2}{N}\sum_{n=1}^{N} x_n e^{-j2\pi f\frac{n-1}{N}} \tag{3.4}$$

Here, N is the sampling number in a sampling window, f, frequency of harmonic (Hz), x_n, the n^{th} sampled value. An anti-aliasing filter is normally required before the sampling to pre-process the data to eliminate the high frequency component which produces aliasing

caused by the data sampling. It is a low pass filter (e.g., the Butterworth filter) and can be modeled as the transfer function in Laplace domain whose typical form is given by (3.5) [35]:

$$\mathrm{AA(s)} = \frac{1}{\sum_{i=0}^{k} A_i \left(\frac{s}{\omega_c}\right)^i} \tag{3.5}$$

Where, k is the order of the denominator, ω_c, cutoff frequency. Based on this transfer function, a digital z-domain filter can be designed in MATLAB for the processing of the sampled signals, e.g., voltages and currents.

3.1.5 Impedance calculation

Using the techniques above, the harmonic voltages and currents can be measured and transformed to dq domain (with zero domain neglected) quantities. For one subsystem connected to PCC bus, its impedance response Z_{sub} can be determined as the ratio of the harmonic (phasor form) voltages of the PCC bus V_{PCC} over the harmonic currents flowing into this subsystem I_{sub}.

However, as shown in the simple system model given in Section 2.3, although there is no coupling between different frequencies in the impedance, there is nevertheless coupling between the d- and q- axis variables of each frequency. Thus, the voltage (or current) is represented as a 2 x 1 vector containing the dq components, as shown in (3.6). The impedance matrix relating the current vector to the voltage vector is given by (3.7).

$$\boldsymbol{V_{PCC}} = \begin{bmatrix} V_{d\_PCC} \\ V_{q\_PCC} \end{bmatrix} = \boldsymbol{Z_{sub} I_{sub}} = \boldsymbol{Z_{sub}} \begin{bmatrix} I_{d\_sub} \\ I_{q\_sub} \end{bmatrix} \tag{3.6}$$

$$\boldsymbol{Z_{sub}} = \begin{bmatrix} Z_{dd} & Z_{dq} \\ Z_{qd} & Z_{qq} \end{bmatrix} \tag{3.7}$$

Where, due to the coupling, the impedance matrix is full (not diagonal) as in (3.7).

To determine $\boldsymbol{Z_{sub}}$, two series of injection are required to get the time domain values of voltages and currents in dq domain: V_{d_PCCi}, V_{q_PCCi}, I_{d_subi} and I_{q_subi} (i = 1,2). Applying DFTs to the time domain data, the frequency domain values can be obtained as:

$$\boldsymbol{V_{PCCi}(f)} = \begin{bmatrix} V_{d\_PCCi}(f) \\ V_{q\_PCCi}(f) \end{bmatrix};\ \boldsymbol{I_{subi}(f)} = \begin{bmatrix} I_{d\_subi}(f) \\ I_{q\_subi}(f) \end{bmatrix} \tag{3.8}$$

Then $\boldsymbol{Z_{sub}}$ can be calculated as:

$$\boldsymbol{Z_{sub}(f)} = \begin{bmatrix} V_{d\_PCC1}(f) & V_{d\_PCC2}(f) \\ V_{q\_PCC1}(f) & V_{q\_PCC2}(f) \end{bmatrix} * \begin{bmatrix} I_{d\_sub1}(f) & I_{d\_sub2}(f) \\ I_{q\_sub}(f) & I_{q\_sub2}(f) \end{bmatrix}^{-1} \tag{3.9}$$

3.2 Case study of an ac-dc system

In this section, a case study is put forward to illustrate the application of frequency scanning. This example system is constructed in the PSCAD/EMTDC environment. Fig. 3-4 shows the circuit configuration in which the system is considered as the connection of two subsystems. Subsystem I is the network in the left of the converter bus (PCC bus). It consists of the synchronous generator connected to the converter's ac bus via a lumped connection representation (the R_s-R_p//L_p//C_p circuit). Subsystem II represents the right side of the converter bus. It includes the VSC's ac side transformer (represented by L_t-R_t), the

ac capacitor C_f, the VSC and the dc side circuit consisting of dc capacitor C_{dc}, dc resistor R_{dc} and dc voltage source E_{dc}.

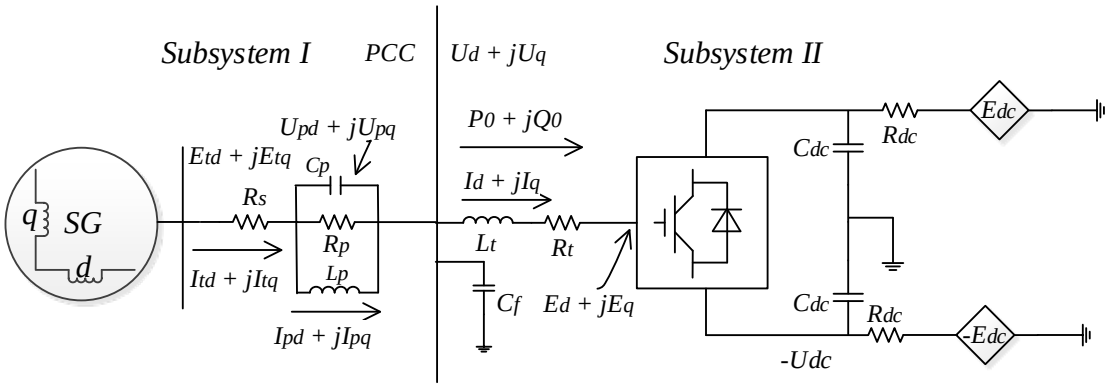

Figure 3-4. Circuit configuration of the scanned system

By injecting a harmonic current into the PCC bus, the harmonic voltages of the PCC and the harmonic currents flowing to both subsystems are excited. Then their impedance responses in the dq0 domain are calculated.

3.2.1 Analytical modeling of the ac and dc subsystems

In this section, both subsystems are modelled analytically to obtain their frequency impedances, which would be used to validate the accuracy of the frequency scanned results. These analytical models can be used directly for determining the frequency response or used as validation when the frequency scan is performed via simulation.

Since the d- and q- axis voltages and currents depend on the reference angle of the dq0 transformation [42], the impedance matrices are also dependent on the reference angle. To simplify the interfacing between different subsystems, the reference angle θ has the form

as in (3.3), and the offset angle θ_0 is selected that the steady state of the q-axis voltage in the PCC bus V_q is zero; i.e., the steady state phase 'a' voltage has the form of $V_a cos(\omega_0 t + \theta_0)$.

Subsystem I can be represented in state space form:

$$\begin{cases} \Delta \dot{\boldsymbol{X}}_{\boldsymbol{ac}} = \boldsymbol{A}_{\boldsymbol{ac}} \Delta \boldsymbol{X}_{\boldsymbol{ac}} + \boldsymbol{B}_{\boldsymbol{ac}} \Delta \boldsymbol{U}_{\boldsymbol{ac}} \\ \Delta \boldsymbol{I}_{\boldsymbol{ac}} = \boldsymbol{C}_{\boldsymbol{ac}} \Delta \boldsymbol{X}_{\boldsymbol{ac}} + \boldsymbol{D}_{\boldsymbol{ac}} \Delta \boldsymbol{U}_{\boldsymbol{ac}} \end{cases} \tag{3.10}$$

The details of (3.10) are given in Appendix A. 1. And the admittance matrix relating the voltage scalar to the current scalar is shown as in (3.11).

$$\Delta \boldsymbol{I}_{\boldsymbol{ac}}(\boldsymbol{s}) = \underbrace{[\boldsymbol{C}_{\boldsymbol{ac}}(\boldsymbol{sI} - \boldsymbol{A}_{\boldsymbol{ac}})^{-1}\boldsymbol{B}_{\boldsymbol{ac}} + \boldsymbol{D}_{\boldsymbol{ac}}]}_{\boldsymbol{admittance\ matrix}} \Delta \boldsymbol{U}_{\boldsymbol{ac}}(\boldsymbol{s}) \tag{3.11}$$

Then the impedance matrix of subsystem I can be obtained by inversing the admittance matrix. Similarly, subsystem II is represented by (3.12) in which the modeling of VSC can be referred to in [43]:

$$\begin{cases} \Delta \dot{\boldsymbol{X}}_{\boldsymbol{con}} = \boldsymbol{A}_{\boldsymbol{con}} \Delta \boldsymbol{X}_{\boldsymbol{con}} + \boldsymbol{B}_{\boldsymbol{con}} \Delta \boldsymbol{I}_{\boldsymbol{con}} \\ \Delta \boldsymbol{U}_{\boldsymbol{con}} = \boldsymbol{C}_{\boldsymbol{con}} \Delta \boldsymbol{X}_{\boldsymbol{con}} + \boldsymbol{D}_{\boldsymbol{con}} \Delta \boldsymbol{I}_{\boldsymbol{con}} \end{cases} \tag{3.12}$$

In Section 2.3, the converter is represented as a linear, time-invariant system. However, when the decoupled controller is introduced as the control system of the converter, as shown in Fig. 3-5, the state equations become non-linear. Linearization is required to get the state space form of the converter, with details in Appendix A. 2. The impedance matrix relating the current scalar to the voltage scalar is shown as in (3.13).

$$\Delta \boldsymbol{U}_{\boldsymbol{con}}(\boldsymbol{s}) = \underbrace{[\boldsymbol{C}_{\boldsymbol{con}}(\boldsymbol{sI} - \boldsymbol{A}_{\boldsymbol{con}})^{-1}\boldsymbol{B}_{\boldsymbol{con}} + \boldsymbol{D}_{\boldsymbol{con}}]}_{\boldsymbol{impedance\ matrix}} \Delta \boldsymbol{I}_{\boldsymbol{con}}(\boldsymbol{s}) \tag{3.13}$$

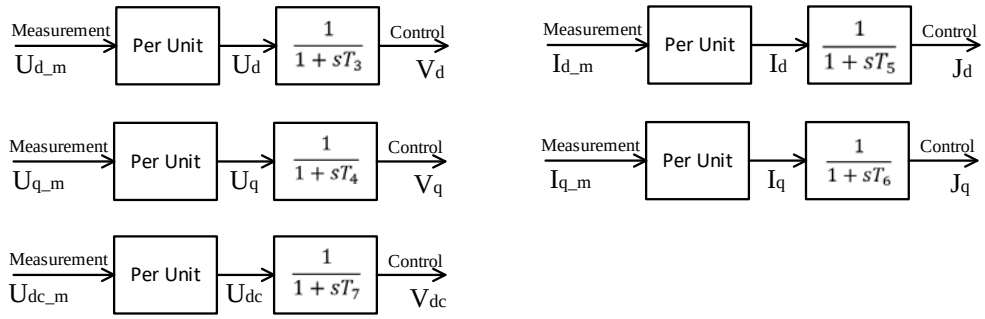

a. Measurement filter and per unit processing

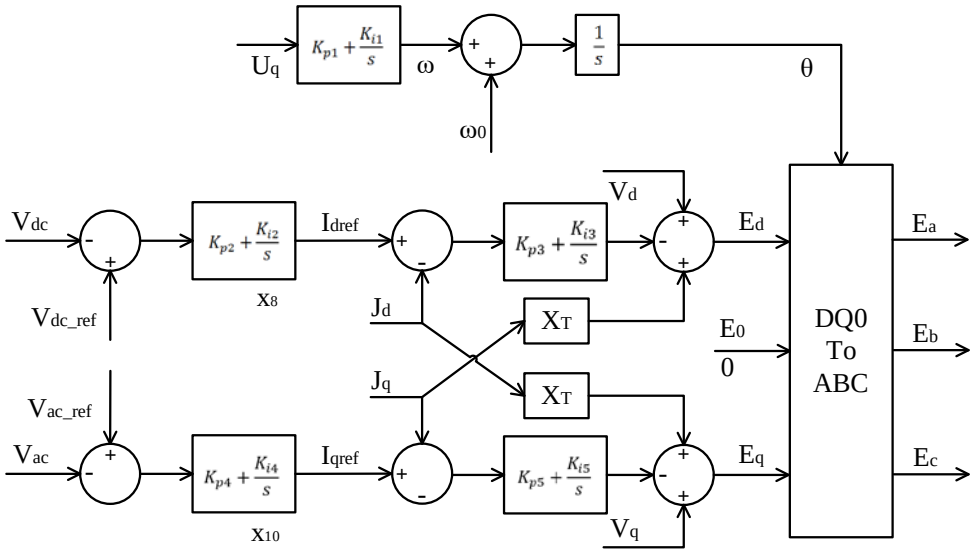

b. Decoupling control logic

Figure 3-5. The control system of the VSC

3.2.2 Frequency scanning of the subsystems

The frequency scanning is used in this section to obtain the impedance responses of both subsystems I and II from EMT simulation. The simulation case models the circuit configuration as in Fig. 3-4 in PSCAD/EMTDC. The control system is as in Fig. 3-5. A component was created in PSCAD to calculate the dq domain harmonic signals which are

injected into the PCC bus. This component also conveys the dq0 domain currents and voltages to the recording files, where the data would be processed in MATLAB.

The injected signals consist of sixty equally spaced frequencies with 1 Hz spread between them in one simulation set. The frequency components have equal magnitude and frequency dependent phase shift (as in equation (3.2)). Totally sixteen simulation sets are run which gives the impedance spectrum from 1Hz to 960Hz. We could also have injected all 960 components simultaneously.

3.2.3 Validation for the scan

Figures 3-6 to 3-9 show the scanned (scanned from simulation) impedance plots as functions of frequency on which the analytically obtained results from (3.11) and (3.13) are superposed. In these figures, the blue lines are the analytical result; and the red lines are the scanned result.

Figure 3-6 shows the magnitude (per unit) of subsystem I (ac side) impedances where:

$$\mathbf{Z}_{\boldsymbol{sub1}} = \begin{bmatrix} Z_{acdd} & Z_{acdq} \\ Z_{acqd} & Z_{acqq} \end{bmatrix} \tag{3.14}$$

Figure 3-7 shows the phase angle in radians for these impedances.

Similarly, Fig. 3-8 and 3-9 are the magnitude and phase angles for subsystem II (dc side) impedances where:

$$\mathbf{Z_{sub2}} = \begin{bmatrix} Z_{dcdd} & Z_{dcdq} \\ Z_{dcqd} & Z_{dcqq} \end{bmatrix} \tag{3.15}$$

All the results match very well.

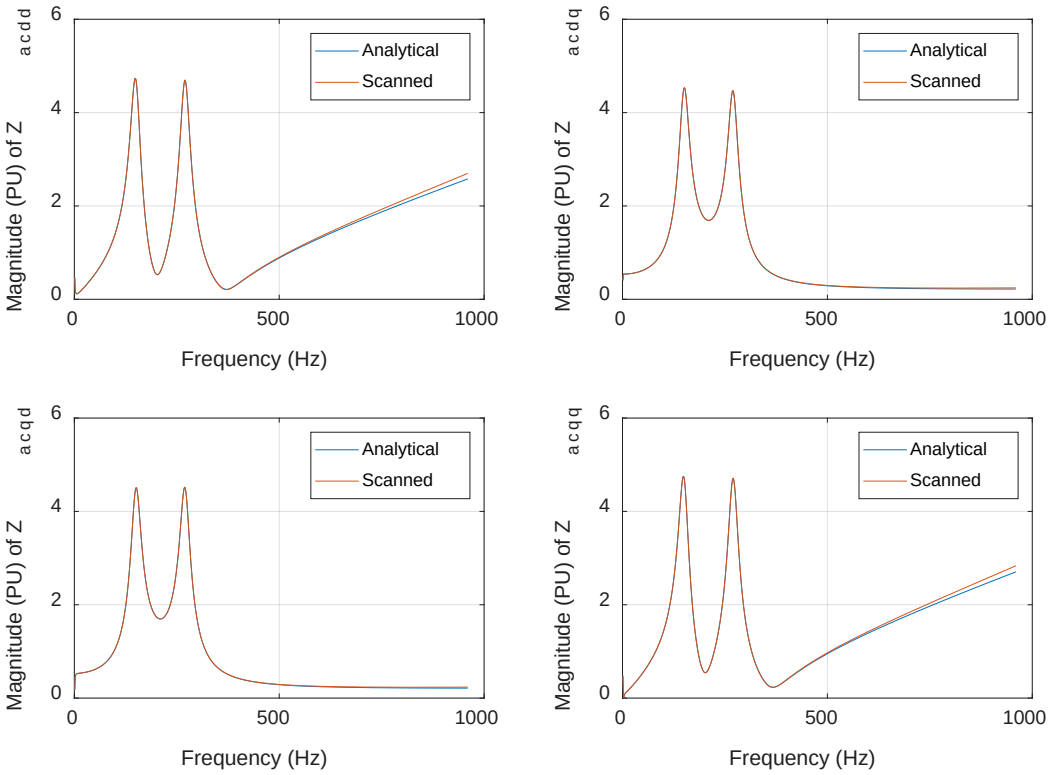

Figure 3-6. Magnitude of the impedance matrix for the subsystem I (ac side)

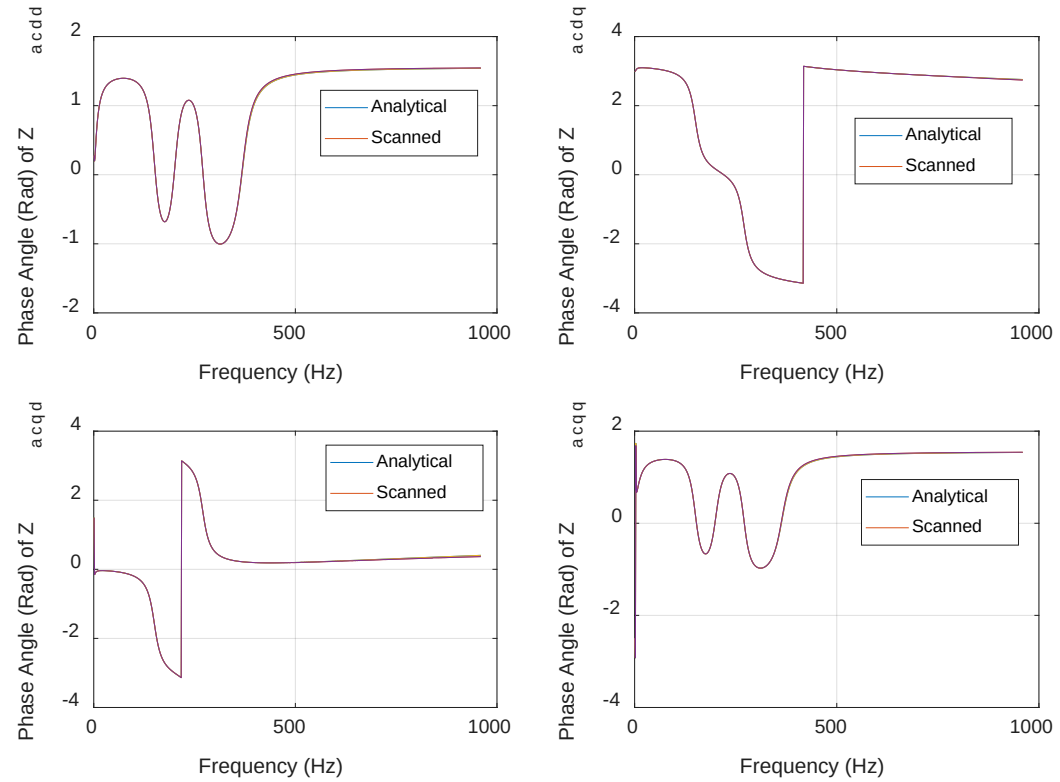

Figure 3-7. Phase angle of the impedance matrix for the subsystem I (ac side)

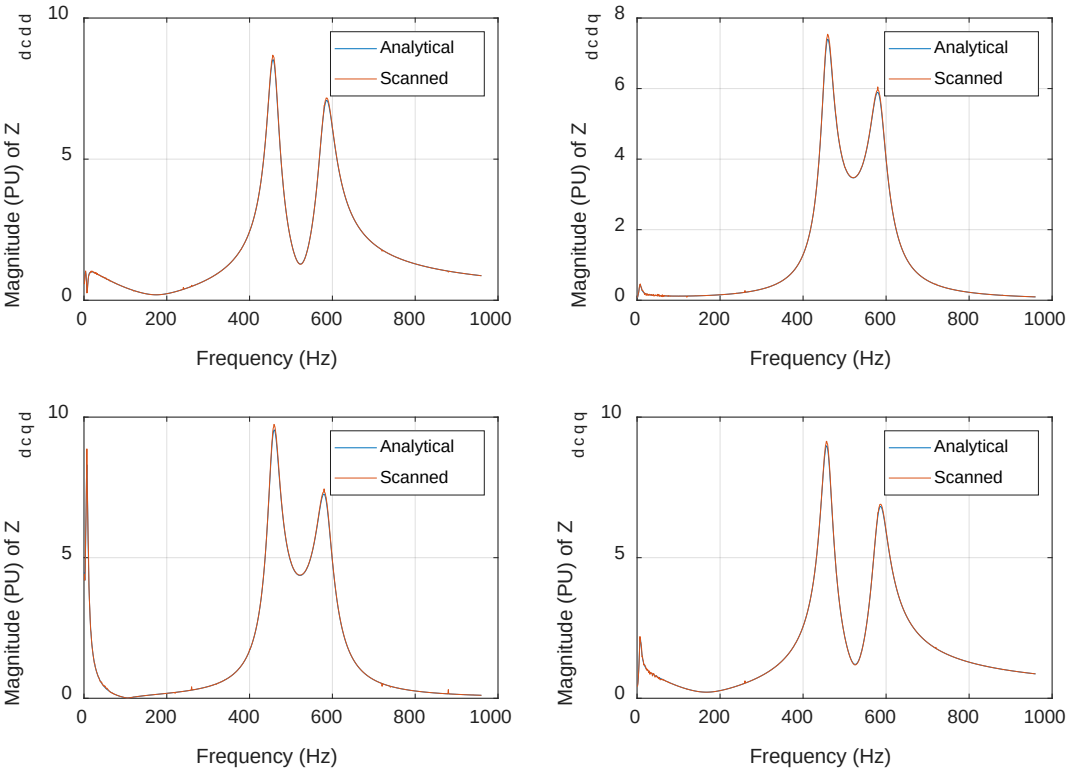

Figure 3-8. Magnitude of the impedance matrix for the subsystem II (dc side)

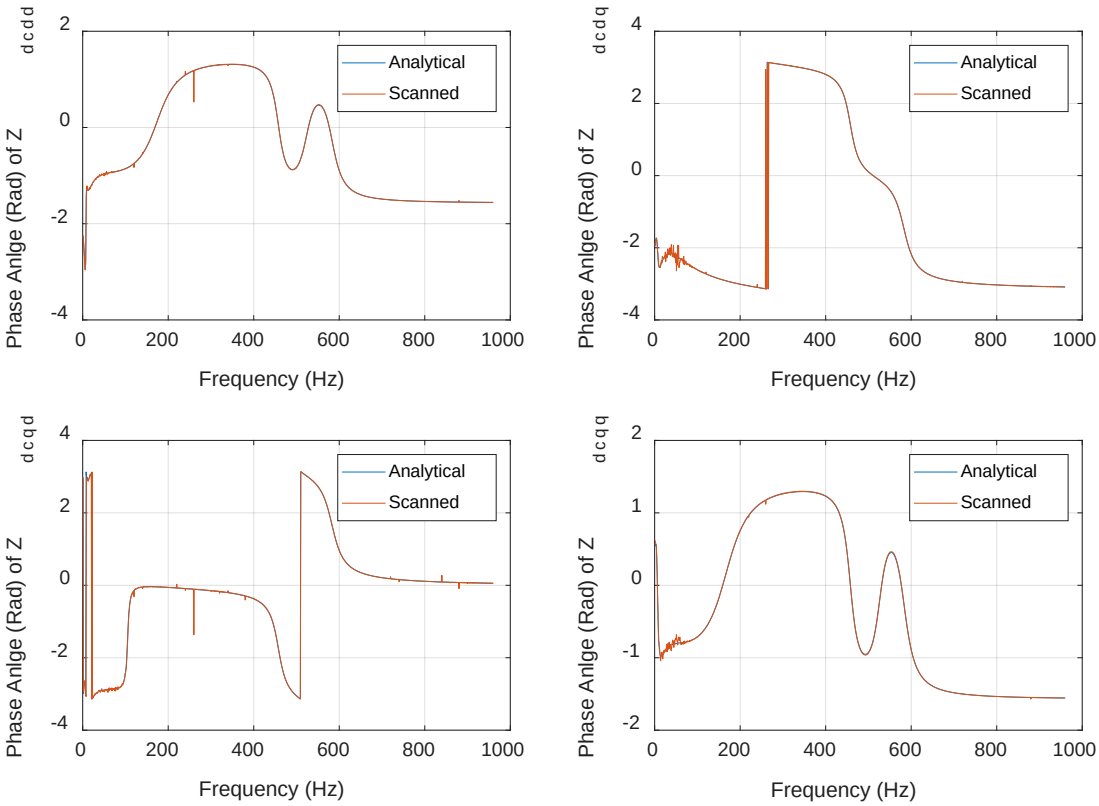

Figure 3-9. Phase angle of the impedance matrix for the subsystem II (dc side)

3.3 Discussions

In this chapter, the impedance responses of two subsystems are obtained from both analytical and frequency scanning approaches. One subsystem includes a synchronous generator, and the other includes a VSC.

The matching between these two results (analytically obtained and scanned) validates the accuracy of the frequency scanning, showing that it is a good approach to identify the impedance response characteristic of an ac-dc network. This scanned impedance of one

subsystem can be used as the benchmark to validate the analytical model, as well as be interfaced with the rest of the system to determine the system stability. In future analysis, either the analytical modeling or the frequency scanning can be used to determine the impedance responses of subsystems.

4 Impedance scanning of the VSC models using a real time simulator

Using the scanning technique, the impedance responses for subsystems can be obtained rapidly from an EMT model. In chapter 3, the impedances of the subsystems (both ac side and dc side) scanned in PSCAD/EMTDC match very well with the responses calculated from the analytical model. However, the PSCAD/EMTDC simulates the systems in non-real time, and it does not allow the hardware-in-loop test. For example, if the controller is black boxed and provided as hardware module, then using a real-time simulator becomes a necessity to simulate the system. Hence this chapter considers conducting frequency scans on a real time simulator. In this case, the RTDS simulator from RTDS Technologies Inc., Winnipeg, Canada was used. Although RTDS also uses Dommel's algorithm [71] to solve network matrices, its typical simulation time step is around 50us (which, in contrast, is flexible in PSCAD). Also, switching accuracy may be less accurate as RTDS does not implement interpolation [72] as PSCAD does [35] [73]. Instead, special techniques are employed, such as multi-rate simulation where a "small time step" module is used to simulate power electronic switches with a smaller time step (e.g., 2us) and a large time-step module is used for simulating the other network parts. Also, the switch representation can be made different to improve the modeling accuracy of the high frequency switches of the VSC. This will be explained in the following sections.

This chapter investigates the application of the scanning technique on RTDS. At the same time, by comparing the impedance responses of the new switch representation with the traditional model, the accuracy of the new switch models can be validated. This work is the extension of the conference paper [74] presented in the 2017 International conference on Power System Transients (IPST). It was also presented in 2017 RTDS Applications & Technology Conference with minor changes.

4.1 Background of the VSC models in RTDS

A real time digital simulator such as RTDS© from RTDS Technologies of Winnipeg, Canada (which is the largest manufacturer of real-time power systems simulators in the world) uses some variant of the EMT algorithm proposed by Dommel [71]. However, the RTDS uses a custom computing architecture so that the algorithm can be executed in real-time (with a reasonable time-step) to enable hardware-in-loop testing of controller or power hardware. Off-line simulators such as PSCAD do not have the real-time constraint and hence can have more elaborate and accurate algorithms. One such algorithm is the switch interpolation algorithm [73] which is used for implementing the opening or closing of a power electronic switch at the precise time. As the command to open or close a switch may fall in between a time-step, linear interpolation is used to adjust the solution to account for the switch opening in between time-steps. Doing so reduces the generation of non-characteristic harmonics and overvoltage spikes due to current chopping in inductive branches. Due to the time-constraint of real-time, the RTDS cannot easily implement this feature. For the LCC, the average switching frequency of the thyristor is quite low (once

per 60Hz cycle) so the errors from not using interpolation are small. But in the VSC, such as the two-level configuration whose gating signals are generated from PWM, the high frequency switching (usually several kHz) cannot be captured by the typical time step around 50us, necessitating a much smaller time step of 2.5us for a good resolution and reasonable accuracy [72] if interpolation is forbidden.

One solution employed by RTDS is to use a portion of the computing hardware which models the VSC, with a small time-step t_s in the range [1.4us, 3.8us]. Naturally, the size of the system which can be modelled in this subsystem (referred to as the "VSC block") is limited. The rest of the system, such as the ac side network, is simulated with a much larger time step t_l, e.g., 50us. A short (fictitious) transmission line is introduced as the interface between the large time step subsystem and the VSC block, as shown in Fig. 4-1.

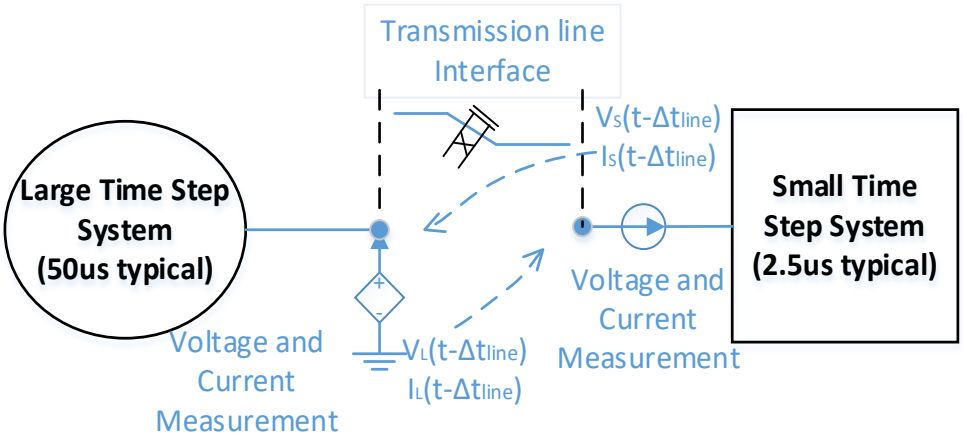

Figure 4-1. The interfacing between the large and small time-step subsystems

Due to the relativistic speed limit (c = 3 x 10^8 km/s), information from one side of the line cannot arrive at the remote side till later, and this allows the solutions on the two sides to

be decoupled [71]. The voltage and current of each end of the transmission line are measured and provided to the other end as history terms with the transmission delay.

EMT simulation uses nodal analysis to calculate the admittance matrix of the network. The most common model for a power electronic switch is referred to as the 'R type' model. In this, if power electronic switch is in the 'ON' state, it is modeled as a small resistance R_{on}, and in the 'OFF' state as a large one R_{off}. When the switch state changes, so does the admittance matrix. The voltage solution for the next time-step can be obtained by pre-multiplying the vector of known source currents and history currents in the present time-step, by the inverse of the admittance matrix [71]. If no switches operate, the admittance matrix and hence its inverse remains unchanged. However, when a switch operates, the admittance matrix must be re-calculated and re-inverted.

In the RTDS, the switch representation of the 'R type' model of a valve is shown in Fig. 4-2b. However, as mentioned above, this limits the size of the network that can be fit on the typical 2.5us time-step. To enable the simulation of larger subsystems, RTDS has also developed an alternative new approach, referred to as 'LC type' approach [75] [76]. This approach is based on an idea primarily from Hui and Christopoulos [77]. In this, the 'ON' state of a switch is modeled by a small inductance L_{sm} and the 'OFF' state by a small capacitance C_{sm} as shown in Fig. 4-2c. The rationale for the model is that at the relatively low frequencies (i.e., up to 2 kHz) used in typical HVDC and other simulations, the impedance of the inductance $j\omega L_{sm}$ is small and it mimics and 'ON' switch. Likewise, for a sufficiently small value of C_{sm}, the capacitance has a large impedance $1/j\omega C_{sm}$, thereby

mimicking an ‘OFF’ switch. In Fig. 4-2c, a small resistor R_{sm} is connected in series with the small capacitor C_{sm} to represent the ‘OFF’ state to avoid unexpected oscillation.

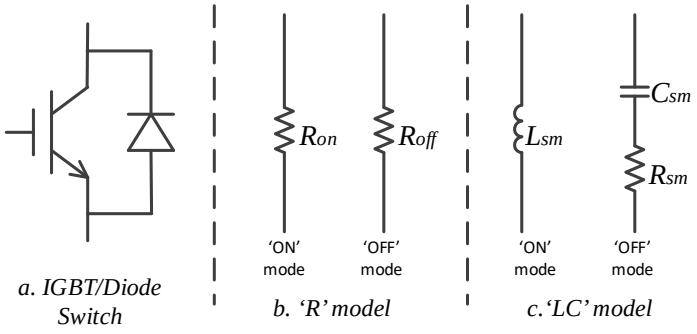

Figure 4-2. Switch representations of the valve in two type of converter models

In the admittance matrix generating of an EMT simulation, the Dommel’s conductance of the small inductance is $\Delta t_s/2L_{sm}$, and of the small capacitance is $2C_{sm}/\Delta t_s$. If we can properly set L_{sm}, C_{sm} and R_{sm}, making $\Delta t/2L_{sm} = (2C_{sm}/\Delta t_s)//(1/R_{sm})$ (same admittance for ‘ON’ and ‘OFF’ states), the system admittance matrix would not change as a switch operates and only the history current term needs to be updated. This technique enables the pre-process of the system admittance matrix and thereby, the efficient modeling of VSC block [72][75-77].

Ideally, one would like the ‘LC type’ model and the ‘R type’ model to provide near-identical results. However, in the ‘LC type’ representation, it is possible that additional dynamic behavior could occur because of the energy storage elements L_{sm} and C_{sm}. Frequency scanning can be used to identify whether the added dynamics are problematic. This requires the comparison with an analytical model of the VSC. For this purpose,

improved analytical models were developed for both the ‘R type’ and ‘LC type’ converters in this research as described in the next section.

The converter models using the ‘R type’ and ‘LC type’ representations appear on the RTDS GUI palette (RSCAD) as in Fig. 4-3. The ‘R type’ converter model is shown in Fig. 4-3a, which also includes the transmission line interface between the large and small time-step subsystems. For the ‘LC type’ model as in Fig. 4-3b, only the six valves are presented, and the transmission line is not integrated inside. Users can connect the valve terminal nodes to the system themselves.

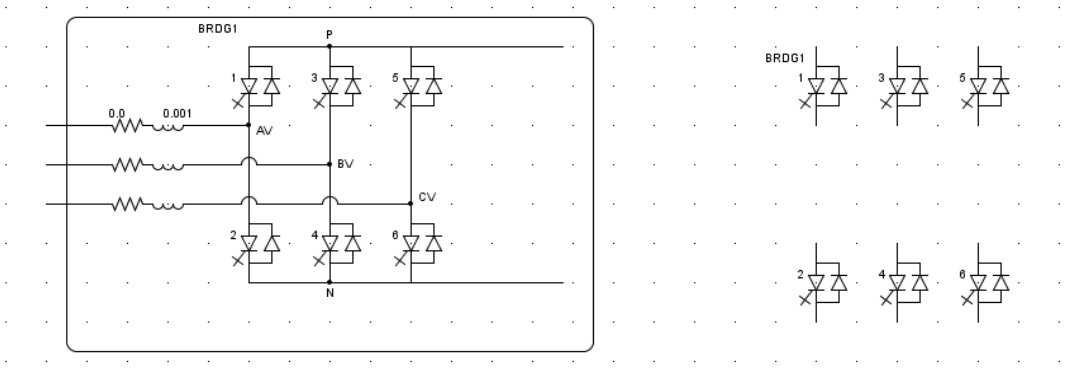

a) ‘R’ type converter (R_{on} / R_{off}) b) ‘LC’ type converter (L_s / C_s-R_s)

Figure 4-3. The ‘R type’ and ‘LC type’ converters in RTDS GUI

4.2 Improvement of the VSC analytical model

As mentioned in the previous section, frequency scanning was identified as a promising approach to validate both the ‘R type’ and ‘LC type’ models. For this purpose, it is necessary to have accurate analytical models of the converters for the two as shown in Fig. 4-3.

The analytical model of VSC reported in the previous chapter (with details shown in Appendix A.2) does not include the effect of the switching resistances, with the 'ON' state of a valve considered as an ideal short circuit and the 'OFF' state as an ideal open circuit. However, in the 'R type' converter, the model uses the 'ON' state resistance R_{on} and 'OFF' state resistance R_{off}. Similarly, the 'LC type' utilizes L_{sm} and R_{sm}-C_{sm} to represent the two states.

To determine whether the 'R type' and 'LC type' models give equivalent frequency scan result, it is necessary to develop analytical models for the two switch representations.

4.2.1 Analytical model for 'R type' converter

To include R_{on} / R_{off}, the switch states for the 'a' phase leg in one three-phase converter is shown in Fig. 4-4. Here the resistances alternately take on values of R_{on} and R_{off} as decided by two complementary PWM modulated waveforms. The resulting waveform in ac side has the same shape as the upper leg PWM signal and alternatively switches between $+U_{dc}$ and $-U_{dc}$, where U_{dc} is the dc capacitor voltage.

The equivalent circuit is shown in Fig. 4-5 for the converter based on the switching modulation shown in Fig. 4-4. As in Fig. 4-5a, the ac side system is connected through 'R_{on}' to the modulated dc voltage $\left({E_d}^s + j{E_q}^s\right) * U_{dc}$ (${E_d}^s$ and ${E_q}^s$ are the outputs of the control system), and through 'R_{off}' to the inversed modulated waveform which is

$-\left(E_d{}^s + jE_q{}^s\right) * U_{dc}$. The superscript 's' indicates that the dq0 transformation used to get dq quantities is the same as defined in Chapter 3, i.e., the reference angle of the dq0 transformation is θ in (3.3).

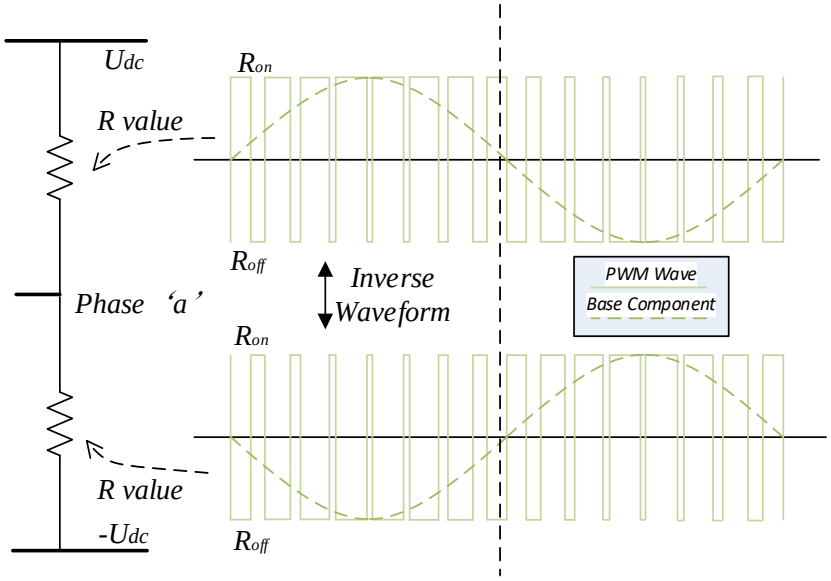

Figure 4-4. The effect of R_{on} / R_{off} based on PWM

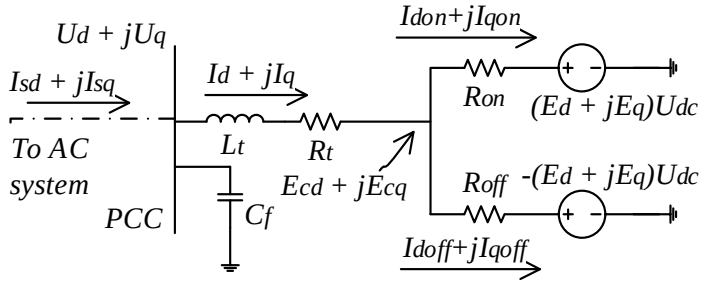

a. Equivalent circuit of the ac side including R_{on} and R_{off}

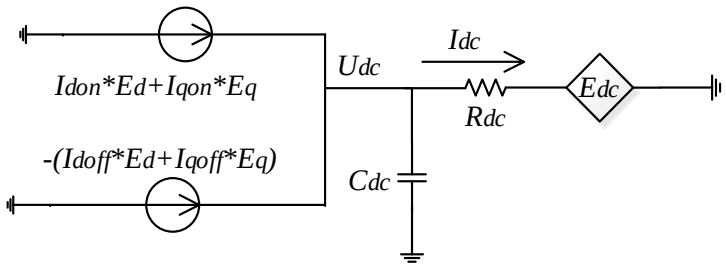

b. Equivalent circuit of the dc positive side with R_{on} and R_{off}

Figure 4-5. Equivalent circuit for the ac and dc side with the ON/OFF resistance

For the dc side, the positive bus is connected to two current sources shown as in Fig. 4-3b, which are the products of two ac current values and the PWM switching function, and the negative dc side is symmetrical to the positive side. The analytical equations for the circuit in Fig. 4-5 are as follows:

$$C_f \frac{d}{dt}\begin{bmatrix} {U_d}^s \\ {U_q}^s \end{bmatrix} + \begin{bmatrix} 0 & -\omega_0 C_f \\ \omega_0 C_f & 0 \end{bmatrix}\begin{bmatrix} {U_d}^s \\ {U_q}^s \end{bmatrix} = \begin{bmatrix} {I_{sd}}^s \\ {I_{sq}}^s \end{bmatrix} - \begin{bmatrix} {I_d}^s \\ {I_q}^s \end{bmatrix} \tag{4.1}$$

$$L_t \frac{d}{dt}\begin{bmatrix} {I_d}^s \\ {I_q}^s \end{bmatrix} + \begin{bmatrix} R_t + R_c & -\omega_0 L_t \\ \omega_0 L_t & R_t + R_c \end{bmatrix}\begin{bmatrix} {I_d}^s \\ {I_q}^s \end{bmatrix} = \begin{bmatrix} {U_d}^s \\ {U_q}^s \end{bmatrix} - \begin{bmatrix} {E_d}^s \\ {E_q}^s \end{bmatrix} U_{dc} * k \tag{4.2}$$

$$\begin{bmatrix} {I_{don}}^s \\ {I_{qon}}^s \end{bmatrix} = \frac{-2\begin{bmatrix} {E_d}^s \\ {E_q}^s \end{bmatrix} U_{dc} + R_{off}\begin{bmatrix} {I_d}^s \\ {I_q}^s \end{bmatrix}}{R_{off} + R_{on}} \tag{4.3}$$

$$\begin{bmatrix} {I_{doff}}^s \\ {I_{qoff}}^s \end{bmatrix} = \frac{2\begin{bmatrix} {E_d}^s \\ {E_q}^s \end{bmatrix} U_{dc} + R_{on}\begin{bmatrix} {I_d}^s \\ {I_q}^s \end{bmatrix}}{R_{off} + R_{on}} \tag{4.4}$$

$$C_{dc} \frac{dU_{dc}}{dt} = \left(\begin{bmatrix} {I_{don}}^s \\ {I_{qon}}^s \end{bmatrix} - \begin{bmatrix} {I_{doff}}^s \\ {I_{qoff}}^s \end{bmatrix}\right)^T \begin{bmatrix} {E_d}^s \\ {E_q}^s \end{bmatrix} - I_{dc} \tag{4.5}$$

The k and Rc in (4.2) are given by:

$$k = (R_{off} - R_{on})/(R_{off} + R_{on}),\ R_c = R_{off} || R_{on}.$$

As the ‘R type’ switch in the converter model requires a matrix re-factorization at each switch turn-on or turn-off, it would result in a significant computational burden if the entire network is modeled as a single system. A computation saving approach that is used in the RTDS is to model the converter as a separate subsystem connected to the main network via a transmission line with a one time-step travel time. The transmission line decouples the networks, and a switching in the converter only requires a re-factorization of the converter side subsystem. This interface transmission line (based on the Bergeron model [3][71]) connecting the ac side system and converter valves may have some influence on the system

frequency response in the high frequency range, i.e., f > 1000 Hz. Although implemented as a distributed parameter system, the transmission line can be viewed as a pi-section model with a virtual capacitor at both ends, whose value is determined by the line inductance and the simulation time step. By properly setting the inductance value as 'Lt', the capacitor value becomes very small compared to the ac capacitor 'Cf' in Fig. 4-5. With this treatment, the effect of the interface model is minimized in the frequency range of f < 1000 Hz.

4.2.2 Analytical model for 'LC type' converter

The circuits in Fig. 4-5 including the effect of non-ideal R_{on} / R_{off}, can be also used to investigate the model of the 'LC' type converter, with Fig. 4-5 updated to Fig. 4-6. However, for the 'LC type' model in RTDS, the updating of the history current for the valves after a switching action is not the same as a regular inductor or capacitor, as some special techniques are applied to enhance the transient behavior after a switching action. Hence, this circuit configuration, as well as the state equations provided below cannot exactly reflect the characteristics of the 'LC type' converter in RTDS.

The purpose of developing this analytical model is to identify that if the frequency response can be greatly influenced by the introduction of the energy storage elements, i.e., if spurious oscillation would happen, even when there is no small resistance R_{sm}.

The state equations representing the circuits in Fig. 4-6 are given as:

$$L_t \frac{d}{dt}\begin{bmatrix} {I_d}^s \\ {I_q}^s \end{bmatrix} + \begin{bmatrix} R_t & -\omega_0 L_t \\ \omega_0 L_t & R_t \end{bmatrix}\begin{bmatrix} {I_d}^s \\ {I_q}^s \end{bmatrix} = \begin{bmatrix} {U_d}^s \\ {U_q}^s \end{bmatrix} - \begin{bmatrix} E_{cd} \\ E_{cq} \end{bmatrix} \quad (4.6)$$

$$L_{sm}\frac{d}{dt}\begin{bmatrix}I_{ld}\\I_{lq}\end{bmatrix}+\begin{bmatrix}0 & -\omega_0 L_{sm}\\ \omega_0 L_{sm} & 0\end{bmatrix}\begin{bmatrix}I_{ld}\\I_{lq}\end{bmatrix}=\begin{bmatrix}E_{cd}\\E_{cq}\end{bmatrix}-\begin{bmatrix}E_d{}^s\\E_q{}^s\end{bmatrix}U_{dc} \qquad (4.7)$$

$$C_{sm}\frac{d}{dt}\left(\begin{bmatrix}E_{cd}\\E_{cq}\end{bmatrix}+\begin{bmatrix}E_d{}^s\\E_q{}^s\end{bmatrix}U_{dc}\right)+\begin{bmatrix}0 & -\omega_0 C_{sm}\\ \omega_0 C_{sm} & 0\end{bmatrix}\left(\begin{bmatrix}E_{cd}\\E_{cq}\end{bmatrix}+\begin{bmatrix}E_d{}^s\\E_q{}^s\end{bmatrix}U_{dc}\right)=\begin{bmatrix}I_{cd}\\I_{cq}\end{bmatrix}=\begin{bmatrix}I_d{}^s\\I_q{}^s\end{bmatrix}-\begin{bmatrix}I_{ld}\\I_{lq}\end{bmatrix} \quad (4.8)$$

$$C_{dc}\frac{dU_{dc}}{dt}=(\begin{bmatrix}I_{ld}\\I_{lq}\end{bmatrix}-\begin{bmatrix}I_{cd}\\I_{cq}\end{bmatrix})^T\begin{bmatrix}E_d{}^s\\E_q{}^s\end{bmatrix}-\frac{U_{dc}-E_{dc}}{R_{dc}} \qquad (4.9)$$

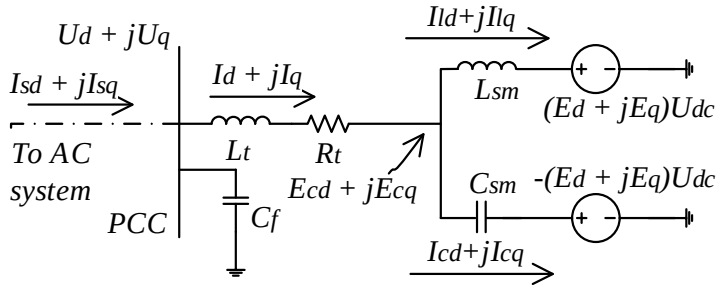

a. Equivalent circuit of AC side with L_{sm} and C_{sm}

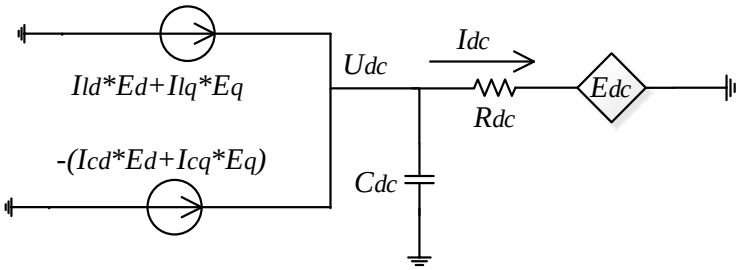

b. Equivalent circuit of DC positive side with L_{sm} and C_{sm}

Figure 4-6. Equivalent circuit for the ac and dc side with the L_{sm} and C_{sm}

With above equations linearized, the analytical state space models of the system with different switch representations, i.e., for both 'R type' and 'LC type' converters, can be obtained.

4.2.3 Comparison between the analytical impedance responses of the 'R type' and 'LC type' converters

To compare the analytical characteristics of the two types of converters, the example system including a VSC converter is studied as in Fig. 4-7, in which the dc side and controller of the system are similar to the system shown in Fig. 3-4 and Fig. 3-5. The ac side includes an L_s-R_s series circuit, and the controller parameter are given as in Appendix B.

This case system is also constructed in RTDS to apply the frequency scanning to validate the two types of converter models, as in Section 4.3 below.

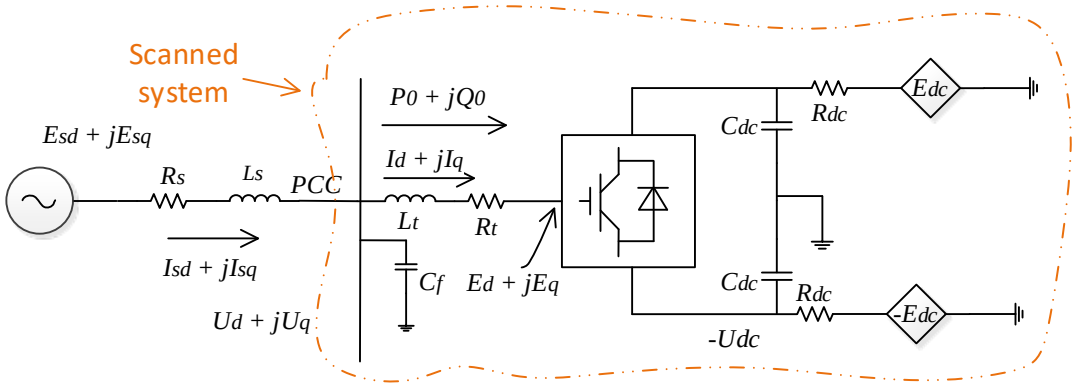

Figure 4-7. Example system used to validate the analytical result and to apply the scanning

As explained above, the Dommel's admittance of L_{sm} and C_{sm} should be the same (with R_{sm} neglected). Also, consistency should be kept between the 'R type' and 'LC type' converters for comparison, that the 'ON' resistance should be equal to the impedance of the L_{sm} at fundamental frequency, and the 'OFF' resistance to the impedance of C_{sm}. Hence, we have:

$$\begin{cases} \dfrac{2C_{sm}}{\Delta t_s} = \dfrac{\Delta t_s}{2L_{sm}} \\ R_{on} = |j\omega_0 L_{sm}| \\ R_{off} = \left|\dfrac{1}{j\omega_0 C_{sm}}\right| \end{cases} \tag{4.10}$$

Here, Δt_s is set as 2.0us which is a typical small time-step. R_{on} is chosen as 0.002 pu. From (4.10), we get: $R_{off} = 14071\,pu$, $L_{sm} = 5.3 * 10^{-6}\,pu$, and $C_{sm} = 1.89 * 10^{-7}\,pu$. Using these parameters and the state space models of the converters, the impedance response of the converter side system, looking from the PCC bus, can be obtained for both type of converters in dq0 domain. The response is a dq coupled 2x2 dimensional matrix with elements Z_{dd}, Z_{dq}, Z_{qd} and Z_{qq}. The magnitudes (in per unit) of the impedance matrix are shown as in Fig. 4-8 and phase angles (in degrees) are in Fig. 4-9.

The curve labelled ‘LC type’ is the analytical result in which the converter is modelled as ‘LC type’ in the case system, and the curve with name ‘R type’ is the result in which the converter is modelled as ‘R type’.

From the comparison we can find that the impedance responses of the ‘LC type’ converter are identical to those of the ‘R type’ converter, indicating that the no significant error is introduced by modelling the switch as an ‘LC’ switch.

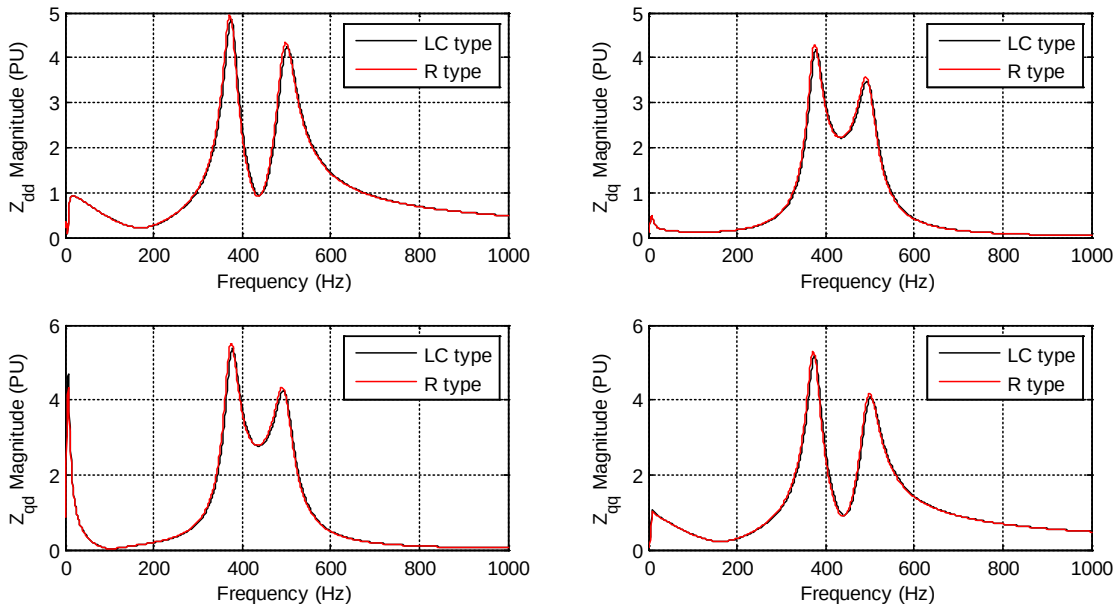

Figure 4-8. Magnitude of the analytical converter side impedance

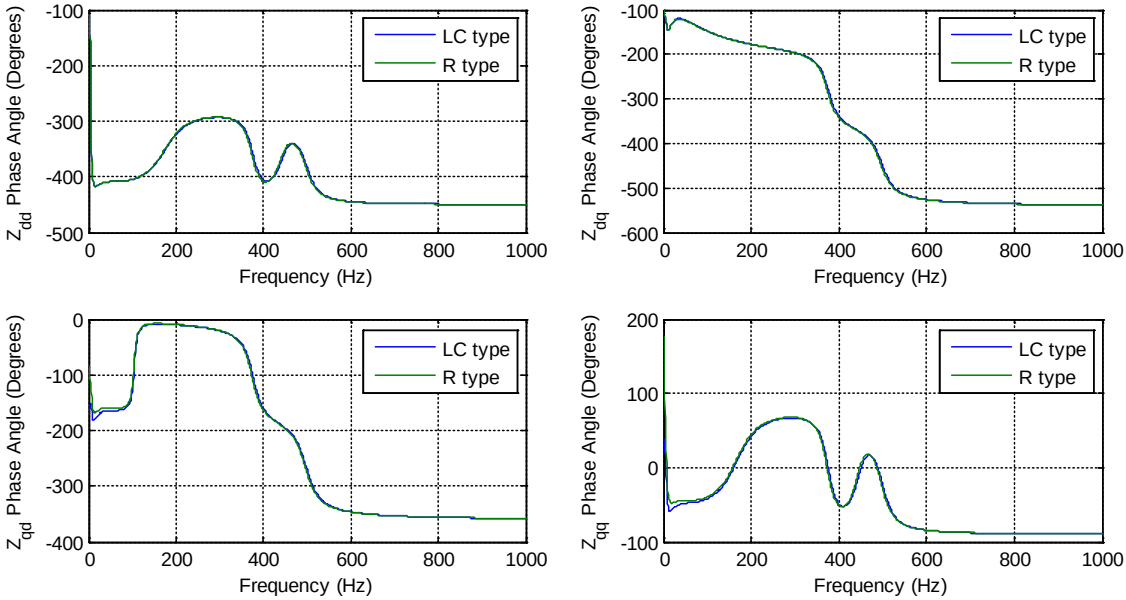

Figure 4-9. Phase angle of the analytical converter side impedance

4.3 Simulation-based frequency scanning of the converter system

To further validate the above models, a simulation-based frequency scan is conducted on the EMT model in which the converter model is the 'R type' as shown in Fig. 4-3b, and on the system with 'LC type' converter in Fig. 4-3c. In the RTDS, the current injection is only possible in the large time-step system for now, and a user-defined component was created using the 'C builder' in RTDS, which provides access to a set of C language features which are a subset of the entire C language. Excited by the harmonic injection, the resultant currents & voltages are saved to MATLAB for further Discrete Fourier transform (DFT) analysis and impedance calculations. The parameters of the ac system, dc system and the control system are the same as in Section 4.2.3.

The valve parameters of the two types of converter representations ('R type' and 'LC type') in RTDS, are given below in Table 4-1. For the 'LC type' converter, the small inductance L_{sm} representing the 'ON' state is the same as in Section 4.2.3 which is determined from (4.11); the 'OFF' state is modeled by the C_{sm}-R_{sm} circuit satisfying (4.12), and a 'damping factor' parameter is used in the model to determine the exact values of C_{sm} and R_{sm}.

$$R_{on} = |j\omega_0 L_{sm}| = 0.002PU \tag{4.11}$$

$$R_{off} = \left|\frac{1}{j\omega_0 C_{sm}} + R_{sm}\right| = 2000PU \tag{4.12}$$

Table 4-1. Parameters of the 'R type' and 'LC type' converter

'R type'	R_{on}	R_{off}	
Values	*0.06ohm*	*156000ohm*	
'LC type'	R_s	C_s	L_s
Values	*132ohm*	*0.017uF*	*0.15mH*

Looking from the ac side, as shown in Fig. 4-10a, the impedance response is measured from the Point of Common Coupling (PCC) bus, and the scanned system includes ac capacitor C_f, the L_t-R_t series circuit, the converter, and the dc side circuit. As in Fig. 4-10b, the ac side system is scanned looking from the PCC bus which includes the dc capacitor C_{dc}, the converter, and the ac side system.

The simulation time step is 50 us for the external ac network and 2 us for the converter model (and dc system). Considering that the frequency responses depend on the operating point, two typical operating points are chosen here for comparison, as in Table 4-2, with different active and reactive powers from the PCC bus to the converter (in per unit), as shown in Fig. 4-7.

Table 4-2. Operating points of the VSC

Operating point	$\boldsymbol{P_0}$	$\boldsymbol{Q_0}$
1	1 PU	0 PU
2	0.6 PU	0.2 PU

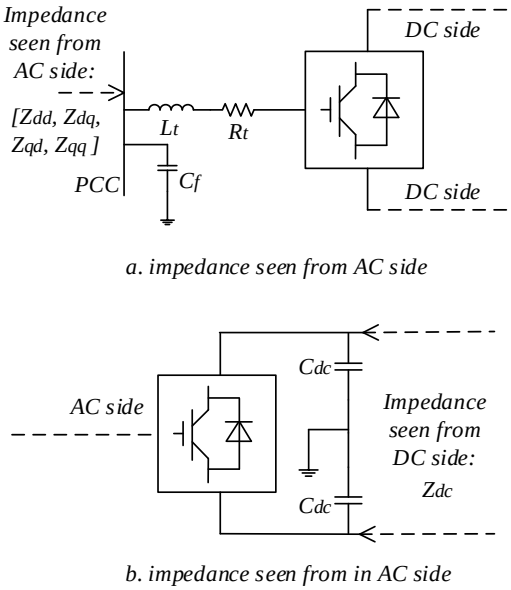

Figure 4-10. Impedances looking from the ac and dc side

4.3.1 Impedance comparison for operating point 1

At operating point 1, the VSC is operating at maximum active power. The comparison of ac and dc impedance scans for the 'R type' model, the 'LC type' model and the analytical results (based on the 'R type' analytical model in Section 4.2.1) is shown in Figs. 4-11 to 4-13 for the frequency range 1 Hz to 1000 Hz. This range is adequate for most network interaction studies (transient stability and low order resonances) carried out on the RTDS with a 50 us time-step.

In Figs. 4-11 and 4-12, the four subplots are the dq domain coupled impedances looking from the ac side: Z_{dd}, Z_{dq}, Z_{qd} and Z_{qq}(see Fig. 4-7a). Fig. 4-11 shows the magnitude (in per unit) and Fig. 4-12 shows the phase angles (in degrees). Fig. 4-13 shows the magnitude (in per unit) and the phase angle (in degrees) of the impedance response looking

from the dc side: Z_{dc} (see Fig. 4-7b). In these figures, the scanned results and the analytical results are matching very in general, except for the additional ripple in the scanned results.

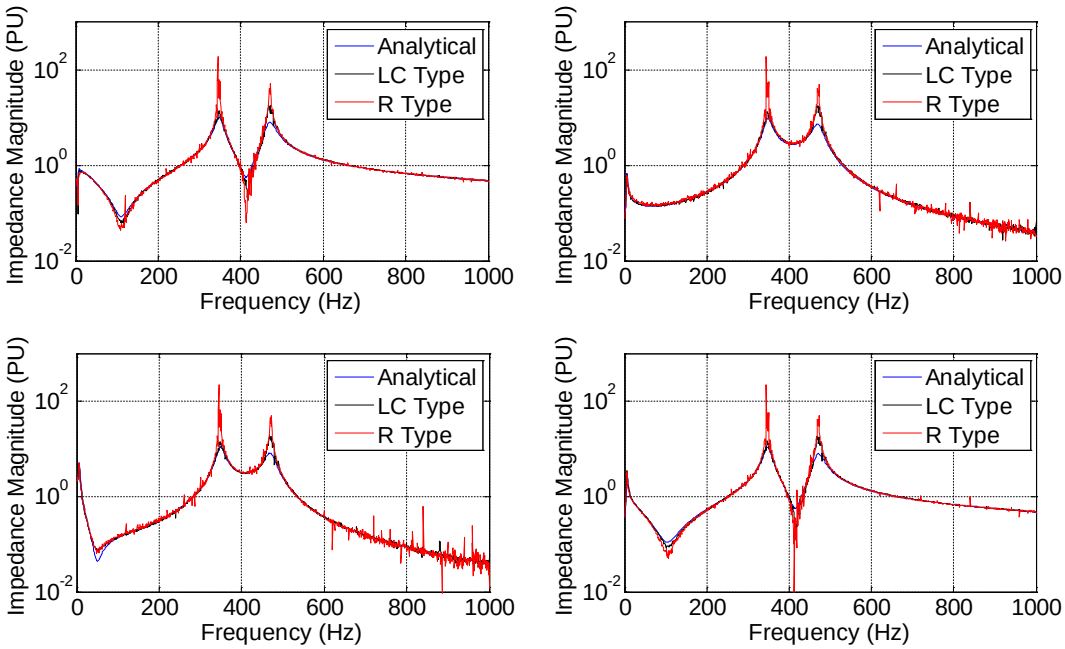

Figure 4-11. Ac side impedance magnitude (Z_{dd} Z_{dq} Z_{qd} Z_{qq})

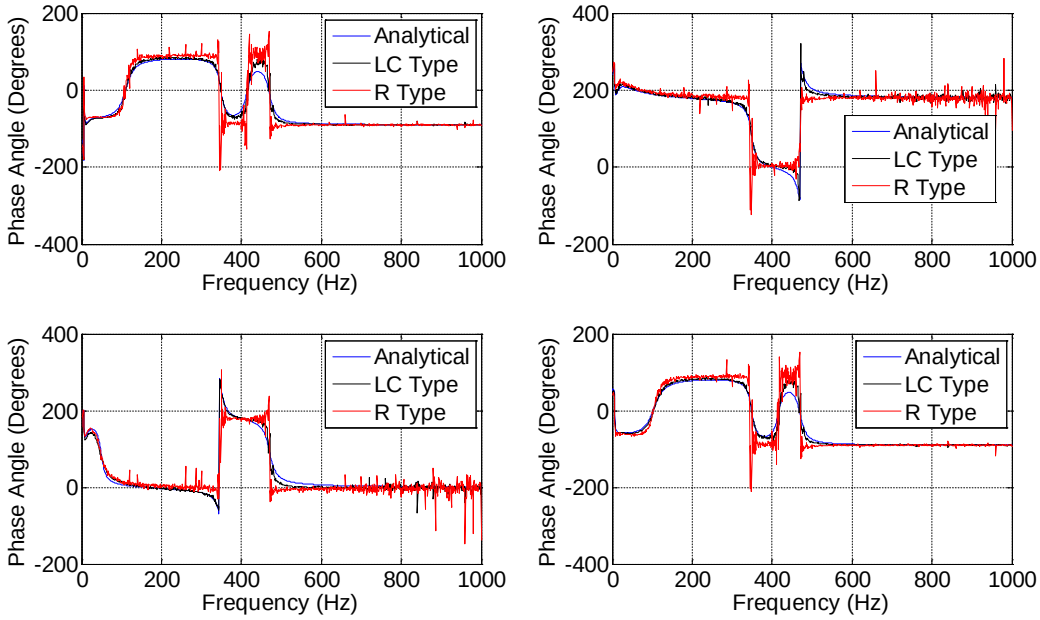

Figure 4-12. Ac side impedance phase angle (Z_{dd} Z_{dq} Z_{qd} Z_{qq})

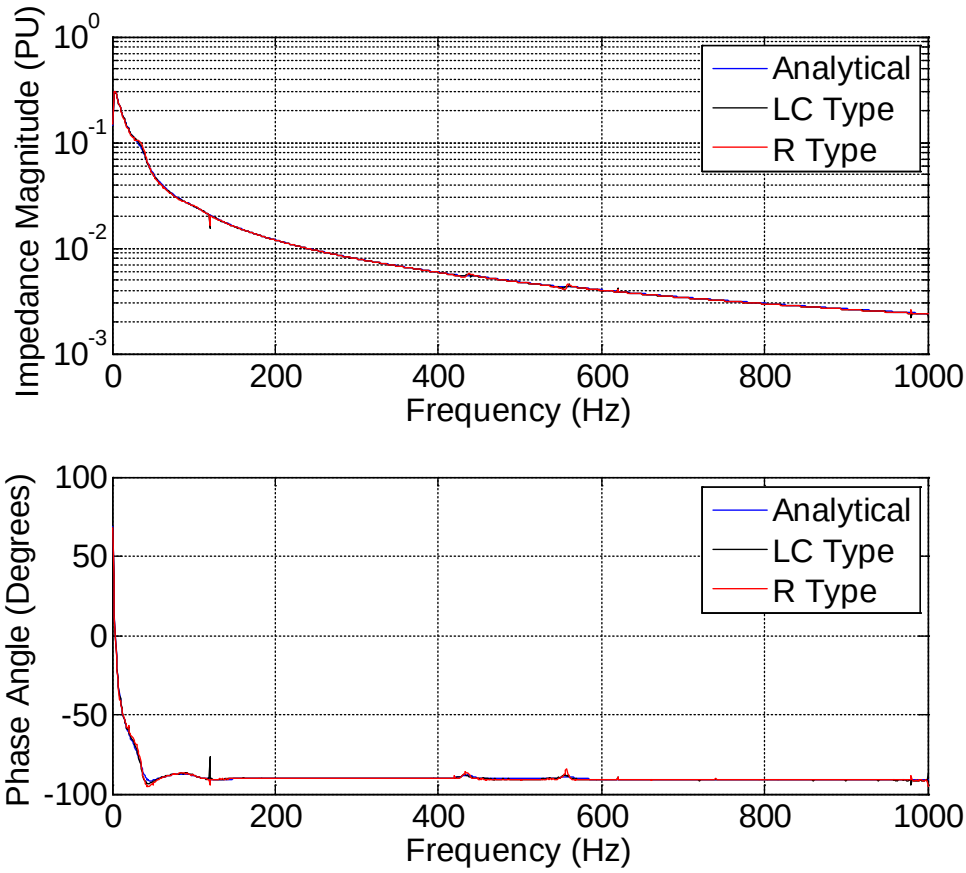

Figure 4-13. Dc side impedance magnitude and phase angle

4.3.2 Impedance comparison for operating point II

Figs. 4-14 and 4-15 are the magnitude and phase angle of impedance looking from the ac side and Fig. 4-16 shows the result looking from the dc side for the operating point II. This impedance response is also obtained from a simulation case with 50 us large time-step for external network (and 2 us for converter network) in RTDS. In this operating point, the impedance results also generally agree. There is some minor difference with the analytical response, particularly visible as slightly higher damping around resonance points. Moreover, there is more ripple. It is interesting to note that the agreement is much better

and the ripple generally much less when the off-line simulator PSCAD/EMTDC was used in Chapter 3. The reason for this is explained next.

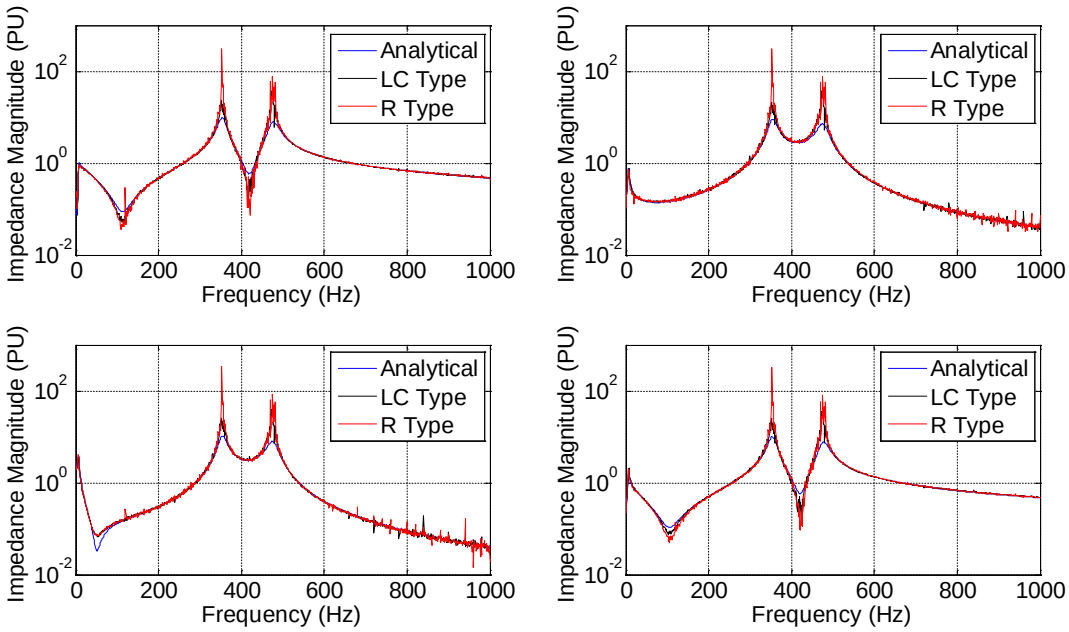

Figure 4-14. Ac side impedance magnitude (Z_{dd} Z_{dq} Z_{qd} Z_{qq})

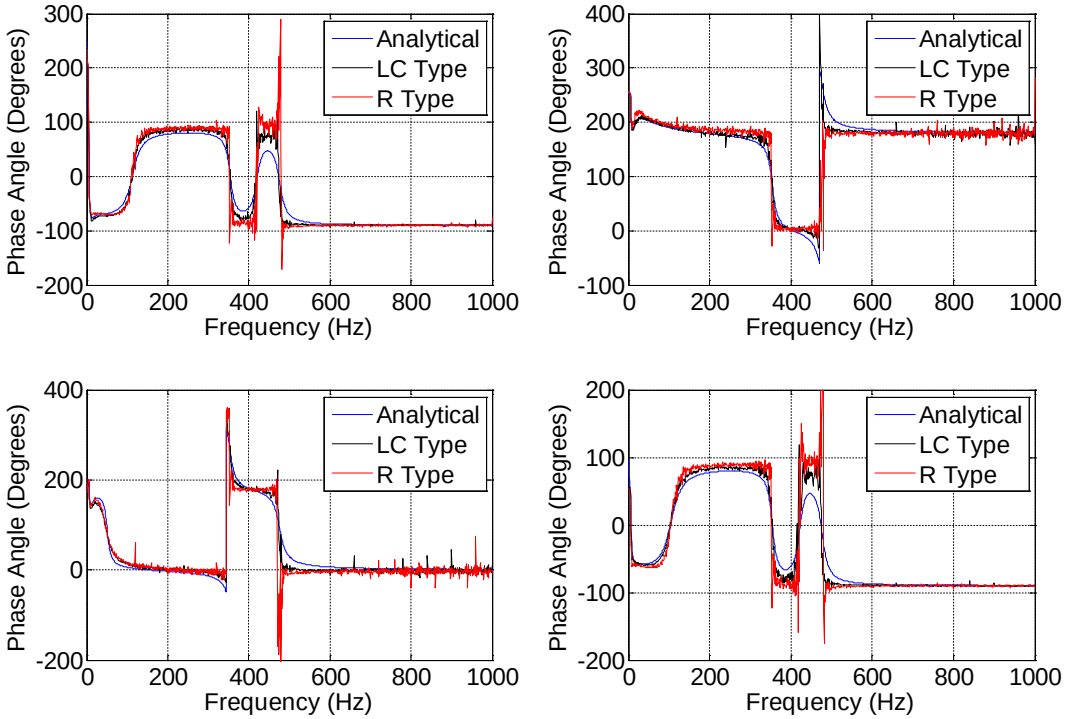

Figure 4-15. Ac side impedance phase angle (Z_{dd} Z_{dq} Z_{qd} Z_{qq})

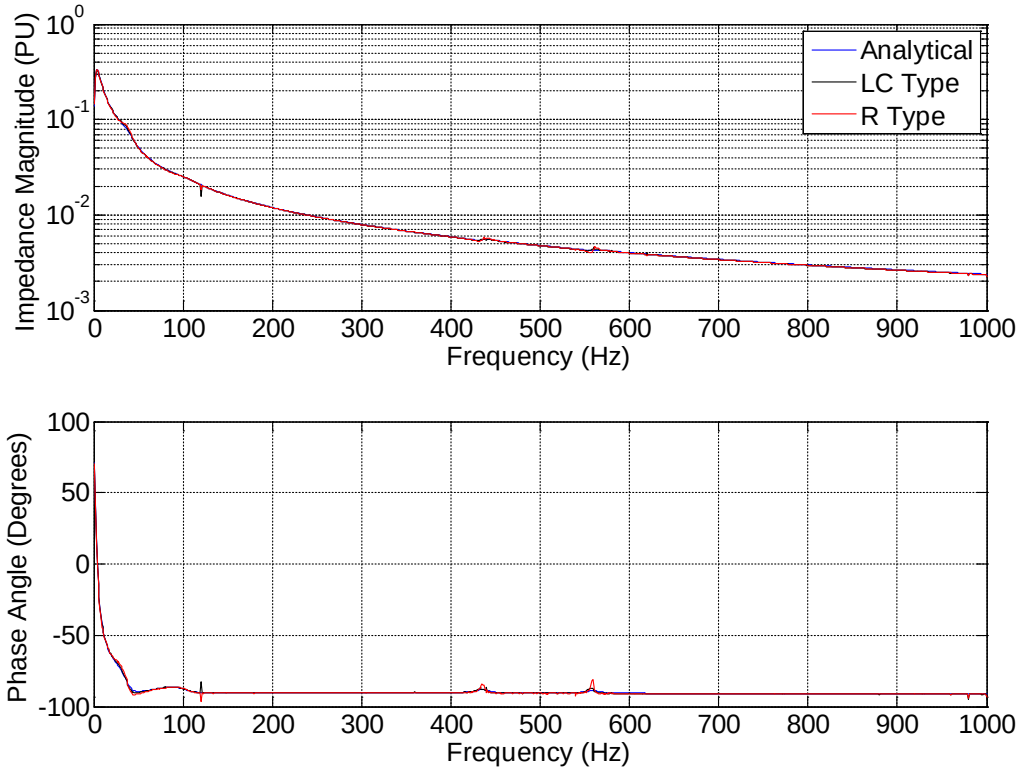

Figure 4-16. Dc side impedance magnitude and phase angle

4.4 Analysis on the noise in the scanned impedance responses in RTDS

In Figs. 4-11 to 4-16, there is a lot of noise shown in the impedance results. This makes it difficult to use a Nyquist plot to determine the system stability based on these results, as some unexpected encirclement can happen due to the ripple in the impedance characteristics. The noise can be due to the PWM switching frequency of 2.16 kHz (36^{th} harmonic), the finite time-step and the fact that interpolation is not allowed on the RTDS to accurately capture the exact switching instant. The true switching waveform from PWM, includes the fundamental frequency waveform based on the reference waveform produced

by the control system, and higher frequency harmonics (clustered around the 2.16 kHz carrier frequency).

In the off-line simulation results obtained from PSCAD/EMTDC in Chapter 3, the impedance responses do not show the noise and show excellent agreement between theoretical and analytical scans. In PSCAD, the PWM carrier frequency is also 2.16 kHz, and the simulation time-step is 2us, and the switching is very accurate because of interpolation.

The likely cause for the discrepancy observed in the RTDS scans is due to lack of interpolation in the PWM, which results the background harmonic in the time-domain waveforms, e.g., voltages. It is not a fundamental problem with the 'R type' or 'LC type' switch representations.

4.4.1 Study on the PWM output waveform with no interpolation

The spectral analysis of the switching waveform from PWM is conducted in MATLAB to see how not using interpolation introduces non-characteristic harmonics into the spectrum. The PWM firing pulse $PWM(t)$ which oughts to also be a scaled version of the output waveform generated by comparing the (scaled) desired sinusoidal output signal $V_{ref}(t)$ with a triangle wave carrier $V_c(t)$ as discussed in Section 2.1 according to equation (4.13).

$$PWM(t) = \begin{cases} +1, if\ V_{ref}(t) > V_c(t) \\ -1, \qquad otherwise \end{cases} \tag{4.13}$$

The carrier waveform $V_c(t)$ is a triangular waveform with frequency 36*f_0=2160 which is the same as in the RTDS simulation, where f_0 is the desired output frequency (fundamental frequency). The reference waveform is:

$$V_{ref} = m\,cos(2\pi f_0 t + \varphi_0) \tag{4.14}$$

Here we set the modulation index $m = 0.8$, $\varphi_0 = 0.2$, $f_0 = 60.0$. The time-step used in MATLAB is also the same as the time-step of the 'VSC block' in the simulation, which is 2 us. The reference, carrier and generated waveforms are shown in Fig. 4-17 for one cycle (1/60s).

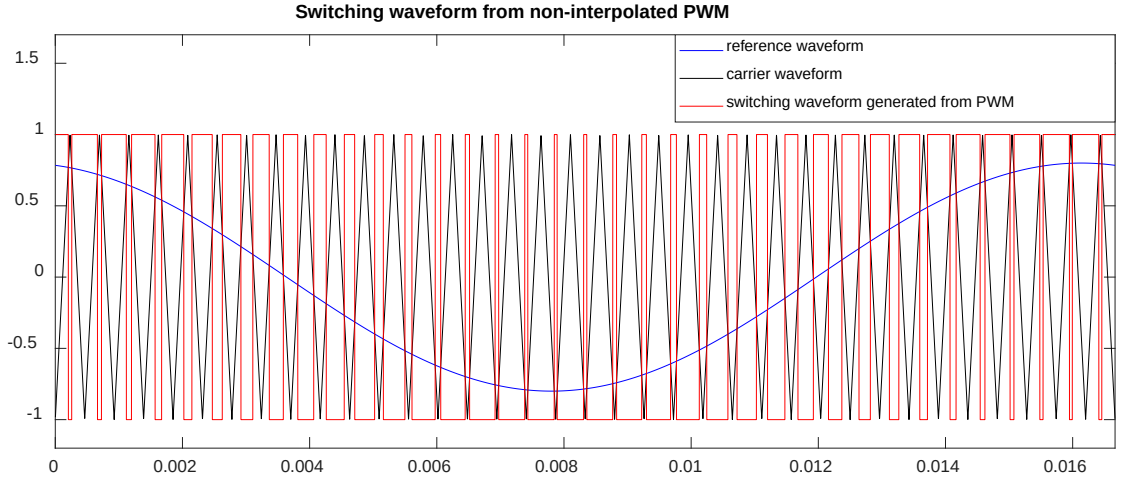

Figure 4-17. Waveforms: Reference, Carrier, and generated switching waveform

The DFT analysis is applied to the generated waveform in Fig. 4-17, with the result shown in Fig. 4-18. In addition to the 60 Hz component with magnitude 0.8, there are a range of background harmonics, typically less than or equal to 0.15% (of base value 0.8). The maximum magnitude of 0.15% occurs for the frequency of 700 Hz. The frequency of the dominant harmonic changes (not shown here) if any of the waveforms in Fig. 4-17 are

phase shifted. These harmonics would appear in the three phase ac voltages. If frequency scanning is applied on this system, it is possible to give accurate impedance result only when the magnitude of the injected voltage harmonic is much larger (e.g., 10 times larger) than this background value (0.15%).

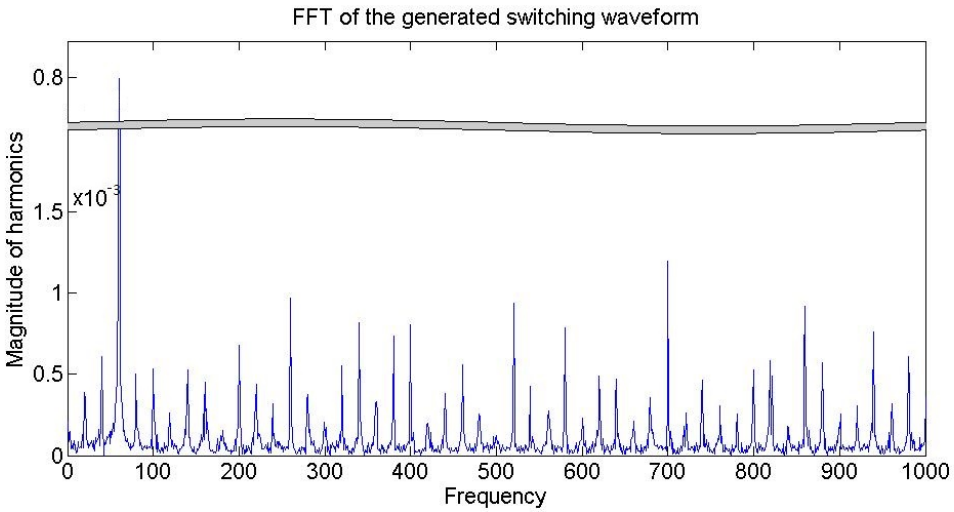

Figure 4-18. FFT of the generated waveform from non-interpolated PWM (background harmonics)

Then let us study that a harmonic at one arbitrary frequency, i.e., the voltage injection, is superposed on the reference waveform that:

$$V_{ref} = mcos(2\pi f_0 t + \varphi_0) + m_h cos(2\pi f_h t + \varphi_h) \qquad (4.15)$$

Where $m_h = 0.04$ (5% of m=0.8, about 33 times of 0.15%), $f_h = 138$, $\varphi_h = 1.0$. The DFT result on the generated waveform is shown in Fig. 4-19 that this harmonic magnitude becomes 0.032 (80% of m_h, 4% of m) as the result of the non-interpolated PWM.

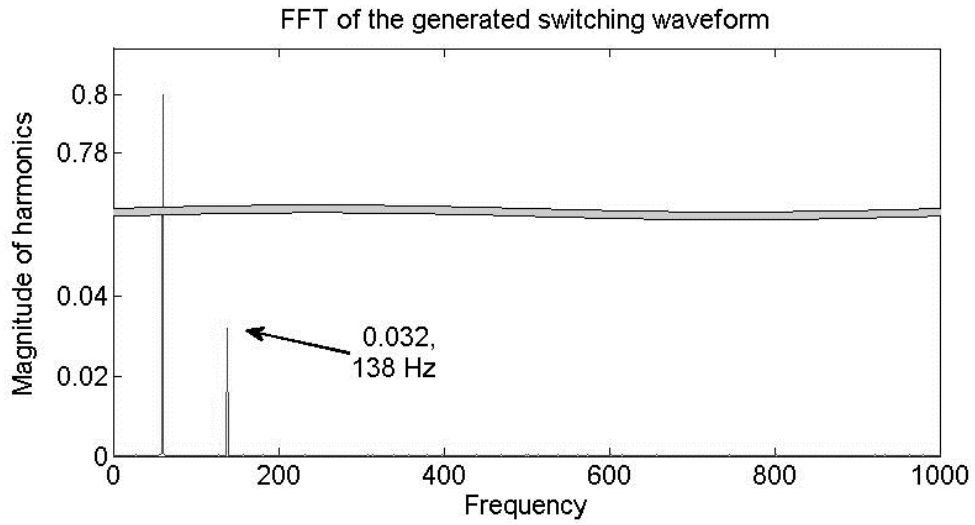

Figure 4-19. FFT of the generated waveform from non-interpolated PWM (with 138Hz harmonic)

From the above analysis, it is found that if the magnitude of the injected harmonic for the scan is not sufficiently large compared to 0.15% (e.g., 0.5%), the measured harmonic result would be influenced by the background harmonic generated from PWM. However, a high-magnitude harmonic injection can disturb the linearity. As shown in Fig. 4-19, when a 5% (of fundamental component) harmonic is superposed to the reference waveform, the measured switching waveform from PWM can still have a very large mismatch (20%).

Therefore, if the switching waveform is generated from the non-interpolated PWM (with time-step kept as 2 us), it is very difficult to get a smooth scan result, as the injected components can be distorted. It is very difficult to improve the accuracy of scan for the system including non-interpolated PWM if the simulation time-step cannot be reduced. And further stability analysis would be restricted by the polluted frequency responses.

4.4.2 The scanned response in PSCAD/EMTDC without interpolation

To prove the statement in Section 4.4.1 in another viewpoint, frequency scanning is applied in PSCAD/EMTDC for the same example system as in Section 3.2. The only difference between this section and Section 3.2, is that the interpolation is disabled here.

The scanned impedance response for the converter side system looking from the PCC bus is shown in Fig. 4-20 for the magnitude and Fig. 4-21 for the phase angle. This result, showing obvious similar noise level in frequency domain as in the RTDS result, proves that the accuracy of the frequency scanning is restricted when the interpolation is disabled. In contrast, the scans in Chapter 3 do not have any significant noise.

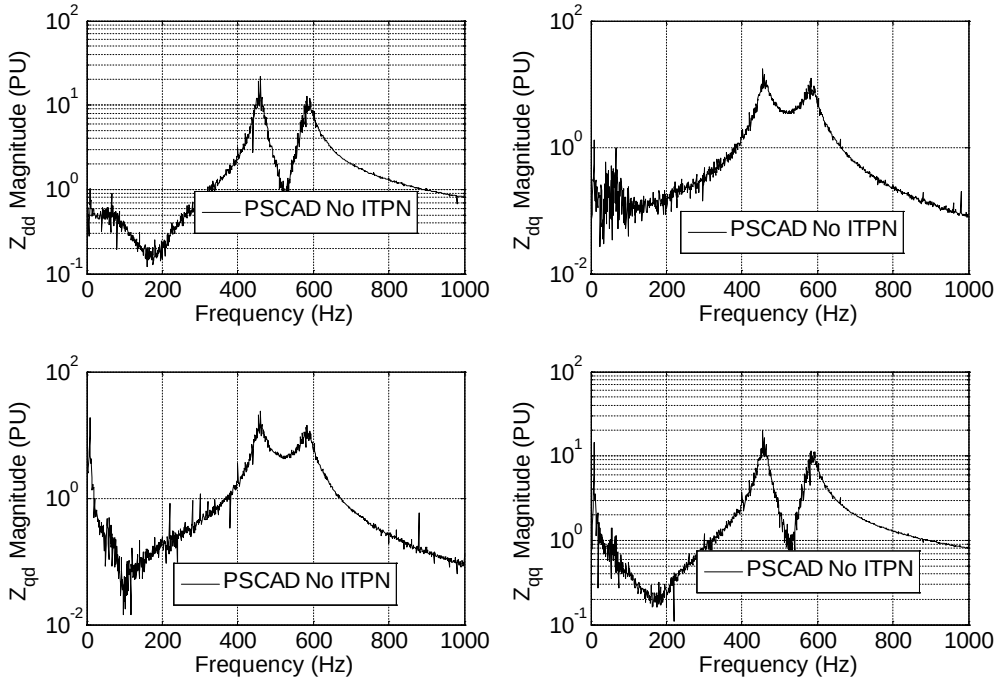

Figure 4-20. Magnitude of the ac side impedance (PSCAD, no interpolation)

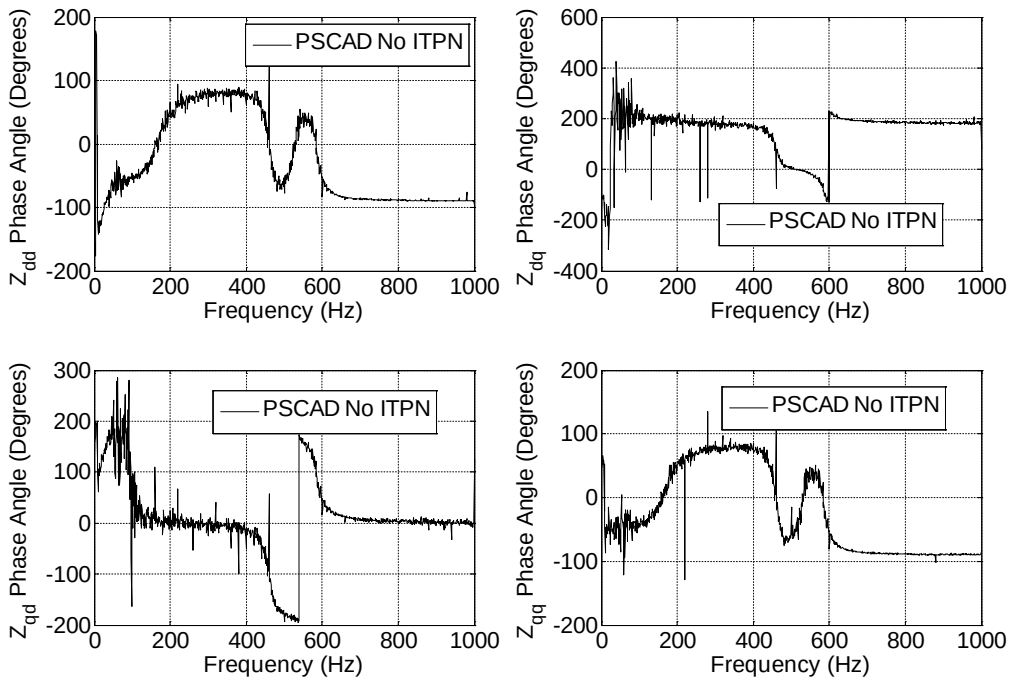

Figure 4-21. Phase angle of the ac side impedance (PSCAD, no interpolation)

4.5 Discussion

The accuracy of the VSC analytical model has been validated in Chapter 3 by the frequency scanning. In this chapter, the effect of the 'ON' and 'OFF' states' resistances of the switching valves are included in the analytical model for the 'R type' converter. Also, the analytical model of the 'LC type' converter is developed and tested.

The impedance responses of the converter looking from the ac side and the dc side are obtained from the scan for system with 'R type' converter and for system with 'LC type' converter in RTDS. Comparison between three results ('R type' analytical, 'R type' scanned, 'LC type' scanned) validates the accuracy of the new (i.e., 'LC type') VSC model developed in RTDS.

However, there is spurious noise appearing in all the simulated responses in RTDS. This problem makes further stability analysis (e.g., Nyquist plot) challenging, since unexpected encirclement may happen in the impedance contour due to the spurious noise. Further analysis showed that the noise in frequency domain comes from the background harmonic in time domain. This is mainly produced when interpolation is disabled or not available for PWM, such as in the RTDS, as the results from PSCAD/EMTDC have similar noise problem when the interpolation is disabled.

For the “VSC block” in RTDS, there is really not much room for the improvement of the scanning accuracy, as interpolation is forbidden, and the time-step cannot be reduced due to computation time constraints. With a faster real time digital simulator (e.g., with a smaller time-step 0.5us, say), the measured spectrum from the simulation should improve considerably.

5 Improvement of the LCC analytical model

Although frequency scanning is a powerful technique for determining resonances as shown in Chapter 3 and 4, it has its some drawbacks. For example, the impedance scan can have noise due to background harmonics. The approach is not suitable for parameter designing as it would require a new scan for every parameter value set and for every operating point. On the other hand, an analytical representation is very beneficial for further system analysis, as it allows for formal control system design and analysis methods such as root locus, eigenvalue analysis, gain and phase margins, etc. This is especially important for the dc converter where additional controller can be added to improve system behavior, and we may want to investigate the impact of the controller parameters on stability. The impedance response obtained from an analytical model also does not have the noise problem shown in Section 4.3, and the changing of parameters and operating points does not require development of a new model.

The analytical models of VSC and MMC had already developed by many researchers and proved to be very accurate [43][78][79]. What makes the VSC (and MMC) model easier to develop is that the turn-on and turn-off of the switch is purely determined by the controller. The switching function can be modeled as the reference waveform provided by the control system in the analytical analysis as the higher order harmonics can generally be neglected. The accuracy of this approximation has been validated in Chapters 3 and 4, as the result from the developed model match that of the frequency scanning.

In contrast, although the LCC HVdc topology was developed much earlier than the VSC HVdc and MMC HVdc topologies, its analytical model is not very accurate for frequency response studies due to the dynamics of the commutation inductance and the commutation overlap. In the LCC, the thyristor valve can be turned on by a gating signal provided from a control system. However, the valve does not immediately turn off the instant the firing pulse ends. There is a commutation interval or, if expressed as an angle, the overlap angle μ, during which there is a transfer of current from the outgoing valve to the incoming valve. This interval is a function of the ac voltage, dc current and commutating inductance value. Representing the LCC's switching function is thus more challenging. The accurate solution of μ as a function of other network quantities and frequency becomes the key point in determining the switching function.

This chapter improves on the analytical model of the LCC. It is the extension of a journal paper published in the IEEE Transactions on Power Delivery [80].

5.1 Traditional modeling of LCC

In traditional studies [27-29], the system including a LCC can be represented by the block diagram shown in Fig. 5-1, where the LCC is shown as a module interfaced with the rest part of the system. As in this figure, the inputs to the LCC are the ac voltage at the PCC bus, the dc current, and the firing angle; and the outputs are the ac current flowing from the converter into the PCC bus, the dc voltage, the overlap angle and the extinction angle. E.

V. Larsen firstly proposed a similar form of the matrix formulation presented here [81] in which the ac side quantities were represented in the sequence (i.e., positive negative and zero sequence) domain. A. R. Wood published several papers [27-29] on the algebraic equations of the commutation process and also developed a small signal model of the LCC block in the sequence domain. By superposing non-characteristic harmonics on the steady state values of the inputs, the harmonic components in the outputs were calculated from the algebraic equations. Thus, the frequency dependent matrix relating the inputs and outputs could be determined [27-29] more accurately than those with Larsen's approach [81]. However, both these approaches have the drawback of frequency coupling between the positive and negative sequence variables.

Later works [30][36][82] represented the LCC converter in the dq0 domain using a constant matrix which eliminated coupling between the frequencies but introduced coupling between d- and q- axis. This quasi-steady state form was easy to linearize, so that state space analysis could be applied. However, these models did not consider the frequency dependent characteristics of the LCC transfer matrix, resulting in errors when conducting oscillation studies as this transfer matrix only accurately represents the steady state.

All the above models, regardless in phase domain or the dq0 domain, failed to include the dynamics due to the commutation inductance which was represented as a complex scalar reactance. The determination of the overlap angle did not consider the frequency dependent terms. There are also other issues not properly handled, i.e., the discrete nature of the overlap angle and the extinction angles.

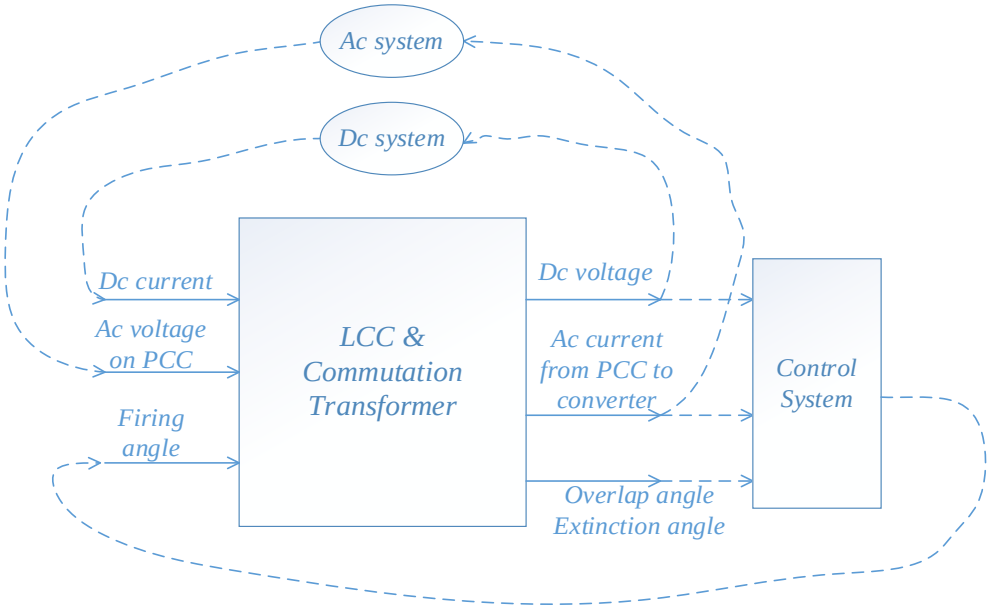

Figure 5-1. Representing the system including an LCC by graphical blocks

In the following Section 5.2, the dq0 domain model of the LCC is improved by including the dynamics due to the commutating inductance and the discrete sampling nature of the firing angle issue and measurement of extinction angle.

5.2 Analytical modeling of LCC

In traditional studies, the firing angle order was taken as one input to the converter model, and the measured overlap angle and extinction angle were considered as continuous output values. However, in a six-pulse converter, firing angle order only turns a valve on every 6^{th} of a cycle when the firing pulse is issued. Similarly, a new measurement for the overlap angle and extinction angle is only generated six times in a cycle. Hence these parameters

are not continuous functions of time as was assumed in earlier models.

The firing pulses are generated by a comparison of the angle reference (typically from a phase locked loop) and the firing angle order. Each valve has its own angle reference phase shifted from its predecessor by 60°. For the i[th] valve, the angle reference can be given by:

$$\Psi_i(t) = \phi_{pll}(t) - (i-2)\pi/3 \tag{5.1}$$

In (5.1), $\phi_{pll}(t)$ is the angle output of the PLL including a component $\omega_0 \mathrm{t}$ at fundamental speed ω_0, and a time-varying transient term $\theta_{pll}(t)$.

$$\phi_{pll}(t) = \omega_0 \mathrm{t} + \theta_{pll}(t) \tag{5.2}$$

The time (or angle) origin of the PLL is defined as the time (or angle) when V_a reaches its peak. Fig. 5-2 shows the generation of the firing pulses and the measurement of the overlap and extinction angles for two valves fired in succession, e.g., valve 1 and valve 2. Only small signal changes are considered in the variables, e.g. $\Delta\alpha(t)$. Fig. 5-2 is drawn for an inverter operating at around 140 degrees' firing angle (2.44 radians).

As in Fig. 5-2b, the firing pulses are issued to the valves when their angle references exceed the firing angle order $\alpha(t)$, which can be modeled as the sampling of $\alpha(t)$ with the period $\pi/3$ (α_i for the i^{th} valve). When the commutation ends for one valve, the overlap angle is measured as μ (μ_i for the i^{th} valve), as in Fig. 5-2c. At the zero-crossing instant of the commutation voltage, the extinction angle is measured as γ (γ_i for the i^{th} valve), as in Fig. 5-2c. Both μ_i and γ_i are dependent on α_i, the dc current and the ac voltage during the commutation. Their discrete nature (issuing of α, measuring of μ and γ) brings about

difficulties to the analytical modeling.

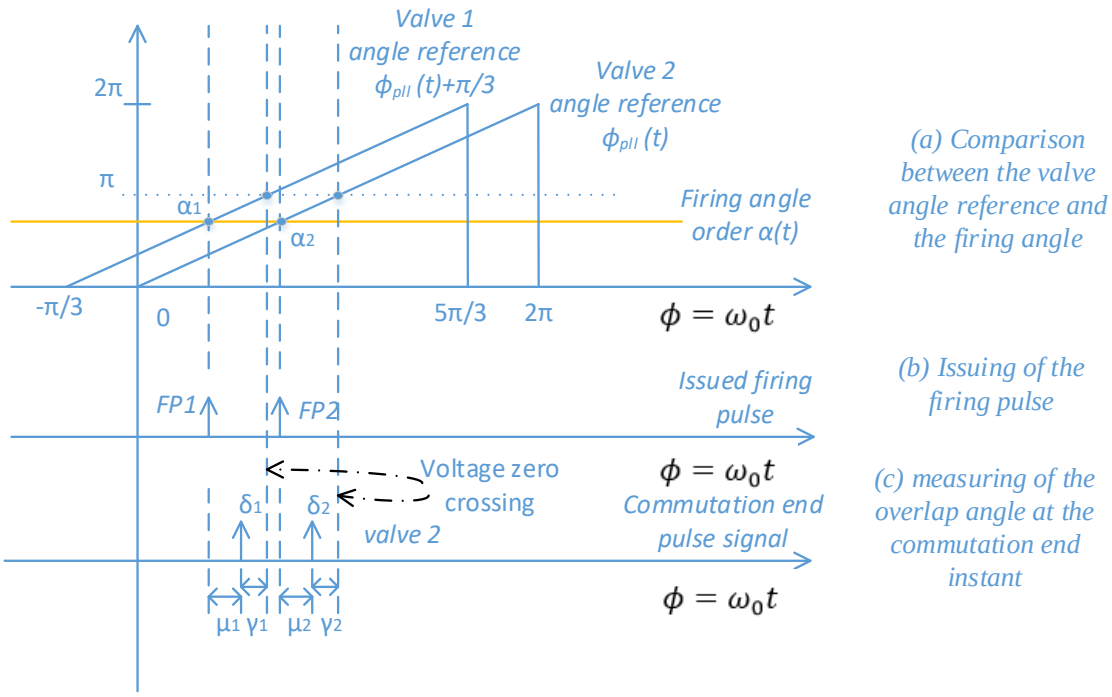

Figure 5-2. Commutation for valve 1 and 2

5.2.1 Assumption of infinite series six-pulse converter

In modern LCC projects, there are usually two six-pulse converters connected in series. The winding connection of the commutation transformer is YY for one converter and YD for the other, hence the secondary side ac voltages for the two converters have the phase shift of 30 degrees. With this topology, the two six-pulse converters make a twelve-pulse configuration. Then the harmonics become $12n^{th}$ order in the dc side (instead of $6n^{th}$ in the six-pulse converter), and $12n\pm1^{th}$ order in the ac side (rather than $6n\pm1^{th}$). Meanwhile, the sampling frequency of $\alpha(t)$, and the measuring frequency of μ and γ both become 12 samples per cycle (from 6 samples per cycle).

Continuing this approach, we can consider converters of higher pulse number, e.g., 24,48…etc., and in the limit, an infinite series pulse converter in which there are N_c number of six-pulse converters ($N_c \to \infty$). It is presented in Fig. 5-3. Each converter connects to its own commutation transformer, which produces a phase shift to the conversion bus voltage.

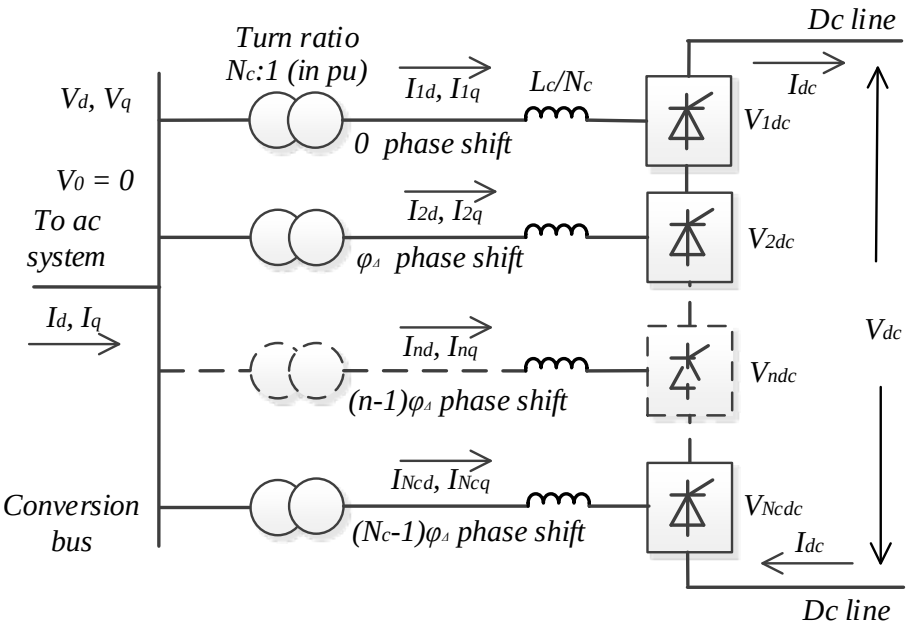

Figure 5-3. The infinite pulse converter configuration

For two nearby transformers, the phase shift difference is an infinitesimally small angle:

$$\varphi_\Delta = \lim_{N_c \to \infty} \pi/(3N_c) \tag{5.3}$$

So for the n^{th} converter, the phase shift is：

$$\varphi_n = (n-1) * \varphi_\Delta \tag{5.4}$$

If this is the $N_c{}^{\text{th}}$ converter, $\varphi_{Nc} = \lim_{N_c \to \infty} (N_c - 1)\pi/3N_c \approx \pi/3$.

Here we define the time origin as the time when V_a of the conversion bus reaches its peak. The dq0 transformation relating the phase 'abc' domain components in primary side and the dq0 domain components is:

$$T_{dq0} = \frac{2}{3}\begin{bmatrix} \cos(\omega_0 t) & \cos(\omega_0 t - \frac{2}{3}\pi) & \cos(\omega_0 t + \frac{2}{3}\pi) \\ -\sin(\omega_0 t) & -\sin(\omega_0 t - \frac{2}{3}\pi) & -\sin(\omega_0 t + \frac{2}{3}\pi) \\ \frac{1}{2} & \frac{1}{2} & \frac{1}{2} \end{bmatrix} \tag{5.5}$$

Then under steady state, we have $V_d(t) = 1.0pu$, and $V_q(t) = 0.0pu$. The angle $\phi_n(t)$ is defined as the static angle reference of the n^{th} converter:

$$\phi_n(t) = \omega_0 t - \varphi_n \tag{5.6}$$

Where φ_n is given as in (5.4). The secondary side three-phase voltages for the n^{th} converter (per unit value) are generated by equation (5.7) to represent the effect of the phase shift transformer presented in Fig. 5-3.

$$\begin{bmatrix} v_{na}(t) \\ v_{nb}(t) \\ v_{nc}(t) \end{bmatrix} = \frac{1}{N_c}\begin{bmatrix} \cos\phi_n(t) & -\sin\phi_n(t) & 1 \\ \cos\left[\phi_n(t) - \frac{2}{3}\pi\right] & -\sin\left[\phi_n(t) - \frac{2}{3}\pi\right] & 1 \\ \cos\left[\phi_n(t) + \frac{2}{3}\pi\right] & -\sin\left[\phi_n(t) + \frac{2}{3}\pi\right] & 1 \end{bmatrix}\begin{bmatrix} V_d(t) \\ V_q(t) \\ V_0(t) \end{bmatrix} \tag{5.7}$$

Given that there are six pulses with $\pi/3$ phase shift between two nearby pulses, and each pulse has the maximum phase shift of φ_{Nc} between the first and the last converters, the issue of firing pulse at the firing angle α, the commutation end angle δ, and the extinction angle γ become continuous variables (the sampling frequency is infinite). The dc voltage V_{dc} is the sum of the (infinitesimal) voltages of all the converters, and the ac currents I_d and I_q are the sum of all the converters' primary side currents I_{nd_pr} and I_{nq_pr}.

$$V_{dc}(\mathrm{t}) = \sum_{n=1}^{N_c} V_{ndc}(\mathrm{t})\,;\; I_d(\mathrm{t}) = \sum_{n=1}^{N_c} I_{nd\_pr}(\mathrm{t})\,; I_q(\mathrm{t}) = \sum_{n=1}^{N_c} I_{nq\_pr}(\mathrm{t})\,; \qquad (5.8)$$

Due to the infinite pulse nature, $V_{dc}(\mathrm{t})$, $I_d(\mathrm{t})$ and $I_q(\mathrm{t})$ are ripple-free waveforms under steady state. The d- and q- axis currents and voltages of the secondary side of a transformer are explained in the next subsection. Hence, the analysis can focus on the way that if a small signal variation of frequency f_h is superposed on any of the input variables above, there would be only harmonics excited at the same frequency in the system. The pollution of characteristic harmonics in a six-pulse or twelve-pulse converter is avoided.

To relate back to the 12-pulse case, the infinite pulse μ / γ measurement is sampled and held as will be described later in Section 5.2.7, for feeding back into the controller.

5.2.2 Inputs and outputs of the converter

As the converter is non-linear, the input and output variables of the LCC model developed here are small signal values evaluated at the operating point. For each of the N_c ($N_c \to \infty$) converters, the secondary side voltages and currents have to be represented in the dq0 domain to get (5.8). Taking the phase shift of the transformer into account, the dq0 transformation matrix of the n^{th} converter, T_{ndq0}, is chosen as:

$$T_{ndq0} = \frac{2}{3}\begin{bmatrix} \cos\phi_n(t) & \cos\left[\phi_n(t) - \frac{2}{3}\pi\right] & \cos\left[\phi_n(t) + \frac{2}{3}\pi\right] \\ -\sin\phi_n(t) & -\sin\left[\phi_n(t) - \frac{2}{3}\pi\right] & -\sin\left[\phi_n(t) + \frac{2}{3}\pi\right] \\ \frac{1}{2} & \frac{1}{2} & \frac{1}{2} \end{bmatrix} \qquad (5.9)$$

Where $\phi_n(t)$ is the angle reference defined in (5.6). The dq0 domain voltages (using

T_{ndq0} as transformation matrix) of the n^{th} converter can obtained from (5.7) and (5.9) as:

$$\begin{bmatrix} V_{nd}(t) \\ V_{nq}(t) \\ V_{n0}(t) \end{bmatrix} = T_{ndq0} \begin{bmatrix} v_{na}(t) \\ v_{nb}(t) \\ v_{nc}(t) \end{bmatrix} = \frac{1}{N_c} \begin{bmatrix} V_d(t) \\ V_q(t) \\ V_0(t) \end{bmatrix} \tag{5.10a}$$

As shown in (5.10a), the d- and q- axis voltages V_{nd} and V_{nq} on the secondary side of each converter transformer are identical, and equal to V_d/N_c and V_q/N_c respectively, where N_c is the converter count and V_d, V_q the d- and q- axis voltages of the ac system. Similarly, if the secondary side currents are I_{nd} and I_{nq}, then the primary side currents can be obtained as:

$$\begin{bmatrix} I_d(t) \\ I_q(t) \end{bmatrix} = \sum_{n=1}^{N_c} \begin{bmatrix} I_{nd\_pr}(t) \\ I_{nq\_pr}(t) \end{bmatrix} = \frac{1}{N_c} \sum_{n=1}^{N_c} \begin{bmatrix} I_{nd}(t) \\ I_{nq}(t) \end{bmatrix} \tag{5.10b}$$

The infinite six-pulse converters of Fig. 5-3 can thus be represented with a small-signal model with input scalar ΔU^*_{LCC} and output scalar ΔY_{LCC} as in equations (5.11-12).

$$\Delta U^*_{LCC} = [\Delta V_d \quad \Delta V_q \quad \Delta i_{dc} \quad \Delta\alpha]^T \tag{5.11}$$

$$\Delta Y_{LCC} = [\Delta I_d \quad \Delta I_q \quad \Delta V_{dc} \quad \Delta\mu \quad \Delta\gamma]^T \tag{5.12}$$

The 5 x 4 dimension transfer matrix K^* relates ΔU^*_{LCC} to ΔY_{LCC} as in equation (5.13).

$$\Delta Y_{LCC} = K^* \Delta U^*_{LCC} \tag{5.13}$$

The converter model in Fig. 5-1 is further revised in Fig. 5-4, which can better represent the commutation inductance and converter separately. To do this, an intermediate matrix K (dimension 5 x 6) is developed as in (5.14) and (5.15), where the two new inputs Δi_{2d} and Δi_{2q} in (5.14) comes from additional differential equations that model the commutation process and include a value for the commutation inductance.

$$\Delta U_{LCC} = [\Delta V_d \quad \Delta V_q \quad \Delta i_{dc} \quad \Delta\alpha \quad \Delta i_{2d} \quad \Delta i_{2q}]^T \tag{5.14}$$

$$\Delta Y_{LCC} = K\Delta \mathrm{U}_{LCC} \tag{5.15}$$

The matrix K in (5.15) has frequency dependent elements.

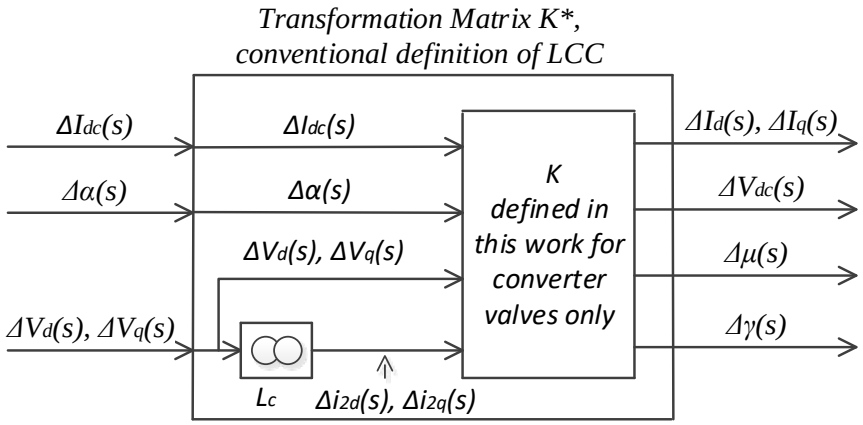

Figure 5-4. Small signal representation of the LCC block

5.2.3 Commutation overlap analysis of one converter

A typical n^{th} $(n \in \{1,2,\dots N_c\})$ converter is considered in this section to develop the algebraic and state equations during commutation. Assume commutation from valve 5 to valve 1 in converter *n*, the circuit configuration is shown in Fig. 5-5 respectively. The voltage and current waveforms as functions of the phase angle (in time units) are shown as in Fig. 5-6. The firing pulse of valve 1 is issued at time t_{nf} when the angle output of the PLL (for valve 1) equals the firing angle, as in (5.16). The PLL output of the n^{th} converter is calculated as the sum of PLL transient term $\theta_{pll}(t_{nf})$ (which is explained in equation (5.2)), the converter's angle reference $\phi_n(t_{nf})$ and the valve phase shift (pi/3 for valve 1). In (5.16), α_* is the firing angle order from the PI controller. Rearranging (5.16) gives (5.17), in which the firing angle order and the PLL dynamic term are combined as the

apparent firing angle order α, which is a constant value in steady state and is used as the input to the converter model.

$$\Psi_{n,1}(t_{nf}) = \theta_{pll}(t_{nf}) + \phi_n(t_{nf}) + \frac{\pi}{3} = \alpha_*(t_{nf}) \tag{5.16}$$

$$\phi_n(t_{nf}) = \alpha_*(t_{nf}) - \theta_{pll}(t_{nf}) - \frac{\pi}{3} = \alpha(t_{nf}) - \frac{\pi}{3} \tag{5.17}$$

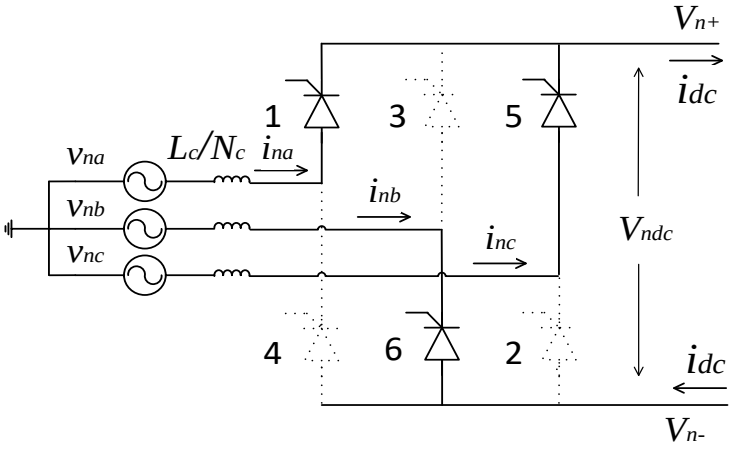

Figure 5-5. Commutation process for the n^{th} converter

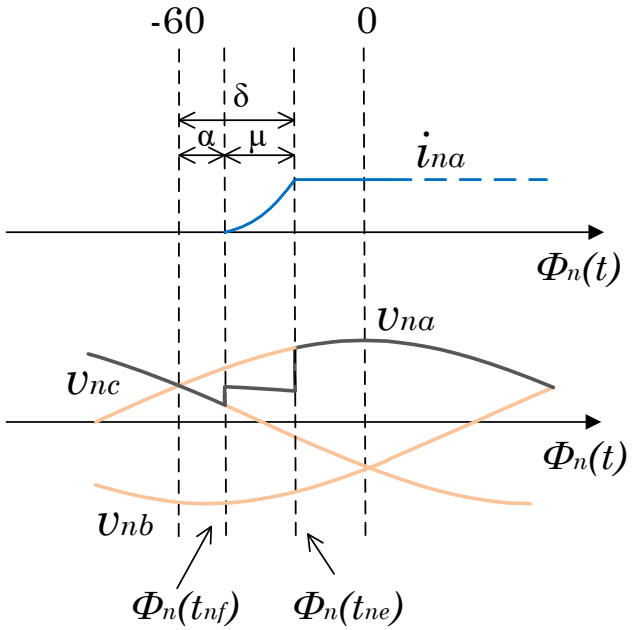

Figure 5-6. Voltage / current waveforms as a function of phase angle (time) for the n^{th} converter

The three-phase state equations representing the commutation interval can be given as:

$$\begin{cases} \frac{L_c}{N_c}\frac{di_{na}}{dt} = v_{na} - V_{n+} \\ \frac{L_c}{N_c}\frac{di_{nb}}{dt} = v_{nb} - V_{n-} \\ \frac{L_c}{N_c}\frac{di_{nc}}{dt} = v_{nc} - V_{n+} \end{cases} \tag{5.18}$$

$$\begin{cases} i_{na} + i_{nc} = -i_{nb} = i_{dc} \\ V_{n+} - V_{n-} = V_{ndc} \end{cases} \tag{5.19}$$

Combining (5.18) and (5.19) one obtains:

$$2\frac{L_c}{N_c}\frac{di_{na}}{dt} - \frac{L_c}{N_c}\frac{di_{dc}}{dt} = v_{na} - v_{nc} \tag{5.20}$$

The phase 'a' commutation current i_{na} can be divided into two parts: $i_{na} = i_{n1a} + i_{n2a}$, where i_{n1a} is dependent on the dc current i_{dc}, and i_{n2a} only involves the ac voltages, as in (5.21).

$$2\frac{L_c}{N_c}\frac{di_{n1a}}{dt} = \frac{L_c}{N_c}\frac{di_{dc}}{dt} \tag{5.21a}$$

$$2\frac{L_c}{N_c}\frac{di_{n2a}}{dt} = v_{na} - v_{nc} \tag{5.21b}$$

Integrating (5.21a) gives i_{n1a} as a function of time:

$$i_{n1a}(t) = \frac{1}{2}\left[i_{dc}(t) - i_{dc}(t_{nf})\right] \tag{5.22}$$

Equation (5.21b) only represents one phase. To get i_{n1a} represented by V_d and V_q, another two equations similar to (5.21b) for the 'b' and 'c' phases are introduced as in (5.23):

$$\begin{cases} 2\dfrac{L_c}{N_c}\dfrac{di_{n2b}}{dt} = v_{nb} - v_{na} \\ 2\dfrac{L_c}{N_c}\dfrac{di_{n2c}}{dt} = v_{nc} - v_{nb} \end{cases} \tag{5.23}$$

Transforming (5.21b) and (5.23) to dq0 domain (using T_{ndq0} as the transformation matrix), i_{n2a}, i_{n2b}, and i_{n2c} becomes i_{2d} and i_{2q} which are the same for all the N_c converters:

$$L_c\frac{d}{dt}\begin{bmatrix} i_{2d} \\ i_{2q} \end{bmatrix} + \begin{bmatrix} 0 & -\omega_0 L_c \\ \omega_0 L_c & 0 \end{bmatrix}\begin{bmatrix} i_{2d} \\ i_{2q} \end{bmatrix} = \frac{\sqrt{3}}{2}\begin{bmatrix} \frac{\sqrt{3}}{2} & \frac{1}{2} \\ -\frac{1}{2} & \frac{\sqrt{3}}{2} \end{bmatrix}\begin{bmatrix} V_d \\ V_q \end{bmatrix} \tag{5.24}$$

Then the term i_{n2a} can be obtained using the inverse dq0 transformation. However, it includes an offset term to satisfy the constraint condition that $i_{n1a}(t_{nf}) = 0$. In (5.25), the offset term in the square bracket is added to give the complete equation for i_{n2a}.

$$\begin{aligned} i_{n2a}(t) = {} & i_{2d}(t)cos\phi_n(t) - i_{2q}(t)sin\phi_n(t) \\ & - \left[i_{2d}(t_{nf})\cos\phi_n(t_{nf}) - i_{2q}(t_{nf})sin\phi_n(t_{nf})\right] \end{aligned} \tag{5.25}$$

When the commutation ends for the n[th] converter at time t_{ne}, the phase 'a' current is equal to the dc current that:

$$i_{n1a}(t_{ne}) + i_{n2a}(t_{ne}) = i_{dc}(t_{ne}) \tag{5.26}$$

The overlap angle, and the commutation end angle δ measured at instant t_{ne} is given by:

$$\begin{cases} \mu(t_{ne}) = \phi_n(t_{ne}) - \phi_n(t_{nf}) = \phi_n(t_{ne}) - \alpha(t_{nf}) + \dfrac{\pi}{3} \\ \delta(t_{ne}) = \alpha(t_{nf}) + \mu(t_{ne}) = \phi_n(t_{ne}) + \dfrac{\pi}{3} \end{cases} \tag{5.27}$$

Equation (5.16) gives the condition for the beginning of the commutation; (5.22), (5.24-25) represent the commutation current components; (5.26) gives the commutation end condition, and the overlap angle is measured at this instant, as in (5.27). In these equations,

the steady state values of the variables (PLL output angle, firing instant angle, overlap angle, commutation end instant angle) can be determined by the following equation set, where the ac voltage and the dc current are both 1.0 pu as the default value.

$$\begin{cases} \theta_{pll} = 0 \\ \phi_n(t_{nf}) = \alpha - \dfrac{\pi}{3} = \alpha_* - \dfrac{\pi}{3} \\ \mu = cos^{-1}(cos\alpha - \dfrac{i_{dc}X_c}{\sqrt{{V_d}^2 + {V_q}^2}}) \\ \phi_n(t_{ne}) = \phi_n(t_{nf}) + \mu = \alpha + \mu - \dfrac{\pi}{3} = \delta - \dfrac{\pi}{3} \end{cases} \tag{5.28}$$

In the following analysis in this chapter, the prefix 'Δ' before a variable means that it is a small signal variable, and absences of 'Δ'indicates the steady state value. Linearizing (5.17) and (5.27) gives the small signal term of commutation end angle $\Delta\phi_n(t_e)$:

$$\Delta\delta(t_{ne}) = \Delta\phi_n(t_{ne}) = \Delta\mu(t_{ne}) + \Delta\alpha(t_{nf}) \tag{5.29}$$

Linearizing (5.22), (5.25), (5.26) and combining these equations with (5.29), the following equation can be obtained to represent the relationship between the small signal variables:

$$\begin{aligned} &-\frac{1}{2}[\Delta i_{dc}(t_{ne}) + \Delta i_{dc}(t_{nf})] + \Delta i_{2d}(t_{ne})cos\phi_n(t_{ne}) - i_{2d}(t_{ne})sin\phi_n(t_{ne}) * \\ &[\Delta\mu(t_{ne}) + \Delta\alpha(t_{nf})] - \Delta i_{2q}(t_{ne})sin\phi_n(t_{ne}) - i_{2q}(t_{ne})cos\phi_n(t_{ne}) * [\Delta\mu(t_{ne}) + \\ &\Delta\alpha(t_{nf})] - \{\Delta i_{2d}(t_{nf})cos\phi_n(t_{nf}) - i_{2d}(t_{nf})sin\phi_n(t_{nf})\Delta\alpha(t_{nf}) - \\ &\Delta i_{2q}(t_{nf})sin\phi_n(t_{nf}) + i_{2q}(t_{nf})cos\phi_n(t_{nf})\Delta\alpha(t_{nf})\} = 0 \end{aligned} \tag{5.30}$$

Considering the N_c (essentially infinite) converters, there are equations similar to (5.29) and (5.30) where $n = 1,2, \dots, N_c$. Each equation uses a different value of t_{nf} and t_{ne}, i.e.,

$[t_{1f}, t_{2f}, \dots t_{N_c f}]$ and $[t_{1e}, t_{2e}, \dots t_{N_c e}]$. As $N_c \to \infty$, the difference $t_{(n+1)f} - t_{nf}$, etc., between subsequent times becomes neglectable and t_{nf} and t_{ne} can be replaced by continuous variables t_f and t_e. Then they can be transformed to the Laplace domain.

As t_f is the start of commutation and t_e the end of commutation, their difference is equal to the overlap time μ/ω_0, where μ is the overlap angle and a constant value under steady state. Hence the Laplace transform of a typical variable x at time t_f, i.e., $\mathcal{L}[x(t_f)]$, can be expressed by multiplying $\mathcal{L}[x(t_e)]$ by the transportation lag $e^{-s\frac{\mu}{\omega_0}}$ as in (5-31):

$$\mathcal{L}[x(t_f)] = e^{-s\frac{\mu}{\omega_0}}\mathcal{L}[x(t_e)] \tag{5.31}$$

From (5.29-31), the equations in the Laplace domain can be given as (where the steady state values are from (5.28)):

$$\Delta\delta(s) = \Delta\phi_n(\mathrm{s}) = \Delta\mu(\mathrm{s}) + \Delta\alpha(\mathrm{s})e^{-s\frac{\mu}{\omega_0}} \tag{5.32a}$$

$$\begin{aligned}
&-\frac{1}{2}\Delta i_{dc}(s)\left(1 + e^{-s\frac{\mu}{\omega_0}}\right) + \Delta i_{2d}(s)\left[\cos\left(\delta - \frac{\pi}{3}\right) - e^{-s\frac{\mu}{\omega_0}}\cos\left(\alpha - \frac{\pi}{3}\right)\right] \\
&\quad - \Delta i_{2q}(s)\left[\sin\left(\delta - \frac{\pi}{3}\right) - e^{-s\frac{\mu}{\omega_0}}\sin\left(\alpha - \frac{\pi}{3}\right)\right] \\
&\quad + \Delta\alpha(s)e^{-s\frac{\mu}{\omega_0}}\left[-i_{2d}\sin\left(\delta - \frac{\pi}{3}\right) + i_{2d}\sin\left(\alpha - \frac{\pi}{3}\right) - i_{2q}\cos\left(\delta - \frac{\pi}{3}\right)\right. \\
&\quad \left. + i_{2q}\cos\left(\alpha - \frac{\pi}{3}\right)\right] + \Delta\mu(s)\left[-i_{2d}\sin\left(\delta - \frac{\pi}{3}\right) - i_{2q}\cos\left(\delta - \frac{\pi}{3}\right)\right] = 0
\end{aligned} \tag{5.32b}$$

The fourth row of K matrix (K_{4m}, m=1, 2… 6) can be determined from (5.32) as:

$$\begin{cases} [K_{41} \quad K_{42}] = \begin{bmatrix} \frac{\Delta\mu(s)}{\Delta V_d(s)} & \frac{\Delta\mu(s)}{\Delta V_q(s)} \end{bmatrix} = [0 \quad 0] \\ K_{43} = \frac{\Delta\mu(s)}{\Delta i_{dc}(s)} = \frac{1 + e^{-\frac{\mu}{\omega_0}s}}{2[-i_{2d}sin\left(\delta - \frac{\pi}{3}\right) - i_{2q}cos\left(\delta - \frac{\pi}{3}\right)]} \\ K_{44} = \frac{\Delta\mu(s)}{\Delta\alpha(s)} = \frac{e^{-\frac{\mu}{\omega_0}s}\{i_{cd}[\sin\left(\delta - \frac{\pi}{3}\right) - \sin\left(\alpha - \frac{\pi}{3}\right)] + i_{cq}[cos\left(\delta - \frac{\pi}{3}\right) - cos\left(\alpha - \frac{\pi}{3}\right)]\}}{-i_{2d}sin\left(\delta - \frac{\pi}{3}\right) - i_{2q}cos\left(\delta - \frac{\pi}{3}\right)} \\ K_{45} = \frac{\Delta\mu(s)}{\Delta i_{2d}(s)} = \frac{-cos\left(\delta - \frac{\pi}{3}\right) + e^{-\frac{\mu}{\omega_0}s}cos\left(\alpha - \frac{\pi}{3}\right)}{-i_{2d}sin\left(\delta - \frac{\pi}{3}\right) - i_{2q}cos\left(\delta - \frac{\pi}{3}\right)} \\ K_{46} = \frac{\Delta\mu(s)}{\Delta i_{2q}(s)} = \frac{sin\left(\delta - \frac{\pi}{3}\right) - e^{-\frac{\mu}{\omega_0}s}sin\left(\alpha - \frac{\pi}{3}\right)}{-i_{2d}sin\left(\delta - \frac{\pi}{3}\right) - i_{2q}cos\left(\delta - \frac{\pi}{3}\right)} \end{cases} \tag{5.33}$$

5.2.4 Dc side voltage calculation

The dc voltage for the n^{th} converter is given (5.34) and is different dependent on whether there is a commutation occurring ($t_{nf} < t < t_{ne}$), or whether an upper and lower group valve are conducting ($t_{ne} < t < t_{nf} + \pi/3\omega_0$):

$$V_{dcn}(t) = \begin{cases} \frac{v_{an}(t) + v_{cn}(t)}{2} - v_{bn}(t) = \frac{3}{2N_c}\left\{V_d(t)cos\left[\phi_n(t) + \frac{\pi}{3}\right] - V_q(t)sin\left[\phi_n(t) + \frac{\pi}{3}\right]\right\}, t_{nf} < t < t_{ne} \\ v_{an}(t) - v_{bn}(t) = \frac{\sqrt{3}}{N_c}\left\{V_d(t)cos\left[\phi_n(t) + \frac{\pi}{6}\right] - V_q(t)sin\left[\phi_n(t) + \frac{\pi}{6}\right]\right\}, t_{ne} < t < t_{nf} + \frac{\pi}{3\omega_0} \end{cases} \tag{5.34}$$

With the infinite converter assumption, at any time t, we can assume that the i^{th} converter valve is firing and undergoing commutation, and the j^{th} converter has just finished the overlap, for some *i* and *j*. The dc voltages of the i^{th} and j^{th} converter can be represented in dq form using (5.34) by replacing $\phi_n(t_f)$ and $\phi_n(t_e)$ by $\alpha(t) - \pi/3$ and $\delta(t) - \pi/3$ as in (5.28):

$$V_{dci}(t) = \frac{3}{2N_c}\left[V_d(t)cos[\alpha(t)] - V_q(t)sin[\alpha(t)]\right] \tag{5.35a}$$

$$V_{dcj}(t) = \frac{\sqrt{3}}{N_c}\left\{V_d(t)cos\left[\delta(t) - \frac{\pi}{6}\right] - V_q(t)sin\left[\delta(t) - \frac{\pi}{6}\right]\right\} \qquad (5.35b)$$

The voltages of other converters can be given by adding the phase shifts in the sinusoidal functions of (5.35), which results from the different dq0 transformation angles specified in the previous section:

$$V_{dcn}{}^{c}(t) = \frac{3}{2N_c}\left\{V_d(t)cos\left[\phi_n(t) + \frac{\pi}{3}\right] - V_q(t)sin\left[\phi_n(t) + \frac{\pi}{3}\right]\right\}, \alpha(t) - \frac{\pi}{3} < \phi_n(t) < \delta(t) - \frac{\pi}{3} \quad (5.36a)$$

$$V_{dcn}{}^{\bar{c}}(t) = \frac{\sqrt{3}}{N_c}\left\{V_d(t)cos\left[\phi_n(t) + \frac{\pi}{6}\right] - V_q(t)sin\left[\phi_n(t) + \frac{\pi}{6}\right]\right\}, \delta(t) - \frac{\pi}{3} < \phi_n(t) < \alpha(t) \quad (5.36b)$$

$V_{dcn}{}^{c}$ is the dc voltage of one converter during commutation and $V_{dcn}{}^{\bar{c}}$ for a converter that is not commutating. The total dc voltage, which is the sum of all the N_c converters, can be calculated by integrating (5.36), because the summation becomes an integral as $N_c \to \infty$:

$$V_{dc} = \frac{3N_c}{\pi}\left[\int_{\alpha}^{\delta} V_{dcn}{}^{c}(\phi_n)\,\mathrm{d}\phi_n + \int_{\delta}^{\alpha+\frac{\pi}{3}} V_{dcn}{}^{\bar{c}}(\phi_n)\,\mathrm{d}\phi_n\right]$$

$$= \frac{3\sqrt{3}}{2\pi}\left[V_d(\cos\alpha + cos\delta) - V_q(\sin\alpha + sin\delta)\right] \qquad (5.37)$$

Linearizing (5.37) and transforming to the Laplace domain, together with (5.32a) and $K_{4n}(n = 1,2,\ldots,6)$, the small signal change of dc voltage with respect to the six inputs, i.e., matrix entries K_{3n}, are obtained as:

$$\begin{cases} K_{31} = \dfrac{\Delta V_{dc}(s)}{\Delta V_d(s)} = \dfrac{3\sqrt{3}}{2\pi}[\cos\alpha + cos\delta] \\ K_{32} = \dfrac{\Delta V_{dc}(s)}{\Delta V_q(s)} = -\dfrac{3\sqrt{3}}{2\pi}[\sin\alpha + sin\delta] \\ K_{33}{}' = \dfrac{\Delta V_{dc}(s)}{\Delta i_{dc}(s)} = \dfrac{3\sqrt{3}}{2\pi}\left(-V_d sin\delta - V_q cos\delta\right)K_{43} \\ K_{34} = \dfrac{\Delta V_{dc}(s)}{\Delta\alpha(s)} = -\dfrac{3\sqrt{3}}{2\pi}\left[\left(V_d sin\delta + V_q cos\delta\right)\left(K_{44} + e^{-\frac{\mu}{\omega_0}s}\right) + \left(V_d sin\alpha + V_q cos\alpha\right)\right] \\ K_{35} = \dfrac{\Delta V_{dc}(s)}{\Delta i_{2d}(s)} = -\dfrac{3\sqrt{3}}{2\pi}\left(V_d sin\delta + V_q cos\delta\right)K_{45} \\ K_{36} = \dfrac{\Delta V_{dc}(s)}{\Delta i_{2q}(s)} = -\dfrac{3\sqrt{3}}{2\pi}\left(V_d sin\delta + V_q cos\delta\right)K_{46} \end{cases} \quad (5.38)$$

In (5.34-5.37), the voltage drop of the commutation inductance is included in the dc voltage. Hence the term $K_{33}{}' = \Delta V_{dc}(s)/\Delta i_{dc}(s)$ as calculated above is incorrect. At any instant, this voltage drop can be calculated as the drop across an equivalent inductance L_{eq} whose value is equal to the sum (i.e., integral) value of the inductances in the N_c converters:

$$L_{eq} = \frac{3N_c}{\pi}\left[\int_{\alpha}^{\delta}\frac{3}{2}\frac{L_c}{N_c}\mathrm{d}\phi_n + \int_{\delta}^{\alpha+\frac{\pi}{3}}2\frac{L_c}{N_c}\mathrm{d}\phi_n\right] = \frac{3N_c}{\pi}\left[\mu * \frac{3}{2}\frac{L_c}{N_c} + \left(\frac{\pi}{3} - \mu\right) * 2\frac{L_c}{N_c}\right] = \left(2 - \frac{3\mu}{2\pi}\right)L_c \quad (5.39)$$

Hence, K_{33} considering the voltage drop of the inductors becomes:

$$K_{33} = \frac{\Delta V_{dc}(s)}{\Delta i_{dc}(s)} = K_{33}{}' - sL_{eq} \quad (5.40)$$

5.2.5 Ac side current calculation

With $i_{na}(t) = i_{\mathrm{n}1a}(t) + i_{\mathrm{n}2a}(t)$, and $i_{\mathrm{n}1a}(t), i_{\mathrm{n}2a}(t)$ as in (5.22) and (5.25), the three-phase currents for one converter undergoing commutation (from valve 5 to valve 1) are given by (5.41), and for a non-commutating converter, the currents are given by (5.42):

$$\begin{bmatrix} i_{na}(t) \\ i_{nb}(t) \\ i_{nc}(t) \end{bmatrix} = \begin{bmatrix} i_{na}(t) \\ -i_{dc}(t) \\ i_{dc}(t) - i_{na}(t) \end{bmatrix} \tag{5.41}$$

$$\begin{bmatrix} i_{na}(t) \\ i_{nb}(t) \\ i_{nc}(t) \end{bmatrix} = \begin{bmatrix} i_{dc}(t) \\ -i_{dc}(t) \\ 0 \end{bmatrix} \tag{5.42}$$

Using similar steps as in section 5.2.4, the first and second rows of the K matrix, i.e., K_{1n} and $K_{2n}(n = 1,2,\dots,6)$, can be determined with the integration of dq components of ac currents. The calculation of $K_{15} = \Delta I_d(s)/\Delta i_{cd}(s)$ is taken as a representative example in this section. For the infinite converters during commutation, the phase 'a' current becomes $i_{na}(t, \varphi_n)$ related to φ_n, similar to (5.36). Transforming (5.41) and (5.42) to dq domain and to the primary side (dividing N_c), the d- axis components of one converter's current during the commutation and non-commutation intervals are given in (5.43):

$$I_{dn}{}^{c}(t) = \frac{2\sqrt{3}}{3N_c}\left[-i_{dc}(t)\sin\phi_n(t) + i_{na}(t)\sin[\phi_n(t) + \frac{\pi}{3}]\right], \alpha(t) - \frac{\pi}{3} < \phi_n(t) < \delta(t) - \frac{\pi}{3} \quad (5.43a)$$

$$I_{dn}{}^{\bar{c}}(t) = -\frac{2\sqrt{3}}{3N_c} i_{dc}(t)\sin\left[\phi_n(t) - \frac{\pi}{3}\right], \delta(t) - \frac{\pi}{3} < \phi_n(t) < \alpha(t) \tag{5.43b}$$

In (5.43a), $i_{na}(t)$ is the sum of $i_{n1a}(t)$ and $i_{n2a}(t)$ obtained from (5.22) and (5.25) each of which includes the offset terms to satisfy initial conditions. These are therefore presented in $I_{dn}{}^{c}(t)$. In the following analysis, the instantaneous part $I_{dpn}{}^{c}(t)$ and the offset part $I_{don}{}^{c}(t)$ necessary for satisfying initial conditions are handled separately as in (5.44a) and (5.44b) respectively.

$$I_{dpn}{}^{c}(t) = \frac{2\sqrt{3}}{3N_c}\Big\{[i_{2d}(t)cos\phi_n(t) - i_{2q}(t)sin\phi_n(t) + \frac{1}{2}i_{dc}(t)]\sin[\phi_n(t) + \frac{\pi}{3}]$$

$$- i_{dc}(t)\sin\phi_n(t)\Big\} \quad (5.44a)$$

$$I_{don}{}^{c}(t) = -\frac{2\sqrt{3}}{3N_c}\Big[i_{2d}(t_{nf})cos\phi_n(t_{nf}) - i_{2q}(t_{nf})sin\phi_n(t_{nf}) + \frac{1}{2}i_{dc}(t_{nf})\Big]$$

$$* \Big[\phi_n(t) + \frac{\pi}{3}\Big] \quad (5.44b)$$

In (5.44b), $t_{nf} = t - \frac{\phi_n(t) - \alpha + \frac{\pi}{3}}{\omega_0}$, $\phi_n(t_{nf}) = \alpha(t_{nf}) - \pi/3$. Then, equation (5.43b) is integrated in a manner similar to that used for equation (5.37) to yield the contribution $I_d{}^{\bar{c}}$ from the converters in the non-commutation interval:

$$I_d{}^{\bar{c}} = \frac{3N_c}{\pi}\int_{\delta-\frac{\pi}{3}}^{\alpha} I_{dn}{}^{\bar{c}}(\phi_n)\,\mathrm{d}\phi_n = \frac{2\sqrt{3}}{\pi}i_{dc}\Big[\cos\Big(\alpha - \frac{\pi}{3}\Big) + cos\Big(\delta + \frac{\pi}{3}\Big)\Big] \quad (5.45)$$

Similarly, the total contribution of the offset free part from the converters during commutation, $I_{dp}{}^{c}$, is given by integrating (5.44a):

$$I_{dp}{}^{c} = \frac{3N_c}{\pi}\int_{\alpha-\frac{\pi}{3}}^{\delta-\frac{\pi}{3}} I_{dpn}{}^{c}(\phi_n)\,d\phi_n = \frac{2\sqrt{3}}{\pi}\Big[c_{i1}i_{2d} + c_{i2}i_{2q} + \frac{1}{2}i_{dc}(cos\alpha - cos\delta)\Big] \quad (5.46)$$

In (5.46):

$$c_{i1} = \frac{-\cos\Big(2\delta - \frac{\pi}{3}\Big) + \cos\Big(2\alpha - \frac{\pi}{3}\Big) + \sqrt{3}\mu}{4}$$

$$c_{i2} = -\frac{-\sin\Big(2\delta - \frac{\pi}{3}\Big) + \sin\Big(2\alpha - \frac{\pi}{3}\Big) + \mu}{4}$$

Equations (5.45) and (5.46) are then linearized to obtain their small-signal transfer

functions, i.e., $\Delta {I_d}^{\bar{c}}(s)/\Delta i_{2d}(s)$, etc.

The offset term (5.44b) for one converter can be linearized and then transformed to the Laplace domain as in (5.47), with the transportation lag included.

$$\Delta {I_{don}}^{c}(s) = -\frac{2\sqrt{3}}{3N_c} e^{-s\frac{\phi_n - \alpha + \frac{\pi}{3}}{\omega_0}} \Big[\Delta i_{2d}(s) cos\phi_n(t_{nf}) - i_{2d} sin\phi_n(t_{nf})\Delta\alpha(s)$$
$$- \Delta i_{2q}(s) sin\phi_n(t_{nf}) - i_{2q} cos\phi_n(t_{nf})\Delta\alpha(s)$$
$$+ \frac{1}{2}\Delta i_{dc}(s)\Big] \sin\left[\phi_n(t) + \frac{\pi}{3}\right] \qquad (5.47)$$

Integrating (5.47) to obtain contributions of all offset terms from converters during commutation, $\Delta {I_{do}}^{c}(s)$, and dividing by $\Delta i_{2d}(s)$ gives:

$$\frac{\Delta {I_{do}}^{c}(s)}{\Delta i_{2d}(s)} = \frac{3N_c}{\pi}\int_{\alpha-\frac{\pi}{3}}^{\delta-\frac{\pi}{3}} \frac{\Delta {I_{don}}^{c}(s)}{\Delta i_{2d}(s)}\,\mathrm{d}\phi_n = \frac{2\sqrt{3}}{\pi}\frac{\omega_0 c_{iof1}\cos\left(\alpha - \frac{\pi}{3}\right)}{s^2 + {\omega_0}^2} \qquad (5.48)$$

Where,

$$c_{iof1} = \omega_0 cos\alpha + s * sin\alpha - (\omega_0 cos\delta + s * sin\delta)e^{-s\frac{\mu}{\omega_0}}$$

The total contribution from $\Delta i_{2d}(s)$ to $\Delta I_d(s)$ is realized by adding its linearized constituent components in (5.45), (5.46) and (5.48), which gives the transfer function K_{15} as:

$$K_{15} = \frac{\Delta I_d(s)}{\Delta i_{2d}(s)} = \frac{\Delta {I_d}^{\bar{c}}(s) + \Delta {I_{dp}}^{c}(s) + \Delta {I_{do}}^{c}(s)}{\Delta i_{2d}(s)}$$
$$= \frac{2\sqrt{3}}{\pi}\left[c_{i1} + \frac{\omega_0 c_{iof1}\cos\left(\alpha - \frac{\pi}{3}\right)}{s^2 + {\omega_0}^2}\right] \qquad (5.49)$$

K_{1n} and K_{2n} $(n = 1,2,\dots,6)$ are similarly obtained as below.

$$\begin{cases} K_{11} = K_{12} = 0 \\ K_{13} = \dfrac{\Delta I_d(s)}{\Delta i_{dc}(s)} = \dfrac{2\sqrt{3}}{\pi}\left[\dfrac{cos\alpha + cos\delta}{2} - \dfrac{\omega_0 c_{iof2}}{2(s^2 + {\omega_0}^2)}\right] \\ K_{14} = \dfrac{\Delta I_d(s)}{\Delta\alpha(s)} = \dfrac{2\sqrt{3}}{\pi}\dfrac{-\omega_0 c_{iof1}}{s^2 + {\omega_0}^2}\left[i_{2d}\, cos\left(\alpha + \dfrac{\pi}{6}\right) - i_{2q}\, sin\left(\alpha + \dfrac{\pi}{6}\right)\right] \\ K_{15} = \dfrac{\Delta I_d(s)}{\Delta i_{2d}(s)} = \dfrac{2\sqrt{3}}{\pi}\left[c_{i1} + \dfrac{\omega_0 c_{iof1}\, cos\left(\alpha - \dfrac{\pi}{3}\right)}{s^2 + {\omega_0}^2}\right] \\ K_{16} = \dfrac{\Delta I_d(s)}{\Delta i_{2q}(s)} = \dfrac{2\sqrt{3}}{\pi}\left[-c_{i2} - \dfrac{\omega_0 c_{iof1}\, cos\left(\alpha + \dfrac{\pi}{6}\right)}{s^2 + {\omega_0}^2}\right] \end{cases} \tag{5.50}$$

$$\begin{cases} K_{21} = K_{22} = 0 \\ K_{23} = \dfrac{\Delta I_q(s)}{\Delta i_{dc}(s)} = \dfrac{2\sqrt{3}}{\pi}\left[-\dfrac{sin\alpha + sin\delta}{2} - \dfrac{\omega_0 c_{iof2}}{2(s^2 + {\omega_0}^2)}\right] \\ K_{24} = \dfrac{\Delta I_q(s)}{\Delta\alpha(s)} = \dfrac{2\sqrt{3}}{\pi}\dfrac{-\omega_0 c_{iof2}}{s^2 + {\omega_0}^2}\left[i_{2d}\cos\left(\alpha + \dfrac{\pi}{6}\right) - i_{2q}\sin\left(\alpha + \dfrac{\pi}{6}\right)\right] \\ K_{25} = \dfrac{\Delta I_q(s)}{\Delta i_{2d}(s)} = \dfrac{2\sqrt{3}}{\pi}\left[c_{i3} - \dfrac{\omega_0 c_{iof2}\sin\left(\alpha + \dfrac{\pi}{6}\right)}{s^2 + {\omega_0}^2}\right] \\ K_{26} = \dfrac{\Delta I_q(s)}{\Delta i_{2q}(s)} = \dfrac{2\sqrt{3}}{\pi}\left[c_{i4} - \dfrac{\omega_0 c_{iof2}\cos\left(\alpha + \dfrac{\pi}{6}\right)}{s^2 + {\omega_0}^2}\right] \end{cases} \tag{5.51}$$

Where,

$$c_{i3} = \frac{\sin\left(2\delta - \frac{\pi}{3}\right) - \sin\left(2\alpha - \frac{\pi}{3}\right) + \mu}{4}$$

$$c_{i4} = \frac{\cos\left(2\delta - \frac{\pi}{3}\right) - \cos\left(2\alpha - \frac{\pi}{3}\right) + \sqrt{3}\mu}{4}$$

$$c_{iof2} = s * cos\alpha - \omega_0 sin\alpha - (s * cos\delta - \omega_0 sin\delta)e^{-s\frac{\mu}{\omega_0}}$$

5.2.6 Extinction angle measurement

In the inverter side, the extinction angle has to be measured when there is an extinction angle controller. So, as shown in Fig. 5-4, γ is taken as an output. This angle is measured as the angle difference between two instants, one is valve turn-off (the end of overlap), and another is the zero-crossing of the commutation voltage. In steady state, the extinction angle is decided by the firing angle and overlap angle:

$$\gamma = \pi - \alpha - \mu \tag{5.52}$$

In transient analysis, the transportation lag is included in the measurement that the small signal variables in Laplace domain satisfy the relationship:

$$\Delta\gamma(s) = \Delta\epsilon_{zc}(s) - \Delta\alpha(s)e^{-s\frac{\pi-\alpha}{\omega_0}} - \Delta\mu(s)e^{-s\frac{\pi-\alpha-\mu}{\omega_0}} \tag{5.53}$$

Where $\Delta\epsilon_{zc}(s)$ is the variation of the zero-crossing time (i.e., the incremental zero crossing time), expressed in units of angle resulting from the ac voltage distortion. In this study, the q-axis steady state voltage is zero, and the zero-crossing angle variation can be obtained from:

$$\Delta\epsilon_{zc}(s) = -\Delta V_q(s) \tag{5.54}$$

Combining K_{4n} and the equations above, we get K_{5n} as:

$$\begin{cases} K_{51} = \dfrac{\Delta\gamma(s)}{\Delta V_d(s)} = 0 \\ K_{52} = \dfrac{\Delta\gamma(s)}{\Delta V_q(s)} = -1 \\ K_{53}{}' = \dfrac{\Delta\gamma(s)}{\Delta i_{dc}(s)} = -e^{-s\frac{\gamma}{\omega_0}} K_{43} \\ K_{54} = \dfrac{\Delta\gamma(s)}{\Delta\alpha(s)} = -e^{-s\frac{\gamma}{\omega_0}} K_{44} - e^{-s\frac{\gamma+\mu}{\omega_0}} \\ K_{55} = \dfrac{\Delta\gamma(s)}{\Delta i_{2d}(s)} = -e^{-s\frac{\gamma}{\omega_0}} K_{45} \\ K_{56} = \dfrac{\Delta\gamma(s)}{\Delta i_{2q}(s)} = -e^{-s\frac{\gamma}{\omega_0}} K_{46} \end{cases} \tag{5.55}$$

In the above derivation, it was assumed that the voltage zero crossing was that of the commutation busbar voltage. However, if the extinction angle measurement uses the voltage measured from the valve terminals, the voltage drop across the commutation inductance has to be included in the calculation of the incremental zero-crossing angle:

$$\Delta\epsilon_{zc}(s) = -\Delta V_q(s) - sL_c\Delta i_{dc}(s) \tag{5.56}$$

Then, we have:

$$K_{53} = K_{53}{}' - sL_c \tag{5.57}$$

Here L_c is the per unit value calculated using the dc side base impedance.

5.2.7 Sampling in the measurement of the angles

In the above Section 5.2.2 to 5.2.6, the model of the infinite series-connected converters is developed. To apply this model to real HVdc converters, which are typically 12-pulse converters is done as discussed below.

The output dc voltage and ac current, as obtained in Section 5.2.4 and 5.2.5, can be explained as the 'averaging' of the original dc voltage and ac current in the twelve-pulse

converter. In the traditional models [30] [36], the instantaneous dc components of the dc voltage and ac current as a function of time (i.e., the dynamic response) cannot be obtained when a small disturbance is superposed on the input variables. As the 12th harmonics were part of the waveforms, we cannot distinguish if the generated small signal variance in the output signals should be part of the dc component or of the 12th harmonic components. With the infinite-converter representation, the calculated outputs (e.g., overlap and extinction angles) are continuous functions of time and can be directly obtained using the developed model in previous subsections. At this stage, the 12-pulse nature of the actual converter is still not included as these quantities can change continuously. To incorporate the feature in real 12-pulse converters, a sampling block followed by a zero-order hold block is inserted in series with the continuous overlap angle output $\mu(t)$, as shown in Fig. 5-7 to give the sampled angle μ_i, and the held angle $\mu_{mea}(t)$. A similar process is applied to the other continuous outputs such as the extinction angle generated by the infinite-converter model. These values are held for the next 1/12 cycle for the twelve-pulse converters until new values are measured. The mechanisms of generating the overlap angle in these two configurations are given as in Fig. 5-7.

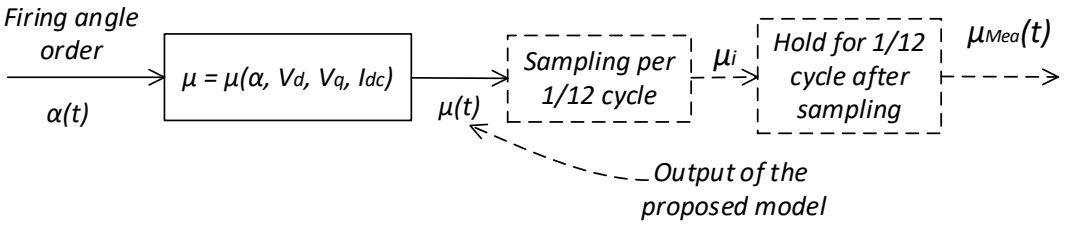

Figure 5-7. The overlap angle generating mechanism

The sample block and hold block are included in the developed model by multiplying the

fourth row (for μ) or fifth row (for γ) of the matrix K by the following zero-order hold transfer function [83]:

$$H(s) = \frac{1 - e^{sT_s}}{sT_s} \tag{5.58}$$

Here, $T_s = 1/12$ of fundamental period. To enable the application of the developed model on the normal six or twelve pulse converters, the *4th* row of the K matrix (for μ) and *5th* row (for γ) must be multiplied by $H(s)$.

5.3 Model validation by frequency scanning

In this section, the accuracy of the developed LCC model (from the assumption of infinite series converters) in Section 5.2 is validated by comparing the frequency response of the analytical transfer matrix K^* with the one obtained from the frequency scanning. Although analytically obtainable from (5.24), in simulation the inputs of K, namely i_{2d} and i_{2q} are internal variables based on the infinite pulse converter assumption and therefore cannot be directly measured. Only the elements of K^* can be extracted from the frequency scanning. Hence, K^* is calculated from K analytically and used for validation purpose. To do this, one obtains i_{2d} and i_{2q} from (5.24) ($\boldsymbol{G_{iv}(s)}$ is the transfer matrix from $[V_d \quad V_q]^T$):

$$\begin{bmatrix} i_{2d}(s) \\ i_{2q}(s) \end{bmatrix} = \boldsymbol{G_{iv}(s)} \begin{bmatrix} V_d(s) \\ V_q(s) \end{bmatrix} = \frac{\sqrt{3}}{4} \begin{bmatrix} sL_c & -\omega_0 L_c \\ \omega_0 L_c & sL_c \end{bmatrix}^{-1} \begin{bmatrix} \sqrt{3} & 1 \\ -1 & \sqrt{3} \end{bmatrix} \begin{bmatrix} V_d(s) \\ V_q(s) \end{bmatrix} \tag{5.59}$$

The matrix T_U relating ΔU^*_{LCC} to $\Delta U_{LCC}(s)$ is given by:

$$\Delta \mathrm{U}_{LCC}(s) = \mathrm{T}_U \Delta \mathrm{U}^*{}_{LCC}(s) = \begin{bmatrix} 1 & 0 & 0 & 0 \\ 0 & 1 & 0 & 0 \\ 0 & 0 & 1 & 0 \\ 0 & 0 & 0 & 1 \\ \boldsymbol{G_{iv}(s)} & & 0 & 0 \\ & & 0 & 0 \end{bmatrix} \Delta \mathrm{U}^*{}_{LCC}(s) \tag{5.60}$$

Considering $\Delta Y_{LCC} = K^* \Delta U^*{}_{LCC} = K \Delta U_{LCC}$, we have:

$$K^* = K T_U \tag{5.61}$$

With the analytical response of K^* obtained as in (5.61), frequency scanning is applied to validate the result. As the response is dependent on the operating point, the steady state values, i.e., the ac voltage, the dc current, the firing angle, are selected first. Then in PSCAD/EMTDC, these values are applied to converter model using a controllable voltage source at PCC bus and controllable current source on the dc side. The steady state value of the firing angle order is sent to the firing pulse generator. A small multi-sine perturbation signal as in (3.2), is superposed on the steady state values of the input vector one element at a time. Finally, the values of the input vector and the output vector in time domain are recorded and the elements of the transfer matrix K^* are calculated using the Discrete Fourier series (as discussed in Section 3.1.4). As K^* is a 4 x 4 dimensional matrix, four separate injection series are required to get all the elements of K^*.

The validation is made for two different operating points of the 12-pulse converter. One operating point is for rectifier operation and the other for inverter operation. The value of the commutation inductance L_c is 0.18 pu. The steady state values of the inputs and outputs are given in Table 5-1. The scanned frequency range is from 1 Hz to 1000 Hz, with a 1 Hz interval.

Table 5-1. Steady state operating points of LCC

Operating point	I	II
Operating as	Inverter	Rectifier
V_d / V_q	1.0 pu / 0.0 pu	1.0 pu / 0.0 pu
I_{dc}	1.0 pu	1.0 pu
α	140.45 deg	15 deg
I_d / I_q	-0.8222 pu / -0.4749 pu	0.8364 pu / 0.4479 pu
V_{dc}	0.98 pu	1.0 pu
μ	21.55 deg	23.2 deg
γ	18 deg	141.8 deg

5.3.1 Result comparison for inverter mode operation

The frequency response plots for the magnitude and phase angle of elements of the matrix K^* obtained by frequency scanning applied to the detailed EMT model as well as those obtained analytically (after sampling to convert to 12-pulse measurements) are shown in Figs. 5-7 and 5-8 for the 12-pulse inverter for operating point 'I' in Table 5-1. Only Plots for typical elements $(K^*_{i,j}; i = 1,2,3,5; j = 1,2,3,4)$ are shown to fit the results on a single page.

The X-axis is frequency (in Hz) and the Y-axis is the magnitude (in per unit for voltages and currents, and in radians for angles). The impedance base for per-unitization is $Z_{base} = {V_{ll}}^2/T_{mva}$, where V_{ll} is the rated line to line ac voltage at PCC bus, and T_{mva} is the total base MVA of the two ac transformers (this definition also applies in the following sections and chapters). The green lines are the analytical result from Section 5.2, and the blue lines

are the result from the scan. As in Figs. 5-8 Fig. 5-9, the plots are virtually overlapping, confirming the accuracy of the proposed analytical model.

5.3.2 Result comparison for rectifier mode operation

The frequency response plots for the converter for operating point 'II' in Table 5-1 of the matrix K^* are shown in Figs. 5-10 and 5-11 for the 12-pulse rectifier. Plots for typical elements ($K^*_{i,j}; i = 1,2,3,4; j = 1,2,3,4$) are shown.

As before, the green lines are the analytical result, and the blue lines are from the scan. The results also match very well.

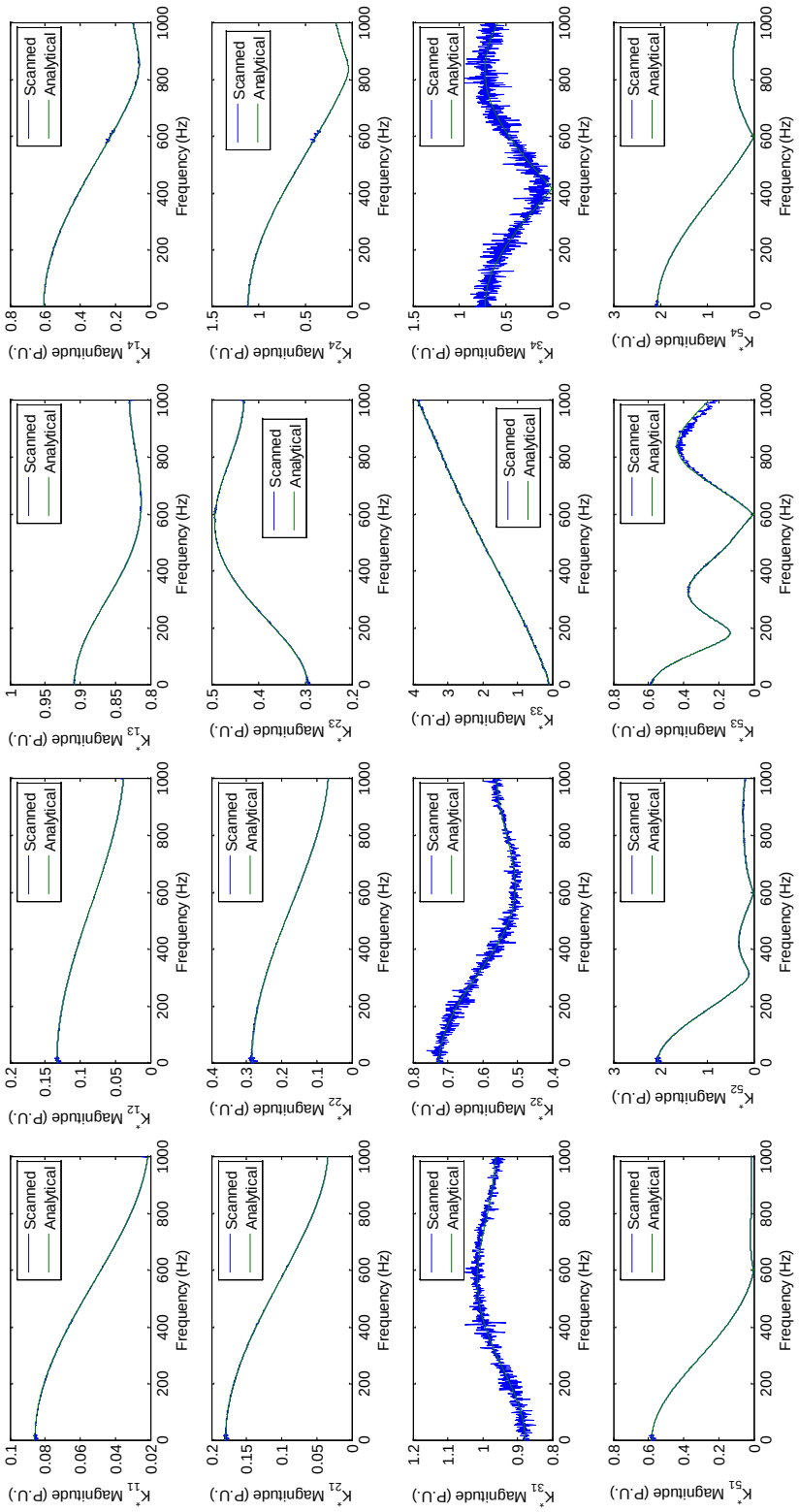

Figure 5-8. Magnitudes of typical elements in the K matrix for the inverter*

Figure 5-8. Magnitudes of typical elements in the *K** matrix for the inverter

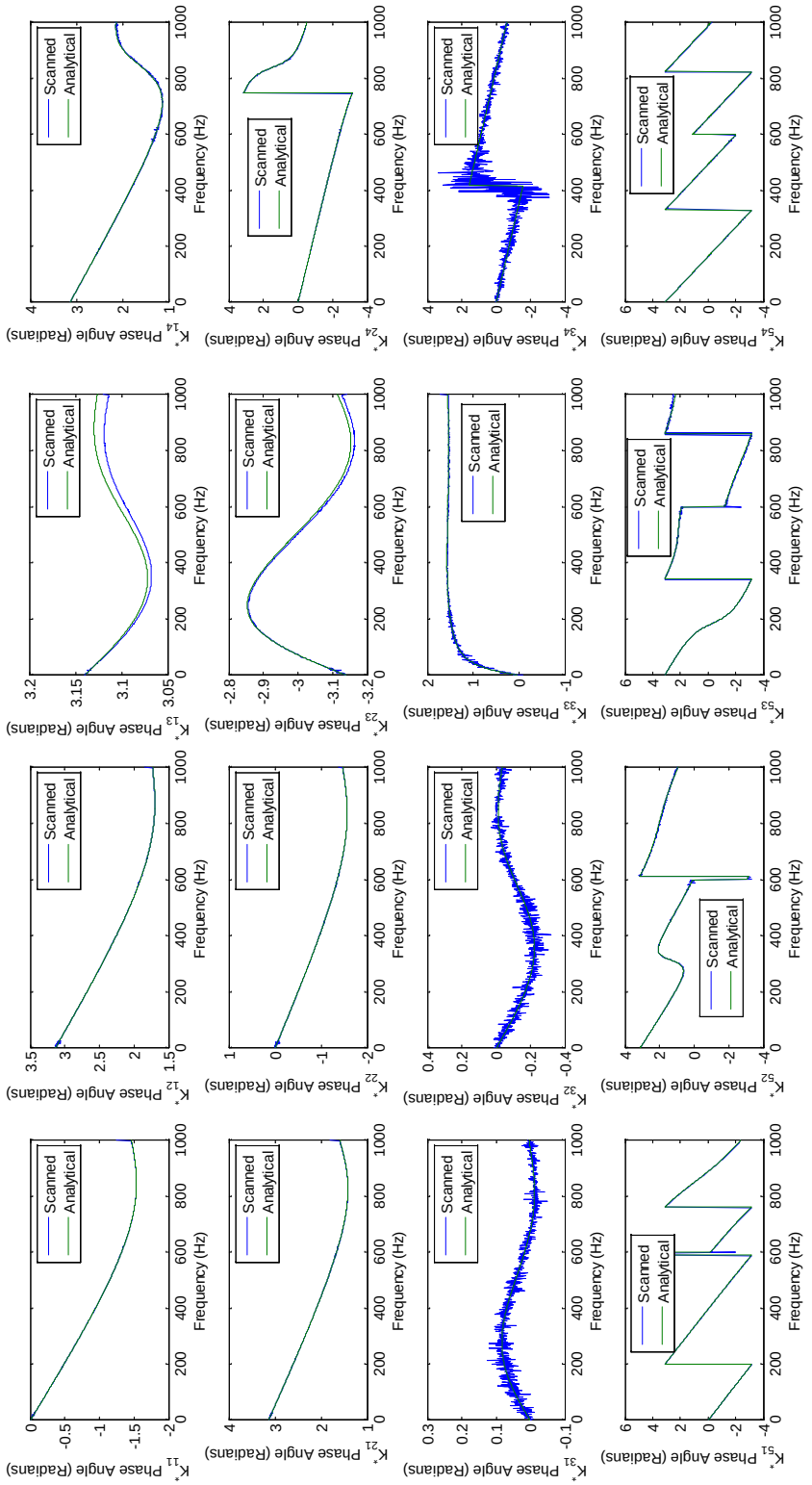

Figure 5-9. Phase angles of typical elements in the K matrix for the inverter*

Figure 5-9. Phase angles of typical elements in the *K** matrix for the inverter

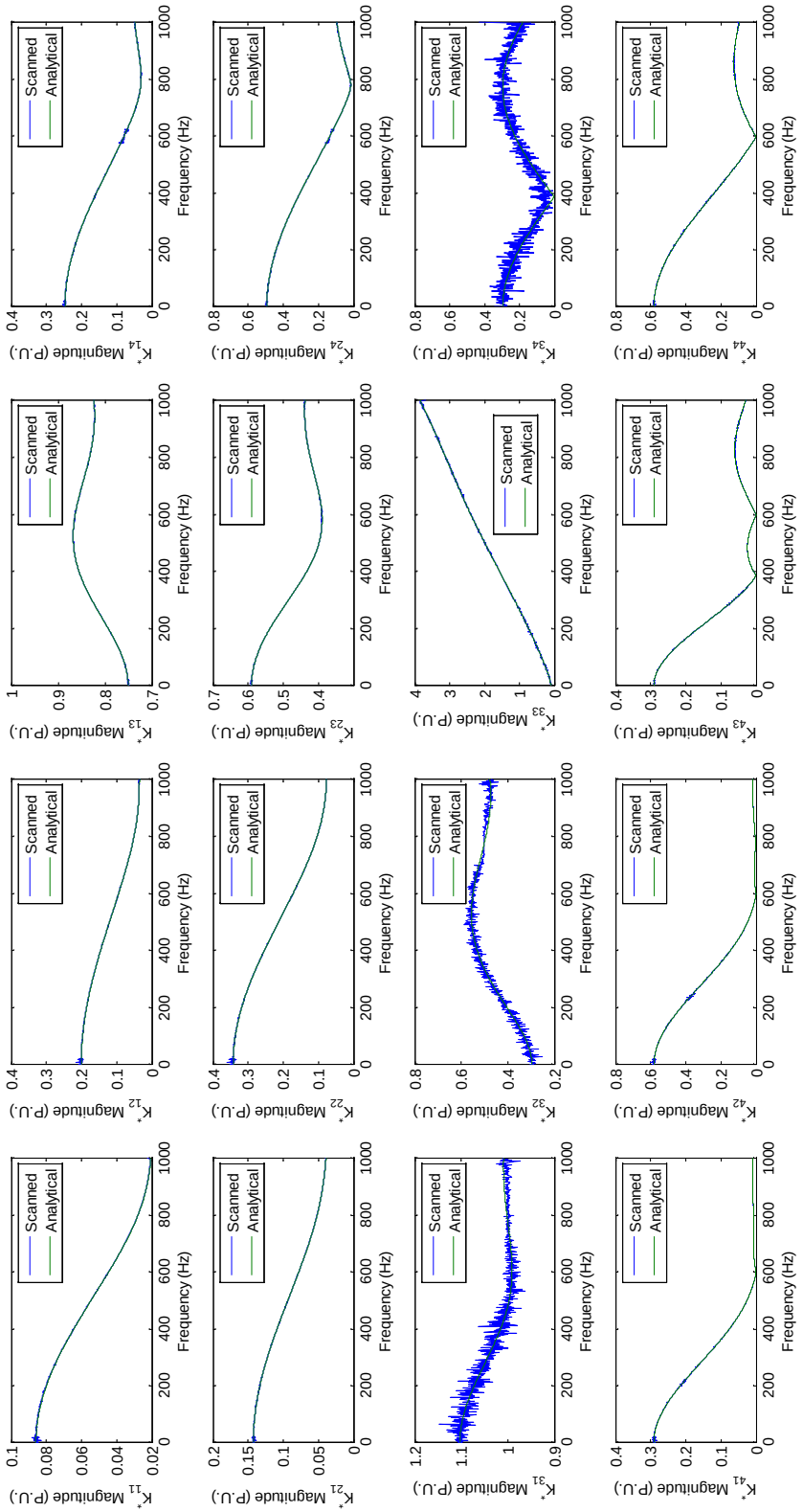

Figure 5-10. Magnitude of typical elements in the K matrix for the rectifier*

Figure 5-10. Magnitude of typical elements in the K* matrix for the rectifier

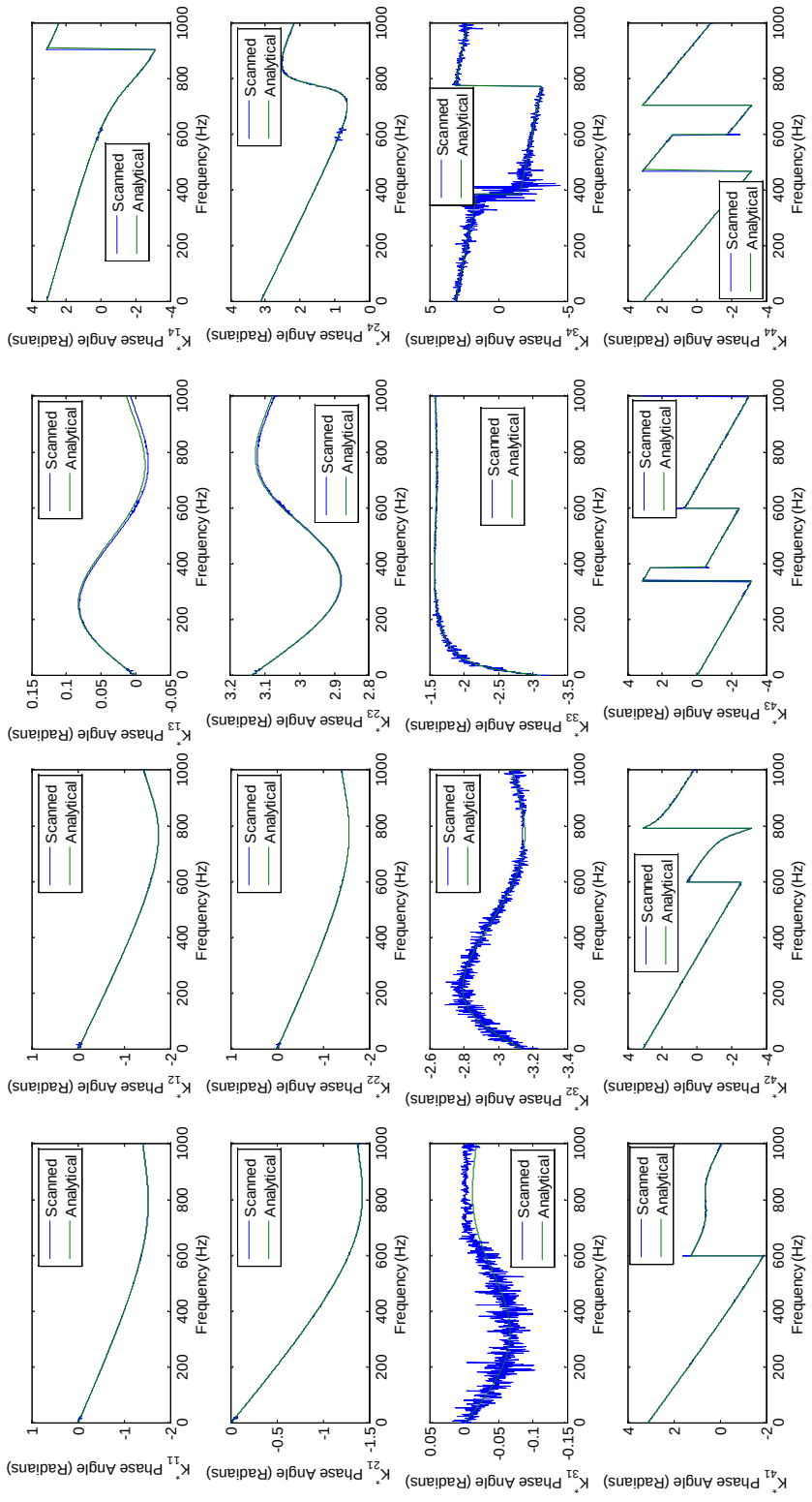

Figure 5-11. Phase angle of typical elements in the K matrix for the rectifier*

Figure 5-11. Phase angle of typical elements in the K* matrix for the rectifier

5.4 Model validation by case studies in EMT simulation

In previous section, the frequency response of the LCC obtained from the analytical model has been validated by the frequency scanning. This section provides two case studies to further validate the improved model using time domain simulation by connecting the converter to external systems and then investigating the system stability.

5.4.1 Case study of LCC connected to a simple network

In the case system studied here, the converter is operating as an inverter and connected to an external system, which includes the ac side system and the dc side system as shown in Fig. 5-12. The control system is shown as in Fig. 5-13.

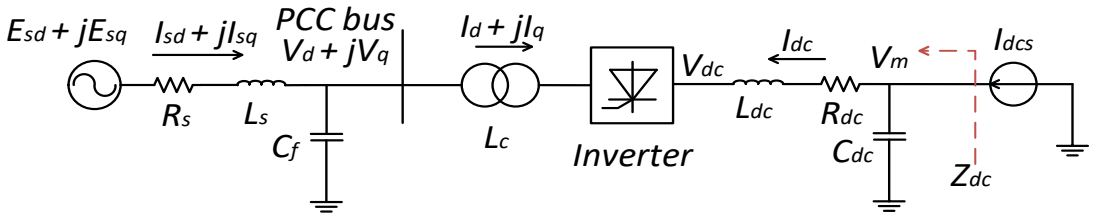

Figure 5-12. Electrical system configuration

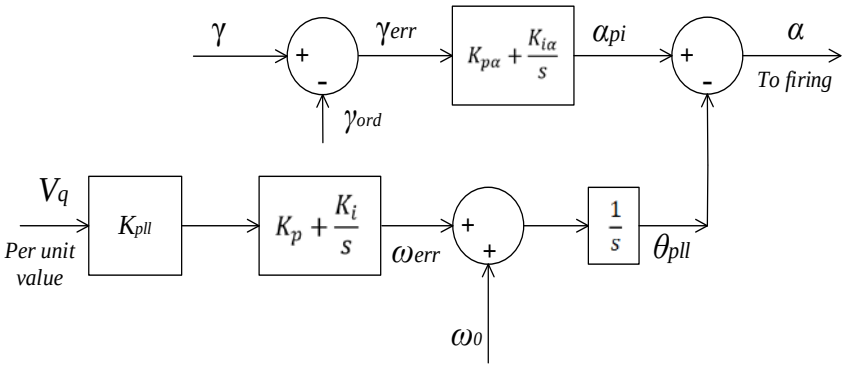

Figure 5-13. Control system blocks

The ac system includes an ac voltage source connected to the PCC bus through an R_s-L_s Thevenin circuit. A shunt capacitor C_f is also connected to the PCC bus and provides reactive power compensation approximately 60% of the rated active power. Tuned filters are not modelled. In a real HVdc system, the injection of the characteristic harmonics to the system from the converter are problematic as they deteriorate the power quality can be very important. However, these harmonics do not affect the system stability and we do not need to specially eliminate them in the simulation.

On the dc side, there is a dc current source I_{dcs} to model the remote rectifier operating in the constant current control mode. This current source is connected to the converter terminal through an L_{dc}-R_{dc} circuit, and to the ground through a capacitor C_{dc}. This inverter side dc circuit topology has the same as the First CIGRE Benchmark model [53].

The controller is made up of a PLL and a constant extinction angle controller, which is a

typical controlling coordination algorithm.

The ac system base voltage is 230kV (L-L RMS), and the base power is 1192.18 MW. Two six-pulse converters are included with commutation transformer (ratio: 230/210.75; base Mva: 596.09Mvar; reactance: 0.18 pu; one has YY winding connection and the other YD). The dc side has the base voltage of 500 kV and base current 2 kA. The other parameters of the system are given as in Tab. 5-2.

Table 5-2. Parameters of the case system

Electrical Circuit	*Value (P.U.)*	*Controller Parameters*	*Value*
R_s	*2.2186 ohm*	K_p	*20.0*
L_s	*0.0424 H*	K_i	*100.0*
C_f	*35.868 uF*	$K_{p\alpha}$	*0.2*
L_{dc}	*0.5968 H*	$K_{i\alpha}$	*6.67*
R_{dc}	*2.5 ohm*		
C_{dc}	*26.0 uF*		

The steady state operating point is given as: dc voltage, 0.98 pu, dc current, 1.0 pu, ac voltage of the commutation bus, 1.0 pu, and the extinction angle is 18 degrees. Based on this operating point, the analytical state model of the system can be constructed below.

The state equations of the ac system in the dq0 domain can be presented:

$$L_s \frac{d}{dt}\begin{bmatrix} I_{sd} \\ I_{sq} \end{bmatrix} = \begin{bmatrix} -R_s & \omega_0 L_s \\ -\omega_0 L_s & -R_s \end{bmatrix}\begin{bmatrix} I_{sd} \\ I_{sq} \end{bmatrix} + \begin{bmatrix} E_{sd} - V_d \\ E_{sq} - V_q \end{bmatrix} \tag{5.62}$$

$$C_f \frac{d}{dt}\begin{bmatrix} V_d \\ V_q \end{bmatrix} = \begin{bmatrix} 0 & \omega_0 C_f \\ -\omega_0 C_f & 0 \end{bmatrix}\begin{bmatrix} V_d \\ V_q \end{bmatrix} + \begin{bmatrix} I_{sd} - I_d \\ I_{sq} - I_q \end{bmatrix} \tag{5.63}$$

The state equations of the dc side system:

$$L_{dc} \frac{di_{dc}}{dt} = -R_{dc} i_{dc} + V_m - V_{dc} \tag{5.64}$$

$$C_{dc}\frac{dV_m}{dt} = I_{dcs} - i_{dc} \tag{5.65}$$

Equations (5.66-68) below are used to model the controller.

$$\frac{d\omega_{err}}{dt} - K_p\frac{dV_q}{dt} = K_i V_q \tag{5.66}$$

$$\frac{d\theta_{pll}}{dt} = \omega_{err} + \omega_0 \tag{5.67}$$

$$\frac{d\alpha_{pi}}{dt} - K_{p\alpha}\frac{d\gamma}{dt} = K_{i\alpha}\gamma \tag{5.68}$$

Using equations (5.15), (5.24) to model the converter and the commutation transformer, and equations (5.62-5.68) to model the external system, the overall system can be linearized and represented as a state equation set with in (5.69a), and the equivalent Laplace (s) domain representation is in (5.69b).

$$M\Delta\dot{X}(t) = A_0\Delta X(t) + A_1\Delta X(t - T_1) + B\Delta U(t) \tag{5.69a}$$

$$Ms\Delta X = (A_0 + A_1 e^{-sT_1})\Delta X + B\Delta U \tag{5.69b}$$

In (5.69a), the system representation includes the time delay terms, which are caused by the transportation lag in *K* matrix. The expressions for M, ΔX and $A = A_0 + A_1 e^{-sT_1}$ are given in Appendix C . As (5.69b) cannot be converted to rational function form (on account of the transportation lag term e^{-sT_1}) the eigenvalues of the system cannot be obtained to provide a root-locus plot. However, a graphical approach, i.e., the Generalized Nyquist Criterion (GNC), is easily applicable for the determination of system stability [84].

Typically, in a multi-input multi-output transfer matrix, all elements have the same poles (neglecting the pathological case of pole-zero cancellations), and so the stability of the system can be determined by observing the Nyquist contour from any one input to one

output. If the contour encircles the origin (0, 0) in the anticlockwise direction when the frequency varies from $-\infty$ to $+\infty$, the system is unstable as there are positive plane poles.

In this case, the transfer function chosen is as in (5.70), which is the impedance looking into the dc bus of the converter as in Fig. 5-12:

$$Z_{dc}(s) = \frac{\Delta V_{dcm}(s)}{\Delta I_{dcs}(s)} \tag{5.70}$$

The dc impedance contour is plotted with respect to the gain K_{pll} of the PLL as shown in Fig. 5-13. By increasing K_{pll}, the system becomes unstable. And the critical value resulting in marginal stability can be found.

The contours are plotted with respect to different K_{pll} values. In Fig. 5-14 below, the encirclement direction is clockwise for $K_{pll} = 4.8$ (blue line) and anti-clockwise for $K_{pll} = 4.9$ (green line). Hence, the critical value of K_{pll} is between 4.8 and 4.9 indicating marginal stability. By more precise contour plotting, the critical value is determined as 4.85.

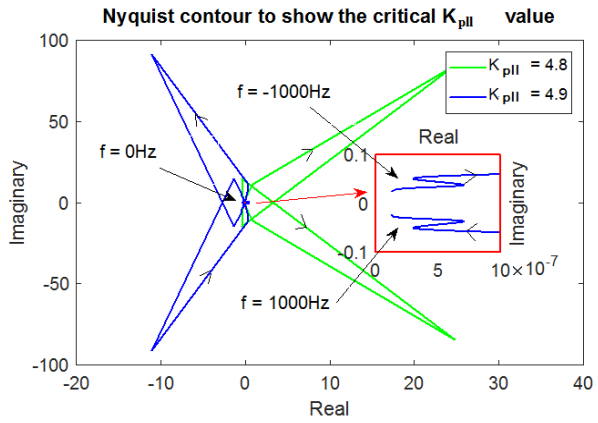

Figure 5-14. Nyquist plot of the dc side impedance for K_{pll} close to the critical value

This result is validated by an EMT simulation (in PSCAD/EMTDC) as follows. At first, the value of K_{pll} was set as 4.5. Then at t =1.0s, the step change of K_{pll} from 4.5 to 5.0 was made. The output of PLL angle as in Fig. 5-15 shows that the system operates stably for $K_{pll} = 4.5$ (which is below the critical value of 4.85) but becomes unstable after the step change of K_{pll} to 5.0 (which is larger than the critical value).

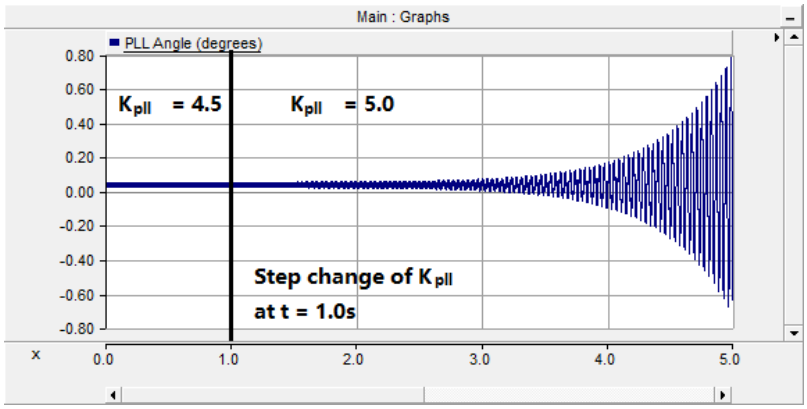

Figure 5-15. The output of the PLL angle with the step change of K_{pll}

At the same time, another analytical approach based on the traditional model (in the dq0 domain) [30][36] of the LCC is also applied to determine the system stability. There is no

transportation lag term in this model and so the state matrix $A(s)$ is constant, and unlike in the more detailed model developed in this thesis, where $A(s)$ becomes frequency dependent. Hence, the eigenvalues of the system matrix are calculable. The root locus is plotted with respect to the value of K_{pll}, as in Fig. 5-16 and shows instability for any positive value of $K_{pll} < 10.0$, since one pair of eigenvalues always have positive real part. This contradicts the simulation experiment. In contrast, the Nyquist plot based on the proposed model accurately predicts the stable range of $K_{pll} < 4.85$ as confirmed by the simulation experiment. This shows the necessity of using the detailed model in stability analysis determination.

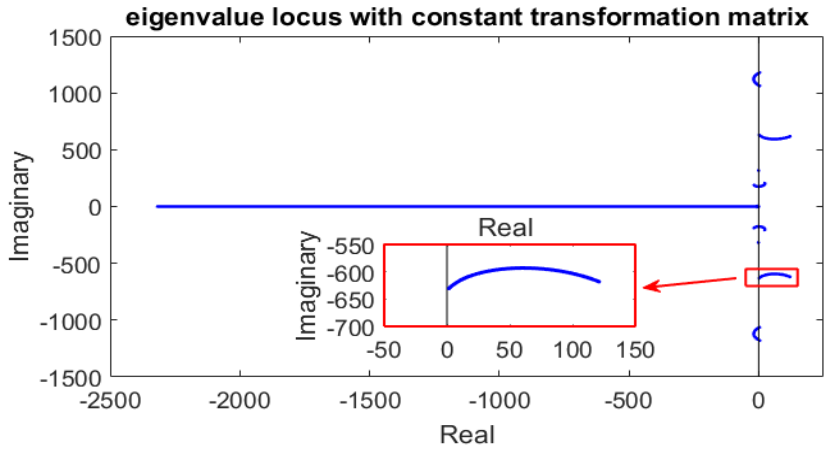

Figure 5-16. Root locus of the case system using the traditional LCC modelling approach

5.4.2 Case study of LCC connected to the IEEE 14-bus system

To study the ability of the proposed model to determine stability of realistic systems, the IEEE 14-bus test system [85][86] is studied here and modelled as shown in Fig. 5-17, with the voltage source originally present at bus No. 1 (138 kV) replaced by a 250 MW HVdc

infeed LCC (inverter). An ac transformer with transform ratio 138.0/115.0 is used to connect the PCC bus to the ac network. Again, the dc side of the LCC is modelled as a constant current source, assuming the remote converter is operating in current control. This typical system can validate the practical application of the proposed model as well as of the GNC.

Also, in contrast with the earlier simplified study, the ac filters connected to the PCC bus are included, with per unit values close to those in the First CIGRE benchmark system [51]. The damping of the filters is reduced to make it easier to excite instabilities, whose parameters are given in Fig. C-1, Appendix. The state equations of the ac filters are also given in equations (C. 2-7), Appendix C.

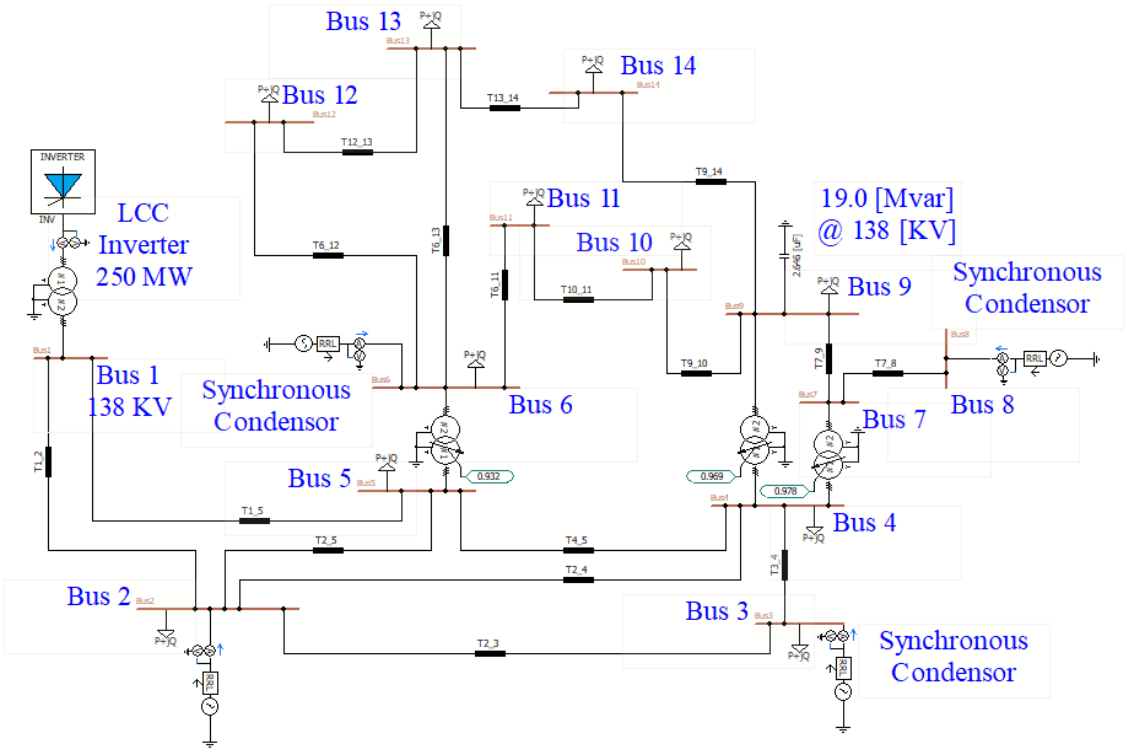

Figure 5-17. The IEEE 14-bus ac system connected to LCC inverter at Bus No. 1

Since the transmission lines of the IEEE 14-bus network are modeled with distributed element parameters, their impedance responses cannot be analytically obtained. Under this circumstance, the frequency scan is applied to extract the admittance response matrix, $\boldsymbol{G_{IEEE}}$ in dq0 domain, of the ac network looking from the PCC bus (Bus No. 1) from the EMT model. The admittance matrix $\boldsymbol{G_{IEEE}}$ relates the voltage injection into the network $[\Delta V_d(j\omega) \quad \Delta V_q(j\omega)]^T$ to the resultant current $[\Delta I_{sd}(j\omega) \quad \Delta I_{sq}(j\omega)]^T$ as in (5.71).

$$\begin{bmatrix}\Delta I_{sd}(j\omega)\\ \Delta I_{sq}(j\omega)\end{bmatrix} = \boldsymbol{G_{IEEE}} \begin{bmatrix}\Delta V_d(j\omega)\\ \Delta V_q(j\omega)\end{bmatrix} = \begin{bmatrix}G_{dd}(j\omega) & G_{dq}(j\omega)\\ G_{qd}(j\omega) & G_{qq}(j\omega)\end{bmatrix}\begin{bmatrix}\Delta V_d(j\omega)\\ \Delta V_q(j\omega)\end{bmatrix} \quad (5.71)$$

The magnitude and phase angle of the elements in $\boldsymbol{G_{IEEE}}$ are scanned and shown as in

Fig. 5-18 and Fig. 5-19.

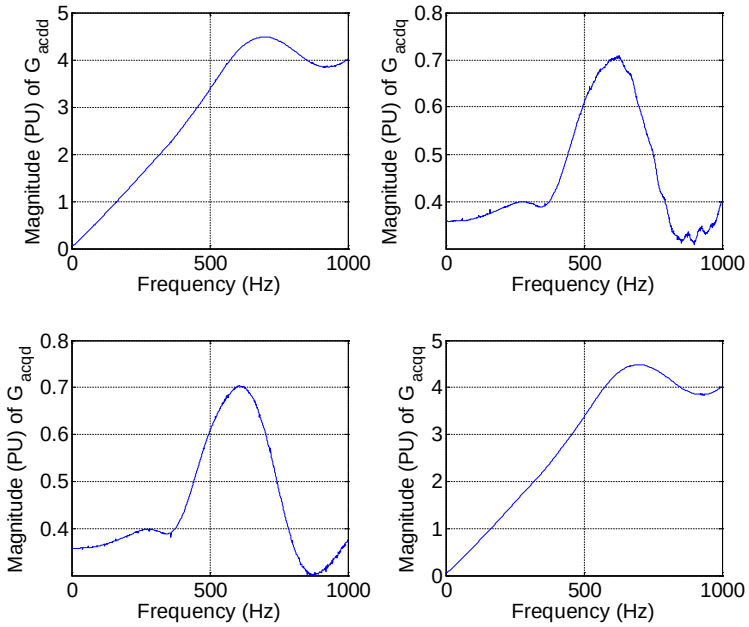

Figure 5-18. Magnitude of the admittance matrix elements of the IEEE 14-bus ac system (per unit)

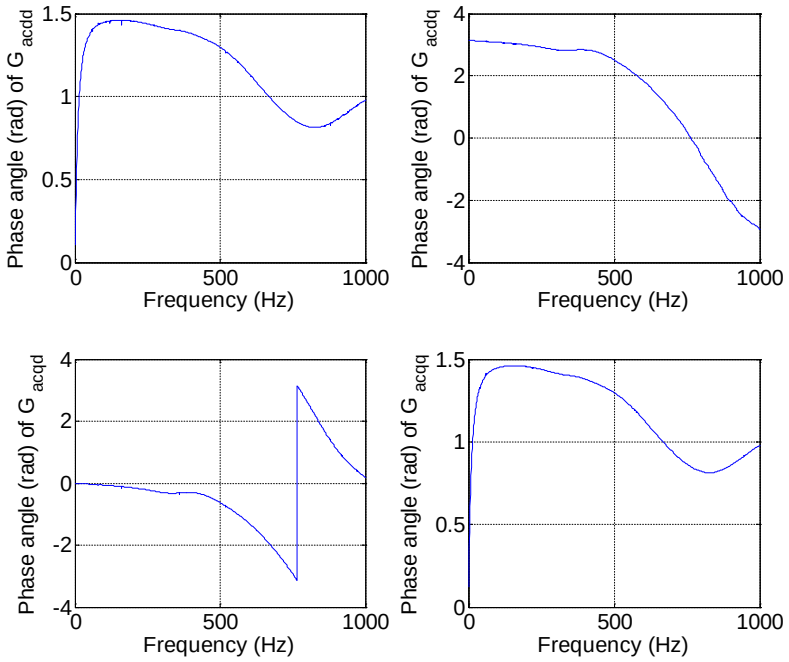

Figure 5-19. Phase angle of the admittance matrix elements of the IEEE 14-bus ac system (radians)

A similar procedure as in Section 5.4.1 is followed to draw the Nyquist plot shown in Fig. 5-20. This time the encirclement of the contour is clockwise for $K_{pll} = 2.5$ and the system is stable; whereas the encirclement is anti-clockwise for $K_{pll} = 3.0$ and the system is unstable. A more precise analysis shows that the critical value is $K_{pll} = 2.76$.

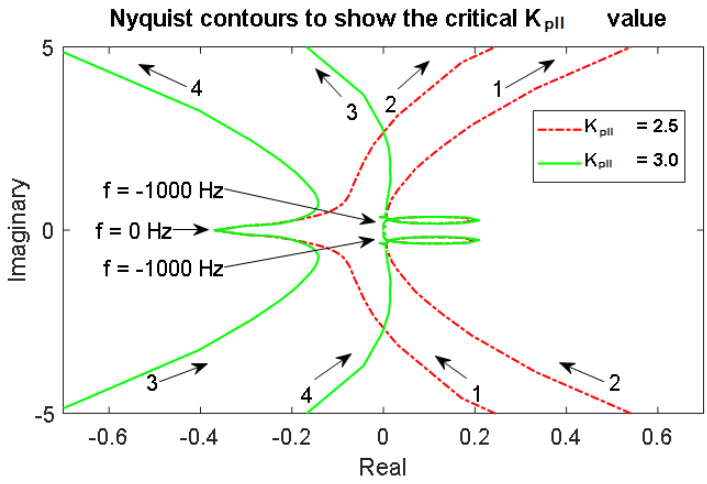

Figure 5-20. The Nyquist contours for K_{pll} values 2.5 and 3.0

The above stability result is also validated by the EMT simulation. Fig. 5-21 shows a plot of the firing angle order α generated by the PI controller in Fig. 5-13. It is clear that the system operates stably with $K_{pll} = 2.5$ at first, however becomes unstable after the change of K_{pll} from 2.5 to 3.0 at t = 1.0 s.

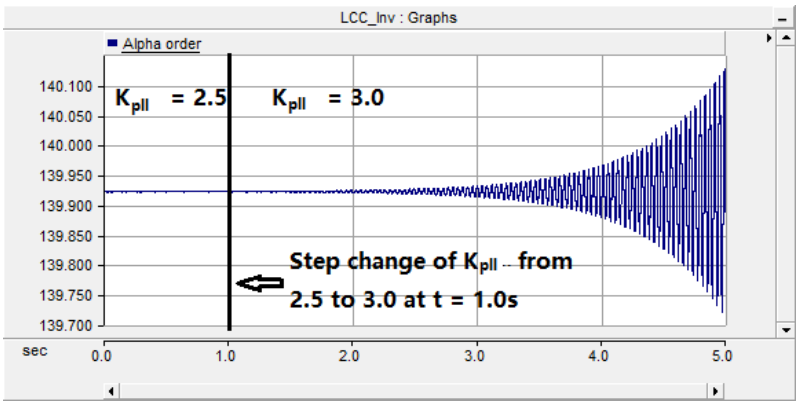

Figure 5-21. The output of the firing angle order with the step change of K_{pll}

5.5 Discussion

In this chapter, an improved model of the LCC is proposed using the artifact of the infinite series-connected converters. With this approach, all the input and output variables of the converter, e.g., currents and voltages, no longer include characteristic harmonics, and the commutation inductance and the converter valves are separately modeled. Also, discrete variables of firing and extinction angle measurements become continuous variables, making them representable by Laplace transforms. The discrete nature of actual 12 pulse converters can be restored via sampling and holding these continuous variables.

The elements of the transfer matrix relating the inputs and outputs obtained from the improved analytical become frequency dependent. When their frequency responses are compared with the frequency scan of a detailed EMT model, the two frequency responses are observed to be almost overlapping, thereby validating the proposed model. Moreover, the Generalized Nyquist stability Criterion can be directly applied to the analytically

obtained small signal model. The stability boundaries (critical value of the PLL gain) so determined agree with time-domain EMT simulations. It is also shown that the improved model has much better accuracy than the traditional model in this case system, and in some cases, the traditional model can indicate erroneous stability results.

The potential practical application of the approach was successfully demonstrated via a larger system that included the IEEE 14-bus network modified with the addition of an HVdc infeed. For any arbitrary system including LCC converters, similar procedure can be used to accurately determine the system stability.

6 Harmonic Stability Margin (HSM) - a proposed index for quantifying the ac-dc system interaction

In the past, simple indices such as the Short Circuit Ratio (SCR) and Effective Short Circuit Ratio (ESCR) were used to quantify the behavior of ac-dc systems. These indices classified the ac system as ‘strong’ or ‘weak’ when the dc converter was connected to the ac side in system planning and design studies. They were useful for identifying fundamental frequency behaviors such as power-voltage instability, but they were not very effective in predicting instability at other frequencies beside the fundamental frequency.

This chapter proposes a new index, Harmonic Stability Margin (HSM) based on the Generalized Nyquist stability Criterion (GNC), to parameterize the interaction level between the ac systems and the dc converters. This index considers the impedance responses of both the ac and dc side, and can identify the system stability and resonance not only in the fundamental frequency, but also in the sub-synchronous and super-synchronous frequency range.

This chapter is the extension of a conference paper in the 14th IET International conference on AC and DC power transmission [87].

6.1 Traditional studies in the ac system strength

In traditional studies, a family of indices were introduced to parameterize the ac system strength, in which the most typical ones were the Short Circuit Ratio (SCR) and the Effective Short Circuit Ratio (ESCR). The SCR is calculated as [15-16]:

$$SCR = \frac{{V_{l-l\,N}}^2 \left| G_{sys} \right|}{P_{dcN}} \qquad (6.1a)$$

Where G_{sys} is the Thévenin admittance of the ac system, $V_{l-l\,N}$, the rated ac voltage of the PCC bus and P_{dcN}, the rated power of the dc converter. The Effective Short Circuit Ratio (ESCR) modifies the SCR to include the admittance of the static elements G_q which supply the reactive power at the PCC bus, e.g., the ac filters and fixed shunt capacitors [6]:

$$SCR = \frac{{V_{l-l\,N}}^2 \left| G_{sys} + G_q \right|}{P_{dcN}} \qquad (6.1b)$$

As the indices only consider fundamental frequency, they naturally cannot account for or parameterize the system behavior at other frequencies.

In the multi-infeed systems, i.e., where there are multiple converters in close proximity, the ESCR was generalized to the "Multi-Infeed Effective Short Circuit Ratio (MIESCR)" based either on the system node admittance matrix, or the voltage interaction level between different PCC buses quantified as the Multi-Infeed Interaction Factor (MIIF) [18-23]. A recent approach made use of the ac side power flow Jacobian matrix as the determination matrix, and defined the smallest eigenvalue of this matrix as the Generalized Short Circuit Ratio (GSCR) [88].

The above indices were frequently used for LCC based system with any rectifiers operating in the constant power control mode. For the standard First CIGRE benchmark system, if the rectifier controls constant active power, the system becomes marginal stable as the SCR is reduced to the neighborhood of 2.06. This value is also defined as the “Critical Short Circuit Ratio (CSCR)”. If the SCR of one ac system is much larger than CSCR, e.g., 2.5, then the ac system was deemed to be ‘strong’ and be recommended for the converter connecting [6].

However, the application of this criterion (by comparing the SCR to the CSCR) to quantify the system strength can be challenging when the LCC operates under a different controlling algorithm, e.g., control a constant dc current. Also, when the converters use VSC technology, the CSCR is closer to 1.3 for a typical system configuration [43]. This critical value is also dependent on the gain of the controllers, such as the PLL.

As concluded above, the traditional indices show their drawbacks: they do not identify the system behavior at sub-synchronous and super-synchronous frequency ranges; and fail to distinguish the difference between different type of converters, e.g., LCC and VSC. As diverse power electronic facilities are introduced to the modern power system, the traditional indices are no longer sufficient to address the system characteristics.

Hence, a new index, ‘Harmonic Stability Margin’ (HSM) is introduced to investigate the ac-dc system interaction problems in the following section.

6.2 Harmonic Stability Margin (HSM)

The studied ac-dc system is divided into two parts – a) the ac subsystem and b) the dc subsystem. The boundary of the two subsystems is the PCC bus. As explained in the previous chapters, the analytical modelling and the frequency scanning are the two approaches to obtain the impedance responses of subsystems.

For the dc side, the VSC model [43] is shown in Chapter 4, and the LCC model is improved in Chapter 5. The model of the MMC, although not presented in this thesis, can be referred to in [78][79]. These analytical forms make the frequency response of converters easily obtainable for different parameter sets, e.g., the controller parameters. The ac side subsystems can be modeled analytically for simple configurations, e.g., as shown in Section 5.4.1. Sometimes the s-domain transfer functions are not available for ac or dc sides, e.g., when 'black boxed' controllers or network segments are present, or the system includes distributed parameter elements such as cables or overhead lines. Under this circumstance, the frequency scanning, is used to get the frequency response, e.g., as we did for the IEEE 14-bus system in Section 5.4.2.

6.2.1 The closed loop representation of ac-dc system

The ac and dc subsystems can be represented as transfer functions (or impedance responses) relating the currents to the voltages in the dq0 domain as $\mathbf{Z}_{ac}(s)$ (or $\mathbf{Z}_{ac}(f)$)

in (6.2) and as $\mathbf{Z_{dc}}(\boldsymbol{s})$ (or $\mathbf{Z_{dc}}(\boldsymbol{f})$) in (6.3). The zero sequence is usually neglected as the zero-sequence component cannot flow into the dc side system.

$$\mathbf{Z_{ac}}(\boldsymbol{s}) = \begin{bmatrix} \mathrm{Z}_{acdd}(s) & \mathrm{Z}_{acdq}(s) \\ \mathrm{Z}_{acqd}(s) & \mathrm{Z}_{acqq}(s) \end{bmatrix} \tag{6.2}$$

$$\mathbf{Z_{dc}}(\boldsymbol{s}) = \begin{bmatrix} \mathrm{Z}_{dcdd}(s) & \mathrm{Z}_{dcdq}(s) \\ \mathrm{Z}_{dcqd}(s) & \mathrm{Z}_{dcqq}(s) \end{bmatrix} \tag{6.3}$$

The model of ac-dc system is represented as in Fig. 6-1a and its closed loop block diagram as in Fig. 6-1b. As the impedance responses in (6.2) and (6.3) are available either as a frequency response or as an analytical transfer function, the Generalized Nyquist stability Criterion (GNC) can be applied. It is more versatile compared to the state space analysis, as it can handle the 'black-boxed' system representations.

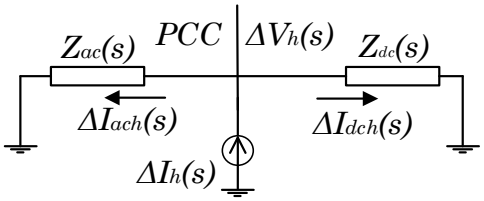

1a) Impedance model of the system

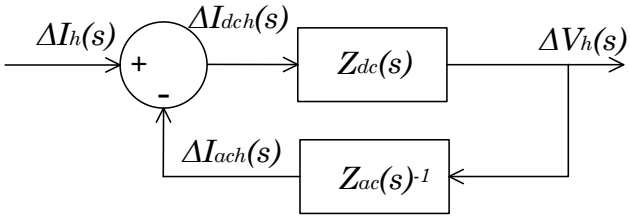

1b) Control block

Figure 6-1. The closed loop system representation of the ac-dc system

6.2.2 Harmonic Stability Margin (HSM)

The loop gain transfer matrix and its eigenvalues in Fig. 6-1 can be given as (6.4) and (6.5). From this, the Nyquist eigenvalue loci 1 can be plotted as a function of frequency.

$$\boldsymbol{H_{cl}(s) = Z_{dc}(s) Z_{ac}(s)^{-1}} \tag{6.4}$$

$$\boldsymbol{\lambda_i(s) = eig[H_{cl}(s)]} \tag{6.5}$$

Two assumptions are made here:

Assumption I: When the ac and dc subsystems are disconnected, the two subsystems are individually stable at the designated operating point.

Assumption II: Let a scalar $K_z \in (0, \infty)$ *be multiplied to the ac impedance matrix* $\boldsymbol{Z_{ac}(s)}$ *to represent an ac system with variable strength. Then the system could become unstable within some range of values* K_z.

If at least one of the eigenloci[1] encircles the (-1+j0) point in a clockwise manner as the frequency goes from $-\infty$ to $+\infty$, the system would be determined as unstable

[1] The eigenloci mentioned here, and in the below sections, are for the eigenvalue of the (open) loop gain matrix. Please note that, it is different from the eigenvalue root locus of a system which is represented as a state space form.

[63][64][89]. Based on this statement, the index HSM is proposed as follows.

If the area in the complex plane encircled by the contour in the clockwise direction is defined as $\mathcal{S}$, and c is any negative real point in the area $\mathcal{S}$, the HSM is defined as:

$$HSM = -max\{c|c \in \mathcal{R}, c \in \mathcal{S}\} \tag{6.6}$$

Thus, the *HSM* is the negative of point c in $\mathcal{S}$ which lies on the negative real axis and has the smallest magnitude. The corresponding frequency at this point is defined as the characteristic frequency f_{HSM}. Fig. 6-2 shows an example explaining the definition. The shaded area is $\mathcal{S}$ (it is the exterior due to the clockwise encirclement requirement). Candidate values for c are indicated by the red line. The HSM value is 1.22 (as -1.22 is the largest value of c) and the characteristic frequency f_{HSM} is 2.75Hz.

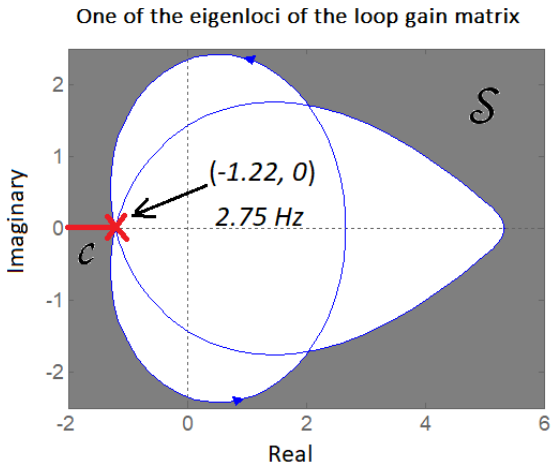

Figure 6-2. An example of the eigenlocus of the loop gain and the definition of *HSM* and f_{HSM}

An HSM value of 1.0 would mean that the locus is on the verge of encircling the (-1+j0) point, i.e., the system is on the verge of instability. Hence, the condition '$HSM < 1$'

indicates an unstable system; '$HSM > 1$' means stable; and how large HSM is compared to unity can be used as a measure of relative stability.

If the loop gain transfer matrix is of dimension N x N (i.e., a multi input – multi output system) there would be N eigenvalue loci resulting in N values, i.e., HSM_i $(i = 1, \dots N)$. The smallest value in this set is then chosen as the final HSM value, and f_{HSM} is the corresponding frequency.

6.2.3 Relationship between the HSM and the traditional SCR

The traditional definition of SCR only takes fundamental frequency impedance into account, and this permits the evaluation of power-voltage instability [6, 16-18]. However, two ac networks can have the same fundamental frequency impedance, but vastly different values at other frequencies. In contrast, the HSM considers the frequency dependent impedance responses of both sides and accurately determine stability margins for different system and converter configurations.

Now consider the case of *a given ac network* whose SCR is SCR_1. A typical eigenvalue locus for such a system is shown Fig. 6-3. First consider the blue curve which is drawn for the original ac system whose short circuit ratio is SCR_1 $(SCR_1 = 4.14)$. In this case the system is stable as there is no clockwise encirclement of the (-1, 0) point, and the closest point of approach, i.e., $HSM = -x$, where $x = -1.27$. However, it is easy to show that if the SCR_1 decreases by a factor y (with a scaling of the network impedance to

$y\boldsymbol{Z_{ac}}(\boldsymbol{f})$), the eigenvalue locus shifts to the red curve in Fig. 6-3. The loop gain transfer matrix is changed from $\boldsymbol{Z_{dc}}(\boldsymbol{f})\boldsymbol{Z_{ac}}(\boldsymbol{f})^{-1}$ to $y\boldsymbol{Z_{dc}}(\boldsymbol{f})\boldsymbol{Z_{ac}}(\boldsymbol{f})^{-1}$ after the scaling, and the eigenvalues of the matrix changed from $\boldsymbol{\lambda_i}(\boldsymbol{f})$ to $y\boldsymbol{\lambda_i}(\boldsymbol{f})$. Consequently, the original blue color eigenloci shrinks proportionally to the new (red) curve. Hence, the location of the intersection of the eigenvalue locus with the real axis becomes $-x/y$.This means that if the SCR is reduced by a factor $y = x$, the system would be on the verge of instability.

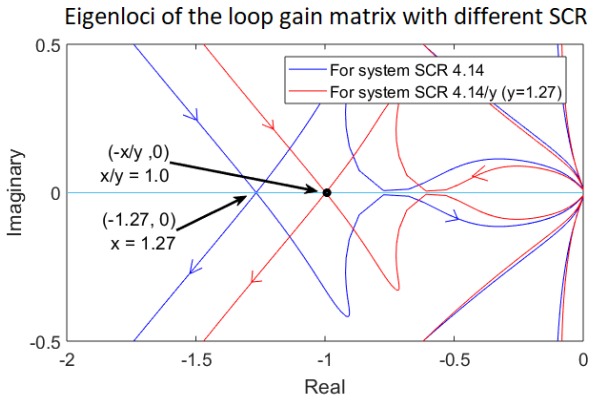

Figure 6-3. Relationship between eigenloci of the loop gain matrix / *HSM* and the value of *SCR*

Interestingly, this means that for any value of SCR_1 and corresponding HSM_1, it becomes immediately evident that the critical value of SCR ($CSCR_h$) which will make the system marginally stable is decided as a constant value:

$$CSCR_h = \frac{SCR_1}{HSM_1} \tag{6.7}$$

Thus, *for a given ac network*, there is a proportional relationship between HSM and SCR when the impedance matrix is scalarly changed (as $CSCR_h$ is a constant value):

$$HSM = SCR/CSCR_h \tag{6.8}$$

The HSM versus SCR relationship for one system, i.e., the same system whose eigenloci of the loop gain was plotted in Fig. 6-3, is presented in the following Fig. 6-4. This figure clearly shows the proportional relationship between HSM and SCR when the SCR is adjusted by scaling the system impedance. However, please note that if the same SCR is achieved with a different impedance topology, a different value of HSM will be obtained. This is further discussed in Section 6.4.4.

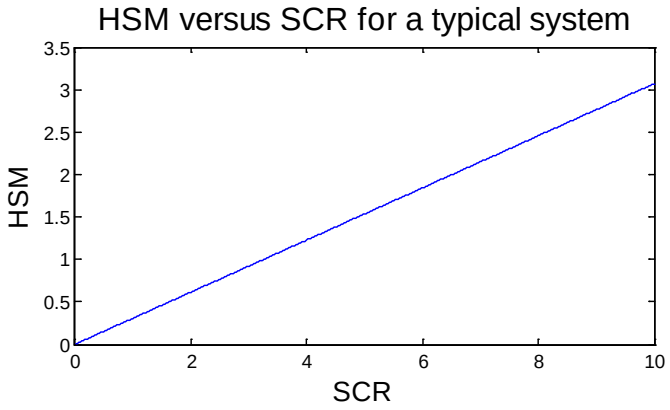

Figure 6-4. The proportional relationship between HSM and SCR for a typical system

6.2.4 Relationship between HSM and dc rated power

The loop gain transfer matrix and the resulting obtained HSM are not only functions of the ac side impedance matrix $\boldsymbol{Z_{ac}(f)}$, but also of the dc side impedance matrix $\boldsymbol{Z_{dc}(f)}$. In the system planning of converter connecting to ac system, the dc rated power has scalar influence on the dc side impedance matrix $\boldsymbol{Z_{dc}(f)}$, as the per unit impedance response $\boldsymbol{Z_{dc,pu}(f)}$ of the converter side system is essentially the same for different rated power values, i.e., $\boldsymbol{Z_{dc}(f)} = \boldsymbol{Z_{dc,pu}(f)} * Z_{base}$. Here, the base impedance Z_{base} is only decided by the rated voltage V and rated power P_{dcN} as V^2/P_{dcN}. In other words, the increase of

the dc rated power by a value y results in a scalar decrease of the dc side impedance $\boldsymbol{Z_{dc}(f)}$ to $\boldsymbol{Z_{dc}(f)/y}$. This is equivalent to a proportional increase of the ac side impedance matrix from $\boldsymbol{Z_{ac}(f)}$ to $\boldsymbol{yZ_{ac}(f)}$.

Hence, similar to (6.7) and (6.8), the HSM has inverse proportional relationship with dc rated power P_{dcN} as in (6.9). Due to the proportional relationships, the maximum possible dc rated power value P_{dc_max} that would result in marginal stability can be determined as in (6.10).

$$HSM \propto \frac{1}{P_{dcN}} \tag{6.9}$$

$$P_{dc\_max} = P_{dcN} * HSM \tag{6.10}$$

6.2.5 Application in the multi-infeed system

The application of HSM on the multi-infeed system is quite straightforward. The impedance response of the ac network can be obtained from scanning or analytical modelling as a multi-port matrix in the dq domain. The frequency response of each of the dc converters, $\boldsymbol{Z_{dcj}}$ for jth converter, is a 2 x 2 matrix as the voltage and current each have a d- and a q- component. Hence, the dc impedance matrix is block diagonal (with 2 x2 dimensioned blocks) of overall dimension $2N$ x $2N$ dimensional (for N HVdc links). As the conversion buses of the converters are connected together, the ac impedance matrix is also of dimension $2N$ x $2N$ but is not block diagonal as all the converter buses are interconnected. The loop gain transfer matrix can be calculated as:

$$\boldsymbol{H_{cl}(s)} = \underbrace{\begin{bmatrix} \boldsymbol{Z_{dc1}} & \boldsymbol{0} & \boldsymbol{0} & \boldsymbol{0} \\ \boldsymbol{0} & \boldsymbol{Z_{dc2}} & \boldsymbol{0} & \boldsymbol{0} \\ \boldsymbol{0} & \boldsymbol{0} & \boldsymbol{\ddots} & \boldsymbol{0} \\ \boldsymbol{0} & \boldsymbol{0} & \boldsymbol{0} & \boldsymbol{Z_{dcN}} \end{bmatrix}}_{dc\ impedance\ matrix} \underbrace{\begin{bmatrix} \boldsymbol{Z_{11}} & \boldsymbol{Z_{12}} & \boldsymbol{\dots} & \boldsymbol{Z_{1N}} \\ \boldsymbol{Z_{21}} & \boldsymbol{Z_{22}} & \boldsymbol{\dots} & \boldsymbol{Z_{2N}} \\ \boldsymbol{\dots} & \boldsymbol{\dots} & \boldsymbol{\ddots} & \boldsymbol{\dots} \\ \boldsymbol{Z_{N1}} & \boldsymbol{Z_{N2}} & \boldsymbol{\dots} & \boldsymbol{Z_{NN}} \end{bmatrix}^{-1}}_{ac\ impedance\ matrix} \tag{6.11}$$

Where, $\boldsymbol{Z_{ij}}$ is the ac impedance matrix elements. With this loop gain transfer matrix, HSM can be calculated using the same procedure as for the single infeed system to indicate the ac system strength. If we are only interested in part of the converters rather than all of them, the impedance responses of the converters not interested can be combined with the ac network impedance responses using size reduction technique, similar as in [24].

6.3 Application of the HSM on SSCI studies

In this section, the Sub-Synchronous Control Interaction (SSCI) phenomenon is studied in the case system of an LCC rectifier connected to the ideal voltage source through the series compensated transmission system. The electrical system and the control system are shown as in Fig. 6-5 and Fig. 6-6. By definition [87, 90-93], SSCI refers to the fact that the control interactions are at sub-synchronous frequency. It is different from the sub-synchronous torsional oscillation phenomenon and may or may not involve the rotor shaft dynamics explicitly.

In the ac side, distributed element model is used for the long line with the parameters given in Tab. 6-1, whose frequency response is obtained by the frequency scanning. The fundamental frequency impedance of the long line is $Z_{long} = 0.0498 + j0.4737$, and the series capacitor compensates 40% of the long line reactance.

Table 6-1. Parameters of the distributed transmission line

Parameters	***Value***	***Parameters***	***Value***
Line Length	*100kM*	*Resistance /m*	*4.5e-7 pu*
Steady State frequency	*50Hz*	*Inductance /m*	*4.5e-6 pu*
		*Capacitance *m*	*3e5 pu*

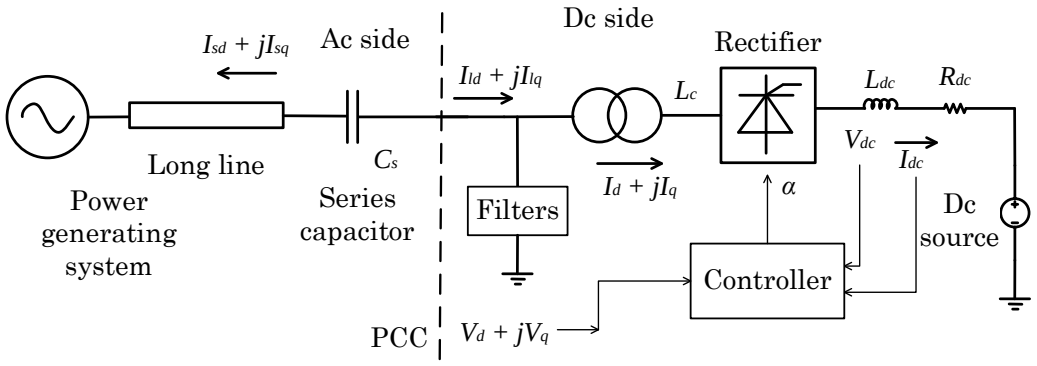

Figure 6-5. The electrical system configuration studying SSCI

On the dc side, an ideal dc voltage source is employed to model the inverter side of the HVdc project and connected to the rectifier via a series $R_{dc} - L_{dc}$ branch. The parameters of the dc circuit as well as the shunt filters at the PCC bus are the same as the First CIGRE benchmark model [53]. The controller of the converter includes a Phase Locked Loop (PLL) and a Constant Dc Current controller (CDC). All related parameters are given in Tab. 6-2. For the eigenvalue plots, the relative ratio of the Proportional and the Integral (PI) gains of the CDC is kept the same, and the single multiplier K_{PLL} or K_{CDC} is varied.

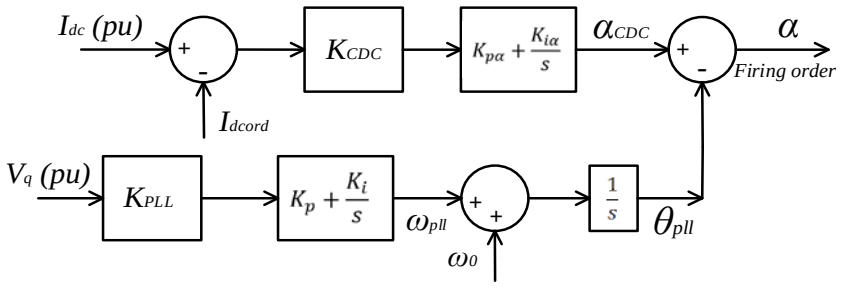

Figure 6-6. The control blocks of the rectifier

Table 6-2. Related parameters for the dc side system

Parameters	***Value***	***Parameters***	***Value***
K_p	*40*	*Transformer Inductance*	*0.18 pu*
K_i	*100*	*Transformer rate*	*597.68Mvar*
$K_{p\alpha}$	*100*	*Transformer Number*	*2*
$K_{i\alpha}$	*100*	*Converter Number*	*2*
K_{CDC}	*1 (nominal)**	K_{PLL}	*1 (nominal)**
R_{dc}	*2.5 ohm*	*L-L RMS voltage*	*345 kV*
L_{dc}	$0.5968H$		

** K_{CDC} and K_{PLL} are the root locus parameters but are nominally unity in the basic model.*

The dc side impedance response can be obtained from the analytical model of converter developed in Section 5.2 and the state equations of the other elements similarly as in Section 5.4.2. With the ac side impedance extracted from the frequency scanning, the value of HSM can be studied as a function of the controller gains to parameterize the SSCI level.

6.3.1 HSM as a function of the CDC gain

The variation of HSM as a function of K_{CDC} (shown in Fig. 6-6) is plotted as in Fig. 6-7.

The value of HSM is critically at unity when $K_{CDC} = 2.6$, and the corresponding oscillation frequency $f_{SCF} = 64.5Hz$. The increase of the CDC gain worsens the system stability, as the HSM decreases below unity.

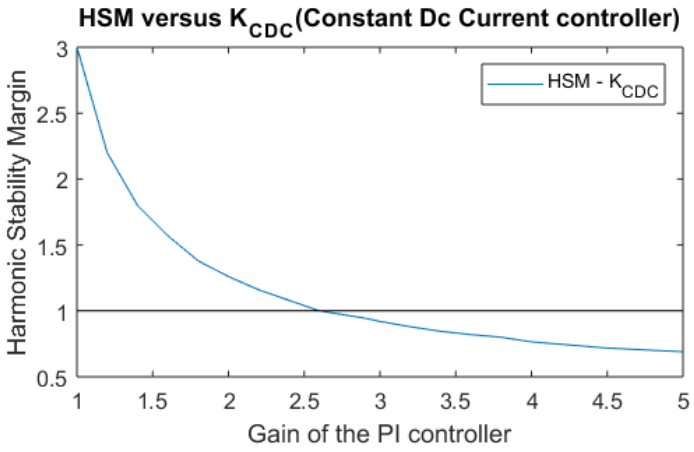

Figure 6-7. *HSM* as a function of K_{CDC}

This result is validated by an EMT simulation. Fig. 6-8 shows the output of the CDC (in degrees) in the simulation, that the system at first operates stably when the value of K_{PLL} is 2.4, however after t = 10.0s the K_{PLL} value is changed to 2.6, the system becomes unstable. The resonance frequency of the unstable system is $1/0.0155s = 64.52\,Hz$, which is very close to the f_{SCF} value obtained analytically (64.5Hz).

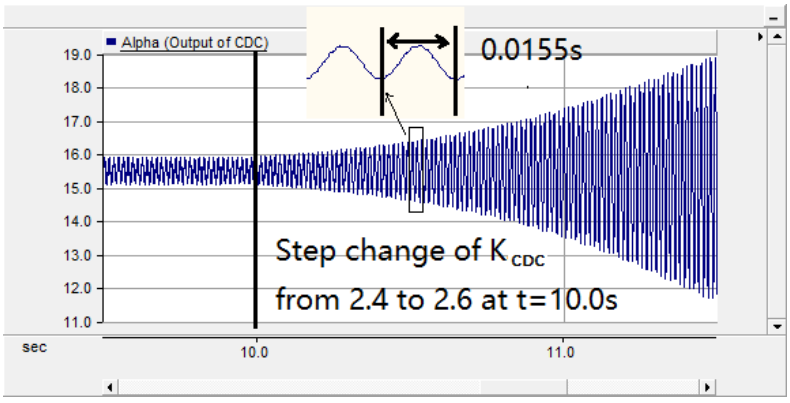

Figure 6-8. Output angle of CDC validating the critical value of K_{CDC}

6.3.2 HSM as a function of the PLL gain

The variation of HSM as a function of K_{PLL} (shown in Fig. 6-6) is plotted in Fig. 6-9. It is shown that the increase of PLL gain strengthens the system stability, which is different from that resulting from the increase of CDC gain reported in Section 6.3.1. The system remains stable for all values of K_{PLL} (from 1.0 to 3.0) and in fact the stability margin increases as K_{PLL} is increased. This is also confirmed by EMT simulation as in Fig. 6-10, which shows the simulated output of the PLL (in degrees), for a step change in K_{PLL} from 1.0 to 10.0. The simulation remains stable, though because of the increased proportional gain, the ripple increases.

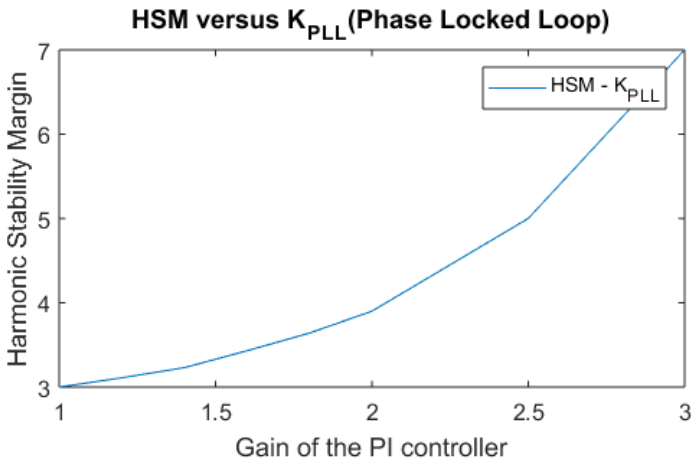

Figure 6-9. *HSM* as a function of K_{PLL}

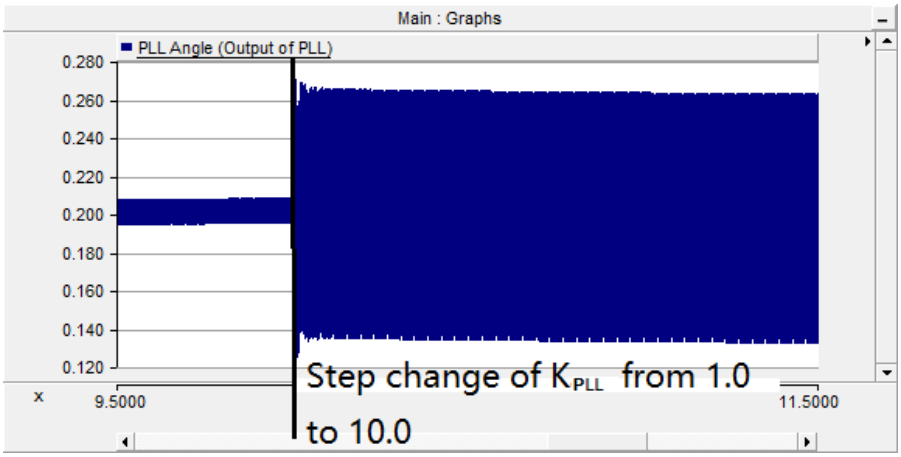

Figure 6-10. Output angle of PLL with the step change of K_{PLL} to 10.0

6.4 Impact of detailed modelling of the remote side (rectifier) converter and ac system

Consider the investigation of the stability of a system studied from the inverter side. Assuming the rectifier side is in current control, one possibility is to model the rectifier as an ideal source [17], e.g., a current source of value equal to the current order as shown in Fig 6-11a. A similar simplification was also made in Section 6.3, where we were investigating the rectifier side and had represented the inverter side as a constant dc voltage source. It has been questioned whether this simplification is still sufficiently accurate or whether it is necessary to fully model the remote (rectifier) side converter as in Fig. 6-11b to accurately determine the system stability.

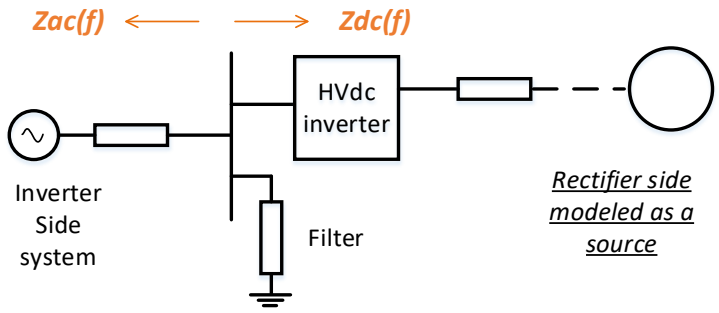

a) Simplified representation:
Rectifier side modeled as a source

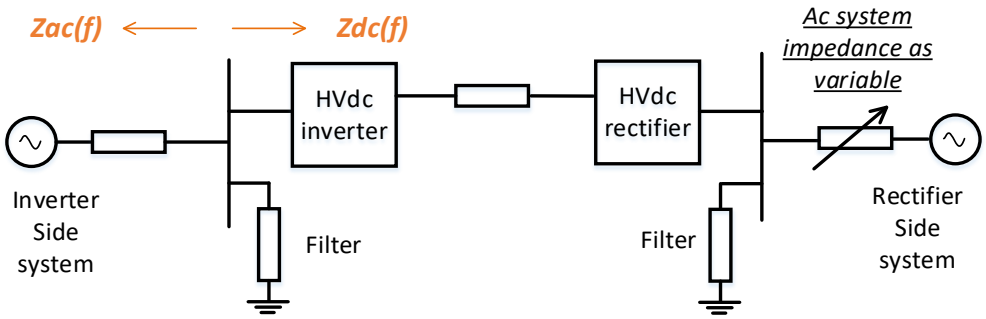

b) Full representation:
Rectifier side modeled in detail, ac system impedance changing

Figure 6-11. Two representations of HVdc system: simplified, and in detail

To answer this question, the HSM is investigated as a function of the remote (rectifier) side configurations, considering a simplified current source representation as in Fig. 6-11a, and a detailed representation of the rectifier side in Fig. 6-11b. The HVdc converter can be either an LCC or a VSC. The impedance of the dc system looking from inverter PCC bus, $\boldsymbol{Z_{dc}}$, is the forward gain in the closed-loop representation as in Fig. 6-1, and the admittance of the inverter side ac system, $\boldsymbol{Z_{ac}}^{-1}$, is taken as the feedback. Then, the HSM can be obtained from the eigenloci plot of the loop gain transfer matrix $\boldsymbol{Z_{dc}Z_{ac}}^{-1}$. These impedance matrices are obtained from analytical models in this section, and can also be acquired from the frequency scanning, as in Section 5.4.2. Typically for a system with one

converter, the loop gain matrix will be of dimension 2 x 2 (i.e., L_{dd}, L_{dq}, L_{qd} and L_{qq}) and will have 2 eigenvalues at each frequency point. Note that these are *NOT* the eigenvalues of the system, which will be of a usually much larger dimension, and equal to the number of system state variables.

At first, the HSM is obtained for the system in Fig. 6-11a, where the rectifier is simplified as an ideal source depending on its controlling algorithm. For example, if the converter uses a constant dc current controller, then a constant dc current source is employed. Let us mark the HSM value as HSM_{simp}.

Then the rectifier side system is modeled in detail, as in Fig. 6-11b, and the HSM (referred to as HSM_{detail}) is a function of the rectifier side ac system strength, i.e., SCR_{rec}. By comparing the value of HSM_{sim} and the $HSM_{detail} - SCR_{rec}$ curve, the influence of the remote side configuration on the system stability can be investigated.

The following studies include both the LCC and VSC system, with different control algorithms considered below. First, a simulation-based approach is proposed below to obtain the HSM from EMT simulation; and then the HSM values are observed from the GNC. These two results can validate each other.

6.4.1 The simulation-based approach to get HSM point by point in simulation

In Section 6.3, after the HSM was obtained as a function of a specific controller gain, EMT

simulation was used to validate the result. The controller gain was slowly increased to find the critical value making the system marginally stable. If a growing oscillation only starts when the controller gain is increased to the critical value where *HSM = 1.0*, then the HSM concept is validated.

To accurately validate the $HSM_{detail} - SCR_{rec}$ curve point by point (also the HSM_{simp} with rectifier modeled as a source), the technique below is applied in EMT simulations. First, the *HSM* at the original system configuration is calculated. Let us call this HSM_1. As explained in Section 6.2.3, if the ac system impedance matrix is scaled by a factor y, there is a decrease of the HSM to HSM_1/y. Assuming only RLC elements in the ac system, if the values of the 'R' and 'L' are increased by $y = HSM_1$, and the values of 'C' reduced by y, then the *HSM* of the new system should be exactly 1.0 resulting continuous oscillation.

One problem of this validation process is that, changing the values of 'RLC' on-line is a large disturbance on the system. To prevent this, a special algorithm is introduced below to start up the system by pre-setting the operating point with the assistance of a supporting ideal voltage source connected to the PCC bus, as in Fig. 6-12.

At first the breaker in Fig. 6-12 is closed. With the 'Ideal Source' forcing the PCC voltage as $V_d = 1.0\,pu$ and $V_q = 0.0\,pu$ (which is a typical voltage status), the system actually operates as two open loop subsystems, i.e., the ac side and the dc side. To set the desired operating point fulfilling the power flow, e.g., from the ac source to the PCC bus as $P_0 + jQ_0$, the d- and q- axis voltages of the non-ideal ac source can be calculated as:

$$\begin{cases} I_{sd} + jI_{sq} = P_0 + jQ_0 + j\omega_0 C_f \\ E_{sd} + jE_{sq} = V_d + jV_q + Z_s(I_{sd} + jI_{sq}) \end{cases} \tag{6.12}$$

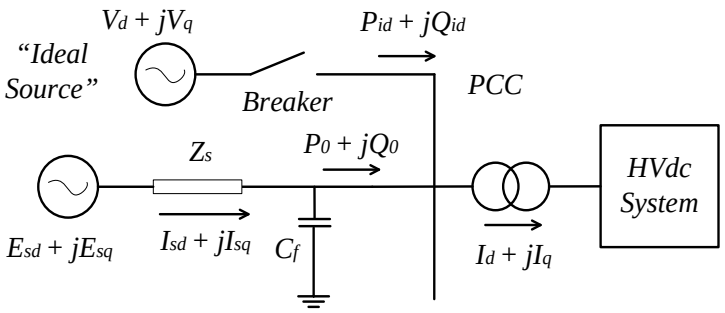

Figure 6-12. Starting up algorithm to set the desired operating point

where, Z_s is the fundamental frequency impedance of the ac system. With properly selected initial conditions, the ac system reaches a steady state power level of $P_0 + jQ_0$, and the real and reactive power output of the "ideal" source become zero. At this time, the breaker may be opened, and the ac network supplies the HVDC converter's real and reactive powers. As there is no longer voltage support, the ac and dc subsystems are inter-connected, and the loop is closed. The critical value of *HSM* can be precisely identified by slowly changing the factor y, starting up the system from the operating point and observing if there are continuous oscillation.

Using this algorithm, the *HSM* as a function of the rectifier side configuration can be obtained point by point from the simulation and be compared with the result from GNC.

6.4.2 HSM as a function of remote converter parameters for LCC systems

If the systems in Fig. 6-11 are considered to have LCC converters, the HVDC system is as in the configuration of the First CIGRE benchmark model [53]. The network parameters are given in Fig. D-1 and Table D-1, Appendix D. The dc circuit and the ac filters are the same as the benchmark model. The 'R' and 'L' values of the inverter system are reduced to half of the original values which increases the inverter side SCR_{inv} equal to 5.0 (from 2.5 in the original system); the SCR of the rectifier side SCR_{rec} is a variable and changed by means of multiplying the 'R' and 'L' values with the scale factor.

One may think that SCR_{inv} is a rather large value. This is purposely done to ensure stable operation. One of the advantages of the HSM approach is that the critical SCR can be determined from GNC analysis from any single stable simulation. For example, if we determine the *HSM* as 2.37 with $SCR_{inv} = 5$, it means instability will occur if SCR_{inv} is reduced to 5/2.37 = 2.11.

In the inverter side, there is a PLL and a constant extinction angle controller as in Fig. 5-12. There are two scenarios for the rectifier controller which are considered below separately, as in Fig. 6-13. The control includes a PLL and a PI controller whose input can be switched to either dc current error signal or dc power error. The parameters of the controllers are given in Appendix D.

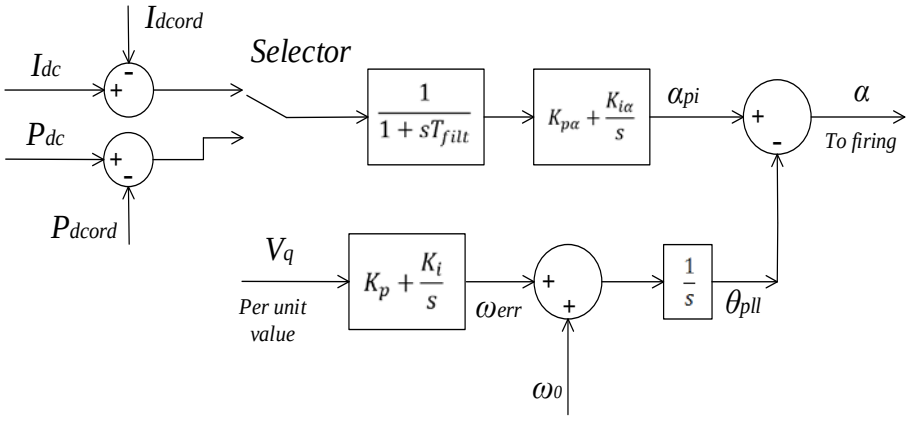

Figure 6-13. Configuration of the rectifier side controller

The impedance matrix $Z_{ac,LCC}$ for the inverter ac system can be easily obtained in the dq domain for the R_1-L_1-($(R_2$-$L_2)//R_3$) circuit [42][43]:

$$Z_{ac,LCC}(\mathrm{s}) = \begin{bmatrix} sL_1+R_1 & -\omega_0 L_1 \\ \omega_0 L_1 & sL_1+R_1 \end{bmatrix} + \left\{ \begin{bmatrix} sL_2+R_2 & -\omega_0 L_2 \\ \omega_0 L_2 & sL_2+R_3 \end{bmatrix}^{-1} + \begin{bmatrix} R_3 & 0 \\ 0 & R_3 \end{bmatrix}^{-1} \right\}^{-1} \quad (6.13)$$

To get $Z_{dc,LCC}$, which is the impedance of the dc side looking from the inverter PCC bus, the state equations representing the system are obtained as the form below:

$$\begin{cases} s\Delta X = A_0\Delta X + e^{-sT_1}A_1\Delta X + B_{LCC}[\Delta I_{sd} \quad \Delta I_{sq}]^T \\ \begin{bmatrix} \Delta V_d \\ \Delta V_q \end{bmatrix} = C_{LCC}\Delta X + D_{LCC}[\Delta I_{sd} \quad \Delta I_{sq}]^T \end{cases} \quad (6.14)$$

The details of how to get the state equations are given as in Appendix D. Hence the dc side impedance matrix is:

$$Z_{dc,LCC}(\mathrm{s}) = C_{LCC}[sI - A_0 - e^{-sT_1}A_1]^{-1}B_{LCC} + D_{LCC} \quad (6.15)$$

With $Z_{ac,LCC}$ and $Z_{dc,LCC}$ obtained, the HSM can be observed from the GNC.

As mentioned above, the LCC rectifier has one of two commonly used controller modes: Constant Dc Current (CDC) control and the Constant Power (CP) control. They have

different behaviors and are studied separately as two scenarios below.

Scenario I: The rectifier controls the dc current (Constant Dc Current controller - CDC).

If the converter is modeled in full detail, GNC analysis shows that the *HSM* becomes a function of the SCR of the rectifier side ac system, i.e., SCR_{rec}. The HSM_{detail} versus SCR_{rec} plot is shown as in Fig. 6-14 for the results obtained from both GNC and EMT simulation. The curve 'GNC' is the result obtained from GNC; 'PSCAD' is the result from EMT simulation using the PSCAD/EMTDC program. Even when SCR_{rec} is quite small, e.g., 1.2, the system can still be stable. Contrary to expectation, the increase of SCR_{rec} reduces the *HSM* when $SCR_{rec} > 2.0$. EMT simulation is in close agreement as shown by the '*' signs in the figure. Also, as the SCR increases asymptotically, the HSM approaches 2.37.

On the other hand, if the rectifier side is simplified and modeled as a constant dc current source (as in Fig. 6-11a), GNC analysis (confirmed by EMT analysis) gives the value of *HSM* as 2.37, i.e., the value obtained from the detailed model for $SCR_{rec} \rightarrow \infty$. Hence, simplifying the remote converter to a current source as was done in Section 5.4 is only valid for large SCR_{rec} values. The *HSM* of 2.37 implies that the system will be unstable if SCR_{inv} is reduced to 5/2.37 = 2.11, as in the experiment we used an SCR_{inv} of 5.0. As the reactive power from the filters is 0.5 x the dc power, this corresponds to an effective short circuit ratio of 1.61.

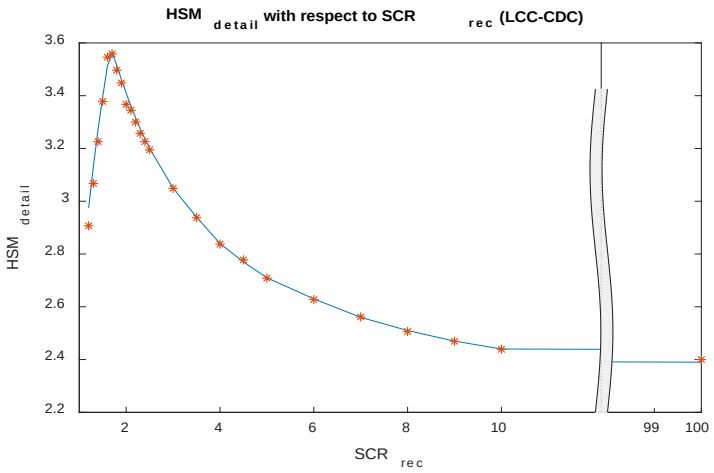

Figure 6-14. HSM_{detail} as a function of SCR_{rec} (with CDC controller in rectifier)

Scenario II: The rectifier controls the dc power (Constant Power control - CP).

Consider first, the case when the converter is modeled in full detail. The corresponding plot of the *HSM* as a function of rectifier ac side SCR (HSM_{detail} versus SCR_{rec}) is shown in Fig. 6-15. Increase of the rectifier side SCR (SCR_{rec}) reduces HSM_{detail}, and its decrease increases HSM_{detail}, but only up to a point! Reducing SCR_{rec} below 2.1 makes the encirclement of the (-1, 0) becomes clockwise, and the system becomes unstable due to HSM having a jump to 0. This can be attributed to an onset of classical voltage instability. At $SCR_{rec} = 2.1$, the converter is operating at the right side of the peak point in the $P_{dc} - I_{dc}$ curve of Fig. 1-1 and increasing the dc current results in a decrease of the transmitted active power. Then regardless how we increase the inverter system strength, the system is unstable, i.e., HSM = 0.

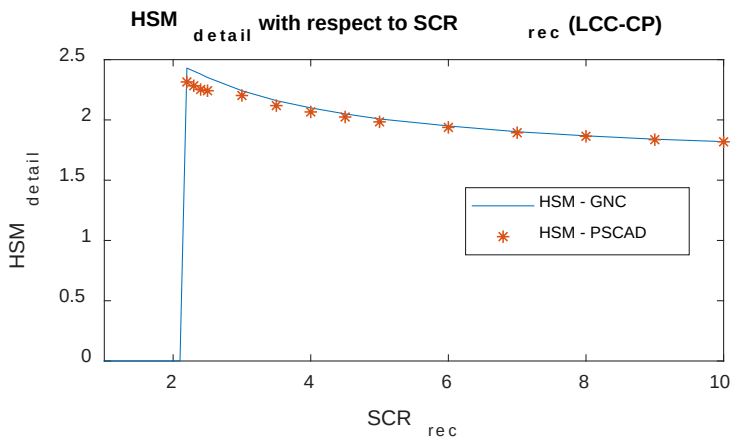

Figure 6-15. HSM_{detail} as a function of SCR_{rec} (with CP controller in rectifier)

Seen from Fig. 6-15, the system strength of the rectifier side has a moderate influence on the inverter side HSM, as (in the stable region), the SCR_{rec} varies between 2.42 and 1.82. Generally, a stronger rectifier side ac system makes the value of HSM smaller, i.e., the critical inverter side SCR to be larger, which is a surprising conclusion.

If on the other hand, we consider a simplified representation of the rectifier side In which the rectifier side is simplified to controlled dc current source of value $I_{dcs} = P_{order}/V_{dc}$ (where V_{dc} is the measured dc voltage at the current source, and P_{order} is power order provided by the control system). The HSM is found to be 2.43, (also confirmed by EMT simulation), which means that for the onset of instability SCR_{inv} should be below 5/2.43 = 2.06. Thus, simplifying the remote converter gives a more optimistic HSM value in comparison to the [1.82, 2.42] range observed with the detailed model.

6.4.3 HSM for VSC based HVdc systems

Here the systems in Fig. 6-11 are considered to have VSC converters. The system configuration, as well as the parameters are given in Appendix D. The inverter side system is modeled as an R-L series circuit whose SCR is 5.0; the rectifier side system is also an R-L circuit whose SCR is a parameter to be adjusted. Both rectifier and inverter use a decoupled controller [42][43] and shown in Fig. 6-16. Variable *I* can be either dc voltage or active power; and variable *II* can be either PCC bus voltage or reactive power flowing into the converter.

The impedance matrix $Z_{ac,VSC}$ for the inverter ac system can be easily obtained [43] in the dq domain for the R_1-L_1 circuit as (6-16):

$$Z_{ac,VSC}(\mathrm{s}) = \begin{bmatrix} sL_1 + R_1 & -\omega_0 L_1 \\ \omega_0 L_1 & sL_1 + R_1 \end{bmatrix} \tag{6.16}$$

Similar steps as in Section 3.2 are used to get $Z_{dc,VSC}$ in analytical form [43][74], which is the impedance of the dc side looking from the inverter PCC bus, and can be given as the form in (6.17).

$$Z_{dc,VSC}(\mathrm{s}) = C_{VSC}[sI - A_{VSC}(s)]^{-1}B_{VSC} + D_{VSC} \tag{6.17}$$

With $Z_{ac,VSC}$ and $Z_{dc,VSC}$ obtained, the *HSM* can be observed from the GNC.

Two scenarios of controlling algorithms are considered below.

Scenario I: The rectifier controls dc voltage and PCC bus ac voltage, and the inverter controls active power and ac voltage.

When the converter is modeled in detail, the HSM_{detail} versus SCR_{rec} plot is given in Fig. 6-17, and shows negligible variation with SCR_{rec}, giving a value close to 16.2, which implies a surprisingly low critical inverter side SCR of $SCR_{inv} = 5/16.2 = 0.31$.

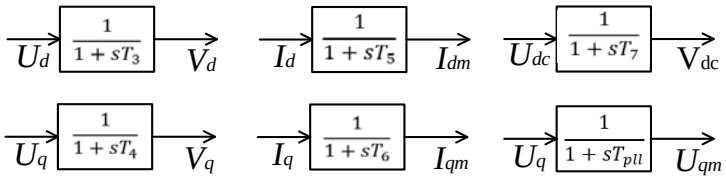

a. Measurement filter and per unit processing

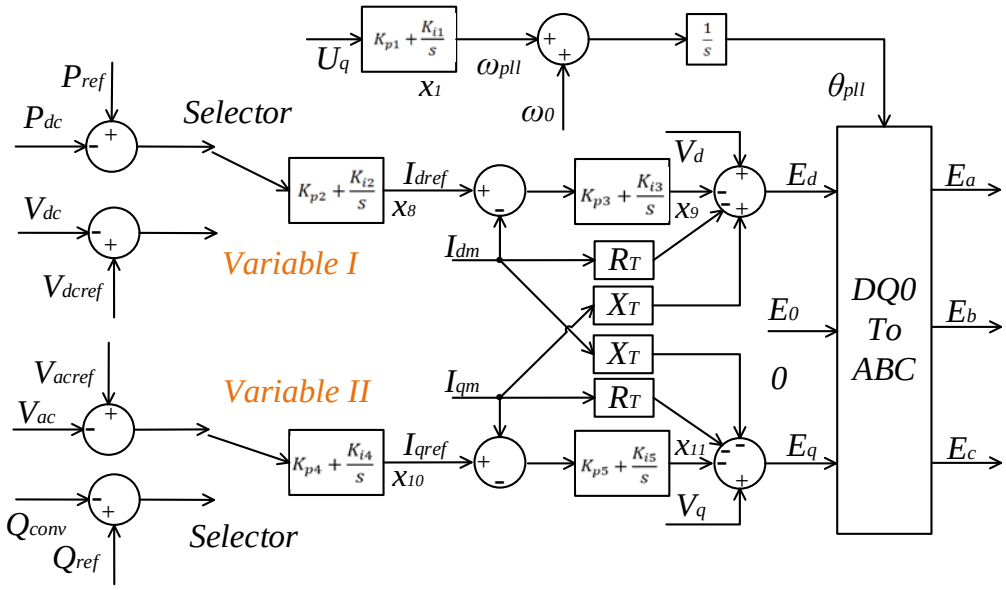

b. Decoupled controller logic

Figure 6-16. Decoupled controller with input variable selector

Also, from the figure, theoretical analysis (GNC) and EMT simulation show essentially identical results. The low value of critical SCR_{inv} appears to contradict earlier publications and will be discussed further later.

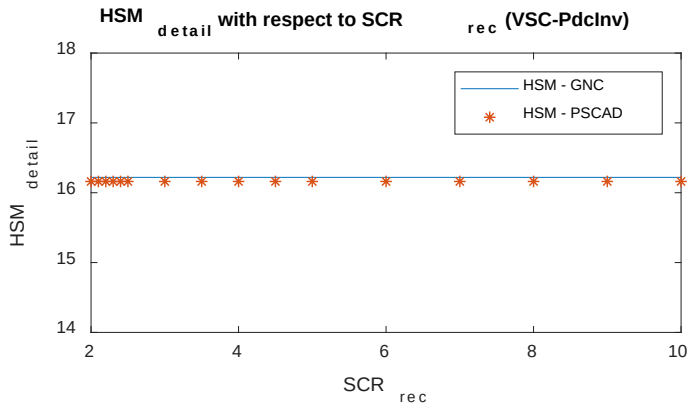

Figure 6-17. HSM_{detail} as a function of SCR_{rec} (inverter controls dc power and PCC voltage)

On the other hand, if the rectifier is simplified to a constant dc voltage source, the value of HSM_{simp} is 16.17, which is essentially the same as that obtained for the detailed model. Hence, the rectifier representation can be simplified to a constant voltage source for inverter side resonance studies.

Scenario II: The rectifier controls active power and ac voltage, and the inverter controls dc voltage and ac voltage.

When the converter is modeled in detail, the HSM_{detail} versus SCR_{rec} plot is shown as in Fig. 6-18, and the simulated (HSM - PSCAD) and calculated (HSM - GNC) are both

approximately 8.5. The values are close (within 3% difference). Also HSM_{detail} is a nearly constant value as a function of SCR_{rec}, i.e., the rectifier side ac system has very slight effect on stability of the system (as long as an operating point is feasible).

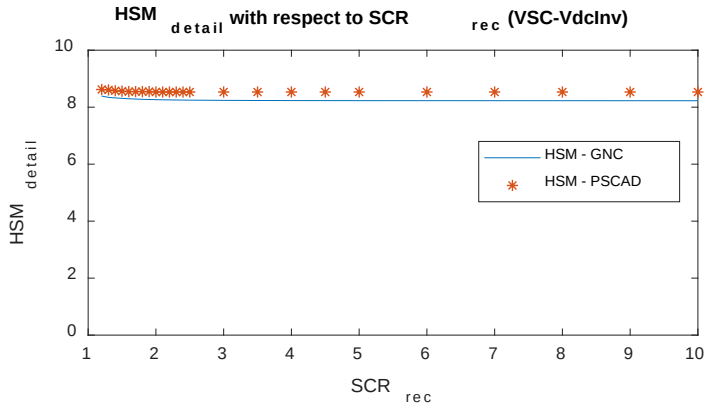

Figure 6-18. *HSM_{detail}* as a function of *SCR_{rec}* (inverter controls dc voltage and PCC voltage)

If the rectifier is modeled as constant power source that $V_{dcs} = P_{order}/I_{dc}$ (where, V_{dcs} is the voltage source magnitude, I_{dc}, the measured dc current of the source, P_{order}, power order provided by the control system), the HSM_{simp} is 9.65 (GNC and PSCAD give the same result). This corresponds to a $SCR_{inv} = 5/9.65 = 0.52$. As the detailed representation of the rectifier side gives an HSM closer to 8.5, it is advisable to include the detailed representation of the rectifier and its ac and dc sides in the model for better accuracy.

6.4.4 Comment on the network topology

Note that the actual topology of the inverter side Thevenin equivalent can affect the numerical *HSM* values calculated above. The studies here mainly consider scalar change

in the impedance matrix (for either ac side or dc side), and we had assumed a constant ac system configuration. If we have another topology with the same fundamental frequency impedance and SCR, the results will be different due to the different frequency response characteristics at frequencies other than fundamental. This is unlike the case of the traditional SCR, which only considers fundamental frequency impedance, and two distinct topologies with the same fundamental frequency impedance magnitude would have the same SCR, and thus the same voltage stability performance.

Consider the LCC based system in control Scenario I with current source representing the rectifier, as in Section 6.4.2. The value of *HSM* was shown as 2.37 (validated by simulation), and the characteristic frequency was $f_{HSM} = 35.0\ Hz$.

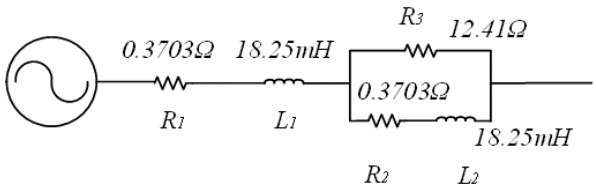

a) Original inverter ac network, SCR = 5.0

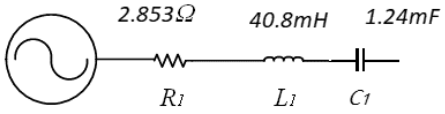

b) The R-L-C network used here, SCR = 5.0

Figure 6-19. Another ac system configuration used to get HSM

Here we build the ac circuit as an R_1-L_1-C_1 circuit in Fig. 6-19b instead of the original R_1-L_1-$((R_2$-$L_2)//R_3)$ configuration in Fig. 6-19a. Properly setting the parameters, gives an SCR

= 5.0, and the impedance phase angle at the fundamental frequency (50 Hz) of 75 degrees, which are the same as those of the original circuit. Figure 6-20 shows the magnitude and the phase angle of the impedance for original CIGRE benchmark network and the R-L-C network.

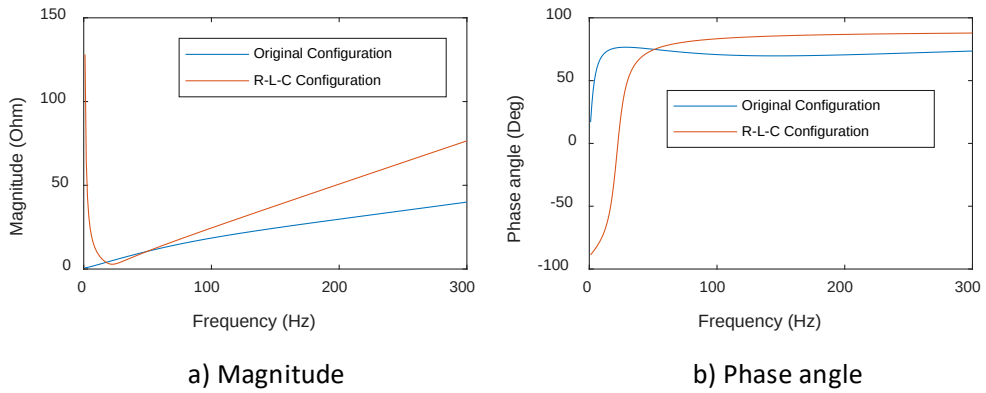

a) Magnitude b) Phase angle

Figure 6-20. Magnitude and phase angle of the original network and the new network

Using the GNC, we obtain the new *HSM* as 0.22 (resulting in a required CSCR of 5/0.22 = 22.7) for the configuration in Fig. 6-19b and new characteristic frequency $f_{HSM} = 155.6\ Hz$. This result is validated in EMT simulation, i.e., only when the SCR of the new system is increased to 23.0, the system can operate stably with an oscillation frequency 156 Hz.

The above conclusion is very surprising. As the SCR and the impedance angle at fundamental frequency are the same, the stability results are completely different. The old configuration is stable and has a CSCR of 2.1; the new one is unstable and has a CSCR of 23.0. Although the controller parameters can be optimized which results in closer stability result for the two configurations, i.e., closer *HSM* values. However, this case clearly shows that the network configuration can have a strong influence on the system stability margin.

6.4.5 Comment on the low SCR_{inv} values as compared with earlier publications

The conclusion in this subsection is based on the fact that the complex power flowing into the converter is constant. Consequently, the ac source Thevenin voltage can be high to fulfill the power flow equations when the fundamental impedance of the ac system is very large. But remember that the Thevenin source is a virtual source, so it could have any value. In some studies [43], the magnitude of the ac source voltage is kept constant, and the power flow is dependent on the fundamental impedance. Hence, the results, i.e., Critical SCR values from those studies, are different from the one obtained in this work. However, it has to be specified, the dc side impedance is dependent on the power flow as the dc system is non-linear. And, assuming a constant power flow (resulting a constant dc side impedance response) brings great convenience to the calculation and validation of *HSM*.

6.5 Case study of applying HSM on an LCC-VSC dual infeed system

In this section, an LCC-VSC dual infeed system is presented to demonstrate the application of HSM to a multi-infeed system, and to investigate whether the stability margin of an LCC infeed system can be enhanced by the connection of a VSC converter.

The configuration of the system is given as in Fig. 6-21. The LCC-HVdc here is the same as in Section 6.4.2 (in per unit). The rectifier is modeled in detail as in Fig. 6-11b with $SCR_{rec} = 4.0$ and operates under constant dc current mode. The inverter is connected to

the ac system at Bus I.

The VSC inverter is connected to Bus II and controls the active power and the PCC bus voltage using a decoupled controller. It is the same as the VSC system in Section 6.4.3 (in per unit), however the rectifier side of the VSC is simplified as a constant dc voltage source, which is justified based on the conclusion in Section 6.4.3.

To simplify the analysis, the two-port ac system is represented by an R-L circuit equivalent with X/R = 5.0 for all branches, i.e., Z_{s1}, Z_{s2} and Z_t. The ac filters connected to the two PCC buses are the same as in Sections 6.4.2 and 6.4.3 (in per unit).

The LCC is rated at 1000 MW, the VSC at 300 MW and the base MVA of the ac system is 1000 MVA. The rated ac voltage is 230kV. For the VSC-HVdc, the original voltage magnitude in Section 6.4.3 is 100kV, hence the values of the electric circuit elements are scaled to have the same per unit values. The per unit voltages in the dq coordinates are: $V_{1d} = V_{2d} = 1.0\,pu;\ V_{1q} = V_{2q} = 0.0\,pu$. The complex power into the converters are $S_{1,pu} = -0.98 + j0.566$ (1000MW as base value) and $S_{2,pu} = -0.3 + j0$ (1000MW as base value). The complex power flow of the tie-line S_{tie} is zero as the two buses have the same voltage magnitude and phase angle, which is known to result in the strongest interaction between the two converters [21]. The per unit ac system impedance is set as: $\mathrm{Z}_{s1} = \mathrm{Z}_{s2} = 0.07 + j0.35;\ \mathrm{Z}_t = 0.02 + j0.1$.

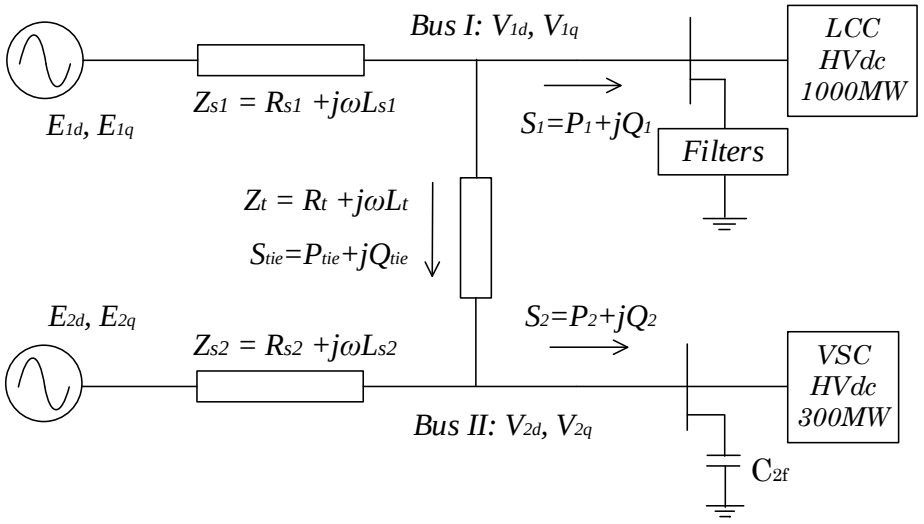

Figure 6-21. Configuration of the dual infeed system

The impedance matrices of the LCC and VSC, i.e., $\boldsymbol{Z_{dc,LCC}}$ from (6.15) and $\boldsymbol{Z_{dc,VSC}}$ from (6.17), had been obtained analytically in Section 6.4, and include the effect of the converter control systems. Following the procedure in Section 6.2.5, the GNC is applied in the dual infeed system. The ac system is represented as a multi-port admittance matrix, which in this section, is a two-port conductance matrix $\boldsymbol{Y_{ac,dual}}$ (4 x 4 dimensional as each port voltage or current has a d- and a q- component). Note that $\boldsymbol{Y_{ac,dual}}$ is the inverse of the impedance matrix $\boldsymbol{Z_{ac,dual}}$. It can be obtained as:

$$\boldsymbol{Y_{ac,dual}} = \begin{bmatrix} \boldsymbol{G_{s1} + G_t} & \boldsymbol{-G_t} \\ \boldsymbol{-G_t} & \boldsymbol{G_{s2} + G_t} \end{bmatrix} \tag{6.18}$$

Where,

$$\boldsymbol{G_{s1}} = \begin{bmatrix} sL_{s1} + R_{s1} & -\omega_0 L_{s1} \\ \omega_0 L_{s1} & sL_{s1} + R_{s1} \end{bmatrix}^{-1};\ \boldsymbol{G_{s2}} = \begin{bmatrix} sL_{s2} + R_{s2} & -\omega_0 L_{s2} \\ \omega_0 L_{s2} & sL_{s2} + R_{s2} \end{bmatrix}^{-1}$$

$$\boldsymbol{G_t} = \begin{bmatrix} sL_t + R_t & -\omega_0 L_t \\ \omega_0 L_t & sL_t + R_t \end{bmatrix}^{-1}$$

Then taking the two HVdc links as the forward gain, and the two-port ac system as the feedback, the loop gain transfer matrix can be calculated as (6.19) (according to (6.11) in Section 6.2.5).

$$\boldsymbol{H_{cl}(s)} = \begin{bmatrix} \boldsymbol{Z_{LCC}} & \boldsymbol{0} \\ \boldsymbol{0} & \boldsymbol{Z_{VSC}} \end{bmatrix} \begin{bmatrix} \boldsymbol{G_{11}} & \boldsymbol{G_{12}} \\ \boldsymbol{G_{21}} & \boldsymbol{G_{22}} \end{bmatrix} \tag{6.19}$$

The four eigenloci curves are shown as in Fig. 6-22, and the *HSM* is observed as 3.07. This value is validated using EMT simulation below, which confirms that if the SCR of the system is reduced by $y = HSM$ (i.e., by multiplying Z_{s1}, Z_{s2} and Z_t by y) the system becomes marginally stable when starting from the operating point (using the technique in Section 6.4.1). And the oscillation frequency is around 4.5Hz.

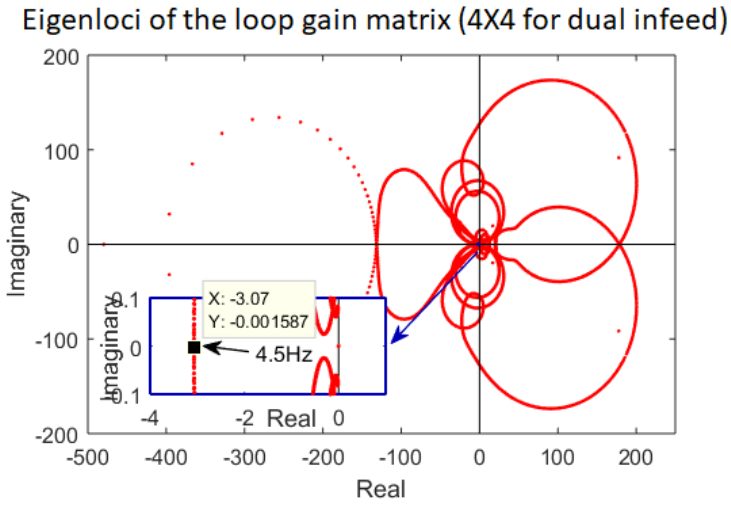

Figure 6-22. Eigenloci plot of the loop gain matrix for the dual infeed system

In Fig. 6-23, the tie line power flow P_{tie} and Q_{tie} are plotted for $y = 3.0$ (slightly smaller than *HSM*). Using the starting up algorithm in Section 6.4.1, the operating point is

pre-set first; the breaker opens at t = 3.0s, and the system is stable. In Fig. 6-24, the tie line power flow is plotted for $y = 3.15$ (slightly larger than *HSM*), it is shown that the system becomes unstable.

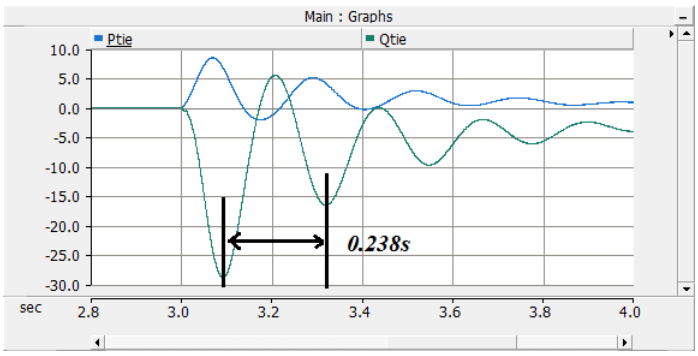

Figure 6-23. Tie line power flow with $Z_{ac} = 3.0 \times Z_{ac,dual}$ starting from the operating point

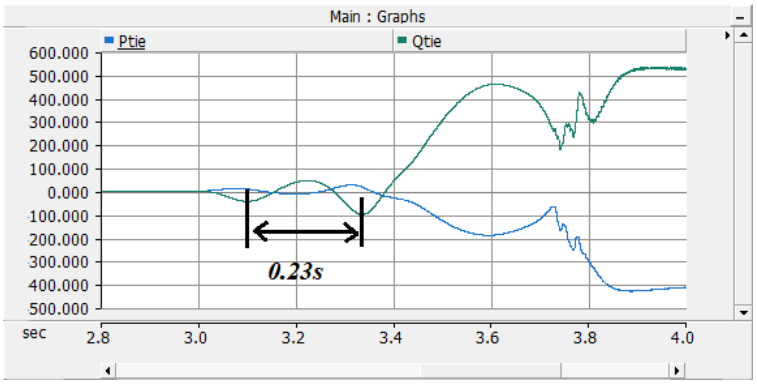

Figure 6-24. Tie line power flow with $Z_{ac} = 3.15 \times Z_{ac,dual}$ starting from the operating point

The power oscillations observed from Fig. 6-23 and Fig. 6-24 have the frequencies of 1/0.238 = 4.2 Hz and 1/0.23 = 4.35 Hz, which agrees with the result from the *HSM* analysis - about 4.5Hz.

If the VSC inverter is not connected to the network, the system degenerates to a single-infeed LCC system whose SCR_{inv} is 5.0 and SCR_{rec} is 4.0, under this circumstance the *HSM*

obtained from GNC is 2.85 (which is 3.07 for dual infeed) and the oscillation frequency is around 1.1Hz. This proves that the connection of VSC into the LCC single infeed system can increase the system stability margin, agreeing with the conclusion in previous studies [21][24][94]. Also, the characteristic frequency has an obvious increase after the connection of VSC (from 1.1 Hz to 4.5 Hz).

6.6 Another form of stability margin – phase margin

The HSM discussed above is the gain margin, which indicates a measure of the distance between the maximum real negative point on the eigenloci of the loop gain matrix and the (-1, 0) point. Alternatively, in control theory, it is also possible to use a phase margin. Assume that the eigenvalue locus of the loop gain matrix crosses (in a coming-out manner) the unit circle at frequency f_{pm} where its phase is ϕ_p, as shown in Fig. 6-25, the corresponding phase margin ϕ_{pm} then can be obtained as $\phi_{pm} = -\phi_p + 180^\circ$. The system would become marginally stable if the phase angle of the open loop response is increased by ϕ_{pm} at frequency f_{pm} [25].

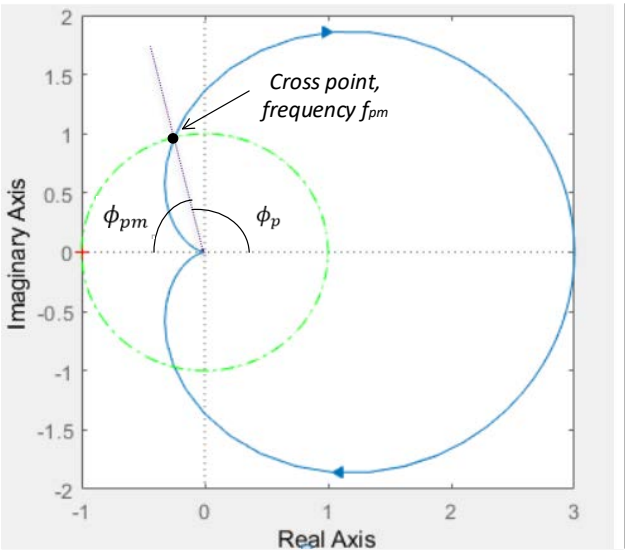

Figure 6-25. The definition of phase margin

However, the closed loop representation in this work uses the impedance of the dc side as the forward gain and the admittance of the ac side as the feedback. In this typical system loop, the forward gain (dc impedance) amplification can be physically explained as the change of dc rated power; the feedback (ac admittance) amplification can be associated with the traditional definition of SCR, and hence the HSM can be used to evaluate the ac system strength. In these applications, the eigenloci as specified in Fig. 6-3 has linearly dependent relationship with the ac system SCR and dc rated power at all frequencies, i.e., the HSM. In contrast, the application of the phase margin is less useful than the gain margin in the examples considered in this thesis.

6.7 Discussion

In this chapter, the ac-dc system is represented as a closed-loop system diagram whose

forward gain is the dc subsystem impedance and the feedback is the ac subsystem admittance. A new index – the HSM is defined based on the Generalized Nyquist stability Criterion. Compared to the traditional indices, e.g., SCR, this index can be employed to investigate not only the fundamental frequency stability, but also the stability in all frequency range. It works for different kind of converter topologies and controlling modes.

Case studies are carried forward to demonstrate the application of *HSM* on different problems. First, SSCI in an LCC system is studied and the value of *HSM* is obtained as a function of controller gains. Second, the influence of the remote side converter and remote ac system strength on the system stability margin is investigated from the plot of HSM versus remote system SCR. Converters including both LCC and VSC are studied and the result can be used as the reference for the future system simplification studies. Third, an LCC-VSC dual-infeed system is presented to show the application of *HSM* to the ac system connected to multiple converters. All these results of *HSM* values are validated by EMT simulations.

With other representations of the ac-dc systems, e.g., the electrical system as the forward gain and the control system as feedback, the proposed HSM can also be applied to solve related problems, e.g., in the design of controllers.

7 Conclusions and recommendations for future work

7.1 Conclusions

In this thesis, an integrated impedance-based technique is proposed to investigate the ac-dc system interaction. Two approaches are employed here, i.e., frequency scanning and analytical modeling, to obtain the impedance responses of subsystems in the dq0 domain. They are applied to a system with either or both LCC and VSC converters, and comparisons are made between the results from these two approaches for validation. With the impedance responses of the converter side and the ac side, the stability margin of the ac-dc system is quantified as a new index – the Harmonic Stability Margin (HSM) based on the Generalized Nyquist stability Criterion (GNC).

The main contributions of this thesis are:

(1) Frequency scanning was exhaustively used to analyze resonances and validate models. During the implementation of scanning, the following observations were made.

   a. *A Limitation in using the simulation-based frequency scanning method was identified. It was shown that the simulation software must be able to accurately consider the precise switching instants, which was best done using*

a program such as PSCAD that uses interpolation. Real-time simulators such as RTDS gave a noisier impedance response unless the timestep could be significantly reduced, which may not be possible in the real time environment.

b. The scanning technique was used to validate alternative methods of modelling power electronic switches, where the switch is represented by a small L and small C for the 'ON' and 'OFF' states. Users of this model had the concern that it may introduce spurious resonances. It was shown that for typically used values of these elements, the frequency response is essentially not significantly modified from that with the more common R_{on}/R_{off} type resistive switch.

(2) An improved analytical model of the Line Commutated Converter was developed, using the artifact of an infinite number of series-connected converters of vanishingly small rating. This made variables such as the firing and extinction angles continuous functions of time and eliminated the characteristic harmonics in the voltage and current waveforms. As measurements of extinction angle and other quantities are only available every 1/12 of a cycle in a 12-pulse converter, the interface from the infinite bus converter to the converter control system was modelled as a sample and hold transfer function with a period equal to 1/12 of a cycle. The dynamics due to the commutation inductance and transportation delays during commutation were included in the model. The theoretically predicted frequency responses of the developed transfer matrices match those obtained from scanning, thereby validating the model.

a. *Using the Generalized Nyquist stability Criterion (GNC), the model was used to accurately predict instability in a small test system with a simple R-L Thevenin source representation of the ac network, as well as for a modified IEEE 14-bus system with an inverter infeed at bus No. 1. The critical gain of the extinction angle (γ) controller at the onset of instability predicted from GNC analysis were confirmed by EMT simulation.*

b. *The model was demonstrated to be more accurate than the traditional LCC model, as it accurately predicts instability when the traditional model does not. The traditional model can only be applied when the system damping is relatively high, e.g., with much larger resistance values of the ac network.*

(3) A new technique to analyze the stability of power systems with power electronics components was developed from the closed-loop representation of the ac-dc system. The index HSM quantifying the stability margin was proposed using the GNC. To apply this technique, the impedances of the ac subsystem and dc subsystem have to be determined as functions of frequency. This can be done analytically from a small signal model, or using an impedance scan using EMT simulation. The plots in the complex plane of the eigenvalues of the resulting loop gain transfer matrix as a function of frequency can be used to define a stability margin by observing how close they approach the (-1,0) point. The scaling factor by which the ac network impedance must be scaled before the onset of instability can be determined with a single plot resulting from a stable system.

a. *Unlike the traditional SCR which considers only the fundamental frequency*

behavior and is useful in predicting power-voltage instability, the proposed HSM can predict instabilities over the full frequency spectrum ranging from steady-state power-voltage instability, Sub-synchronous Control Interaction and harmonic instability.

b. The HSM considers different converter topologies with their individual controlling algorithms. Hence it can be used to identify stabilities for any converter topologies with arbitrary controllers

(4) The HSM method was applied to investigate the stability of systems with LCC, VSC and multi-infeed HVdc systems with both types of converters. The predictions from HSM analysis were accurate and confirmed by comparison with EMT simulations. Additionally, the following observations were made:

a. The Sub-Synchronous Control Interaction (SSCI) phenomenon is accurately identified for an LCC rectifier-based system using the GNC and HSM. The increase of the gain in the constant current controller would result in the decrease of the HSM. A higher PLL gain can make the HSM larger.

b. When modelling LCC networks with the inverter in extinction angle control and the rectifier in current control, it is necessary to model both set of converters unless the sending end SCR is very high.

c. When modelling LCC networks with the inverter in extinction angle control and the rectifier in power control, simplifying the remote converter gives a more optimistic HSM value.

d. *When modelling VSC networks with the inverter in dc power control and the rectifier in dc voltage control, simplifying the remote converter is reasonable as the HSM value is not changed at all.*

e. *When modelling VSC networks with the inverter in dc voltage control and the rectifier in dc power control, it is advisable to include the detailed representation of the rectifier in the model for better accuracy.*

f. *The extension of GNC and HSM analysis to multi-infeed systems with N HVdc links is straightforward, as we just need to observe $2N$ eigenloci contours instead of 2 for a single infeed system to determine HSM. The HSM analysis was carried out for a dual infeed LCC-VSC system, and the result shows that the connection of VSC enhances the system stability margin of the LCC single infeed system, agreeing with the conclusions of previous researchers.*

7.2 Related publications

This thesis work produces the publications below:

1. *Yi Qi, Aniruddha Gole, Hui Ding, Yi Zhang, "Evaluation of the Accuracy of Real-time Digital Simulator Voltage Source Converter Models Determined from Frequency Scanning," in* ***International Conference on Power System Transients (IPST 2017)****, Seoul, South Korea, June 26-29, 2017.*
2. *Yi Qi, Aniruddha Gole, Xiuyu Chen, "Investigation of Subsynchronous Control Interaction for LCC using the Generalized Nyquist Stability Criterion", The* ***15th IET***

***international conference on AC and DC Power Transmission**, Manchester, Feb 5-7, 2019.*

3. *Y. Qi, H. Zhao, S. Fan, A. M. Gole, H. Ding and I. T. Fernando, "Small Signal Frequency-Domain Model of a LCC-HVDC Converter Based on an Infinite Series-Converter Approach," in **IEEE Transactions on Power Delivery, vol. 34, no. 1,** pp. 95-106, Feb. 2019.*

7.3 Recommendations for future work

The related studies, which can be put forward in the future based on this research, are listed below.

7.3.1 Impedance scanning of the MMC HVdc

In this work, the responses of the LCC and two-level VSC were investigated using both the frequency scanning and the analytical modeling. And these two approaches validated each other. However, similar study of MMC HVdc was not conducted in this thesis. The analytical equations of an MMC would of course be different. The second harmonic circulation currents in the MMC arms, which have large magnitudes, make it necessary to model the converter using the Generalized State Space approach [95]. Although a model was developed [78][79] and time-domain responses were compared to the EMT simulation, in which an accelerating simulation model was used [96], its response did not get validated

in frequency domain, i.e., by comparing the frequency responses with the result from the scanning.

7.3.2 Application of HSM on controller design

In chapter 6, the GNC was applied to the closed loop representation of the ac-dc system and the HSM was proposed in which the dc system impedance is the forward gain and the ac system admittance is the feedback gain, or vice-versa. In the future studies, the application of GNC can be generalized to any closed-loop representations, e.g., take one of the controllers as the forward gain and the rest part of the system as feedback. This is not complicated at all as the responses of any part of system can be obtained using the frequency scanning. Using the GNC and HSM, accurate controller design can be made, e.g., a controller can be added to target only low frequencies.

7.3.3 System simplification and equivalence based on the HSM

The study in Section 6.4 gave the result that how the system stability margin was affected, quantified as the HSM, by the remote side converter and ac system configurations. This showed under which circumstances the system could be simplified to include only a single converter. Systematic studies on these kinds of problems in the future should be performed and guides produced for future researchers working on this area to identify the level of

network detail required for accurate analysis.

7.3.4 Analytical modeling of other power-electronic apparatus

New power electronic converter topologies are being proposed [97]. Analytical models for these need to be developed. Base on the analysis in Chapter 5, similar equations and models can be developed using the assumption of infinite series-connected units. The frequency scanning approach can be used to validate these models. GNC and HSM analysis can be extended to these topologies to investigate system stability and other interactions.

References

[1] John J. Grainger, William D. Stevenson. Power System Analysis. McGraw-Hill, 1994.

[2] E.W. Kimbark., Direct Current Transmission, Volume 1. New York: John Wiley & Sons, 1971.

[3] P. Kundur, Power System Stability and Control. McGraw-Hill, 1994.

[4] Chan-Ki Kim, Vijay K. Sood, Gil-Soo Jang, Seong-Joo Lim, Seok-Jin Lee, HVDC Transmission: Power Conversion Applications in Power Systems. Wiley-IEEE Press, 2000.

[5] G. Asplund, K. Eriksson, and H. Jiang, “DC transmission based on voltage source converters,” in Cigre Colloquium on HVDC and FACTS, South Africa, 1997.

[6] CIGRE Working Group 14.07., "Guide for Planning DC Links Terminating at AC Systems Locations Having Low Short Circuit Capacities", CIGRE Brochure 68, 1992.

[7] CIGRE Working Group B4.41, “Systems with Multiple DC Infeed”, Paris: CIGRE, 2008.

[8] C. W. Mueller and J. Hilibrand, "The "Thyristor": A new high-speed switching transistor," in IRE Transactions on Electron Devices, vol. 5, no. 1, pp. 2-5, Jan. 1958.

[9] A. R. Hefner and D. L. Blackburn, "Performance trade-off for the Insulated Gate Bipolar Transistor: Buffer layer versus base lifetime reduction," 1986 17th Annual IEEE Power Electronics Specialists Conference, Vancouver, Canada, 1986, pp. 27-38.

[10] IEEE Standard Practices and Requirements for Thyristor Converters for Motor Drives

Part 1- Converters for DC Motor Armature Supplies," in ANSI/IEEE Std 444-1973 , vol., no., pp.1-98, Jan. 25, 1974.

[11] A. Lesnicar and R. Marquardt, "An innovative modular multilevel converter topology suitable for a wide power range," 2003 IEEE Bologna Power Tech Conference Proceedings, 2003, pp. 6 pp. Vol.3.

[12] J. Reeve and T. S. Rao, "Dynamic Analysis of Harmonic Interaction Between AC AND DC Power Systems," in IEEE Transactions on Power Apparatus and Systems, vol. PAS-93, no. 2, pp. 640-646, March 1974.

[13] J. D. Ainsworth, "Harmonic instability between controlled static convertors and a.c. networks," in Electrical Engineers, Proceedings of the Institution of, vol. 114, no. 7, pp. 949-957, July 1967.

[14] P. S. Bodger, G. D. Irwin and D. A. Woodford, "Controlling harmonic instability of HDVC links connected to weak AC systems," in IEEE Transactions on Power Delivery, vol. 5, no. 4, pp. 2039-2046, Oct 1990.

[15] Kauferle, J.; Mey, R.; Rogowsky, Y., "H.V.D.C. Statsion Connected to Weak A.C. Systems", in Power Apparatus and Systems, IEEE Transactions on , vol.PAS-89, no.7, pp.1610-1619, Sept. 1970.

[16] Gavrilovic, A., "AC/DC system strength as indicated by short circuit ratios", in AC and DC Power Transmission, 1991, International Conference on, vol., no., pp.27-32, 17-20 Sep 1991.

[17] Franken, B.; Andersson, G., "Analysis of HVDC converters connected to weak AC systems", in Power Systems, IEEE Transactions on , vol.5, no.1, pp.235-242, Feb 1990.

[18] Denis Lee Hau Aik; Andersson, G., "Voltage stability analysis of multi-infeed HVDC

systems," in Power Delivery, IEEE Transactions on , vol.12, no.3, pp.1309-1318, Jul 1997.

[19] Denis Lee Hau Aik., Voltage and Power Stability of HVDC Systems, Ph. D thesis, Royal Institute of Technology, 1998.

[20] de Toledo, P.F.; Bergdahl, B.; Asplund, G., "Multiple Infeed Short Circuit Ratio - Aspects Related to Multiple HVDC into One AC Network," in Transmission and Distribution Conference and Exhibition: Asia and Pacific, 2005 IEEE/PES , vol., no., pp.1-6, 18-18 Aug. 2005.

[21] Xiuyu Chen; Gole, A.M.; MinXiao Han, "Analysis of Mixed Inverter/Rectifier Multi-Infeed HVDC Systems," in Power Delivery, IEEE Transactions on, vol.27, no.3, pp.1565-1573, July 2012.

[22] Rahimi, E.; Gole, A.M.; Davies, J.B., "Analysis of multi-infeed HVDC systems with inverter and rectifier connected to the same AC network," in AC and DC Power Transmission, 2010. ACDC. 9th IET International Conference on, vol., no., pp.1-5, 19-21 Oct. 2010.

[23] I. T. Fernando, K. L. Kent, J. B. Davis, E. Rahimi, and A. M. Gole, “Parameters for planning and evaluation of multi-infeed HVDC schemes,” presented at the CIGRÉ Osaka Symp., 2007.

[24] X. Ni, A. M. Gole, C. Zhao and C. Guo, "An Improved Measure of AC System Strength for Performance Analysis of Multi-Infeed HVdc Systems Including VSC and LCC Converters," in IEEE Transactions on Power Delivery, vol. 33, no. 1, pp. 169-178, Feb. 2018.

[25] Katsuhiko Ogata. Modern Control Engineering (fifth edition). Prentice Hall, 2010.

[26] Persson, Erik V., "Calculation of transfer functions in grid-controlled convertor

systems. With special reference to h.v. d.c. transmissions," in Electrical Engineers, Proceedings of the Institution of, vol.117, no.5, pp.989-997, May 1970.

[27] Wood, A.R.; Arrillaga, J., “The frequency dependent impedance of an HVDC converter”, in Power Delivery, IEEE Transactions on , vol.10, no.3, pp.1635-1641, Jul 1995.

[28] Wood, A.R.; Arrillaga, J., "Composite resonance; a circuit approach to the waveform distortion dynamics of an HVdc converter," in Power Delivery, IEEE Transactions on, vol.10, no.4, pp.1882-1888, Oct 1995.

[29] Alan R. Wood, An analysis of non-ideal HVDC converter behavior in frequency domain, and a new control proposal, Ph. D thesis, University of Canterbury, 1993.

[30] Wood, A.R.; Osauskas, C.M.; Hume, D.J., "Small signal modelling of HVDC transmission systems," in AC-DC Power Transmission, 2001. Seventh International Conference on (Conf. Publ. No. 485), vol., no., pp.107-112, 28-30 Nov. 2001.

[31] Kundur, P.; Rogers, G.J.; Wong, D.Y.; Wang, L.; Lauby, M.G., "A comprehensive computer program package for small signal stability analysis of power systems," in Power Systems, IEEE Transactions on , vol.5, no.4, pp.1076-1083, Nov 1990.

[32] S. Arabi, G.J. Rogers, D.Y. Wong, P. Kundur, and M.G. Lauby, "Small Signal Stability Program Analysis of SVC and HVDC in AC Power Systems", IEEE Transactions on Power SEstems, vol. 6, no.3, pp.7147-1153, August 1991.

[33] Venkataraman, S.; Khammash, M.H.; Vittal, V., "Analysis and synthesis of HVDC controls for robust stability of power systems," in Power Systems, IEEE Transactions on, vol.10, no.4, pp.1933-1938, Nov. 1995.

[34] Jovcic, D.; Pahalawaththa, N.; Zavahir, M., "Analytical modelling of HVDC-HVAC

systems," in Power Delivery, IEEE Transactions on, vol.14, no.2, pp.506-511, Apr 1999.

[35] PSCAD/EMTDC User's Manual, Manitoba HVDC Research Centre, Winnipeg, Canada, 2002.

[36] Chandana Karawita, HVDC Interaction Studies Using Small Signal Stability Assessment, Ph. D Thesis, University of Manitoba, 2009.

[37] Ye, Y.; Kazerani, M.; Quintana, V.H., "A novel modeling and control method for three-phase PWM converters," in Power Electronics Specialists Conference, 2001. PESC. 2001 IEEE 32nd Annual, vol.1, no., pp.102-107 vol. 1, 2001.

[38] Jovcic, D.; Lamont, L.A.; Xu, L., "VSC transmission model for analytical studies," in Power Engineering Society General Meeting, 2003, IEEE , vol.3, no., pp.1742 Vol. 3, 13-17 July 2003.

[39] J. Svensson, "Voltage angle control of a voltage source inverter, application to a grid-connected wind turbine," in 6th European Conference on Power Electronics and Applications, Sevilla, 1995.

[40] J.W. Choi and S. K. Sul, "Fast current controller in three-phase AC/DC boost converter
using d-q axis crosscoupling," IEEE Trans. Power Electron., vol. 13, no. 1, pp. 179–185, January 1998.

[41] Chao Zheng; Zhou Xiaoxin; Ruomei Li, "Dynamic Modeling and Transient Simulation for VSC based HVDC in Multi-Machine System," in Power System Technology, 2006. PowerCon 2006. International Conference on, vol., no., pp.1-7, 22-26 Oct. 2006.

[42] Lidong Zhang, Modeling and Control of VSC-HVDC Links Connected to Weak AC Systems, Ph. D thesis, Royal Institute of Technology, 2010.

[43] Zhou, J.Z.; Hui Ding; Shengtao Fan; Yi Zhang; Gole, A.M., "Impact of Short-Circuit Ratio and Phase-Locked-Loop Parameters on the Small-Signal Behavior of a VSC-HVDC

Converter", in Power Delivery, IEEE Transactions on , vol.29, no.5, pp.2287-2296, Oct. 2014.

[44] Hingorani, N.G.; Burbery, M.F., "Simulation of AC System Impedance in HVDC System Studies", in Power Apparatus and Systems, IEEE Transactions on , vol.PAS-89, no.5, pp.820-828, May 1970.

[45] N. R. Watson, Frequency-Dependent A.C. System Equivalents for Harmonic Studies and Transient Convertor Simulation, Ph. D thesis, University of Canterbury, 1987.

[46] Morched, A.S.; Ottevangers, J.H.; Marti, L., "Multi-port frequency dependent network equivalents for the EMTP," in Power Delivery, IEEE Transactions on , vol.8, no.3, pp.1402-1412, July 1993.

[47] Xi Lin, System Equivalent for Real Time Digital Simulator, Ph. D thesis, University of Manitoba, 2010.

[48] B. Gustavsen and A. Semlyen, “Rational approximation of frequency domain responses by Vector Fitting”, IEEE Trans. Power Delivery, vol. 14, no. 3, pp. 1052-1061, July 1999.

[49] B. Gustavsen, “Improving the pole relocating properties of vector fitting”, IEEE Trans. Power Delivery, vol. 21, no. 3, pp. 1587-1592, July 2006.

[50] D. Deschrijver, M. Mrozowski, T. Dhaene, and D. De Zutter, “Macromodeling of Multiport Systems Using a Fast Implementation of the Vector Fitting Method”, IEEE Microwave and Wireless Components Letters, vol. 18, no. 6, pp. 383-385, June 2008.

[51] de Oliveira, A.; de Oliveira, J.C.; Resende, J.W.; Miskulin, M.S., "Practical approaches for AC system harmonic impedance measurements," in Power Delivery, IEEE Transactions on , vol.6, no.4, pp.1721-1726, Oct 1991.

[52] Robert, A.; Deflandre, T.; et al., "Guide for assessing the network harmonic impedance," in Electricity Distribution. Part 1: Contributions. CIRED. 14th International Conference and Exhibition on (IEE Conf. Publ. No. 438), vol.1, no., pp.3/1-310 vol.2, 2-5 June 1997.

[53] Szechtman, M.; Wess, T.; Thio, C.V., "A benchmark model for HVDC system studies," in AC and DC Power Transmission, 1991., International Conference on , vol., no., pp.374-378, 17-20 Sep 1991.

[54] Xiao Jiang; Gole, A.M., "A frequency scanning method for the identification of harmonic instabilities in HVDC systems", in Power Delivery, IEEE Transactions on , vol.10, no.4, pp.1875-1881, Oct 1995.

[55] Wilsun Xu; Ahmed, E.E.; Xiqin Zhang; Xian Liu, "Measurement of network harmonic impedances: practical implementation issues and their solutions", in Power Delivery, IEEE Transactions on, vol.17, no.1, pp.210-216, Jan 2002.

[56] Mohaddes, M.; Gole, A.M.; Elez, S., "Steady state frequency response of STATCOM", in Power Delivery, IEEE Transactions on , vol.16, no.1, pp.18-23, Jan 2001.

[57] Park, R.H., "Two-reaction theory of synchronous machines generalized method of analysis-part I," in American Institute of Electrical Engineers, Transactions of the , vol.48, no.3, pp.716-727, July 1929.

[58] Familiant, Y.A.; Jing Huang; Corzine, K.A.; Belkhayat, M., "New Techniques for Measuring Impedance Characteristics of Three-Phase AC Power Systems," in Power Electronics, IEEE Transactions on , vol.24, no.7, pp.1802-1810, July 2009.

[59] Jing Huang; Corzine, K.A.; Belkhayat, M., "Small-Signal Impedance Measurement of Power-Electronics-Based AC Power Systems Using Line-to-Line Current Injection,"

in Power Electronics, IEEE Transactions on, vol.24, no.2, pp.445-455, Feb. 2009.

[60] Francis, G.; Burgos, R.; Boroyevich, D.; Wang, F.; Karimi, K., "An algorithm and implementation system for measuring impedance in the D-Q domain," in Energy Conversion Congress and Exposition (ECCE), 2011 IEEE , vol., no., pp.3221-3228, 17-22 Sept. 2011.

[61] Nyquist, H. (1932), Regeneration Theory. Bell System Technical Journal, 11: 126–147. doi: 10.1002/j.1538-7305.1932.tb02344.x.

[62] Yao, Z.; Therond, P.G.; Davat, B., "Stability analysis of power systems by the generalised Nyquist criterion," in Control, 1994. Control '94. International Conference on, vol.1, no., pp.739-744 vol.1, 21-24 March 1994.

[63] A. G. J. MAcFARLANE & I. POSTLETHWAITE (1977), “The generalized Nyquist stability criterion and multivariable root loci”, International Journal of Control, 25:1, 81-127.

[64] Mukesh Kumar Das, D-Q and Dynamic Phasor based Frequency Scanning Analysis of Grid-Connected Power electronic systems, Ph. D thesis, Indian Institute of Technology, Bombay, 2016.

[65] J. Cooley, P. Lewis and P. Welch, "The finite Fourier transform," in IEEE Transactions on Audio and Electroacoustics, vol. 17, no. 2, pp. 77-85, Jun 1969.

[66] F. Verhulst and J. A. Sanders. Averaging Methods in Nonlinear Dynamical Systems. Springer-Verlag, N. Y., 1985.

[67] J. Guckenheimer and P. Holmes. Nonlinear Oscillations, Dynamical Systems, and Bifurcations of Vector Fields, volume 42 of AMS. Springer Verlag, N.Y., 1990.

[68] Patricio Antonio Vela, Averaging and Control of Nonlinear Systems, Ph. D thesis,

California Institute of Technology, 2003.

[69] S. Chiniforoosh, J. Jatskevich, V. Dinavahi, R. Iravani, J. A. Martinez and A. Ramirez, "Dynamic average modeling of line-commutated converters for power systems applications," 2009 IEEE Power & Energy Society General Meeting, Calgary, AB, 2009, pp. 1-8.

[70] Cigre Working Group B4.46., Voltage Source Converter (VSC) HVDC for Power Transmission – Economic Aspects and Comparison with other AC and DC Technologies, 2012.

[71] H. W. Dommel, EMTP Theory Book, Microtran Power System Analysis Corporation, Vancouver, British Columbia, 1996.

[72] Real Time Digital Simulation for the Power Industry – Manual Set. RTDS Technologies Inc., Winnipeg, Manitoba, 2017.

[73] A.M. Gole, I.T. Fernando, G.D. Irwin , O.B. Nayak, “Modeling of Power Electronic Apparatus: Additional Interpolation Issues”, International Conference on Power System Transients, IPST’97, Seattle, June 22-26, 1997, Proceedings: pp 23-28.

[74] Yi Qi, Aniruddha Gole, Hui Ding, Yi Zhang, "Evaluation of the Accuracy of Real-time Digital Simulator Voltage Source Converter Models Determined from Frequency Scanning," in IPST conference in Seoul, July 2017.

[75] Trevor Maguire and James Giesbrecht, “Small Time-step (<2uSec) VSC Model for the Real Time Digital Simulator”, Proceeding of IPST 2005, Montreal Canada, June 2005, Paper No. IPST-168-25c.

[76] P. Pejovic and D. Maksimovic, "A method for fast time-domain simulation of networks with switches," in IEEE Transactions on Power Electronics, vol. 9, no. 4, pp.

449-456, July 1994.

[77] S. Y. R. Hui and C. Christopoulos, "A discrete approach to the modeling of power electronic switching networks," in IEEE Transactions on Power Electronics, vol. 5, no. 4, pp. 398-403, Oct. 1990.

[78] T. Li, A. M. Gole and C. Zhao, "Harmonic Instability in MMC-HVDC Converters Resulting From Internal Dynamics," in IEEE Transactions on Power Delivery, vol. 31, no. 4, pp. 1738-1747, Aug. 2016.

[79] T. Li, A. Gole and C. Zhao, "Stablity of a modular multilevel converter based HVDC system considering DC side connection," 12th IET International Conference on AC and DC Power Transmission (ACDC 2016), Beijing, 2016, pp. 1-6.

[80] Y. Qi, H. Zhao, S. Fan, A. M. Gole, H. Ding and I. T. Fernando, "Small Signal Frequency-Domain Model of a LCC-HVDC Converter Based on an Infinite Series-Converter Approach," in IEEE Transactions on Power Delivery, vol. 34, no. 1, pp. 95-106, Feb. 2019.

[81] E. V. Larsen, D. H. Baker and J. C. McIver, "Low-order harmonic interactions on AC/DC systems," in IEEE Transactions on Power Delivery, vol. 4, no. 1, pp. 493-501, Jan 1989.

[82] C. Osauskas and A. Wood, "Small-signal dynamic modeling of HVDC systems," in IEEE Transactions on Power Delivery, vol. 18, no. 1, pp. 220-225, Jan 2003.

[83] Ken C. Pohlmann. Principles of Digital Audio (fifth edition.). McGraw-Hill, 2000.

[84] Gerhard Manfred Schoen, Stability and Stabilization of Time-Delay Systems, Ph. D thesis, Swiss Federal Institute of Technology Zurich, 1995.

[85] Illinois Center for a Smarter Electric Grid. (2013). [Online]. Available FTP:

http://publish.illinois.edu/smartergrid/

[86] Anderson, P.M.; and Fouad, A.A. eds. 2003. Power System Control and Stability, IEEE Press, John Wiley and Sons Inc. Publication.

[87] Yi Qi, Aniruddha Gole, Xiuyu Chen, “Investigation of Subsynchronous Control Interaction for LCC using the Generalized Nyquist Stability Criterion”, The 15th IET international conference on AC and DC Power Transmission, Manchester, Feb 2019.

[88] Huanhai Xin, Wei Dong, Deqiang Gan, Xiaoming Yuan, "Generalize Short Circuit Ratio for Multi Power Electronic based Devices Infeed Systems: Definition and Theoretical Analysis," arxiv: 1708.08046 [cs.SY], Aug. 2017.

[89] Emami-Naeini and R. L. Kosut, "The generalized Nyquist criterion and robustness margins with applications," 2012 IEEE 51st IEEE Conference on Decision and Control (CDC), Maui, HI, 2012, pp. 226-231.

[90] G. D. Irwin, A. K. Jindal and A. L. Isaacs, "Sub-synchronous control interactions between type 3 wind turbines and series compensated AC transmission systems," 2011 IEEE Power and Energy Society General Meeting, Detroit, MI, USA, 2011, pp. 1-6.

[91] L. Wang, X. Xie, Q. Jiang and X. Liu, "Centralised solution for subsynchronous control interaction of doubly fed induction generators using voltage-sourced converter," in IET Generation, Transmission & Distribution, vol. 9, no. 16, pp. 2751-2759, 3 12 2015.

[92] K. M. Alawasa, Y. A. I. Mohamed and W. Xu, "Active Mitigation of Subsynchronous Interactions Between PWM Voltage-Source Converters and Power Networks," in IEEE Transactions on Power Electronics, vol. 29, no. 1, pp. 121-134, Jan. 2014.

[93] W. Du, Q. Fu and H. Wang, "Method of Open-Loop Modal Analysis for Examining the Subsynchronous Interactions Introduced by VSC Control in an MTDC/AC System," in

IEEE Transactions on Power Delivery, vol. 33, no. 2, pp. 840-850, April 2018.

[94] C. Guo, Y. Zhang, A. M. Gole and C. Zhao, "Analysis of Dual-Infeed HVDC With LCC–HVDC and VSC–HVDC," in IEEE Transactions on Power Delivery, vol. 27, no. 3, pp. 1529-1537, July 2012.

[95] S. R. Sanders, J. M. Noworolski, X. Z. Liu and G. C. Verghese, "Generalized averaging method for power conversion circuits," in IEEE Transactions on Power Electronics, vol. 6, no. 2, pp. 251-259, April 1991.

[96] U. N. Gnanarathna, A. M. Gole and R. P. Jayasinghe, "Efficient Modeling of Modular Multilevel HVDC Converters (MMC) on Electromagnetic Transient Simulation Programs," in IEEE Transactions on Power Delivery, vol. 26, no. 1, pp. 316-324, Jan. 2011.

[97] C. Guo, Z. Yang, B. Jiang and C. Zhao, "An Evolved Capacitor-Commutated Converter Embedded With Antiparallel Thyristors Based Dual-Directional Full-Bridge Module," in IEEE Transactions on Power Delivery, vol. 33, no. 2, pp. 928-937, April 2018.

Appendix A – State space model for the subsystems in Chapter 3

A.1 Analytical modeling of subsystem I

The reference angle selected to transform the voltages and currents to dq0 domain is selected as the rotor angle δ_g, which is given as a state variable below. The speed of the system ω_g is also a state variable. The equivalent circuits of the synchronous machine in d- and q- direction can be referred to as in [3]. Based on those circuits, the internal flux linkages and d-q domain terminal currents are chosen as state variables in the modeling, and the synchronous generator is represented as the equations below (linearized). The prefix 'Δ' before a variable indicates that it is a small signal variable and the absence of 'Δ' means its steady state value.

$$\Delta\dot{\varphi}_{fd} = \omega_0 \left[\frac{\Delta E_{fd}}{L_{ad}} R_{fd} - \frac{\Delta\varphi_{fd} - \Delta\varphi_{ad}\left(\Delta\varphi_{fd}, \Delta\varphi_{1d}, \Delta i_d\right)}{L_{fd}} R_{fd} \right] \quad (A.1)$$

$$\Delta\dot{\varphi}_{1d} = -\omega_0 \frac{\Delta\varphi_{1d} - \Delta\varphi_{ad}\left(\Delta\varphi_{fd}, \Delta\varphi_{1d}, \Delta i_d\right)}{L_{1d}} R_{1d} \quad (A.2)$$

$$\Delta\dot{\varphi}_{1q} = -\omega_0 \frac{\Delta\varphi_{1q} - \Delta\varphi_{aq}\left(\Delta\varphi_{1q}, \Delta\varphi_{2q}, \Delta i_q\right)}{L_{1q}} R_{1q} \quad (A.3)$$

$$\Delta\dot{\varphi}_{2q} = -\omega_0 \frac{\Delta\varphi_{2q} - \Delta\varphi_{aq}\left(\Delta\varphi_{1q}, \Delta\varphi_{2q}, \Delta i_q\right)}{L_{2q}} R_{2q} \quad (A.4)$$

$$\begin{bmatrix} L_l + L''_{ad} & 0 \\ 0 & L_l + L''_{aq} \end{bmatrix} \begin{bmatrix} \Delta \dot{I}_{td}{}^{g} \\ \Delta \dot{I}_{tq}{}^{g} \end{bmatrix} - \begin{bmatrix} \frac{L''_{ad}}{L_{fd}} \Delta \dot{\varphi}_{fd} + \frac{L''_{ad}}{L_{1d}} \Delta \dot{\varphi}_{1d} \\ \frac{L''_{aq}}{L_{1q}} \Delta \dot{\varphi}_{1q} + \frac{L''_{aq}}{L_{2q}} \Delta \dot{\varphi}_{2q} \end{bmatrix}$$

$$= \begin{bmatrix} -\omega_0 (\Delta \varphi_{aq} - L_l \Delta I_{tq}) - R_a \Delta I_{td} \\ \omega_0 (\Delta \varphi_{ad} - L_l \Delta I_{td}) - R_a \Delta I_{tq} \end{bmatrix} + \Delta \omega_g \begin{bmatrix} -\varphi_{aq} - L_l I_{tq} - R_a I_{td} \\ \varphi_{ad} - L_l I_{td} - R_a I_{tq} \end{bmatrix} - \begin{bmatrix} \Delta E_{td} \\ \Delta E_{tq} \end{bmatrix} \quad (A.5)$$

$$2H \Delta \dot{\omega}_g = \Delta T_m - \left(\Delta \varphi_{ad} I_{tq}{}^{g} + \varphi_{ad} \Delta I_{tq}{}^{g} - \Delta \varphi_{aq} I_{td}{}^{g} - \varphi_{aq} \Delta I_{td}{}^{g} \right) \quad (A.6)$$

$$\Delta \dot{\delta}_g = \omega_0 \Delta \omega_g \quad (A.7)$$

Where $\Delta \varphi_{ad}$ and $\Delta \varphi_{aq}$ are given as:

$$\begin{bmatrix} L_{fd} + L_{ad} & L_{ad} & 0 \\ L_{ad} & L_{1d} + L_{ad} & 0 \\ L_{ad} & L_{ad} & -1 \end{bmatrix} \begin{bmatrix} \Delta i_{fd} \\ \Delta i_{1d} \\ \Delta \varphi_{ad} \end{bmatrix} = \begin{bmatrix} L_{ad} & 1 & 0 \\ L_{ad} & 0 & 1 \\ L_{ad} & 0 & 0 \end{bmatrix} \begin{bmatrix} \Delta I_{td} \\ \Delta \varphi_{fd} \\ \Delta \varphi_{1d} \end{bmatrix}$$

$$\begin{bmatrix} L_{1q} + L_{aq} & L_{aq} & 0 \\ L_{aq} & L_{2q} + L_{aq} & 0 \\ L_{aq} & L_{aq} & -1 \end{bmatrix} \begin{bmatrix} \Delta i_{1q} \\ \Delta i_{2q} \\ \Delta \varphi_{aq} \end{bmatrix} = \begin{bmatrix} L_{aq} & 1 & 0 \\ L_{aq} & 0 & 1 \\ L_{aq} & 0 & 0 \end{bmatrix} \begin{bmatrix} \Delta I_{tq} \\ \Delta \varphi_{1q} \\ \Delta \varphi_{2q} \end{bmatrix}$$

The superscript ‘g’ in the voltage and current variables indicates that the dq0 transformation used to get this variable has the reference angle as $\Delta \delta_g$. The relationship between $\Delta I_{td}/\Delta I_{tq}$ whose reference angle of the dq0 transformation is θ and $\Delta I_{td}{}^{g}/\Delta I_{tq}{}^{g}$ with reference angle δ_g is given by:

$$\begin{bmatrix} \Delta I_{td} \\ \Delta I_{tq} \end{bmatrix} = \begin{bmatrix} \cos(\theta - \delta_g) & \sin(\theta - \delta_g) \\ -\sin(\theta - \delta_g) & \cos(\theta - \delta_g) \end{bmatrix} \begin{bmatrix} \Delta I_{td}{}^{g} \\ \Delta I_{tq}{}^{g} \end{bmatrix} - \begin{bmatrix} -\sin(\theta - \delta_g) & \cos(\theta - \delta_g) \\ -\cos(\theta - \delta_g) & -\sin(\theta - \delta_g) \end{bmatrix} \begin{bmatrix} I_{td}{}^{g} \\ I_{tq}{}^{g} \end{bmatrix} \Delta \delta_g$$

Additionally, an arbitrary governor is employed to generate the mechanical torque T_m provided to the machine, and an exciter is used to provide the exciter voltage E_{fd}. They can be modelled as the control block in Fig. A-1.

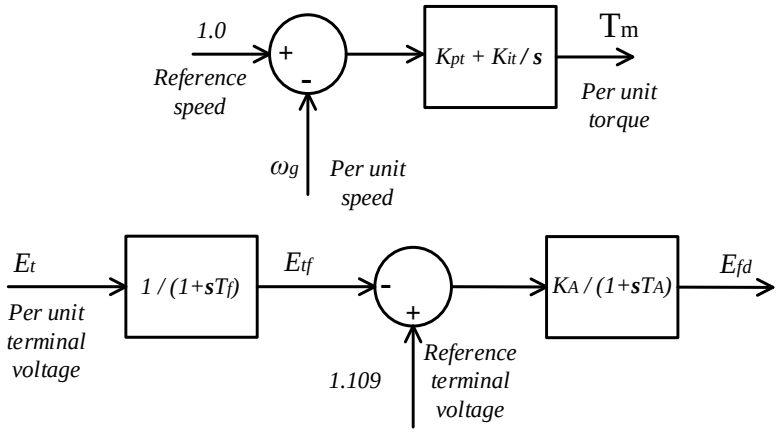

Figure A-1. Model of the arbitrary governor and exciter

The state equations (small signal) for the governor and exciter can be given by:

$$K_{pt}\Delta\dot{\omega}_g + \Delta\dot{T}_m = -K_{it}\Delta\omega_g \qquad (A.8)$$

$$T_f\Delta\dot{E}_{tf} = -\Delta E_{tf} + \frac{E_{td}\Delta E_{td} + E_{tq}\Delta E_{tq}}{\sqrt{{E_{td}}^2 + {E_{tq}}^2}} \qquad (A.9)$$

$$T_A\Delta\dot{E}_{fd} = -\Delta E_{fd} + K_A\left(\Delta E_{t_{ref}} - \Delta E_{tf}\right) \qquad (A.10)$$

Where the d-q domain terminal voltages of the generator are given by:

$$\begin{bmatrix}\Delta E_{td}\\ \Delta E_{tq}\end{bmatrix} = \begin{bmatrix}\Delta U_{pd} + \Delta I_{td} * R_s + {\Delta U_d}^g\\ \Delta U_{pq} + \Delta I_{tq} * R_s + {\Delta U_q}^g\end{bmatrix}$$

And the linearized state equations for the R-R//L//C circuit are:

$$C_p\begin{bmatrix}\Delta\dot{U}_{pd}\\ \Delta\dot{U}_{pq}\end{bmatrix} = -\begin{bmatrix}0 & -\omega_0 C_p\\ \omega_0 C_p & 0\end{bmatrix}\begin{bmatrix}\Delta U_{pd}\\ \Delta U_{pq}\end{bmatrix} - \begin{bmatrix}0 & -\Delta\omega_g C_p\\ \Delta\omega_g C_p & 0\end{bmatrix}\begin{bmatrix}U_{pd}\\ U_{pq}\end{bmatrix} + \begin{bmatrix}\Delta I_{td} - \Delta I_{pd} - \dfrac{\Delta U_{pd}}{R_p}\\ \Delta I_{tq} - \Delta I_{pq} - \dfrac{\Delta U_{pq}}{R_p}\end{bmatrix} \qquad (A.11)$$

$$L_p\begin{bmatrix}\Delta\dot{I}_{pd}\\ \Delta\dot{I}_{pq}\end{bmatrix} = -\begin{bmatrix}0 & -\omega_0 L_p\\ \omega_0 L_p & 0\end{bmatrix}\begin{bmatrix}\Delta I_{pd}\\ \Delta I_{pq}\end{bmatrix} - \begin{bmatrix}0 & -\Delta\omega_g L_p\\ \Delta\omega_g L_p & 0\end{bmatrix}\begin{bmatrix}I_{pd}\\ I_{pq}\end{bmatrix} + \begin{bmatrix}\Delta U_{pd}\\ \Delta U_{pq}\end{bmatrix} \qquad (A.12)$$

The relationship between ${\Delta U_d}^g/{\Delta U_q}^g$ and $\Delta U_d/\Delta U_q$ is:

$$\begin{bmatrix}\Delta U_d{}^g \\ \Delta U_q{}^g\end{bmatrix} = \begin{bmatrix}\cos(\delta_g-\theta) & \sin(\delta_g-\theta) \\ -\sin(\delta_g-\theta) & \cos(\delta_g-\theta)\end{bmatrix}\begin{bmatrix}\Delta U_d \\ \Delta U_q\end{bmatrix} + \begin{bmatrix}-\sin(\delta_g-\theta) & \cos(\delta_g-\theta) \\ -\cos(\delta_g-\theta) & -\sin(\delta_g-\theta)\end{bmatrix}\begin{bmatrix}U_d \\ U_q\end{bmatrix}\Delta\delta_g$$

Based on (A.1 – A.12), the state variables, the input variables and the output variables are selected as:

$$\Delta \boldsymbol{X_{ac}} = [\Delta\varphi_{fd} \quad \Delta\varphi_{1d} \quad \Delta\varphi_{1q} \quad \Delta\varphi_{2q} \quad \Delta I_{td} \quad \Delta I_{tq} \quad \Delta U_{pd} \quad \Delta U_{pq} \quad \Delta I_{pd} \quad \Delta I_{pq} \quad \Delta\omega_g \quad \Delta\delta_g \quad \Delta E_t \quad \Delta E_{fd}]^T$$

$$\Delta \boldsymbol{U_{ac}} = [\Delta U_d \quad \Delta U_q]^T$$

$$\Delta \boldsymbol{I_{ac}} = [\Delta I_{td} \quad \Delta I_{tq}]^T$$

The state space form of the system can be easily obtained from (A.1-12); hence the details of the matrixes **A, B, C** and **D** are not presented here. The parameters in the state equations of subsystem I are given as in Tab. A-1 and Tab. A-2.

Table A-1. Parameters of the R_s-R_p//L_p//C_p circuit

Circuit Parameters	*Value*	*Circuit Parameters*	*Value*
R_s	*2.2965ohm*	R_p	*300ohm*
C_p	*20uF*	L_p	*0.028547H*

Table A-2. Parameters of the synchronous generator, the governor and the exciter

Machine Parameters	*Value*	*Machine Parameters*	*Value*	*Machine Parameters*	*Value*
L-L RMS voltage	*100kV*	R_{fd}	*0.00043pu*	*H*	*6*
Rated power	*300MW*	L_{1d}	*0.0437pu*	K_{pt}	*50*
R_a	*0.0025pu*	R_{1d}	*0.0051pu*	K_{it}	*40*
L_l	*0.14pu*	L_{1q}	*0.106pu*	T_f	*0.02*
L_{ad}	*1.52pu*	R_{1q}	*0.00842pu*	K_a	*100*
L_{aq}	*1.31pu*	L_{2q}	*0.0942pu*	T_a	*0.01*
L_{fd}	*0.2004pu*	R_{2q}	*0.0082pu*		

A.2 Analytical modeling of subsystem II

The state equations for PLL (all electrical variables are per unit values below):

$$\begin{cases} \Delta\dot{x}_1 = K_{i1}\Delta V_q \\ \Delta\dot{\theta}_{pll} = (\Delta x_1 + K_{p1}\Delta V_q) \end{cases} \tag{A.13}$$

$$\Delta\omega = \Delta x_1 + K_{p1}\Delta V_q$$

The dq0 transformation for the voltages and currents uses the reference angle as the output of the PLL here, so there is superscript 'v' added for the voltages and currents. Similar as in subsystem I, the speed ω is a state variable. The differential equations of the voltage and current measurement can be given by:

$$\begin{cases} T_3\Delta\dot{V}_d = \Delta {U_d}^v - \Delta V_d \\ T_4\Delta\dot{V}_q = \Delta {U_q}^v - \Delta V_q \\ T_5\Delta\dot{J}_d = \Delta {I_d}^v - \Delta J_d \\ T_6\Delta\dot{J}_q = \Delta {I_q}^v - \Delta J_q \\ T_7\Delta\dot{V}_{dc} = \Delta U_{dc} - \Delta V_{dc} \end{cases} \tag{A.14}$$

The relationship between $\Delta I_d/\Delta I_q$ whose dq0 domain reference angle is θ and $\Delta {I_d}^v/\Delta {I_q}^v$ with reference angle θ_{pll} is given by (relationship of the voltages is the same):

$$\begin{bmatrix} \Delta {I_d}^v \\ \Delta {I_q}^v \end{bmatrix} = \begin{bmatrix} \cos(\theta_{pll}-\theta) & \sin(\theta_{pll}-\theta) \\ -\sin(\theta_{pll}-\theta) & \cos(\theta_{pll}-\theta) \end{bmatrix}\begin{bmatrix} \Delta I_d \\ \Delta I_q \end{bmatrix} + \begin{bmatrix} -\sin(\theta_{pll}-\theta) & \cos(\theta_{pll}-\theta) \\ -\cos(\theta_{pll}-\theta) & -\sin(\theta_{pll}-\theta) \end{bmatrix}\begin{bmatrix} I_d \\ I_q \end{bmatrix}\Delta\theta_{pll}$$

And the decoupled controller equations can be given by:

$$\begin{cases} \Delta\dot{x_8} = K_{i2}\left(\Delta V_{dc,ref} - \Delta V_{dc}\right) \\ \Delta\dot{x_9} = K_{i3}\left(I_{dref} - \Delta J_d\right) \\ \Delta\dot{x}_{10} = K_{i4}\left(-\dfrac{V_d\Delta V_d + V_q\Delta V_q}{V} + \Delta V_{acref}\right) \\ \Delta\dot{x}_{11} = K_{i5}\left(\Delta I_{qref} - \Delta J_q\right) \end{cases} \tag{A.15}$$

$$\begin{cases} \Delta I_{dref} = \Delta x_8 + K_{p2}\left(\Delta V_{dcref} - \Delta V_{dc}\right) \\ \Delta I_{qref} = \Delta x_{10} + K_{p4}\left(-\dfrac{V_d \Delta V_d + V_q \Delta V_q}{V} + \Delta V_{acref}\right) \\ \Delta E_d = -\Delta x_9 - K_{p3}\left(\Delta I_{dref} - \Delta J_d\right) + Z\Delta J_q + \Delta V_d \\ \Delta E_q = -\Delta x_{11} - K_{p5}\left(\Delta I_{qref} - \Delta J_q\right) - Z\Delta J_d + \Delta V_q \end{cases}$$

The dynamic equation of the dc capacitor is:

$$C_{dc}\Delta\dot{U}_{dc} = E_d\Delta {I_d}^v + \Delta E_d {I_d}^v + E_q\Delta {I_q}^v + \Delta E_q {I_q}^v - \frac{\Delta U_{dc} - \Delta E_{dc}}{R_{dc}} \qquad (A.16)$$

For the ac side transformer (represented as a R-L circuit) and the ac capacitor connect to the PCC bus:

$$L_t\begin{bmatrix}\Delta\dot{I}_d{}^v \\ \Delta\dot{I}_q{}^v\end{bmatrix} = -\begin{bmatrix}R_t & -\omega L_t \\ \omega L_t & R_t\end{bmatrix}\begin{bmatrix}\Delta {I_d}^v \\ \Delta {I_q}^v\end{bmatrix} - \begin{bmatrix}0 & -\Delta\omega L_t \\ \Delta\omega L_t & 0\end{bmatrix}\begin{bmatrix}{I_d}^v \\ {I_q}^v\end{bmatrix} + \begin{bmatrix}\Delta {U_d}^v - U_{dc}\Delta E_d - E_d\Delta U_{dc} \\ \Delta {U_q}^v - U_{dc}\Delta E_q - E_q\Delta U_{dc}\end{bmatrix} \quad (A.17)$$

$$C_f\begin{bmatrix}\Delta\dot{U}_d{}^v \\ \Delta\dot{U}_q{}^v\end{bmatrix} = \begin{bmatrix}0 & \omega \mathrm{C_f} \\ -\omega \mathrm{C_f} & 0\end{bmatrix}\begin{bmatrix}\Delta {U_d}^v \\ \Delta {U_q}^v\end{bmatrix} + \begin{bmatrix}0 & \Delta\omega \mathrm{C_f} \\ -\Delta\omega \mathrm{C_f} & 0\end{bmatrix}\begin{bmatrix}\Delta {U_d}^v \\ \Delta {U_q}^v\end{bmatrix} + \begin{bmatrix}\Delta I_{td} - \Delta {I_d}^v \\ \Delta I_{td} - \Delta {I_q}^v\end{bmatrix} \quad (A.18)$$

The superscript ‘v’ means that the reference angle of the dq0 transformation is the angle output of the PLL $\Delta\theta_{pll}$. Choose state variables, input variables and output variables as:

$$\Delta \boldsymbol{X_{con}} = [\Delta x_1 \quad \Delta\theta_{pll} \quad \Delta V_d \quad \Delta V_q \quad \Delta J_d \quad \Delta J_q \quad \Delta V_{dc} \quad \Delta x_8 \quad \Delta x_9 \quad \Delta x_{10} \quad \Delta x_{11} \quad \ldots$$

$$\Delta U_{dc} \quad \Delta I_d \quad \Delta I_q \quad \Delta U_d \quad \Delta U_q]^T;$$

$$\Delta \boldsymbol{I_{con}} = [\Delta I_d \quad \Delta I_q]^T;$$

$$\Delta \boldsymbol{U_{con}} = [\Delta U_d \quad \Delta U_q]^T;$$

The state space form of subsystem can be obtained based on (A. 13-18) where the output can be given by:

$$\begin{bmatrix}\Delta U_d \\ \Delta U_q\end{bmatrix} = \begin{bmatrix}\cos(\theta - \theta_{pll}) & \sin(\theta - \theta_{pll}) \\ -\sin(\theta - \theta_{pll}) & \cos(\theta - \theta_{pll})\end{bmatrix}\begin{bmatrix}\Delta {U_d}^v \\ \Delta {U_q}^v\end{bmatrix} - \begin{bmatrix}-\sin(\theta - \theta_{pll}) & \cos(\theta - \theta_{pll}) \\ -\cos(\theta - \theta_{pll}) & -\sin(\theta - \theta_{pll})\end{bmatrix}\begin{bmatrix}{U_d}^v \\ {U_q}^v\end{bmatrix}\Delta\theta_{pll}$$

The parameters in the state equations of subsystem II are given as in Tab. A-3 for the

electrical system parameters and in Tab. A-4 for the control system parameters.

Table A-3. Electric system parameters for subsystem II

System rated parameters	*Value*	*Ac side Parameters*	*Value*	*Dc side Parameters*	*Value*
Ac L-L RMS	*100kV*	L_t	*0.013263H*	C_{dc}	*1000uF*
Rated power	*300MW*	R_t	*1.0ohm*	R_{dc}	*66.67ohm*
Dc rated voltage	*100kV*	C_f	*7.9677uF*	E_{dc}	*0 kV*
DC rated current	*1.5kA*	L_p	*0.028547H*		

The parameters of the control system in Fig. 3-5 are given as in Tab. A-4.

Table A-4. Control system parameters for subsystem II

Control Parameters	*Value*	*Control Parameters*	*Value*	*Control Parameters*	*Value*
T_3	*0.01*	K_{p1}	*20*	K_{i1}	*33.33*
T_4	*0.01*	K_{p2}	*10*	K_{i2}	*500*
T_5	*0.002*	K_{p3}	*1*	K_{i3}	*10*
T_6	*0.002*	K_{p4}	*2*	K_{i4}	*50*
T_7	*0.005*	K_{p5}	*1*	K_{i5}	*10*

Appendix B – Parameters of the VSC system in Section 4.3

The parameters of the studied system including the VSC in Section 4.3 are given as in Tab. B-1 for the electrical system and B-2 for the control system.

Table B-1. Electrical system parameters for subsystem II

System rated parameters	*Value*	*Ac side Parameters*	*Value*	*Dc side Parameters*	*Value*
Ac L-L RMS	*100kV*	L_t	*0.013263H*	C_{dc}	*1000uF*
Rated power	*300MW*	R_t	*1.0ohm*	R_{dc} *for OP I*	*66.67ohm*
Dc rated voltage	*100kV*	C_f	*11.937uF*	E_{dc}	*0 kV*
DC rated current	*1.5kA*	R_s	*2.0ohm*	R_{dc} *for OP II*	*111.11ohm*
		L_s	*0.026526H*		

Table B-2. Control system parameters for subsystem II

Control Parameters	*Value*	*Control Parameters*	*Value*	*Control Parameters*	*Value*
T_3	*0.02*	K_{p1}	*20*	K_{i1}	*33.33*
T_4	*0.02*	K_{p2}	*2*	K_{i2}	*50*
T_5	*0.004*	K_{p3}	*1*	K_{i3}	*10*
T_6	*0.004*	K_{p4}	*2*	K_{i4}	*50*
T_7	*0.005*	K_{p5}	*1*	K_{i5}	*10*

Appendix C – System configuration and related state equations used in Section 5.4

The representation of the system studied in Section 5.4.1 is given in (5.69b), which is the form in the Laplace domain:

$$Ms\Delta X = (A_0 + A_1 e^{-sT_1})\Delta X + B\Delta U \qquad (C.1)$$

The details of ΔX, M and $A = (A_0 + A_1 e^{-sT_1})$ are shown ($K_{i,j}$ are elements of K in Fig. 5-4, and some of them include delay terms):

$$\Delta \boldsymbol{X} = [\Delta i_{cd} \quad \Delta i_{cq} \quad \Delta i_{dc} \quad \Delta \alpha_{pi} \quad \Delta V_d \quad \Delta V_q \quad \Delta V_m \quad \Delta I_{sd} \quad \Delta I_{sq} \quad \Delta \omega_{err} \quad \Delta \theta_{pll}]^T$$

$$M = \begin{bmatrix} L_c & & & & & & & & & & \\ & L_c & & & & & & & & & \\ & & \mathrm{L}_{dc} & & & & & & & & \\ -\mathrm{K}_{45}K_{p\alpha} & -\mathrm{K}_{46}K_{p\alpha} & -\mathrm{K}_{43}K_{p\alpha} & 1-\mathrm{K}_{44}K_{p\alpha} & -\mathrm{K}_{41}K_{p\alpha} & -\mathrm{K}_{42}K_{p\alpha} & & & & & 1 \\ & & & & C_f & & & & & & \\ & & & & & C_f & & & & & \\ & & & & & & C_{dc} & & & & \\ & & & & & & & L_s & & & \\ & & & & & & & & L_s & & \\ & & & & & & & & & 1 & \\ & & & & & & & & & & 1 \end{bmatrix}$$

$$A = \begin{bmatrix}
 & \omega_0 L_c & & & \frac{3}{4} & \frac{\sqrt{3}}{4} & & & & \\
-\omega_0 L_c & & & & -\frac{\sqrt{3}}{4} & \frac{3}{4} & & & & \\
-K_{35} & -K_{36} & -R_{dc} - K_{33} & -K_{34} & -K_{31} & -K_{32} & 1 & & & \\
K_{i\alpha}K_{45} & K_{i\alpha}K_{46} & K_{i\alpha}K_{43} & K_{i\alpha}K_{44} & K_{i\alpha}K_{41} & K_{i\alpha}K_{42} & & & & \\
-K_{15} & -K_{16} & -K_{13} & -K_{14} & -K_{11} & \omega_0 C_f - K_{12} & & 1 & & \\
-K_{25} & -K_{26} & -K_{23} & -K_{24} & -\omega_0 C_f - K_{21} & -K_{22} & & & 1 & \\
 & & -1 & & & & & & & \\
 & & & & -1 & & & -R_s & \omega_0 L_s & \\
 & & & & & -1 & & -\omega_0 L_s & -R_s & \\
 & & & & -K_i sin\theta_{pll} & K_i cos\theta_{pll} & & & & -K_i(cos\theta_{pll} V_d + sin\theta_{pll} V_q) \\
 & & & & -K_p sin\theta_{pll} & K_p cos\theta_{pll} & & & 1 & -K_p(cos\theta_{pll} V_d + sin\theta_{pll} V_q)
\end{bmatrix}$$

The configurations of ac filters and dc circuit in the case study in section 5.4.2 are shown as in Fig. C-1 which is based on the First CIGRE benchmark system [51]. The state equations representing the ac filters can be given as in (C. 2-7).

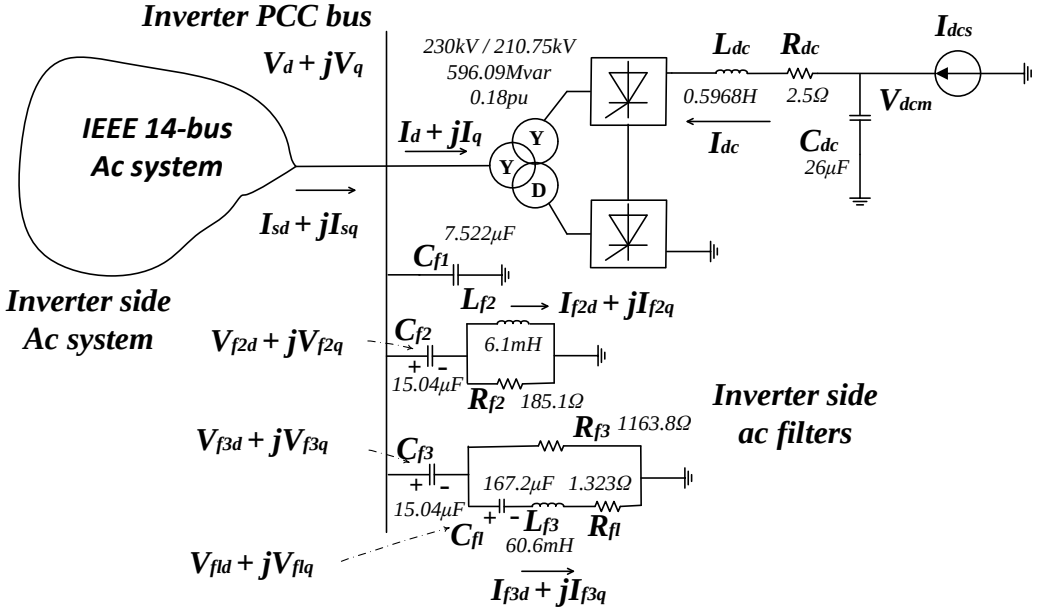

Figure C-1. The ac filters and dc circuit based on the First CIGRE benchmark system

$$C_{f1}\frac{d}{dt}\begin{bmatrix}V_d\\V_q\end{bmatrix}=\begin{bmatrix}-\frac{1}{R_{f2}}-\frac{1}{R_{f3}} & \omega_0 C_{f1}\\ -\omega_0 C_{f1} & -\frac{1}{R_{f2}}-\frac{1}{R_{f3}}\end{bmatrix}\begin{bmatrix}V_d\\V_q\end{bmatrix}-\begin{bmatrix}i_{f2d}\\i_{f2q}\end{bmatrix}-\begin{bmatrix}i_{f3d}\\i_{f3q}\end{bmatrix}+\frac{1}{R_{f2}}\begin{bmatrix}V_{f2d}\\V_{f2q}\end{bmatrix}$$

$$+\frac{1}{R_{f3}}\begin{bmatrix}V_{f3d}\\V_{f3q}\end{bmatrix}+\begin{bmatrix}I_{sd}\\I_{sq}\end{bmatrix}-\begin{bmatrix}I_d\\I_q\end{bmatrix} \qquad (C.2)$$

$$C_{f2}\frac{d}{dt}\begin{bmatrix}V_{f2d}\\V_{f2q}\end{bmatrix}=\begin{bmatrix}-1/R_{f2} & \omega_0 C_{f2}\\ -\omega_0 C_{f2} & -1/R_{f2}\end{bmatrix}\begin{bmatrix}V_{f2d}\\V_{f2q}\end{bmatrix}+\begin{bmatrix}i_{f2d}\\i_{f2q}\end{bmatrix}+\frac{1}{R_{f2}}\begin{bmatrix}V_d\\V_q\end{bmatrix} \qquad (C.3)$$

$$L_{f2}\frac{d}{dt}\begin{bmatrix}i_{f2d}\\i_{f2q}\end{bmatrix}=\begin{bmatrix}0 & \omega_0 L_{f2}\\ -\omega_0 L_{f2} & 0\end{bmatrix}\begin{bmatrix}i_{f2d}\\i_{f2q}\end{bmatrix}+\begin{bmatrix}V_d-V_{f2d}\\V_q-V_{f2q}\end{bmatrix} \qquad (C.4)$$

$$C_{f3}\frac{d}{dt}\begin{bmatrix}V_{f3d}\\V_{f3q}\end{bmatrix}=\begin{bmatrix}-1/R_{f3} & \omega_0 C_{f3}\\ -\omega_0 C_{f3} & -1/R_{f3}\end{bmatrix}\begin{bmatrix}V_{f3d}\\V_{f3q}\end{bmatrix}+\begin{bmatrix}i_{f3d}\\i_{f3q}\end{bmatrix}+\frac{1}{R_{f3}}\begin{bmatrix}V_d\\V_q\end{bmatrix} \qquad (C.5)$$

$$C_{fl}\frac{d}{dt}\begin{bmatrix}V_{fld}\\V_{flq}\end{bmatrix}=\begin{bmatrix}0 & \omega_0 C_{fl}\\-\omega_0 C_{fl} & 0\end{bmatrix}\begin{bmatrix}V_{fld}\\V_{flq}\end{bmatrix}+\begin{bmatrix}i_{f3d}\\i_{f3q}\end{bmatrix} \qquad (C.6)$$

$$L_{f3}\frac{d}{dt}\begin{bmatrix}i_{f3d}\\i_{f3q}\end{bmatrix}=\begin{bmatrix}R_{fl} & \omega_0 L_{f3}\\-\omega_0 L_{f3} & R_{fl}\end{bmatrix}\begin{bmatrix}i_{f3d}\\i_{f3q}\end{bmatrix}+\begin{bmatrix}V_d-V_{f3d}-V_{fld}\\V_q-V_{f3q}-V_{flq}\end{bmatrix} \qquad (C.7)$$

Appendix D – Configuration and modeling of the systems used in Section 6.4

D.1 The system configuration and parameters

The case system used in Section 6.4.2 is shown in Fig. D-1.

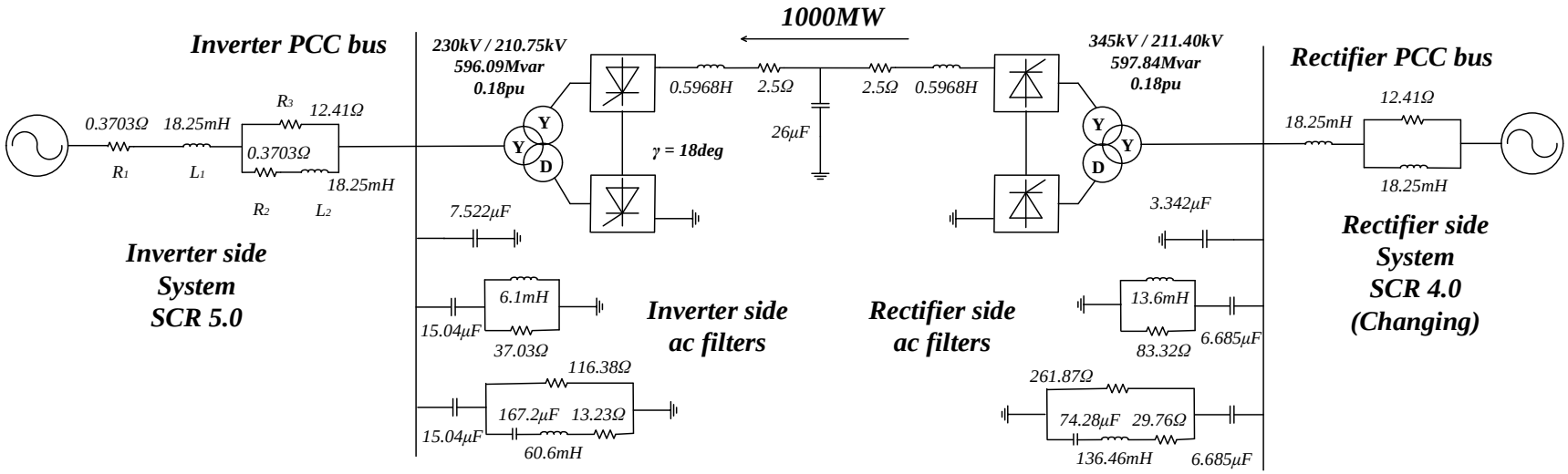

Figure D-1. Configuration of the LCC studied system

The inverter has a constant extinction angle controller as in Fig. 5-12; there is either a constant dc power control or a constant dc current controller in the rectifier side with the form in Fig. 6-4, in which the input of the upper controller is either the dc power or the dc current. All the parameters of the controllers are given in Tab. D-1.

Table D-1 Parameters of the controllers

Rectifier Controller	Value of K_p	Value of K_i	Inverter Controller	Value of K_p	Value of K_i
PLL	40.0	100.0	PLL	40.0	100.0
CDC / CP	2.182	2.182	CEC	0.5	16.667

The case system used in Section 6.4.3 is shown as in Fig. D-2. One side of the converter controls the dc voltage and ac voltage; another controls the active power and ac voltage.

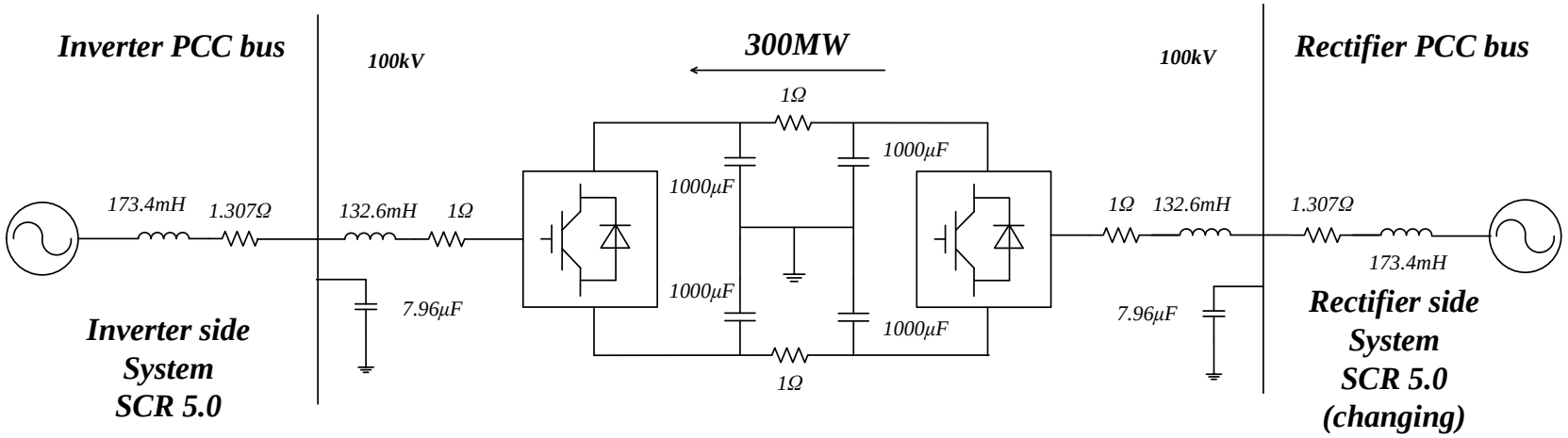

Figure D-2. Configuration of the VSC studied system

The structures of the control systems (both rectifier and inverter sides) are the same as in Fig. 3-5. Two sets of controllers are used for two sides of converters. One controls the dc voltage and ac voltage (called as 'Vdc-Vac'); the other controls the dc power and ac voltage (called as 'Pdc-Vac'). Their parameters of the decoupled controller are given as in Tab. D-2.

Table D-2. Parameters of the decoupled controller

Vdc-Vac Controller	Value of K_p	Value of K_i
PLL	20.0	33.3
Outer loop of Vdc	10.0	500.0
Inner loop of Vdc	1.0	10.0
Outer loop of Vac	2.0	50.0
Inner loop of Vac	1.0	10.0
Pdc-Vac Controller	Value of K_p	Value of K_i
PLL	20.0	33.3
Outer loop of Pdc	2.0	50.0
Inner loop of Pdc	1.0	10.0
Outer loop of Vac	2.0	50.0
Inner loop of Vac	1.0	10.0
Measure filters	Values	
T_3	0.005	
T_4	0.005	
T_5	0.002	
T_6	0.002	
T_7	0.01	

D.2 The system state equations

For the LCC system in Section 6.4.2, to get $Z_{dc,LCC}(s)$, the state equations of the rectifier ac system, the rectifier, the dc system, the inverter have to be obtained.

The model of the converters, including rectifier and inverter can be given as in (5.15) and (5.24); the rectifier side ac system can be easily modeled as it only includes a R_1-R_2//L_2 circuit and the impedance is given as:

$$Z_{ac,rec}(s) = \left[\begin{bmatrix} sL_2 & -\omega_0 L_2 \\ \omega_0 L_2 & sL_2 \end{bmatrix}^{-1} + \begin{bmatrix} R_2 & 0 \\ 0 & R_2 \end{bmatrix}^{-1} \right]^{-1} + \begin{bmatrix} R_1 & 0 \\ 0 & R_1 \end{bmatrix}$$

The ac filters in the rectifier and the inverter have same configuration as in (C.1-6), Appendix C, and can be modeled similarly.

Together with the dc system equations similar as in (5.64) and (5.65), we can get the state equation form of the dc subsystem, as in (6.14).